

N° d'ordre : 42364

THÈSE

Présentée à

L'UNIVERSITÉ DES SCIENCES ET TECHNOLOGIES DE LILLE

Ecole Doctorale des Sciences de la Matière, du Rayonnement et de l'Environnement
UFR de PHYSIQUE

Pour obtenir le grade de

DOCTEUR

Discipline : Sciences des Matériaux

par

Baptiste PANNIER

Towards the prediction of microstructure evolution under irradiation of model ferritic alloys with an hybrid AKMC-OKMC approach

Soutenue le 27 juin 2017 devant la commission d'examen :

R. SMITH	Rapporteur
C. PAREIGE	Rapporteur
E. MESLIN	Examineur
A. LEGRIS	Président
C. DOMAIN	Co-encadrant
C.S. BECQUART	Directrice de thèse
R. NGAYAM HAPPY	Invité

Remerciements

À l'issue de ces trois années de thèse, je tiens à remercier toutes les personnes qui ont contribué directement ou indirectement à la réalisation de ce travail.

En premier lieu, je souhaite remercier Charlotte Becquart, ma directrice de thèse ainsi que Christophe Domain, mon co-encadrant à EDF. Durant ces années de thèse, ils m'ont accordé le temps ainsi que le suivi nécessaire au bon déroulement de ce travail. Je tiens à saluer leurs compétences scientifiques, leurs disponibilités ainsi que leurs patiences.

Je remercie également, Philippe Ollar, Chef du département Matériaux et Mécanique des Composants (MMC) au sein d'EDF ainsi qu'Oliver Dupond et Bertrand Chassignole chefs du groupe Métallurgie T27 pour leur accueil.

Ce travail faisant partie du projet EDF R&D PERFORM II et du projet Européen SOTERIA, il a été en partie supervisé par Marc Berveiller, chef de ce projet, que je remercie pour son implication et sa participation.

Je tiens tout d'abord à remercier M. Alexandre Legris pour avoir accepté de présider ma soutenance de thèse. Je remercie aussi les deux rapporteurs M. Roger Smith et Mme Cristelle Pareige qui ont accompli un travail appliqué dans la lecture de ce manuscrit. Leurs remarques ont permis d'aboutir à une discussion constructive et enrichissante lors de la soutenance de cette thèse.

Je remercie également Mme Estelle Meslin et M. Raoul Ngayam Happy d'avoir accepté d'être présent lors de la soutenance. Leurs questions pertinentes ont permis d'éclairer certains points importants de ce travail.

Un grand merci aussi à Gilles Adjanor pour sa bonne humeur quotidienne, pour son support aussi bien scientifique que technique.

Durant le bref temps où nous nous sommes croisés à EDF, Julien Vidal a toujours su apporter un point de vue complémentaire lors de nos nombreuses discussions. Je l'en remercie.

Cette aventure n'aurait bien évidemment pas été la même sans le plateau MAI. Pour cette raison, je tiens à remercier chaleureusement tous mes collègues thésards. Ainsi, je remercie Emeric Plancher, Camille Trottier, Benjamin Christiaen, Abel Rapetti, Baptiste Stephan, Christoph Lechner, Marylou Boisson et Paul-Émile Plantet pour l'entre-aide et la camaraderie qui s'est dégagée de notre proximité.

Je remercie évidemment mes proches et ma famille pour le soutien qu'ils m'accordent depuis toujours.

Pour terminer, je remercie la communauté de logiciel libre qui m'a fourni les formidables outils dont je me suis servi quotidiennement.

Résumé étendu

Les matériaux de structures des réacteurs à eau pressurisée (REP) voient leur limite élastique augmenter et leur température de transition ductile-fragile se décaler vers des hautes températures sous l'effet de l'irradiation neutronique ce qui indique que les matériaux deviennent fragiles sur des plages de températures plus importantes. Afin d'améliorer les prédictions concernant le vieillissement sous irradiation de ces matériaux, il est impératif de mieux caractériser les mécanismes élémentaires conduisant aux changements des propriétés mécaniques et la microstructure (notamment la formation d'amas riches en atomes de solutés). Les processus élémentaires impliqués étant à petite échelle, il est difficile de déterminer par la seule voie expérimentale tous les mécanismes gouvernant l'évolution de la microstructure. Dans ce contexte, la méthode de Monte Carlo cinétique atomique (MCCA) est adaptée pour simuler le devenir des défauts, impuretés et solutés sous irradiation sur des temps simulés importants.

Ce travail de thèse consistait en premier lieu à accélérer un modèle de MCCA visant à simuler l'évolution d'alliages modèles du type FeCuMnNiSiP sous irradiation neutronique. Cette accélération était désirée pour atteindre des doses ainsi que des flux comparables à l'expérience en des temps raisonnables. Pour cela, une accélération algorithmique du code de calcul LAKIMOCA a été réalisée. Les diverses optimisations apportées ont permis d'accélérer le code d'un facteur 7. Bien que cette accélération ne s'avère pas suffisante pour atteindre la dose ciblée (~0.1 dpa), elle s'est néanmoins avérée fortement appréciable pour l'étude des propriétés cinétique des amas de défauts ponctuels.

L'approche finalement retenue a été le développement d'une approche hybride entre une approche Monte Carlo atomique et Monte Carlo d'objets. Dans un premier temps, la paramétrisation du modèle objet a été réalisée dans le cas du Fe pur le biais de simulations MCCA. Ces simulations ont permis de mieux comprendre les macro évènements intervenant dans les simulations. Notamment, il a été montré que le modèle prédit que les amas d'interstitiels sont immobiles à partir de la taille 13. De plus, ces amas n'émettent pas à la température d'intérêt (~600 K). En introduisant la paramétrisation ainsi obtenue dans le modèle objet, nous avons pu comparer les résultats obtenus avec l'approche hybride avec ceux obtenus avec la méthode MCCA « classique ». Les deux approches conduisent à des résultats identiques comme le montre la Figure 1 illustrant le bon accord obtenu par une comparaison directe entre la méthode hybride et le MCCA dans le cas d'un recuit isochrone. Le temps de calcul pour obtenir ces résultats a été divisé par 200.

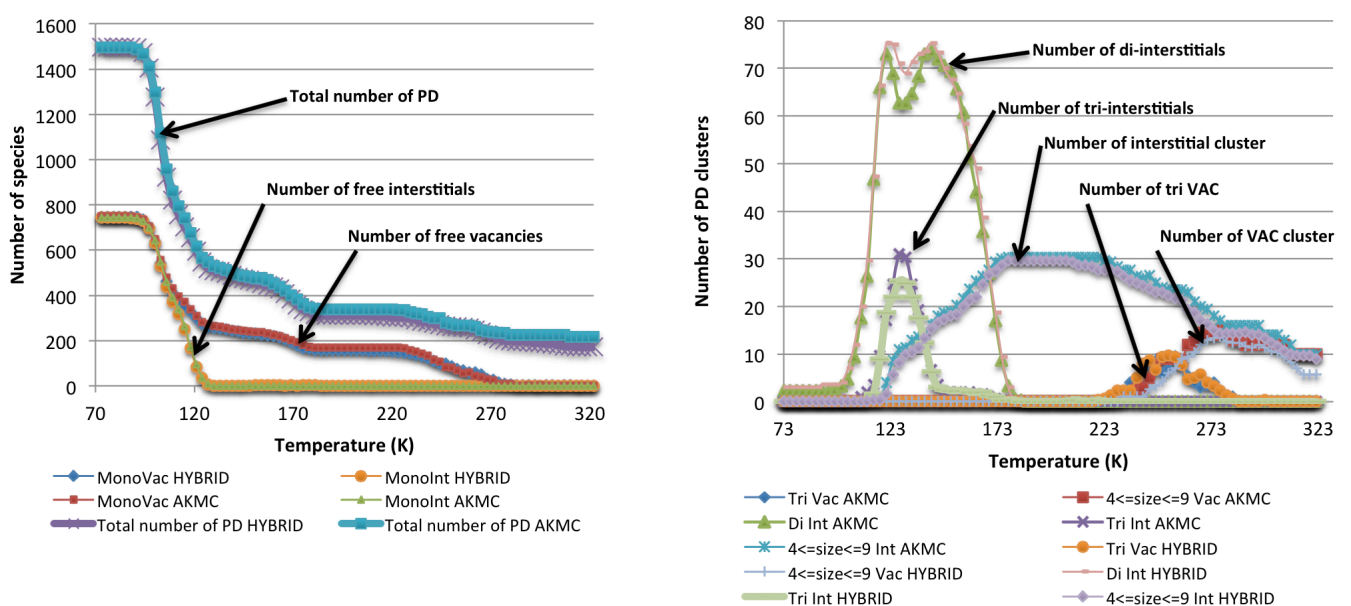


Figure 1 : Évolution de la population de défauts ponctuels en fonction de la température par la méthode hybride et le MCCA.

Pour les simulations sous irradiations (avec la paramétrisation « Pair2NN-Vincent » [1-2]), l'approche hybride a conduit une accélération des temps de calcul d'environ deux ordres de grandeur, permettant ainsi de simuler des doses correspondant à 40 ans d'irradiation dans le Fe pur. Ces résultats ont mis en évidence différentes limitations du modèle : absence d'amas de lacunes à la plus haute dose et pas d'effet de flux. L'incapacité du modèle à reproduire des effets de flux a été comblée par l'ajout d'un absorbeur visant à réduire la force de puits des joints de grains ainsi que par l'ajout de pièges permettant de rendre compte de la présence d'impuretés dans le fer pur.

Dans un deuxième temps, la méthode hybride a été adaptée à la présence de solutés. Pour mettre au point la paramétrisation des objets mixtes (défauts-solutés), les propriétés des amas de défauts ponctuels ont été étudiées par MCCA dans le cadre des alliages binaires. Nous avons constaté qu'obtenir des lois « simples » permettant de prédire les propriétés d'un objet en fonction de sa composition/taille s'est révélée être très difficile. En effet, le comportement des différents types de solutés en présence de défauts ponctuels varie fortement d'une espèce à l'autre. Néanmoins, en exploitant le fait que les amas de SIA sont immobiles d'après le modèle MCCA, il a été possible d'atteindre la dose ciblée dans le cas d'alliages complexes. La Figure 2 présente une comparaison entre la composition moyenne des amas de solutés simulés et celle observée expérimentalement.

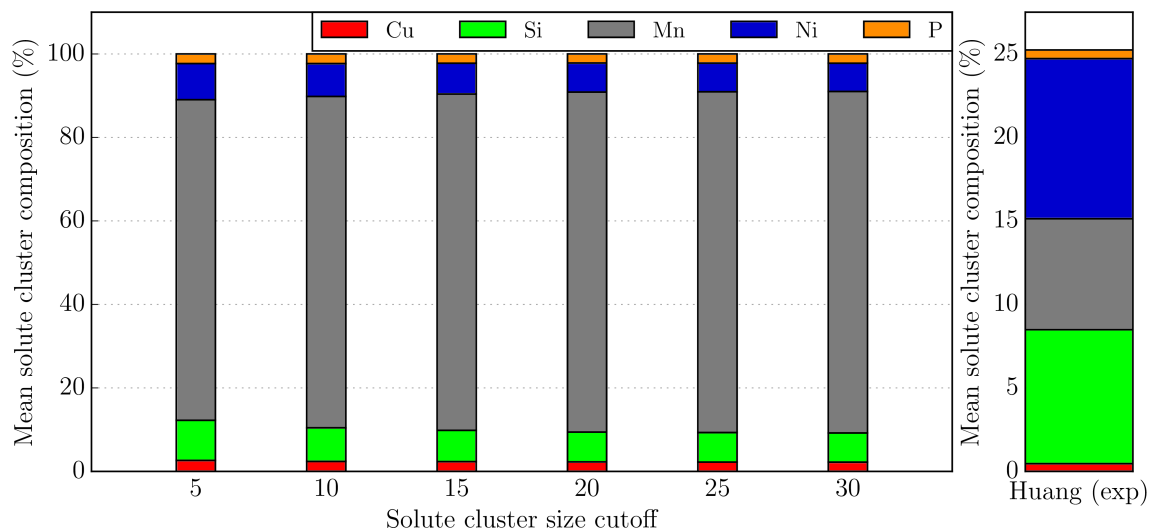


Figure 2 : Évolution de la composition moyenne des amas de solutés simulés dans Fe-0.05Cu-1.38Mn-0.69Ni-0.47Si-0.01P (at.%) à 150 mdpa. Un résultat expérimental provenant de la thèse de Huang [3] pour un alliage similaire est aussi présenté. La fluence expérimentale correspond à 60 ans d'irradiation en production (150 mdpa).

Les simulations à hautes doses dans les alliages du type FeCuMnNiSiP ont aussi mis en évidence des différences entre les microstructures simulées et celles observées expérimentalement. Pour pallier ce problème, un nouveau modèle de cohésion basé sur des interactions de paires dépendantes de la concentration locale a été développé et paramétré (modèle « CDP »). L'avantage de ce modèle est qu'il offre un nombre plus important de degrés de liberté permettant de reproduire les prédictions de DFT PAW sur une large variété d'objets. L'objectif du nouveau modèle de cohésion était d'une part d'assurer un transport des solutés par mécanisme lacunaire en meilleur accord avec les résultats récents issus de la DFT et d'autre part de prédire une stabilité plus importante des amas de Mn-Ni-Si en accord également avec les calculs DFT. Une librairie pour la recherche de paramétrisations possibles a été développée pour faciliter l'ajustement du plus grand nombre de paramètres présents dans le modèle CDP. La Figure 3 illustre les améliorations du nouveau modèle de cohésion par rapport au précédent pour des amas de taille 6 contenant du Cu, Ni, Mn et des lacunes.

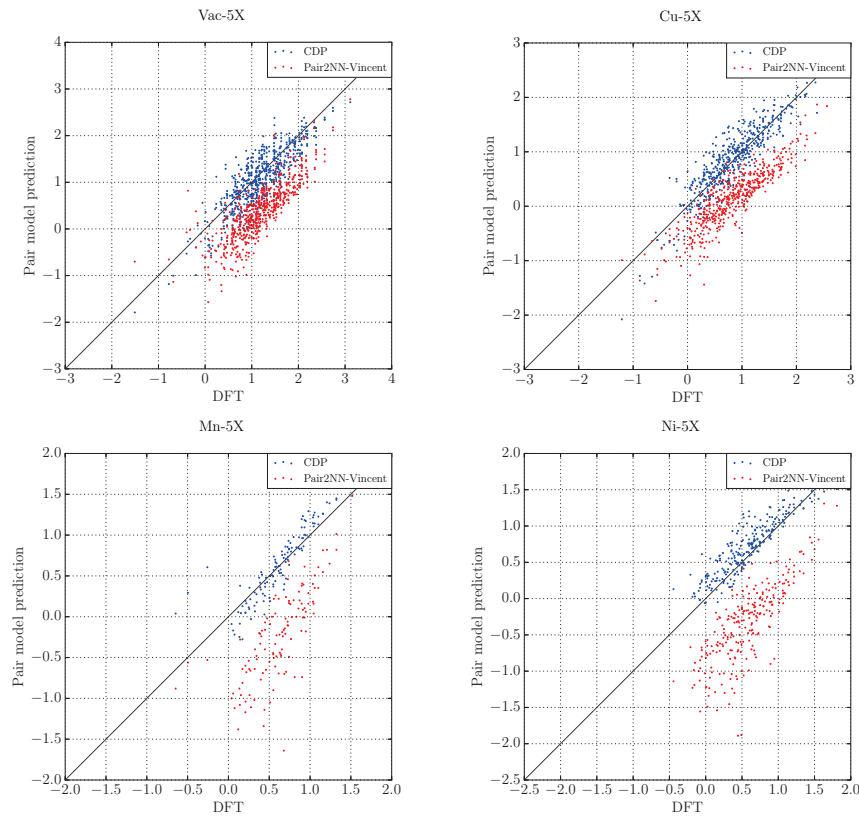


Figure 3 : Énergies de liaison entre une espèce Y et un amas de taille 5. Y peut être un Cu, un Mn, un Ni ou une lacune. L’amas de taille 5 peut être composé de différents solutés ou non. Les prédictions du modèle CDP ainsi que celles de la précédente paramétrisation « Pair2NN-Vincent » sont comparées à la DFT.

Les résultats obtenus sont plus en accord avec les calculs DFT récents. Bien que le nouveau modèle de cohésion soit numériquement plus lourd, il a été possible d’atteindre la dose visée en le couplant à l’approche hybride. Comme le montre la Figure 4, les prédictions concernant la composition moyenne des amas de solutés sont également en meilleur accord avec l’expérience. En particulier, la teneur en Ni et Si de ces amas est plus élevée que celle obtenue en utilisant l’ancienne paramétrisation.

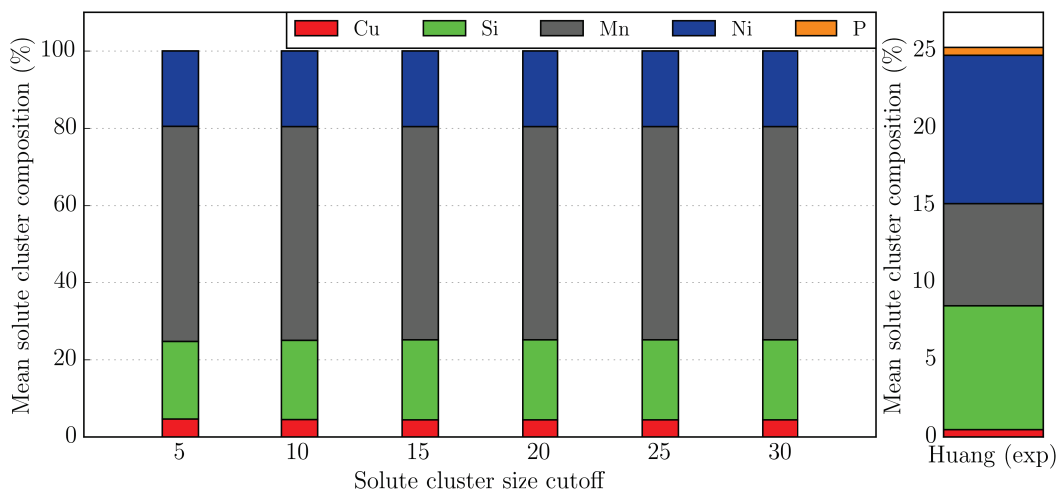


Figure 4 : Évolution de la composition moyenne des amas de solutés simulés avec le modèle CDP dans Fe–0.05Cu–1.38Mn–0.69Ni–0.47Si (at.%) à 85 mdpa. Un résultat expérimental provenant de la thèse de Huang pour un alliage similaire est aussi présenté [3]. La fluence expérimentale correspond à 60 ans d’irradiation en production (150 mdpa).

Références :

- [1] E. Vincent, PhD thesis, “Simulation numérique à l'échelle atomique de l'évolution microstructurale sous irradiation d'alliages ferritiques”, Lille University, 2006.
- [2] R. Ngayam-Happy, PhD thesis, “Prévisions de l'évolution microstructurale sous irradiation d'alliages ferritiques par simulations numériques à l'échelle atomique”, Lille University, 2010.
- [3] H. Huang, PhD thesis, “Influence de l'irradiation aux neutrons sur le vieillissement des aciers de cuves des réacteurs nucléaires à eau pressurisée,” Rouen University, 2012.

Glossary

AKMC: Atomic Kinetic Monte Carlo
APT: Atom Probe Tomography
BCC: Body Centered Cubic
CALPHAD: Calculation of Phase Diagrams
CDB: Coincidence Doppler Broadening
CDP: Concentration Dependent Pairs
DBTT: Ductile-Brittle Transition Temperature
DFT: Density Functional Theory
DPA: Displacement Per Atom
FISE: Final-Initial System Energy
KMC: Kinetic Monte Carlo
LAE: Local Atomic Environment
LDA: Local Density Approximation
MMC: Metropolis Monte Carlo
MNP: Manganese-Nickel Precipitate
MNS: Manganese-Nickel-Silicon
MTR: Material Test Reactors
NEB: Nudged Elastic-Band
NN: Nearest Neighbor
OKMC: Object Kinetic Monte Carlo
PAS: Positron Annihilation Spectroscopy
PAW: Projector Augmented Wave
PBC: Periodic Boundary Condition
PBE: Perdew-Burke-Ernzerhof
PD: Point Defect
PKA: Primary Knocked-on Atom
PSI: Programme de Surveillance à l'Irradiation
PWR: Pressurized Water Reactor
RPV: Reactor Pressure Vessel
SANS: Small-Angle Neutron Scattering
SAXS: Small Angle X-rays Scattering
SCMF: Self-Consistent Mean Field
SIA: Self Interstitial Atom
TEM: Transmission Electron Microscopy
USPP: Ultra-Soft Pseudopotential
VWN: Vosko-Wilk-Nusair

Contents

Introduction	1
Chapter 1. Nanofeatures under irradiation	7
1.1 Introduction	7
1.2 Vacancy clusters	8
1.2.1 Experimental techniques	8
1.2.2 Pure iron	9
1.2.3 Solute effects	12
1.2.3.1 Effects of copper	12
1.2.3.2 Effects of nickel and manganese	13
1.2.3.3 Vacancy affinity with solutes	15
1.2.4 RPV steels	16
1.3 Solute clusters	17
1.3.1 Experimental techniques	17
1.3.2 The effect of Cu	17
1.3.3 The effects of nickel and manganese	18
1.3.4 RPV steels	19
1.3.4.1 Thermal ageing	19
1.3.4.2 Irradiation	20
1.3.4.3 MNS thermal stability	22
1.3.4.4 MNS formation mechanism	22
1.4 Self interstitial clusters	24
1.4.1 Experimental techniques	24
1.4.2 The mono interstitial in α iron	24
1.4.3 Isochronal annealings	24
1.4.4 Dislocation loops	25
1.4.4.1 Formation mechanism	25
1.4.4.2 Solute effect	26
1.4.5 The C15 clusters	26
1.5 Conclusion	27
1.6 Bibliography	28
Chapter 2. Simulation methods and models	33
2.1 Introduction	33
2.2 Atomic jump processes	34
2.2.1 Uncorrelated random walk	35
2.2.2 Correlated random walk	35
2.2.3 Transport coefficients	36
2.2.4 Energetic considerations	36
2.3 Cohesive models	37
2.3.1 The ab-initio method	37
2.3.1.1 Generalities	37
2.3.1.2 Variational principle	38
2.3.1.3 The Hartree-Fock approximation	38
2.3.1.4 Density functional theory (DFT)	39
2.3.1.5 DFT Code and methodology	40
2.3.2 The cluster expansion model	41
2.3.3 Concentration dependent model	42
2.4 Migration energy and prefactor	42
2.5 The Monte Carlo method	44
2.5.1 Generalities	44
2.5.2 The Metropolis algorithm	45

2.6	The Kinetic Monte Carlo method	45
2.6.1	Generalities.....	45
2.6.2	The AKMC approach retained.....	48
2.6.2.1	The energetic model.....	48
2.6.2.2	The migration model.....	50
2.6.3	Simulated versus physical time.....	51
2.6.4	The irradiation model.....	52
2.6.5	The grain boundary model.....	52
2.6.6	Analysis of the AKMC results.....	52
2.7	The Object Kinetic Monte Carlo method	52
2.8	AKMC acceleration methods	53
2.8.1	Temperature Accelerated Dynamics.....	54
2.8.2	Parallel Kinetic Monte Carlo.....	54
2.8.3	First passage KMC.....	55
2.8.4	The energy basin finding algorithm.....	55
2.8.5	Hybrid AKMC/OKMC.....	56
2.8.6	Coarse-grained KMC.....	56
2.9	Conclusion	57
2.10	Bibliography	57
Chapter 3.	Improvements of the AKMC model	61
3.1	Introduction	61
3.2	Algorithmic optimization of the code	62
3.2.1	Generalities.....	62
3.2.2	Jump frequency calculation.....	63
3.2.3	Jump selection algorithm.....	65
3.2.4	Back-jump algorithm.....	67
3.2.5	Other optimizations.....	67
3.2.6	LAKIMOCA restructuring.....	68
3.3	The hybrid AKMC/OKMC method	68
3.3.1	The model in pure iron.....	68
3.3.1.1	Point defect cluster's diffusion.....	70
3.3.1.2	Point defect cluster's emission.....	70
3.3.2	Parameterization of the hybrid method for the pure iron system.....	71
3.3.2.1	AKMC study of point defect cluster properties.....	71
3.3.2.2	Validation of the parameterization.....	74
3.3.3	Pure iron under irradiation.....	74
3.3.4	Model with solute treatment.....	76
3.3.5	Parameterization.....	77
3.3.5.1	The FeCu system.....	77
3.3.5.2	Properties of the vacancy-Mn/Ni clusters.....	80
3.3.5.3	Properties of the vacancy-Si clusters.....	80
3.3.5.4	Outcomes of the hybrid AKMC/OKMC method with solutes.....	82
3.3.6	The hybrid method in the RPV system.....	82
3.4	Features for grain microstructure modeling	89
3.4.1	The grain boundary model.....	89
3.4.1.1	Probabilistic absorbing surfaces.....	89
3.4.1.2	The absorber model.....	90
3.4.1.3	Comparing absorbing surfaces and the absorber model.....	90
3.4.2	Traps in the AKMC.....	94
3.4.2.1	The model.....	94
3.4.2.2	Parameterization.....	95
3.4.2.3	Results.....	97
3.5	Conclusion	98
3.6	Bibliography	100

Chapter 4. Concentration dependent cohesive model: parameterization development and irradiation results	101
4.1 Introduction.....	101
4.2 Comparison of the parameterizations found in the literature.....	102
4.2.1 Thermodynamic aspects	103
4.2.2 Metropolis Monte Carlo simulations.....	104
4.2.3 Kinetic aspects.....	105
4.2.4 Transport through a vacancy mechanism	106
4.2.5 Transport through a SIA mechanism.....	107
4.2.6 Outcome of the parameterization comparison.....	109
4.3 Development of a concentration dependent parameterization.....	110
4.3.1 Principle of the CDP type approach	111
4.3.2 Parameterization strategies	114
4.3.3 Parameterization of the binary systems.....	117
4.3.3.1 The FeCu system.....	117
4.3.3.2 The FeMn, FeNi and FeSi systems	119
4.3.4 Parameterization of the ternary/ quaternary systems.....	122
4.3.5 Parameterization of the vacancies	125
4.3.6 Parameterization validation	128
4.3.7 Monte Carlo simulations on RPV model alloy.....	130
4.3.8 Kinetic properties	131
4.4 Simulations of irradiation	133
4.4.1 Comparison between CDP and “Pair2NN-Vincent” at low dose.....	133
4.4.2 Coupling the CDP model with the hybrid AKMC/OKMC	137
4.4.3 Vacancy object parameterization effects.....	138
4.4.4 Flux and temperature effects	141
4.4.5 Copper effects.....	143
4.4.6 Synthesis of the irradiation simulations with the hybrid CDP model	149
4.5 Conclusion.....	150
4.6 Bibliography	150
General conclusions and perspectives.....	153
Annex I: LAKIMOCA profilings.....	157
Annex II: Proposal for future developments	160
Annex III: Performance aspects of the CDP model	162
Annex IV: New commands in LAKIMOCA inputs	164
Annex V: New input file formats.....	166
Annex VI: The speed-check file.....	168
Annex VII: X-Y-Z clusters properties using the CDP model.....	169

Introduction

1. Industrial context

Structural materials of the Pressurized Water Reactor (PWR) are exposed to neutron irradiation during in-service conditions. These conditions can change the mechanical properties of important components such as the Reactor Pressure Vessel (RPV) [1]. Since the RPV cannot be changed, its lifetime directly rules the exploitation duration of the whole reactor. This component is made of low-alloyed ferritic steels containing different solutes. Some solutes are added to improve the properties of the steel or for metallurgic necessities. Others such as copper or phosphorus are impurities. Table 1 shows the typical range of solute content.

Cu	Mn	Ni	Si	Mo	Cr	P	C
0.04—0.17	0.3—1.5	0.19—1.3	0.2—1.2	0.2—0.63	0.05—0.53	<0.02	0.23—1.15

Table 1: Range of typical solute content present in the RPV steels in at.% (from [2]).

Concerning the French RPV steel, the typical composition of the base metal is given in Table 2:

Cu	Mn	Ni	Si	Mo	Cr	P	C
0.06	1.26	0.7	0.38	0.32	0.26	0.01	0.74

Table 2: Solute content present in the French RPV steels (at.%).

In order to guarantee the mechanical integrity of the vessel, a surveillance program of the irradiation (PSI – Programme de Surveillance à l'Irradiation) has been established during the 1970s [3]. For each reactor, representative samples of the considered RPV steels are placed in the reactor in order to receive flux, 2 – 3 times higher than the flux received by the pressure vessel, to anticipate the ageing of the steels. These samples are periodically extracted from the reactors in order to evaluate the evolution of the material in its environment. This program, coupled with neutron-irradiated materials from experimental reactors (MTR – Material Test Reactors), has allowed collecting an important database of irradiated microstructures. These microstructures have been characterized using various techniques that cover the macroscopic to the atomic scales. All these experiments are part of an international effort aiming at a better understanding of the mechanisms leading to the microstructural evolution of these alloys under irradiation. One way commonly used to quantify the embrittlement experienced by the material is to measure its ductile-brittle transition temperature (DBTT). This property is known to exhibit a shift after irradiation indicating that the material is brittle at higher temperatures in the irradiated case than in the as-received condition. Figure 1 illustrates the shift of this transition temperature (called ΔTT).

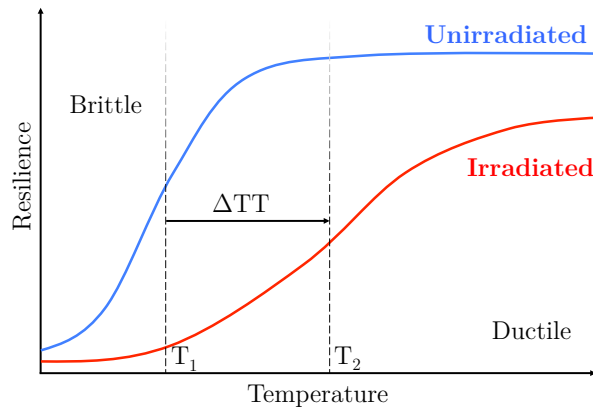


Figure 1: Illustration of the shift in the ductile-brittle transition temperature (DBTT) induced by the irradiation.

Since it is crucial to predict the ΔTT evolution over time, data collected from the surveillance program were employed in statistical model to provide an empirical embrittlement formula. In France, for example, one of the formula is [4]:

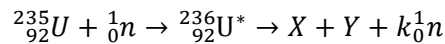
$$\Delta_{TT} = (13.7 + 1537(P - 0.008) + 238(Cu - 0.08) + 192Ni^2Cu)\phi^{0.35}$$

where Cu, Ni and P correspond to the corresponding solute content in the steel (given in wt.%) and ϕ is the fluence expressed in 10^{19} n.cm⁻² ($E > 1$ MeV). The terms $(P - 0.008)$ and $(Cu - 0.08)$ are set to zero if they are negative.

This embrittlement formula is periodically revised to take into account new results from the PSI. While statistical tools are powerful, they lack physical basis. Building an embrittlement model based on physical considerations is a challenging task and a necessary step for a better understanding of the elementary mechanisms leading to the microstructural evolution under irradiation. This PhD thesis takes place in the intention to improve the microstructure evolution prediction in order to better determine the embrittlement rate of the RPV steels.

2. Irradiation at the atomic scale

Changes at the macroscopic scale are induced by structural modifications at the atomic level. Presently, nuclear energy production is carried out by fission of heavy nuclei. The principle of this reaction is given below in the case of the uranium-235 [5]:



where n is a neutron, U^* is a uranium atom in an excited state, X and Y are fission products, k is a positive integer.

The fission reaction produces therefore an important amount of energetic neutrons (of the order of MeV), which interact with surrounding materials. In the case of an elastic interaction between a neutron and an atom in the material, a certain amount of energy is transmitted. If this energy is higher than the threshold displacement energy¹ E_d , the atom is ejected from its crystallographic site. There is creation of one vacancy and one interstitial. If the transmitted energy to the target atom is higher than $2E_d$, the target atom can become a projectile called PKA² and remove other atoms from their crystallographic sites. This phenomenon is called

¹ Threshold displacement energy: required energy to remove an atom from its crystallographic site without recombination happens. It is equal to about 40 eV in Fe [6].

² PKA: Primary Knocked-on Atom

atomic displacement cascade and is responsible for a point-defect oversaturation in the material. Figure 2 illustrates this phenomenon.

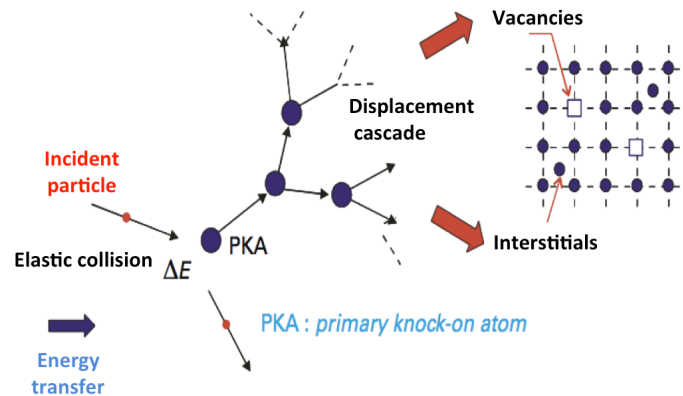


Figure 2: Illustration of a displacement cascade created by a neutron.

An atomic displacement cascade can be decomposed into two distinct phases [7]:

- A collision phase where the maximal number of point defects is reached;
- A recombination phase where the number of point defects decreases. At the end of these phases, some point defects remain, some of them agglomerated in clusters.

With the aim of quantifying the irradiation damage, the notion of displacement per atom (dpa) has been introduced. This notion is related to the number of atoms removed from their crystallographic site. In order to evaluate the dpa, the NRT [8] standard is widely used in the community. In this context, the number of Frenkel pairs generated by the PKA is expressed as:

$$N_d = \frac{0.8E_{DAM}}{2E_d}$$

Where E_{DAM} corresponds to the kinetic energy transferred to the PKA.

From the number of Frenkel pairs generated by the PKA, the mean number of time an atom in the material has been ejected from its crystallographic site can be calculated. This quantity corresponds to the dpa_{NRT} . For example, at 0.1 dpa, one in ten atom in the material has been ejected from its site. After 40 years of in service condition, the mean displacement per atom experienced by the vessel is about 0.1 dpa. This corresponds to an important amount of point defects introduced in the system.

When one point defect (PD) encounters another PD of the same type, it can agglomerate to form a dimer. Other point defects can agglomerate with the dimer and thereby increase the size of the aggregate. This leads to the formation of point defect clusters such as cavities and vacancy/interstitial dislocation loops.

One important issue concerning the RPV steels under irradiation is the formation of several nanofeatures that contribute to the mechanical properties evolution:

- Accumulation of point defect clusters such as interstitial loops and vacancy clusters;
- Formation of solute-rich clusters. Figure 3 illustrates these nanofeatures;
- Solute atoms segregation at the grain boundaries.

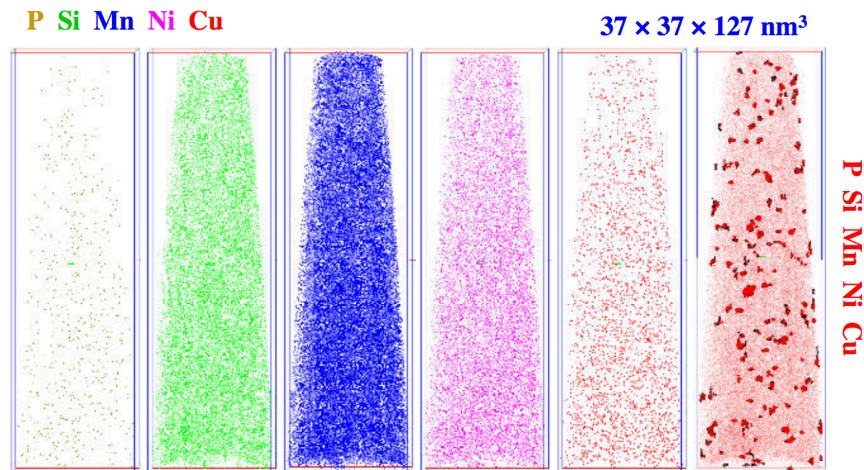


Figure 3: Solute-rich clusters observed by Atom Probe Tomography (APT) in a RPV steel irradiated at $11.4 \cdot 10^{23} \text{ n.m}^{-2}$ [9]. The different solute atoms are displayed in different colors. The distribution of solutes is not homogeneous after irradiation.

The point-defect oversaturation has two consequences. Firstly, it can lead to a radiation-accelerated diffusion making the system return faster to its equilibrium state: this is referred to as radiation-enhanced diffusion in the literature [10]. Secondly, because of the tendency of the point defects to eliminate on sinks (e.g. dislocations, grain boundaries, surfaces), the concentration of PD near the sinks is lower than the average concentration. This results in concentration gradients inducing a flow of PD nearby sinks. In the case of the existence of an affinity between solute atoms and PD, the solute flux can point in the same direction as the PDs flux. This can lead to solute segregation at sinks (for example solute segregation at the grain boundaries). In the absence of affinities between solute atoms and PDs, the solute flux and the PD flux can point to opposite directions (involving a possible solute depletion at sinks). This solute-defect flux coupling is typical of non-equilibrium phenomena observed under irradiation. Nanofeatures formed by these processes are denoted as radiation-induced.

In this thesis, the focus is made on the point defect as well as the solute clusters formed during irradiation. The mechanisms responsible for the formation of solute-rich clusters are indeed still under debate in the community, because, among other issues, the phase diagram of such a complex system is unknown. It is thus difficult to balance the contributions of radiation enhanced or radiation induced mechanism in their formation.

3. Scientific approach

Due to the important number of processes involved in the microstructure evolution, the fact is that these questions cannot be solved only by the experimental approach. Numerical simulations are then necessary to support the experimental effort. From the numerical simulation point of view, predicting the evolution of the material is a challenging task that requires a multi-scale approach. In this context, EDF, in collaboration with Lille University, has been contributing for more than 20 years to research activities and European projects (PERFECT and PERFORM60) [11] [12] aiming to propose a multi-scale model for the RPV and core internals evolutions under irradiation. The idea behind this approach is to adopt a bottom-up strategy. Starting from the lowest time/scale, the results obtained with one scale are used as input data the higher scale models. Figure 4 presents this method (starting from first principles electronic structure calculations to finite element studies at the scale of the component). Currently, a platform consisting of a chain of different code exists and

allows to compute the hardening of a specific alloy from the knowledge of the PKA spectrum [13]. Furthermore interaction and exchange between modeling works and experimental work is crucial and provides more than a simple experimental validation. In this framework, EDF, Lille University and Rouen University have formed a joint laboratory EM2VM (Étude et Modélisation des Mécanismes de Vieillessement des Matériaux).

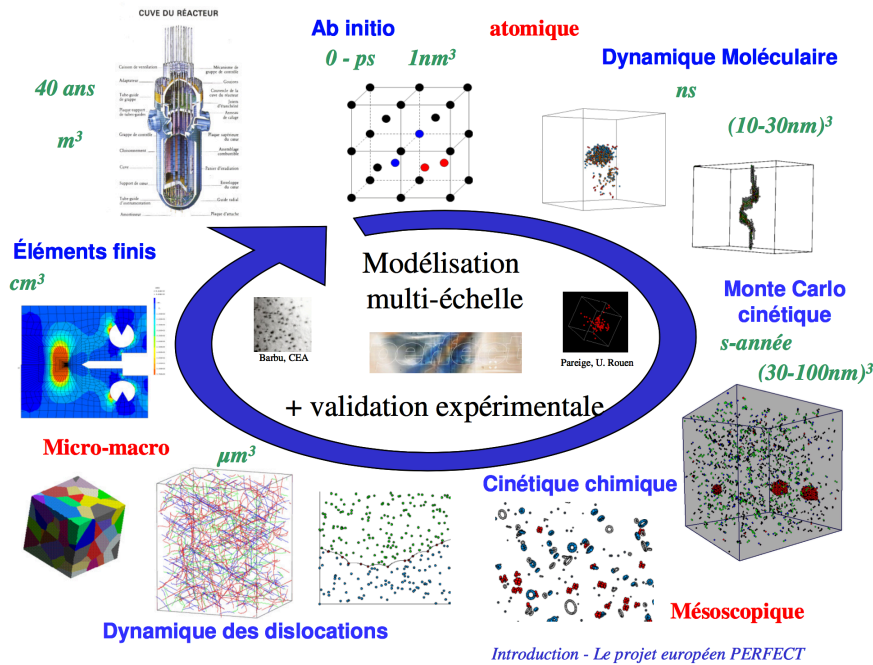


Figure 4: Schematic representation of the links between the different simulation techniques used in PERFECT, PERFORM60 and SOTERIA to simulate the microstructural evolution of RPV steels [14].

This thesis work takes place at the edge of the atomic model, i.e. using an atomic kinetic Monte Carlo approach. And this work contributes to the EDF R&D project PERFORMII and the European project SOTERIA.

4. Thesis objectives

Kinetic Monte Carlo simulations are quite adapted and widely used to treat diffusion problems requiring very large time scales (typically some decades). A computer code based on KMC methods named LAKIMOCA (LAtice KInetic MOnte CARlo) has been developed at EDF [15]. Two approaches can be used: an "object" approach as well as an "atomic" approach. The object approach has the advantage of being fast but explicit chemical effects are not taken into account. In contrast, the "atomic" approach takes into account chemical effects but it is much slower and the parameterization a very complex task: it has already been the objective of two PhD theses between EDF and the UMET laboratory at Lille 1 University [16], [17].

The "atomic" version of LAKIMOCA cannot perform long time irradiation simulations without getting away from the real reactor core conditions (especially low flux condition). Computation takes several months to reach 30 mdpa doses whereas the targeted dose is instead of 0.1 dpa. To overcome this limitation, this PhD thesis focuses on accelerating the AKMC code. The other objective was to improve the model. It turned out during this thesis that the model developed earlier had some limitations. Hence, an important part of this PhD work has been dedicated to the development of an alternative model to overcome these issues.

5. Manuscript organization

The manuscript is organized in four chapters. In the bibliographic chapter, the different types of nanofeatures observed under irradiation will be exposed. Experimental observation will also be compared to simulation results. In the second chapter, the numerical methods employed in this thesis will be exposed as well as the KMC acceleration techniques available in the literature. The third chapter will be mainly dedicated to the hybrid AKMC/OKMC method that has been implemented in order to accelerate the AKMC simulations. Due to deviations between the high doses simulated microstructures from the microstructures observed experimentally, a new cohesive model has been developed and parameterized. This will be the subject of the fourth chapter.

6. Bibliography

- [1] C. English and J. Hyde, "Radiation Damage of Reactor Pressure Vessel Steels", in *Comprehensive Nuclear Materials*, Elsevier, pp. 151–180, 2012.
- [2] J. E. Zelenty, "Understanding thermally induced embrittlement in low copper RPV steels utilising atom probe tomography", *Materials Science and Technology*, vol. 31, no. 8, pp. 981–988, Nov. 2014.
- [3] M. Akamatsu, C. Brillaud, R. Lloret, and C. Rieg, "L'irradiation de la cuve: un phénomène sous surveillance", *Revue générale du nucléaire*, 1993.
- [4] P. Petrequin, "Ames Report No 6", 1996.
- [5] C. M. Diop, "Physique des réacteurs – Les réactions nucléaires", *Techniques de l'ingénieur Physique nucléaire*, vol. 200.
- [6] ASTM E693, *Standard Practice for Characterizing Neutron Exposures in Iron and Low Alloy Steels in Terms of Displacements Per Atom (DPA)*, 1994.
- [7] R. E. Stoller, "Primary Radiation Damage Formation", in *Comprehensive Nuclear Materials*, Elsevier, pp. 293–332, 2012.
- [8] M. J. Norgett, M. T. Robinson, and I. M. Torrens, "A proposed method of calculating displacement dose rates", *Nuclear Engineering and Design*, vol. 33, no. 1, pp. 50–54, 1975.
- [9] H. Huang, PhD thesis, "Influence de l'irradiation aux neutrons sur le vieillissement des aciers de cuves des réacteurs nucléaires à eau pressurisée", Rouen University, 2012.
- [10] B. Radiguet, PhD thesis, "Etude de la formation d'amas diffus de solutés sous irradiation dans des alliages modèles ferritiques", Rouen University, 2004.
- [11] J.-P. Massoud, S. Bugat, B. Marini, D. Lidbury, and S. V. Dyck, "PERFECT - Prediction of Irradiation Damage Effects on Reactor Components: A summary", *Journal of Nuclear Materials*, vol. 406, no. 1, pp. 2–6, Nov. 2010.
- [12] A. Al Mazouzi, A. Alamo, D. Lidbury, D. Moinereau, and S. Van Dyck, "PERFORM 60: Prediction of the effects of radiation for reactor pressure vessel and in-core materials using multi-scale modelling – 60 years foreseen plant lifetime", *Nuclear Engineering and Design*, vol. 241, no. 9, pp. 3403–3415, Dec. 2010.
- [13] G. Adjanor, S. Bugat, C. Domain, and A. Barbu, "Overview of the RPV-2 and INTERN-1 packages: From primary damage to microplasticity", *Journal of Nuclear Materials*, vol. 406, no. 1, pp. 175–186, Nov. 2010.
- [14] C. S. Becquart and C. Domain, "Modeling Microstructure and Irradiation Effects", *Metallurgical and Materials Transactions A*, vol. 42, no. 4, pp. 852–870, Dec. 2010.
- [15] C. Domain, C. S. Becquart, and L. Malerba, "Simulation of radiation damage in Fe alloys: an object kinetic Monte Carlo approach", *Journal of Nuclear Materials*, vol. 335, no. 1, pp. 121–145, Oct. 2004.
- [16] R. Ngayam-Happy, PhD thesis, "Prévisions de l'évolution microstructurale sous irradiation d'alliages ferritiques par simulations numériques à l'échelle atomique", Lille University, 2010.
- [17] E. Vincent, PhD thesis, "Simulation numérique à l'échelle atomique de l'évolution microstructurale sous irradiation d'alliages ferritiques", Lille University, 2006.

Chapter 1. Nanofeatures under irradiation

1.1	Introduction	7
1.2	Vacancy clusters	8
1.2.1	Experimental techniques	8
1.2.2	Pure iron	9
1.2.3	Solute effects	12
1.2.3.1	Effects of copper	12
1.2.3.2	Effects of nickel and manganese.....	13
1.2.3.3	Vacancy affinity with solutes.....	15
1.2.4	RPV steels	16
1.3	Solute clusters	17
1.3.1	Experimental techniques	17
1.3.2	The effect of Cu.....	17
1.3.3	The effects of nickel and manganese.....	18
1.3.4	RPV steels	19
1.3.4.1	Thermal ageing	19
1.3.4.2	Irradiation.....	20
1.3.4.3	MNS thermal stability.....	22
1.3.4.4	MNS formation mechanism.....	22
1.4	Self interstitial clusters	24
1.4.1	Experimental techniques	24
1.4.2	The mono interstitial in α iron.....	24
1.4.3	Isochronal annealings	24
1.4.4	Dislocation loops	25
1.4.4.1	Formation mechanism.....	25
1.4.4.2	Solute effect	26
1.4.5	The C15 clusters	26
1.5	Conclusion	27
1.6	Bibliography	28

1.1 Introduction

Understanding the elementary mechanisms involved in the embrittlement of the reactor pressure vessel under irradiation requires decoupling the different contributions responsible for this phenomenon (matrix damage, formation of precipitates and grain boundary segregation). To do so, experimental studies of model alloys (from pure iron to RPV steels) is a solid approach that has been adopted during the last decades. From the microstructure evolution under irradiation point of view, experiments are usually performed at high temperature (~600 K). Several types of irradiation that can be performed. For the neutron irradiations, the studied materials come from the PSI or from material test reactors (MTR). Electron irradiations can also be used to avoid the atomic displacement cascades and to create only Frenkel pairs. Ions can also be used to mimic neutron irradiation without activating the sample. When it comes to investigate the properties of the defects (such as mobility), irradiation at low temperature coupled with isochronal annealing is preferred. To study the stability of the nanofeatures formed under irradiation, post irradiation annealing is an adapted technique. Despite these efforts, such a complex task cannot only be done by means of experiments. Multiscale modeling is often a necessity to support experimental observations.

In this bibliographic chapter, the different types of nanofeatures observed under irradiation will be exposed. Experimental observations will also be compared to simulation results.

1.2 Vacancy clusters

1.2.1 Experimental techniques

Positron annihilation spectroscopy (PAS) is a method adapted for studying the presence of nano-voids in materials. The physical principle behind this technique is that positrons are trapped at open-volume regions where the repulsive nucleus interactions are lower than in the average bulk. When a positron annihilates with an electron, two 511 keV γ rays are emitted in the opposite directions. They escape from the system without any interaction. Several information about the annihilation site can be extracted from these γ quanta:

- Increasing the size of the defects leads to an increase of the positron lifetime. Thus, measuring it can lead to an estimation of the size of the nano-voids (for cluster sizes larger than ~ 50 vacancies, the life-time tends to saturate making the technique unable to distinguish these types of defects [1]).
- The intensity collected in comparison with the one from a reference defect-free material gives information about the defect density.
- Due to the total momentum of the positron-electron annihilation pair, the annihilation energy gets Doppler shifted. This shift in energy can directly be recorded by means of a Coincidence Doppler Broadening spectrometer (CDB). The momentum distribution is then split in two regions. The first one is the low-momentum region. From this region, the so-called S parameter representing the ratio of low-momentum region to the total region can be extracted. This quantity is sensitive to the presence of open volume. The low-momentum region reflects annihilations with valence electrons. The second region is the high-momentum (e.g. the tail of the spectrum). The W parameter corresponds to the fraction of high-momentum annihilations. The high-momentum region is related to the core electron annihilations that hold information about the chemical nature at the annihilation site. Since positrons can get trapped at different defect sizes with different lifetimes associated, a direct observation of the size distribution and density is a non-trivial task. Hence, trapping models correspond to rate equations which are commonly used to fit the measured spectrum.

In the following sections, the vacancy cluster will be referred to as V_{size} (where size is the number of vacancies in the cluster).

A convenient way to get information about small point defect mobility is to perform isochronal annealing experiments. In general, an electron irradiation at low temperature (under 100 K) is employed to avoid displacement cascades and diffusion. Then, the temperature is increased every Δt time steps in order to unlock thermally activated events one after the other. During the experiments, a physical property is measured (generally the electrical resistivity). This property is assumed to be proportional to the number of defects. The evolution of the property or more precisely of the derivative of this property versus temperature exhibits different peaks at various temperatures, and one can associate a peak to the unlocking of a thermally activated event. Figure 1 presents a typical differential resistivity recovery spectrum in Fe.

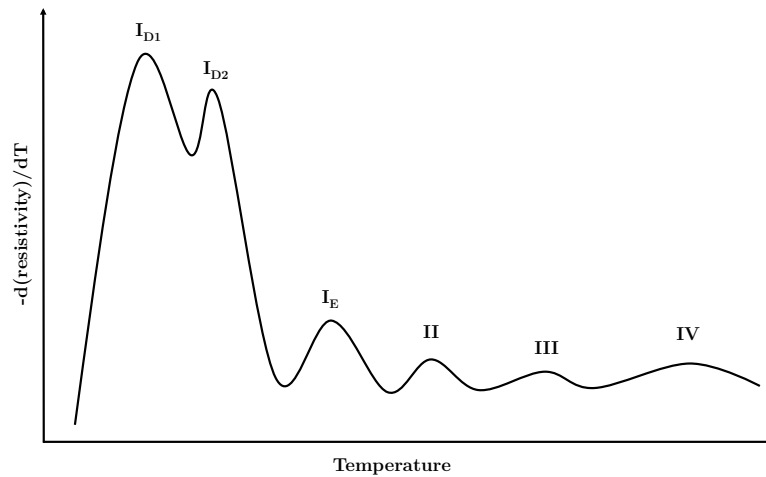


Figure 1-1: Denomination of the peaks observed on the differential resistivity recovery of irradiated iron.

Two peaks are associated to the vacancies in pure iron [2]:

- Peak III is observed beyond 200 K and is attributed to the migration of the vacancies. The estimated activation energy is equal to 0.55 ± 0.03 eV.
- Peak IV appears for very high temperature and corresponds to the dissolution of vacancy clusters.

More details concerning results from this technique (especially from the SIA cluster point of view) are provided in section 1.4.3.

1.2.2 Pure iron

Experimental observations:

Pure iron is usually employed as a reference for direct comparison with more complex systems. However, the number of PAS studies providing quantitative information such as mean sizes and densities of vacancy and vacancy clusters is limited. In their study, Eldrup et al. [3] studied a Fe specimen of 99.994 wt% purity irradiated with neutrons at 0.23 dpa ($E > 1$ MeV) at 373 K. The specimen was then annealed from 323 to 923 K with a step of 50 K every 50 min. This study provides useful information about the vacancy cluster population as well as their thermal stabilities. In the irradiated material, the authors observed two populations of vacancy clusters. The first one corresponds to vacancy clusters with an average size of ~ 9 – 14 vacancies. The second one corresponds to large cavities (sizes greater than 40 vacancies). The densities estimated are $1 \times 10^{24} \text{ m}^{-3}$ and $1.3 \times 10^{23} \text{ m}^{-3}$ respectively for the small clusters and the large ones. By increasing the temperature up to 523 K, the density and potentially the mean size of the largest vacancy cluster increases. At the same time, the density of the small vacancy clusters tends to decrease while their mean size tends to increase and reaches 10–15 vacancies. The authors suggest that this phenomenon is due to the coalescence of the smallest cavities because of their migrations. When reaching 573 K, the population composed of the smallest sizes disappears (the remaining life-time observed is associated to trapped vacancy clusters containing a few numbers of vacancies). From this temperature to the end of the annealing treatment, the population of the largest vacancy clusters decreases and becomes null at 773 K. This can be explained by the migration of these clusters (allowing their agglomerations) and by their dissociation through vacancy emissions.

Concerning the impact of the temperature during the irradiation, another study from the same authors gives interesting data [4]. The pure iron sample has been irradiated at 0.23 dpa between 323 and 623 K. The

population of large vacancy clusters (size > 50) is observed in the whole temperature range. The maximum density is observed at 473 K. Concerning the population of small vacancy cluster (size < 14), its density gradually decreases when the irradiation temperature increases. Beyond 373 K, the average size of this population starts to decrease.

Results concerning the dose dependency of the vacancy cluster population can be found in two complementary studies. Eldrup et al. [5] studied a Fe specimen of 99.995 wt% purity irradiated with neutrons at 343 K using a flux of $4 \times 10^{18} \text{ n m}^{-2} \text{ s}^{-1}$ ($E > 1 \text{ MeV}$). At 0.0001 dpa, only small vacancy clusters have been observed (size between 1 and 3 vacancies). At 0.001 dpa, the majority of the vacancy clusters are still composed of V_{1-3} but some larger cluster appears (size ~ 10 –15 vacancies). At 0.01 dpa, the distribution shifts and is centered on ~ 10 vacancy in the cluster. Moreover, large vacancy clusters (size > 50) appear. When reaching the highest dose (0.23 dpa), the majority of the population is composed of V_{10-15} clusters with a number density of $\sim 4.2 \times 10^{24} \text{ m}^{-3}$. The density of the largest vacancy clusters is about $1.0 \times 10^{23} \text{ m}^{-3}$. In a complementary study, Meslin et al. [6] studied a specimen of 99.955 at.% iron irradiated at 573 K with a flux of $9 \times 10^{17} \text{ n m}^{-2} \text{ s}^{-1}$ ($E > 1 \text{ MeV}$). They observed a decrease of vacancy cluster density when increasing the dose (from 0.025 to 0.2 dpa). During the irradiation, the average size of vacancy clusters increases from $\sim V_{1-3}$ at the lowest dose and reaches V_{10} at the highest one. Meslin et al. suggested that the decrease in the vacancy cluster density is due to the agglomeration of small vacancy clusters. According to the authors, the differences between their results and those of Eldrup et al. are induced by the lower irradiation temperature used by Eldrup. In this condition vacancy clusters are less mobile making agglomeration and elimination at sinks more difficult.

Vacancy clusters are observed in irradiated pure iron. Depending on the irradiation temperature, the vacancy cluster population can either increase (at the low temperature regime) or decrease (at the high temperature regime) when the dose increases. Mean sizes appear to increase with the dose. Increasing the annealing temperature leads to a decrease of the smallest vacancy cluster population. In the meantime, the mean size of this population tends to increase. Annealing at 773 K appears to be sufficient to erase the vacancy population.

Simulation results:

From the simulation point of view, the Object Kinetic Monte Carlo (OKMC) is a method adapted to observe the time evolution of point defect population over time (a description of the method will be provided in chapter 2). Because solute treatment is rather difficult to implement in this method, it is usually employed for the simulations of almost pure systems. In their study, Domain et al. [7] used the OKMC method to simulate the microstructure evolution of pure iron under neutron irradiation. In this model, different parameterizations were employed (allowing or not migration for species different than mono-vacancies and mono-SIA, different capture radii and trap concentration). Emission events were taken into account for both vacancy and SIA objects. Traps were also employed to simulate the presence of C and N atoms, which are present as impurities even in high purity alloys. The simulation conditions were chosen to reproduce experimental PAS analysis performed at 70 K in high purity iron by Eldrup et al. [5]. The authors observed that the set of parameters that reproduces the most experimental PAS measurements is the one allowing migration for all object sizes. It was also noticed that variations of the capture radius and the binding energy between the traps and the SIA clusters do not have much effect on the final simulated microstructure ($\sim 0.2 \text{ dpa}$ with a flux set to $10^{-6} \text{ dpa.s}^{-1}$). In a more recent study, Jansson et al. also simulated the microstructural evolution of high-purity iron under irradiation [8]. The authors also highlighted the importance of the C impurity to explain the damage accumulation. They use immobile traps to simulate the presence of C impurities along with another type of trap corresponding to the C_2V [9] complex. This complex is known to trap strongly interstitial objects.

According to the good agreements between experimental observations and the prediction of the model, the hypothesis of immobile traps appears to be acceptable as well as the assumption made of large objects mobility.

As mentioned above, being able to estimate the mobility of point-defect clusters is a crucial for long-term irradiation models such as Object Kinetic Monte Carlo and cluster dynamics. The evaluation of these quantities is usually done by means of simulations, often using the Atomic Kinetic Monte Carlo method. Figure 1-2 and Figure 1-3 present results extracted from the literature using different cohesive models for the AKMC simulations. Castin et al. employed an interatomic potential to train an artificial neural network and obtain vacancy migration parameters as a function of the local atomic environment [10]. Messina et al. as well as Konstantinovic et al. employed pair interactions based on a rigid lattice approximation [11].

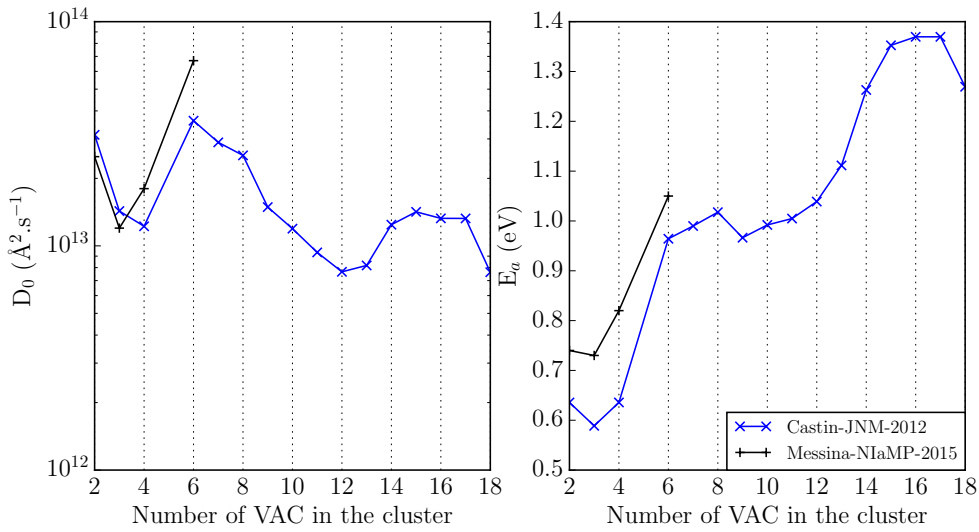


Figure 1-2: Evolution of the D_0 as well as the E_a activation energy for diffusion as a function of the number of vacancies in the cluster. References: Castin-JNM-2012 [10], Messina-NiaMP-2015 [12].

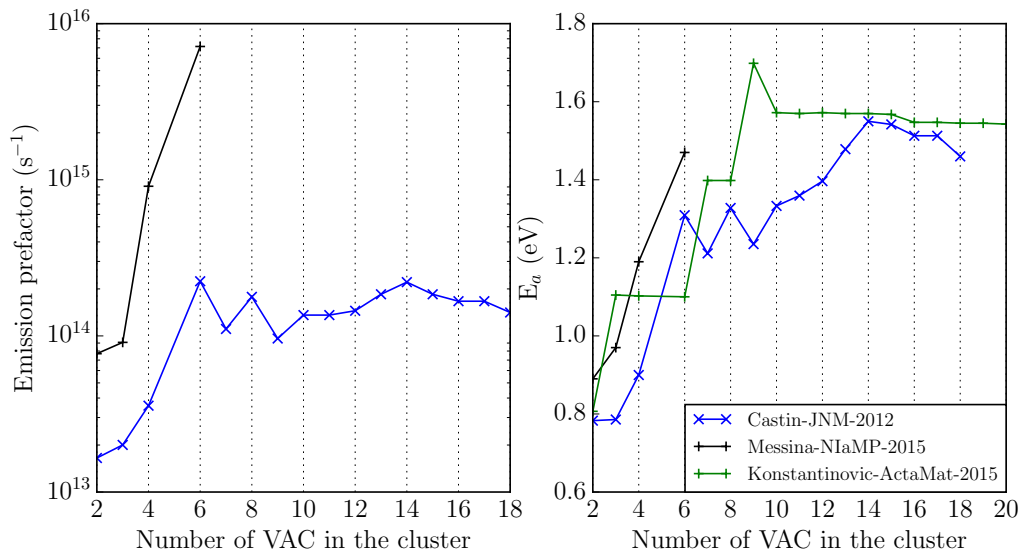


Figure 1-3: Evolution of the emission prefactor as well as the E_a activation energy for emission as a function of the number of vacancies in the cluster. References: Castin-JNM-2012 [10], Messina-NiaMP-2015 [12], Konstantinovic-ActaMat-2015 [11].

From these results, it can be seen that object properties are highly cohesive model dependent. When increasing the size of the defect, geometrical effect can be observed making the extrapolation with simple laws difficult. However, it seems that the largest vacancy clusters are less mobile than the smallest ones. Concerning the emission rates, they seem to saturate above size 10 in the Konstantinovic model while it decreases in Castin's model.

OKMC models highlight the importance of object mobilities on the microstructure evolution. However, the computations of these properties are very dependent on the AKMC cohesive model employed. Impurities such as carbon also appear to play a major role in the damage accumulation.

1.2.3 Solute effects

1.2.3.1 Effects of copper

Experimental observations:

In their study, Glade et al. studied a Fe-0.91Cu (wt.%) alloy irradiated with neutrons at relatively low doses (the highest one is about 8×10^{-4} dpa) [13]. The irradiation was performed at 563 K under a neutron flux of 7.0×10^{14} n m⁻² s⁻¹. By means of PAS, the authors observed an increase of the fraction of positrons annihilating at vacancy clusters when increasing the dose (from 1.4×10^{-4} dpa to 6.4×10^{-4} dpa). The authors also noticed the signature of copper in their results (indicating that vacancy clusters are associated with Cu atoms). The mean lifetime increases with the dose and a new component associated with the lowest intensity appears at 6.4×10^{-4} dpa. Hence, larger vacancy clusters are formed at the highest dose. Concerning the high doses regime, Lambrecht et al. [14] study gives information on FeCu system irradiated up to 0.2 dpa. Two specimens with different Cu contents (0.1 and 0.3 at.%) were irradiated at 565 K under a neutron flux of 9.5×10^{17} n m⁻² s⁻¹. From 0.1 to 0.2 dpa, both alloys present an increase of the S parameter and a decrease of the W parameter. The authors conclude that the number of vacancies increases in the vacancy-copper complexes with the dose. This point can also be supported by fact that increasing the dose leads to an augmentation of the positron lifetime while the intensity collected remains the same. Accordingly, vacancies newly produced seem to be likely to aggregate to existing vacancy-copper complexes. When compared to pure iron, it appears that both mean lifetime and intensity are higher in the FeCu system. Thus, vacancy complexes seem to be larger and more numerous in FeCu than in pure iron.

The Cu content has an impact on the vacancy cluster population. On the one hand, adding copper in the iron matrix results in an increase of the collected intensity. On the other hand, the mean lifetime is reduced when adding more copper (from 0.1 to 0.3 at.%). Vacancy cluster density is therefore raised when increasing the Cu content whereas their mean size decreases. The extrapolated densities and mean sizes are available in [6]. These observations and interpretations are also supported by Verheyen et al. study on material coming from the same experimental matrix [15].

Using Fe ion irradiation, Chen et al. provide results concerning the effect of the irradiation temperature on a Fe-0.5Cu wt.% alloy [16]. The samples were irradiated up to 0.14 dpa at 563 K as well as at room temperature. The flux employed was set to 1.2×10^{15} ions m⁻² s⁻¹. The main differences between these two conditions concern the S and W parameters. In the specimen irradiated at high temperature, the W parameter is higher than the one from the room temperature irradiation. The S also presents difference. It is much lower in the high temperature condition. This suggests that Cu clusters are more likely to form in the high temperature condition while vacancy clusters are favorably formed at the low temperature. Thus, lowering the irradiation temperature results in a high trapping effect making vacancy elimination and Cu precipitation more difficult.

Thermal stabilities of vacancy-copper complexes have also been investigated. In their study [11], Konstantinovic et al. performed post irradiation annealing on the Fe-0.3Cu at.% sample studied by Lambrecht et al. [14]. The selected material was the one irradiated at 0.1 dpa. The annealing (30 min) was performed at different temperatures between 573 K and 973 K. When reaching ~680 K, vacancy clusters start to dissociate (this is observed by a large decrease of the S parameter). Cu cluster dissolution leading to the recovery of the material occurs at ~900 K.

To understand elementary mechanisms, electron irradiation is quite a useful method since only Frenkel pairs are created during the process. Nagai et al. studied a Fe-0.3Cu wt.% irradiated with electrons at ~323 K [17]. The dose reached was about 0.0001 dpa. In these conditions, only monovacancies were formed (while V_4 were observed in pure Fe). The density of the vacancy objects is also much higher than the one in pure Fe. The authors report that these monovacancies are surrounded by many Cu atoms (~80% of the first eight nearest neighbor atoms). During the post irradiation annealing, the recovery temperature was found to be ~623 K.

In the FeCu system, vacancies produced under irradiation are likely to be associated to copper. Vacancy clusters are found to be more numerous in FeCu than in pure iron. They also appeared to be larger. Increasing the Cu content in the FeCu system leads to an increase of the vacancy population density while the mean size of these objects decreases. Lowering the irradiation temperature slows down the precipitation kinetic. In this condition, the Cu atoms trap the vacancies. Concerning the thermal stability of the Vac-Cu complexes, it seems to be higher than the one of the vacancy clusters without Cu. The temperature corresponding to the full recovery of the material after post irradiation annealing is indeed higher in the FeCu alloys than in Fe (900 K versus 773 K).

1.2.3.2 Effects of nickel and manganese

Studies concerning the vacancy population in irradiated FeNi and FeMn systems are rare. However, Nagai also provides results on these systems (Fe-0.7Ni and Fe-1.5Mn wt.%) [17]. Important differences in the behavior of the vacancy population are found between these two alloys. In the FeMn alloy, only monovacancies are observed. The density associated is higher than in Fe but it remains lower than in FeCu. Adding Ni to the iron matrix has a large impact from the vacancy point of view, as vacancy clusters appear in this alloy. The mean lifetime associated to these objects corresponds to V_{10} and is much higher than those observed in the pure Fe. The density is higher than in pure iron and lower than in FeMn. The authors report that vacancy clusters are associated with Ni while it is not possible to validate/invalidate the presence of Mn near the vacancies (due to the similarity of the Mn electron momentum in the high momentum region with those of Fe). Concerning the annealing compartment, vacancy clusters in FeNi tend to be larger and V_{15} are observed from 473 to 573 K. In the FeMn matrix, the mean lifetime remains constant during the annealing process (only monovacancies are observed). At 623 K, a complete recovery of all alloys is observed. It is also interesting to compare the Fe-0.2C (wt.%) with the Fe-1.5Mn (wt.%). As in the FeMn system, the irradiated FeC sample only contains monovacancies (in higher density than in FeMn). Hence, both materials appear to behave in the same manner from the vacancy point of view. The complete recovery in the FeC sample occurs 200 K before that of the manganese rich sample. Due to the similarities observed in FeMn and FeC vacancies in presence of Mn appear to be stabilized (some way or another) in a similar way as in FeC. Small manganese complexes could act as trap for the vacancies making their migrations/aggregations more difficult. Additional stability in presence of Mn was also noticed by Konstantinovic's after PAS characterization of various model alloys including a Fe-1.11Mn-0.71Ni (at.%) sample which had been annealed post irradiation [11]. They indeed observe an additional annealing stage at high temperature (~800 K) in this alloy.

These results are in contrast with the current knowledge regarding vacancy-solute interactions. According to DFT calculations, the binding energies (Table 1) between vacancy and Mn/Ni are not that different.

X	Mn	Ni	C
Eb(V-X) 1NN (eV)	0.17 [18]	0.11 [18]	0.65 [19]
Eb(V-X) 2NN (eV)	0.10 [18]	0.20 [18]	0.09 [19]

Table 1: Vacancy-solute binding energy predicted by PAW DFT (a positive value stands for attraction).

Furthermore, differences in the Vac-Mn and Vac-C binding energies make it difficult to understand the fact that the full recovery of the FeC system occurs before that of the FeMn. Moreover the carbon occupies interstitial sites while the Mn is in a substitutional position in the matrix. This makes the direct comparison of the binding energies more difficult. A possible explanation to the appearing stabilization of the vacancy in FeMn could come from the high Mn content in comparison of the carbon one.

When adding Mn and Ni together in the iron matrix, the vacancy population seems to follow the tendency observed in the FeMn system. A neutron irradiated Fe-1.11Mn-0.71Ni at.% model alloy has been studied by Lambrecht and collaborators [14]. The sample was irradiated at 565 K under a neutron flux of $9.5 \times 10^{17} \text{ n m}^{-2} \text{ s}^{-1}$ up to 0.2 dpa. The lifetimes observed at 0.1 and 0.2 dpa correspond to V_2 species. The intensity collected was the highest observed in comparison with the other specimens. The corresponding densities were $3 \times 10^{24} \text{ m}^{-3}$ and $1 \times 10^{25} \text{ m}^{-3}$ respectively for 0.1 and 0.2 dpa [6]. According to the previous results, it seems that manganese might be responsible for the absence of large vacancy clusters in the FeMnNi system. This assumption is supported by Murakami et al. study concerning the isochronal annealing of the FeMn and FeNi alloys [20]. In the Fe-1.5Mn at.% irradiated with protons at 70 K, the peaks denoted III_{Mn} and III'_{Mn} were observed in the highest temperature investigated (respectively 240 K and 310 K). These peaks were assumed to come from the monovacancy migrations. In this range of temperature, there is no observable peak in pure iron as well as in Fe-0.6Ni at.%. Hence, the authors also concluded that Mn could have a trapping effect on the vacancy.

Studying the influence of Mn/Ni in presence of Cu has also been investigated. Glade et al. compared the PAS observation between neutron irradiated Fe-0.91Cu and Fe-0.89Cu-1.03Mn wt.% at low doses (the highest was about 0.8 mdpa) [13]. The irradiation was performed at 563 K. While several lifetime components were present in the FeCu system, only one was detected in the FeCuMn alloy. The lifetime value was quite close to that of the non-irradiated alloy. Copper rich precipitates were also found to be smaller and more numerous in the FeCuMn matrix than in FeCu. Chen et al. experiments provide information about the effect of nickel in presence of Cu [16]. According to their studies, large differences are observed in the FeCuMnNi alloy in comparison with the Mn free FeCuNi sample (especially at room temperature). These results are in agreement with those of Lambrecht and suggest that the vacancy population from FeMnNi and FeCuMnNi alloys to RPV steels is (in the majority) driven by the presence of Mn.

Manganese atoms appear to have an important impact on the evolution of the vacancy population in the Fe based alloys under irradiation. No vacancy clusters are observed in the FeMn matrix, but a high density of mono-vacancies can be found. This is also the case during post irradiation annealing. Manganese seems thus to act as a trap for the vacancies. Contrary to the manganese, the presence of nickel allows the formation of vacancy clusters, that also grow during post irradiation annealing. These results are difficult to explain by means of the current knowledge obtained from atomistic modeling. In alloys containing both Mn and Ni, the trends observed concerning the vacancy population are similar to those observed in the FeMn alloys.

1.2.3.3 Vacancy affinity with solutes

DFT calculations highlight the fact that vacancies are likely to bind with solute atoms (more detail are provided in chapter 2). Beyond the second nearest neighbor distance (also denoted as 2NN) interactions, most vacancy-solute binding energies becomes negligible [18], [21]. However, a small attraction between vacancy and Cu, Mn, Ni can be found at a 5NN distance. Figure 1-4 summarizes results extracted from the literature.

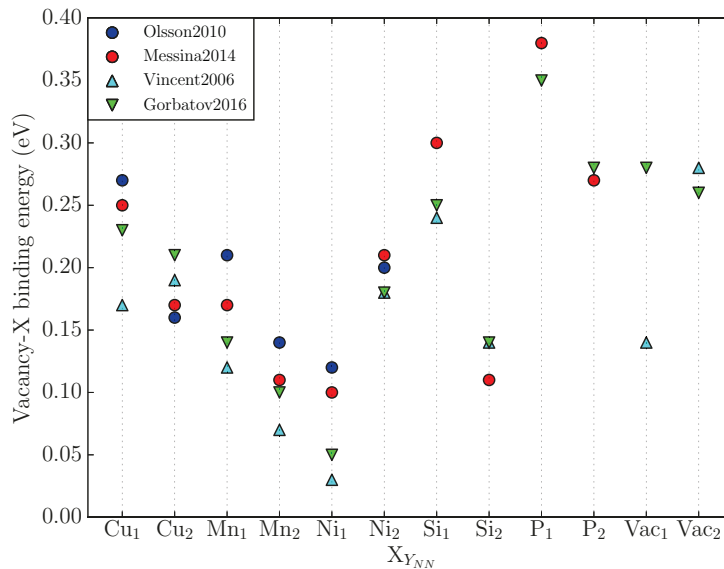


Figure 1-4: 1NN and 2NN binding energies between vacancy and the solutes of interest (positive value stands for attraction). The underscript number corresponds to the NN distance. **Olsson2010** [18]: PAW - GGA method using VWN interpolation in the PW91 parameterization. Supercells of 128 atoms with 27 k points. Energy cut-off = 300 eV. Relaxations were performed under constant volume conditions. **Messina2014** [21]: VASP - PAW - PBE. Supercells of 128 atoms with 27 k points. Energy cutoff = 300 eV. **Gorbatov2016** [22]: VASP - PAW - PBE. Supercells of 128 atoms with 64 k points. Energy cutoff = 350 eV. **Vincent2006** [23]: VASP - USPP - GGA. Supercells of 128 atoms with 27 k points. Energy cut-off = 240 eV.

According to these DFT calculations, all solute atoms bind attractively with the vacancy. Note that for the same system, differences of ~0.1 eV can be observed which corresponds thus somehow to the “resolution” limits of DFT.

After calculating a large database of DFT computed migration energies by means of the nudged elastic band (NEB) method, Messina et al. showed, using a self-consistent mean field (SCMF) theory approach, that solute drag by vacancy mechanism occurs for Cu, Mn, Ni, Si and P at 563 K [21]. The solute-drag factors were obtained for systems containing only one vacancy and one solute atom. Another important result of this

study concerns the relevant barriers that have to be considered. Messina showed that only considering the jumps that bring the vacancy to a 1NN distance of the solute atom in the set of barrier is not sufficient. Hence considering a larger set of barriers (bringing the vacancy to a 2NN or a 5NN distance from the solute) was required. It appears that the 2NN and 5NN sets of barriers provide comparable results. Hence, employing only the 2NN set of barriers appeared to be acceptable. Using the vacancy-solute binding energies from PAW DFT, the Final-Initial State Environment (FISE) model (presented in chapter 2 – section 2.4) was able to reproduce the tendencies observed from the explicit barrier model (the 2NN and 5NN sets of barriers). These results were successfully compared to diffusion tracer experiments.

1.2.4 RPV steels

From the vacancy population point of view, there is not much difference between the FeCuMnNi alloys and the RPV steels. It is important to highlight the point that the vacancy population seems to be driven by the presence of Mn/Ni in these alloys [14]. Thus, no large vacancy clusters are observed. Vacancies are rather alone (V_1) or sometimes in small aggregate (V_{2-3}).

Using electron irradiation, Fujii et al. studied low nickel / high copper RPV steels [24]. The irradiation was performed up to 22 mdpa at 563 K with a flux between 4 and $7 \times 10^{18} \text{ e m}^{-2} \text{ s}^{-1}$. In these conditions, no vacancy cluster was observed. The intensity and the mean lifetime of the PAS analysis were very similar between both alloys (one containing 0.12 wt.% Cu and the other 0.16 wt.%). However, the sample containing the highest content of Cu presented a higher W parameter. The authors suggest that the positrons were more likely to annihilate near Cu atoms due to the highest density of Cu clusters formed. In another study, Fujii et al. compared the behavior of RPV irradiated with electrons and neutrons [25]. Like the previous study, the dose reached was low (~ 10 mdpa). The irradiation was also performed at 563 K on 3 samples with various amounts of copper (0.03, 0.12 and 0.16 wt.%). In these three alloys, no vacancy clusters were observed whether for the neutron case and the electron case. In the two high Cu steels, the vacancies were found to be associated with copper atoms. In the case of the low Cu case, the absence of the broad peaks characteristic of the Cu-3d electrons were confirmed by the absence of solute clusters by means of atom probe tomography. From the vacancy population point of view, the authors did not observe much difference between the electron and the neutron irradiation (at least in this low-dose regime). However, the electron irradiation seems to induce a larger amount of remaining vacancies in the samples compared to the neutron irradiation case. The absence of vacancy clusters in this range of doses was also confirmed by Toyama et al. [26].

The effect of the dose and copper is clearer in another study from Toyama [27]. Two RPV steels containing a low amount of Ni (0.11 wt.%) and a high quantity of Cu (0.13 and 0.30 wt.%) were irradiated with neutrons from about 20 mdpa to 0.1 dpa. The flux employed was $\sim 8 \times 10^{14} \text{ n m}^{-2} \text{ s}^{-1}$ and the temperature corresponded to 577 K. In these conditions, vacancy clusters were observed, the densities of which seems to be higher in the high Cu sample. On the other hand, their mean size appears to be larger in the low Cu sample. Other studies present similar observations concerning the copper effect [28]. At ~ 0.1 dpa, V_{3-4} were observed in both alloys which is consistent with Lambrecht observations [14].

In the same range of doses (~ 0.061 dpa), Kuramoto et al. observed monovacancies only [29]. However the flux employed was 200 times higher than the one of Toyama [27]. Thus, a reduction of the flux seems to allow vacancies to aggregate.

As in the FeMnNi case, the vacancy clusters are rather small in the RPV steels (<V₄). In these alloys, the signature of Cu has been observed in the PAS spectra. This suggests that vacancies are associated to copper atoms. Increasing the Cu content of the steel leads to an increase of the vacancy object density while their mean size is reduced.

1.3 Solute clusters

1.3.1 Experimental techniques

The main experimental technique used to the study solute rich clusters formed under irradiation is the Atom Probe Tomography (APT). APT is the association of a field ion microscope, a time of flight mass spectrometer and a position sensitive detector. The sample is prepared to have the shape of a needle. Its extremity has to present a very low radius of curvature (about 90 nm). The analysis is performed under ultra-high vacuum condition (of the order of 1×10^{-10} mBar) and the sample is exposed to a constant electric potential E . Since the radius of curvature R is low, the electric field V at the apex of the tip is high ($V \propto E/R$). The applied electric potential must not be too high so that evaporation of the sample by field effect does not occur. In order to evaporate atoms one after the other, a pulse has to be applied to the sample (either electric or laser). Once an atom is extracted from the sample, its time of flight (from the sample to the detector) is measured. Since its potential energy is converted to kinetic energy, the ratio of ion mass and its charge state can be determined from the flight time. Using the position sensitive detector and employing inverse projection, it is possible to rebuild the evaporated volume at the atomic scale.

Trajectory aberrations are an artifact typical during analysis of materials containing heterogeneity [30]. This artifact is due to the fact that when two phases have different evaporation fields, they have locally radius of curvature differences that alter the ion trajectories. These trajectory aberrations may introduce bias into the 3D reconstruction and the chemical composition measurements [31]. If the clusters have lower field evaporation than the matrix, they tend to evaporate more rapidly than the matrix. Thus, the concentrations of matrix atoms in the clusters may be overestimated. The APT also has a detection efficiency: not all the atoms evaporated are detected. This phenomenon is due largely to the effective area available on the position sensitive device. The detection efficiency is about 50%.

Another experimental technique that can be used to detect heterogeneities in a material is the Small-Angle Neutron Scattering (SANS). This is a non-destructive technique that uses a neutron beam to characterize the specimen. The advantage of SANS over APT is its ability to analysis large volume (about 10 mm^3). This makes the results statistically more significant. The scattering cross-section is composed of a nuclear contribution and a magnetic one. The origin of the nuclear contribution is induced by the short-range interactions between the neutrons and the nucleus. The magnetic contribution comes for the interactions between the neutron spins and the magnetic moment of the atoms. In order to decouple these two contributions, a magnetic field is applied to the sample. After the neutrons have interacted with the material, their intensity as well as their scatter angle are collected. The detection limit is about 0.5 nm in cluster radius. This method has to be coupled with other techniques since hypothesis have to be done on the shape, the chemical nature and the crystallographic structure of the scatterers in order to interpret the measures.

1.3.2 The effect of Cu

Copper is an impurity present in the RPV steels. In the sixties, the formation of Cu rich clusters under irradiation was identified. Hence, new generation of RPV steels is designed to contain less than 0.05 wt.% of Cu [32]. Since the presence of copper has a large effect on the formation of solute clusters under irradiation,

several important results from the literature are summarized below (for more information about the FeCu system under thermal annealing and irradiation, the reader can refer to Vincent thesis [33]):

- The mechanism responsible of the formation of Cu clusters in the high Cu (>0.09 wt.%) binary alloys is the precipitation accelerated by irradiation [34]. This mechanism is consistent with the lack of solubility of copper in iron. For the low Cu (<0.1 wt.%) binary alloys, the heterogeneous precipitation on point defect clusters is the mechanism retained in literature, because Cu clusters are not observed after electron irradiation while they are present after an ion irradiation calibrated to introduce the same number of point defects [30].
- Increasing the Cu content (from 0.1 to 0.3 at.%) leads to an increase of both radius and density of the Cu clusters formed [6].
- Increasing the dose (from 0.026 to 0.19 dpa) leads to an increase of the size of the precipitates [6], [35].
- The nucleation stage is already completed at low dose (0.026 dpa) [36].
- The reduction of the flux by a factor 60 (from 0.024×10^{-7} dpa s⁻¹ to 1.35×10^{-7} dpa s⁻¹) does not change the cluster number density but reduces the copper content in the matrix by a factor 5 and increases the cluster size [36].
- Reducing the flux (from 0.024×10^{-7} dpa s⁻¹ to 1.35×10^{-7} dpa s⁻¹) enhances the kinetics of copper precipitation for a given dose [36].

1.3.3 The effects of nickel and manganese

Manganese-Nickel precipitates (MNP) are observed to form under irradiation in the FeMnNi system as well as in low copper RPV steels.

Using APT, Meslin et al. studied a Fe-1.11Mn-0.71Ni (at.%) irradiated with neutrons up to 0.2 dpa [36]. The irradiation was performed at 563 K using a high flux ($\sim 9.0 \times 10^{17}$ n m⁻² s⁻¹) and a low one ($\sim 0.15 \times 10^{17}$ n m⁻² s⁻¹) in BR2 MTR. In the high flux sample, MNP appeared at 0.1 dpa (Mn and Ni were not homogeneously distributed after 0.05 dpa). Concerning the lowest flux, the highest dose reached was 0.032 dpa and MNP were observed in this condition. This indicates that a reduction of the flux leads to an increase of the solute segregation kinetics. The MNP densities were 6.9×10^{23} m⁻³ and 3.8×10^{23} m⁻³ respectively for the highest flux at 0.2 dpa and the lowest flux at 0.032 dpa. In these two conditions, the associated mean radius of the clusters was 0.8 nm. In the low flux condition, the clusters Ni content was very low (0.9%) while the Mn one was $\sim 7\%$. The MNP formed in the high flux condition contain more Mn ($\sim 9.1\%$ at 0.1 dpa and $\sim 13.7\%$ at 0.2 dpa). The Ni content however remains constant when the dose increases ($\sim 3\%$).

Using an AKMC based on from results of DFT calculations, Ngayam-Happy et al. showed that Mn-Ni solutes in a cluster form are associated to SIA clusters [37]. According to the model, small Mn-Ni-SIA clusters are formed early on during the irradiation process. However, the small size of these objects does not make them observable by APT. The authors point-out the fact that the cohesive model employed to perform the simulation does not predict that Mn-Ni clusters are thermodynamically stable. Hence, according to them, the formation of Mn-Ni clusters is a radiation-induced mechanism based on the segregation of solute atom on SIA clusters. This is in contradiction with results obtained by Bonny et al. [38]. Bonny built an EAM type interatomic potential for the FeCuMnNi system, based on the results of DFT calculations. Then, the predictions of the potential were investigated using Metropolis Monte Carlo simulations. For the FeMnNi system, the authors obtained two different behaviors depending on the concentration ratio of Ni over Mn. When this ratio is higher or equal to one, the authors observed the coexistence of two phases in the simulated volume. The first one corresponds to the Fe-rich matrix and the second one to B2 structure Mn-Ni cluster. When the concentration ratio is lower than one, another phase corresponding to a Mn rich precipitate with

some Ni homogeneously distributed in the cluster. Hence, according to the EAM potential, the Mn-Ni clusters are an equilibrium phase.

The thermal stability has also been investigated by Meslin et al. [39]. The Fe-1.11Mn-0.71Ni (at.%) sample irradiated at high flux up to 0.1 dpa was annealed at 673 K for 50 hours. After the annealing, a decrease of the MNP density was observed (from 6.9×10^{23} to $4.4 \times 10^{23} \text{ m}^{-3}$). The mean radius remained unchanged and only the Mn content decreased. The same tendencies were found by Bergner et al. using Small Angle Neutron Scattering (SANS) [40] on the same sample thermally annealed. However, in their study, they also investigated a sample irradiated at the 0.2 dpa and observed that during thermal annealing, a decrease of the mean radius distribution had taken place. Note that the mean radius of the MNP observed by SANS was slightly higher than the one observed by APT (~1.5 versus 0.8 nm).

Another interesting point concerns the absence of solute clusters in the matrix in the Fe-1.0Mn (at.%) alloy. Meslin et al. studied this model alloy with Fe ion irradiation up to 0.5 dpa with a damage rate of $\sim 1 \times 10^{-4} \text{ dpa s}^{-1}$ [41]. The irradiation was performed at 673 K. In these conditions, Mn clusters were only observed on a planar object. According to the authors, this object could be a dislocation or a grain boundary. Because of the high solubility of Mn in iron, the formation of these clusters was assumed to be radiation-induced.

Concerning the effect of copper, Meslin et al. [36] observed a Fe-0.09Cu-1.1Mn-0.7Ni (at.%) model alloy irradiated with neutrons using APT. Two fluxes were employed ($\sim 9.0 \times 10^{17} \text{ n m}^{-2} \text{ s}^{-1}$ and $0.15 \times 10^{17} \text{ n m}^{-2} \text{ s}^{-1}$) at 573 K. The first observation concerns the composition of the clusters. Two groups of clusters were found: clusters mainly enriched in copper and clusters mainly enriched in manganese-nickel (or in manganese only). In the low flux conditions, these two groups can be observed at 0.032 dpa while they appear in the high flux condition only at 0.1 dpa. The volume fraction observed by SANS increases (monotonically) faster than the sum of the volume fractions in Fe-0.1%Cu and Fe-Mn-Ni [6]. This indicates a synergistic effect of Mn and/or Ni with Cu. No indication of a saturation-like behavior of the volume fraction was found.

Due to its very low solubility limit in iron, the copper tends to precipitate by radiation enhanced diffusion in the model FeCu alloys. On the contrary, Mn and Ni have a high solubility limit in iron and the Mn-Ni rich precipitates observed in FeMnNi model alloys are radiation-induced nanostructures. An interesting point is that solute clusters are not observed homogeneously distributed in the matrix in FeMn model alloys (containing a low Mn content). This can indicate a synergy between Mn and Ni since MnNi clusters are observed homogeneously distributed in irradiated FeMnNi model alloys.

1.3.4 RPV steels

In the next sections, RPV steels containing high and low Cu contents will be distinguished. Steels are considered high copper steels when the Cu content exceeds 0.09 at.%. This distinction is made because mechanisms leading to the formation of solute clusters appear to differ depending on the Cu content of the alloy.

1.3.4.1 Thermal ageing

Results concerning thermal annealing of high Cu RPV steels are provided by Styman et al. [42]. Using APT on a Fe-0.44Cu-1.66Ni-1.38Mn-0.75Si-0.19C-0.24Mo-0.018P-0.054Cr (at.%) system, this study gives information concerning the cluster composition after 50000 hours and 90000 hours of thermal annealing at 638 K. Between 50000 hours and 90000 hours the authors observed a decrease of the cluster volume fraction

and density (from 1.15 to 1.10 % for the volume fraction and from 0.57 to $0.29 \times 10^{23} \text{ m}^{-3}$ for the density) whereas the mean radius of the clusters increases (from 3.6 to 4.5 nm). Concerning the evolution of clusters composition, the Cu content seems to be stable over the time (28 %). However, the Ni and Mn content increase at the expense of the Fe content respectively from 17 to 19 % and 13 to 16 %. The Si content in the clusters is about 3 % (for all cluster sizes). The increase of the concentration of Mn-Ni at the interface cluster/matrix shows that clusters at 5000 h have not reached the segregation equilibrium. Moreover, it is important to note that some MNPs were also observed at the grain boundaries.

Another study from Pareige et al. provides results for lower Cu and Ni content [43]. In this work, thermally aged RPV steels were observed using Field Ion Microscopy (FIM). The materials were aged for 100000 h at 573 K. The copper content of the studied materials was between 0.017 and 0.26 at.% while the nickel content was between 0.49 and 0.72 at.% (nominal composition). For this large range of composition, the authors did not observe any significant microstructure evolution.

The formation of solute clusters during thermal ageing was also observed by Hyde et al. [44]. A Fe-0.55Cu-1.36Mn-1.63Ni-0.80Si-0.24Mo-0.02P-0.21C and a Fe-0.34Cu-1.44Mn-0.32Ni-0.77Si-0.30Mo-0.06P-0.21C (at.%) RPV steels were studied. The longest thermal ageing lasted 18620 hours at 603 K. Since both alloys contained solute rich cluster, copper seems to be the responsible for their formation (at least in this range of thermal ageing duration).

Experimental observations concerning the microstructural evolution of RPV steels under thermal ageing are quite rare. Results from different studies suggest that the copper content in the steel is the one of key factor for the appearance or lack of solute clusters.

1.3.4.2 Irradiation

High copper steels

High copper RPV steels evolution under irradiation are the easiest "RPV" system to understand since their Cu content is beyond the solubility limit of Cu in iron (~ 0.1 at.% at 773 K [45]). Nanoscale precipitates containing Cu, Mn, Ni and Si atoms are observed. The structure of the clusters corresponds most of the time to a core of Cu ($\sim 80\%$) with a shell composed of Mn, Ni and Si atoms [46], [47].

In Toyama et al. study, the effect of both dose and Cu content is exposed [27]. The solute composition of the alloys was Fe-0.13/0.30Cu-1.1Mn-0.11Ni-0.39Si-0.05P-0.2C wt.%. The irradiation was performed at 577 K up to ~ 0.1 dpa with a flux set to $8 \times 10^{14} \text{ n m}^{-2} \text{ s}^{-1}$. In these conditions, the sample containing 0.30 wt.% of copper presents at every dose larger solute clusters than in the other sample. For the two alloys, the number density of solute clusters slightly decreases when the dose increases while their mean radius tends to increase. At the highest dose, the number density of solute clusters was the same in both alloys (about $0.5 \times 10^{23} \text{ m}^{-3}$).

Low copper steels

Meslin et al. studied by APT a french 16MND5 RPV steel irradiated with neutrons at the 573 K up to 0.2 dpa in the high flux condition and 0.032 dpa in the low flux one (BR2 MTR) [36]. The solute content was 0.05Cu-1.31Mn-0.71Ni-0.38Si-0.01P-0.65/0.048C. The flux employed was $0.15 \times 10^{17} \text{ n m}^{-2} \text{ s}^{-1}$ and $9.5 \times 10^{17} \text{ n m}^{-2} \text{ s}^{-1}$. In both cases, solute clusters were observed. The mean radius of the clusters was 0.6 nm in both cases. The associated density was higher in the low flux case ($7.4 \times 10^{23} \text{ m}^{-3}$ versus $3.7 \times 10^{23} \text{ m}^{-3}$). The clusters were enriched in Mn (other solutes were found but the enrichment was not judged significant). Huang PhD thesis provides additional APT results concerning the dose effect on a large RPV steel grades irradiated with neutrons at 561 K from the PSI [48]. The flux employed was about $2 \times 10^{15} \text{ n m}^{-2} \text{ s}^{-1}$ and the

highest doses correspond to ~40 years of in-service conditions (0.1 dpa). The range composition of the solutes investigated was Fe-(0.026-0.07)Cu-(1.26-1.5)Mn-(0.62-0.70)Ni-(0.38-0.53)Si-(0.011-0.015)P (at.%).

The main conclusions of Huang's study are:

- The mean radius of the clusters remains globally unchanged when the dose increases (~1.5 nm).
- The cluster density increases linearly with the dose. Moreover, increasing the Cu content of the steel clearly increases the cluster density (at a given dose). Thus, the kinetics of the cluster formation depends on the Cu nominal composition.
- The cluster density does not vary when the flux increases (from $0.7 \times 10^{15} \text{ n m}^{-2} \text{ s}^{-1}$ to $2.0 \times 10^{15} \text{ n m}^{-2} \text{ s}^{-1}$).
- The mean solute content of the clusters is of the order of 15-30%. Contrarily to Meslin observations, the clusters contain Cu, Mn, Ni, Si and P atoms. The solute content slightly increases with the dose.
- The P and Mn cluster content does not evolve with fluences, whereas the amount of Ni and Si in the clusters seems to increase with the dose.
- The Cu content in the clusters is directly linked to the nominal content of the material.

These results are difficult to compare with those of Meslin. The cluster radii are higher than those observed in Meslin study (about 1.5 nm versus 0.6 nm). Moreover, the density observed is higher in Huang experiments (the lowest cluster density observed by Meslin is never observed by Huang at the same dose). In the alloy containing the highest Cu content, the density is $\sim 1.5 \times 10^{23} \text{ m}^{-3}$. These differences in density, mean size and composition of the solute clusters may come from the flux employed in the two studies (between 1 and 2 orders of magnitude higher in Meslin's experiments).

Mn-Ni-Si rich precipitates formed under irradiation were also observed in high nickel RPV steels. In several studies, Miller et al. analyzed by APT high nickel (from 1.19 to 1.69 at.%) low copper (from 0.04 to 0.06 at.%) neutron irradiated steels [46], [49], [50]. In 2006, Miller studied this type of steel up to a medium dose (~30 mdpa). In these conditions, the cluster composition was about 10–15% Ni, 4–6% Mn and 4–6% Si. The Cu distribution appeared to be random. The observations made on the cluster density and mean size are comparable to those of Huang (about $1.0 \times 10^{23} \text{ m}^{-3}$ for the density and between 1-2 nm for the mean radius). Three years later, the same samples were irradiated at high dose (about 0.25 dpa). This allowed the authors to study the dose effect [49]. A mean radius of ~0.9 nm (slightly lower than the one observed in Huang PhD thesis [48]) was observed at every dose. As also observed by Huang, the cluster density increases linearly with the dose. Huang suggests that these tendencies indicate a radiation-induced mechanism. The mean composition of the clusters found by Miller in 2009 is 50% Ni, 25% Si, 10% Mn, and 0.15% Cu. Thus, the solute content in the clusters is higher than in their previous study from 2006. Unfortunately, the authors did not mention it (making it difficult to know if there really is a dose effect or simply because they employed another detection algorithm).

Even in very small amount, Cu seems to have a great impact. In their study, Wells et al. studied RPV type steels in "quasi" absence of copper (< 0.02 at.%) [51]. An interesting point of these experiments is that both high and low nickel steels (respectively 1.68 and 0.74 at.%) were analyzed. The samples were irradiated with neutrons at two doses. The first one corresponds to 0.26 dpa with a flux employed of $1.0 \times 10^{18} \text{ n m}^{-2} \text{ s}^{-1}$. The second one was a very high dose (2.2 dpa) with a flux of $2.3 \times 10^{18} \text{ n m}^{-2} \text{ s}^{-1}$. In the "low" dose condition, the volume fraction of the precipitates was very low (~0.08%) when compared to other steels containing Cu. However, in the very high dose condition, a large quantity of MnNiSi precipitates appeared. Their volume fractions were 1.33 and 2.82% respectively for the low and the high Ni steel. The mean radius associated to these clusters was 1.25 (for low Ni steel) and 1.52 nm (for the high Ni steel). In the case of the high Ni steel, the volume fraction even exceeds the ones of the other RPV steels containing Cu. The authors assume that the iron observed in the cluster is an artifact and propose that the mean cluster compositions are 46% Ni, 31%

Mn, 22% Si for the low nickel steel and 52% Ni, 35% Mn, 12% Si for the high nickel steel. It is noteworthy interesting to highlight the fact that the cluster density is always higher in the copper free samples than in the others.

Solute clusters are observed in both high/low Cu RPV alloys. In the high Cu alloys, the dominant mechanism seems to be the precipitation of copper enhanced by the irradiation. Concerning the low Cu alloys, the results are more difficult to interpret due to the low Cu content in the solute clusters observed after irradiation, a radiation-induced mechanism appears to be more probable. The solute cluster density increases linearly with the dose while the mean size remains unchanged.

1.3.4.3 MNS thermal stability

Styman et al. performed post-irradiation annealing on a low Cu (0.07 at.%) and high Ni (1.50 at.%) RPV steel irradiated at 0.13 dpa at the temperature of 557 K [52]. In the as-irradiated sample, a large amount of MNPs was found, the composition of which is remarkably consistent with the Γ_2 phase ($\text{Mn}_2\text{Ni}_3\text{Si}$) predicted by Xiong et al. [53]. After an annealing treatment at 723 K during 30 min, the population of MNPs did not evolve much: the volume fraction changed from 1.4 to 1.1% due to the small reduction of the cluster density. This annealing was then followed by another one at 773 K during 10 min. The effect of this second treatment is clearer: the volume fraction decreased a lot and reached 0.5%. The size distribution became bimodal with a large amount of small MNPs (~1.8 nm). After analysis of the clusters, it was found that manganese had diffused out of the clusters during the dissolution process (as reported in [29]). This was interpreted by the authors as a possible indication of the presence of point-defects in the MNP since Mn is known to interact strongly with them.

Wells performed the same types of experiments during his PhD work [54]. However, the long term annealing was realized at a slightly lower temperature (698 K) on the very high fluence samples irradiated (~2 dpa). Both alloys were low Cu (0.01-0.02 at.%). In the low nickel sample (0.7 at.%), a full recovery was observed after 7 weeks. Concerning the high Ni steels (1.7 at.%), MNPs were still observed after 29 weeks. The volume fraction was then very low, close to 0.1% (it was 2.8% in the as-irradiated sample) but the remaining clusters were very large (5.5 nm in diameter). This observation was not in agreement with the CALPHAD (Calculation of Phase Diagrams) prediction. In the low Ni steel, the CALPHAD model predicted a complete dissolution of the MNPs which in this case is in agreement with the observation. However, the volume fraction predicted in the high nickel case was about 1.5%. The authors suggested that most of the precipitates are below a critical radius of 2.2 nm making the cluster less stable. This could explain the large decrease of the cluster density observed. Another study that might validate the fact that MNPs are equilibrium comes from Wagner et al. [55]. In this study, three RPV steels containing a low quantity of Cu (0.01 wt.%) were irradiated at 528 K up to 0.17 dpa. The as-irradiated samples were then annealed at 563 K for 38 days. Using SANS, the authors did not observe any significant dissolution of the solute clusters. The interface precipitate/matrix was less diffuse in the annealed samples. It could correspond to a local return to the equilibrium of the MNPs.

1.3.4.4 MNS formation mechanism

The formation of Mn-Ni-Si precipitates is a major concern for the potential lifetime extension of the nuclear power plants. Understanding how they form is therefore a high stake. The most polarizing point in the scientific community is related to the radiation enhanced or induced character of the phenomena leading to their formation.

Since Mn and Ni content is far below their solubility limits in their respective binary system, one can argue that their radiation-induced character makes no doubt. However in 1995, Odette was the first to make the hypothesis that these clusters were thermodynamically favorable [56].

In the high Cu RPV steels, mechanisms at the origin of the formation of solute clusters are well understood. Due to the lack of solubility of copper in iron, Cu rich clusters quickly form by a radiation-enhanced mechanism. The decoration of these clusters by Mn, Ni and Si comes from the lowering of the Cu/matrix interfacial energy [57]. Hence, Cu seems to act as a preferential nucleation site for the Mn-Ni-Si precipitates. This assumption is supported by the formation (at high enough dose) of Mn-Ni-Si precipitates on Cu clusters [51]. It was also suggested at more reasonable dose (~30 mdpa) by Eldmondson et al. [58].

In 2014, Xiong et al. developed a thermodynamic equilibrium model based on the CALPHAD method to predict the precipitation of late-blooming phases [53]. Two databases were used, a commercial one and another based on results from the literature. To compare the thermodynamic models to the experiments, the authors made two assumptions. The first one was that irradiation affects precipitation kinetics by accelerated diffusion. The second one was that at sufficiently high fluence, the precipitates formed are those of an equilibrium phase. The study predicts that Mn-Ni-Si precipitates may be formed in the steels at operating temperature since these phases are stable. Moreover, the results concerning the molar fractions of precipitates as well as on their compositions are in agreement with experimental results on irradiated samples [51]. The model predicts the formation of a Γ_2 phase (Mn_2Ni_3Si) for the high Ni steel and a mixture of Γ_2 and G phases ($Mn_6Ni_{16}Si_7$) for the low Ni one. Recently, a direct observation of these phases has been achieved by X-ray diffraction [59]. This result is consistent with APT and SAXS analysis performed by the authors on Wells samples [51]. These results seem to confirm the thermodynamic model predicting the Mn-Ni-Si precipitates to be stable crystalline intermetallic phases. According to this possible formation mechanism, it can again be assumed that copper may act as preferential nucleation sites. In absence of copper, point defect clusters may play this role. The reason of the stationary sizes of the Mn-Ni-Si clusters is still an open question. The previous results also suggest that the presence of iron atoms observed in the solute clusters by APT (estimated at about 55% of the cluster composition in Wells study) are indeed artifacts.

Whether the formation of the Mn-Ni-Si clusters is radiation-enhanced or induced, MNS precipitates are either difficult to nucleate or their growth rate is very low or maybe both at the same time. The first assumption seems reasonable since these clusters were never observed in thermally aged low Cu RPV steels. It is also supported by the low number of Cu presents in the solute clusters at realistic dose (< 0.2 dpa). Point defect clusters might also act as preferential nucleation site. They are more likely to be of interstitial nature since vacancy clusters are not observed in FeMnNi model alloys and in the RPV steels. Employing an Object Kinetic Monte Carlo approach (more details about the method are presented in chapter 2), Chiapetto et al. showed that the SIA clusters density (invisible by TEM) is the same as the Mn-Ni cluster density observed by APT in the FeMnNi matrix [60][47]. Concerning the low growth rate, it might be explained by the fact that Ni, Si and Cu atoms reach the solute clusters only by vacancy mechanism. Indeed, Messina showed in his PhD thesis that solute atoms (Cu, Mn, Ni, Si, P) are dragged by vacancies at 600 K [61]. Mn can also be dragged by interstitials (as well as P and Cr).

The mechanism leading to the formation of MNS precipitates is still an open question. Results from atomistic simulations are contradictory concerning the potential thermodynamics stability of these clusters. In presence of Cu, Mn-Ni-Si atoms are observed at the interface of the Cu clusters, as a consequence of a possible interfacial energy reduction. The Fe/Cu interface may thus act as a preferential nucleation site for the MNS precipitates. In absence of Cu, some of the studies propose that MNS precipitates are stable phases (thermodynamic stable) while others suggest that they are formed as the result of radiation-induced segregation on SIA clusters (SIA clusters acting as another preferential nucleation site).

1.4 Self interstitial clusters

1.4.1 Experimental techniques

Large interstitial loops are observed in irradiated iron based alloys. The main experimental technique to characterize these large objects is the Transmission Electron Microscopy (TEM). Beforehand, the sample is prepared to obtain a thin foil. Using an electron beam, this technique allows obtaining a projected picture of the internal structure of a material. The electrons are transmitted through the specimen or diffracted. TEM provides quantitative information about density and sizes of large enough nanofeatures (≥ 1.5 nm).

1.4.2 The mono interstitial in α iron

Like vacancies, interstitials are produced under irradiation. The most stable interstitial in α iron is the one oriented along $\langle 110 \rangle$ [62]. The migration mechanism for the self interstitial is more complex than the one of the vacancy. The most energetically favorable path for the migration is known as the Johnson mechanism [63]. Figure 1-5 illustrates this mechanism. It corresponds to a translation followed by a 60° rotation. Due to the low migration energy compared to the vacancy migration energy (~ 0.3 versus 0.6 eV), the self interstitials will diffuse much faster and at lower temperatures.

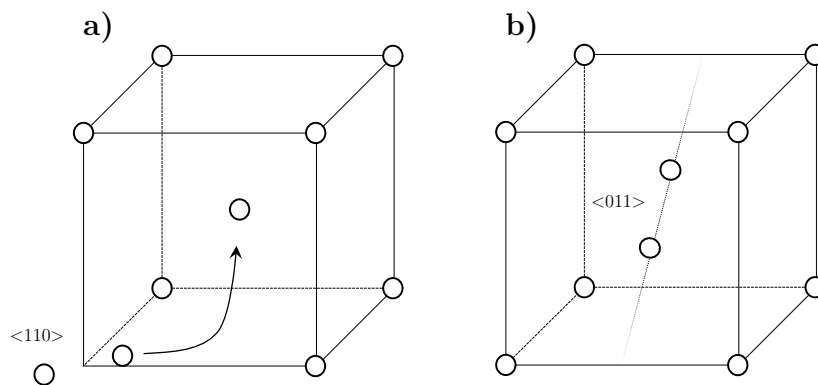


Figure 1-5: Illustration of the translate-rotation migration of the SIA in the α iron denoted as the Johnson mechanism [63].

1.4.3 Isochronal annealings

The main article concerning isochronal annealing in pure iron comes from Takaki et al. [2]. The doses reached with the electron irradiation were between 2×10^{-6} and 2×10^{-4} dpa. The increment of the temperature was set to $\Delta t / T = 0.03$ and $\Delta t = 300$ s.

The different peaks associated to SIA (Figure 1.1) in pure Fe [2] correspond to:

- I_{D1} corresponds to the recombination between close pairs. Its observation seems not to depend on the condition of the study. It is always observed at 101K. The estimated activation energy is equal to 0.23 ± 0.02 eV.
- I_{D2} corresponds to the recombination of correlated Frenkel pairs. It is always observed at 108 K. The estimated activation energy is equal to 0.23 ± 0.02 eV.
- I_E is dose dependent. It corresponds to the recombination of uncorrelated Frenkel pairs. For a higher dose, the peak shifts to a lower temperature. It is observed between 123 and 135 K. The estimated activation energy is equal to 0.27 ± 0.04 eV.
- Stage II is assigned to recovery between 150 and 200 K. The single peak is assigned to the migration of the di-interstitial. As I_E , its position is dose dependent. For the lowest dose the peak is observed at 164 K while at the highest it is observed at 175 K. The estimated activation energy is equal to 0.42 ± 0.03 eV.

Concerning the solute effect, Maury et al. performed isochronal annealing on binary steels with various amount of solutes [64], [65]. The I_E peaks gradually disappears when the content of Cu, Mn, and Ni atoms in the alloys increases. According to the authors, this disappearance is due to the trapping of the interstitials by copper and nickel. For manganese, the authors attribute this peak to the formation of mobile mixed dumbbells. This mixed dumbbell appears to be stable according to DFT calculations [19].

1.4.4 Dislocation loops

$\langle 100 \rangle$ loops are observed in the pure α iron under irradiation. To a lesser extent, $\frac{1}{2}\langle 111 \rangle$ loops are also observed [66]. Their mean sizes as well as their densities increase with the dose [6], [66]. $\langle 111 \rangle$ loops as opposed to the $\langle 100 \rangle$ loops have also been reported as being very mobile

1.4.4.1 Formation mechanism

The precise mechanism leading to the formation of $\langle 100 \rangle$ loop is still not well known. Using Fe EAM potential, Marian et al. [67] proposed a mechanism to form $\langle 100 \rangle$ dislocation type from two $1/2\langle 111 \rangle$ loops. A $\langle 100 \rangle$ type junction could form according to this relation:

$$\frac{1}{2}[111] + \frac{1}{2}\overline{[111]} = [001]$$

However, only the first stage of the process was reached through MD simulations. In 2013, Xu et al. [68] presented the first direct calculation of the formation of $\langle 100 \rangle$ type loop from two $\langle 111 \rangle$ loops. They used a self-evolving atomistic kinetic Monte Carlo (SEAKMC) method which is an on-the-fly kinetic Monte Carlo method [69] (presented in chapter 2). Just like the MD simulations, this method only requires a potential and an input geometry. The advantage of SEAKMC over MD simulation is the longer time that can be simulated (which is a key factor in diffusion process studies) [70]. Figure 1-6 presents the evolution of the system leading to the observation of $\langle 100 \rangle$ loop formation at 600 K. The authors noticed that the final Burgers vector is $[100]$ (not $[001]$ as mentioned in the previous dislocation reaction). Moreover, from multiple simulations (over 100 runs), the authors observed a multiple varieties of final configurations. Thus, the evolution of the sessile junction during its transformation seems to be a stochastic phenomenon.

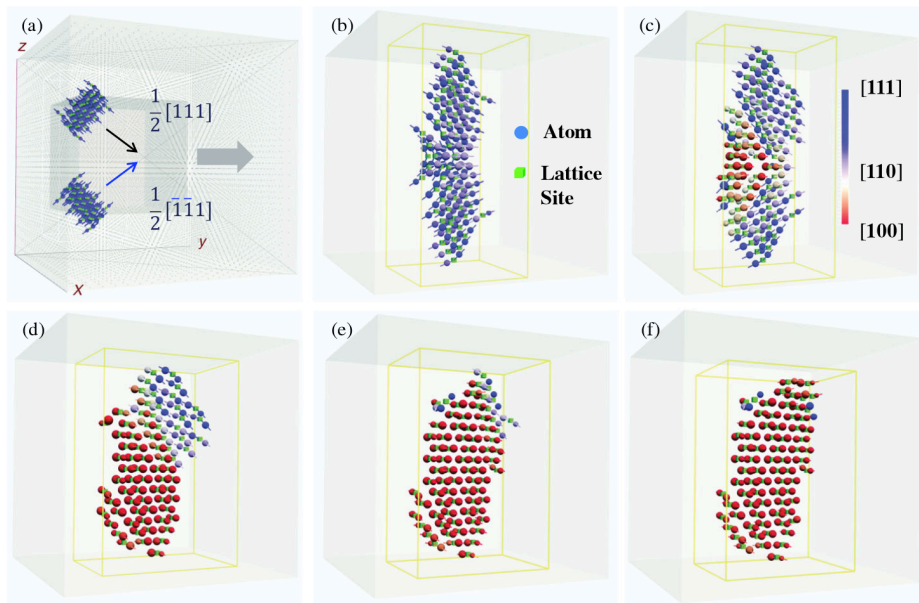


Figure 1-6: Snapshot describing the evolution of the system. (a) Initial state (37 interstitials in each loop). (b) Formation of a sessile junction after the encounter of the two clusters. (c) The system after $2\mu\text{s}$. (d) Partial $[100]$ orientation. (e) Propagation of $[100]$ orientation. (f) Complete $[100]$ loop formed. Figure extracted from [68].

1.4.4.2 Solute effect

As part of the PERFECT Project, Hernández-Mayoral et al. studied the formation of dislocation loops in various model alloys with increasing complexity (from pure iron of 16MND5) [66]. The model samples were pure iron, Fe-0.1Cu, Fe-0.3Cu, Fe-1.2Mn-0.7Ni, Fe-0.1Cu-1.2Mn-0.7Ni (wt.%). The irradiation was performed at 573 K up to 0.19 dpa with flux of $0.95 \times 10^{18} \text{ n m}^{-2} \text{ s}^{-1}$ (BR2 MTR).

In all materials (except in the RPV steels), a majority of $\langle 100 \rangle$ dislocation loops were observed, which were believed to be of interstitial type. Increasing the dose always leads to an increase of the loop density. The same observation was made for their mean sizes. In the FeCu system, the size distribution of loops is narrower than in pure iron. The mean size is also smaller. The size distribution seems not to be affected by the addition of copper (from 0.1 to 0.3 wt.%). However, the loop density is higher in the Fe-0.3Cu (wt.%) case. This might be due to the fact that the proportion of $1/2\langle 111 \rangle$ increases with the Cu content. In the FeMnNi system, the size distribution of the loops is even narrower than the one observed in FeCu. The loop density is the lowest observed at 0.19 dpa ($\sim 1 \times 10^{21} \text{ m}^{-3}$) and the mean size is also rather low when comparing to pure iron (4 versus 10 nm). The absence of visible loop in the RPV steel is justified by the reduction of their size when the solute content increases.

1.4.5 The C15 clusters

The C15 clusters are another type of SIA cluster arrangement. The peculiarity of these clusters comes from their 3D structure (in comparison to the 2D structure of SIA loops). Initially, "sessile" clusters were observed in displacement cascade simulations [71], [72]. Recently, Marinica et al. showed by DFT calculations that the structure of these clusters was actually related to the C15 Laves phases (MgCu_2 structure). The corresponding space group is $\text{Fd}3\text{m}$ [73]. For SIA clusters above size 4, this geometry appears to be more stable than the parallel-dumbbell configurations. The M07 interatomic potential employed was in very good agreement with the DFT values. Coupling the simulated displacement cascade by molecular dynamics and the Activation Relaxation Technique nouveau (ARTn) method, Marinica observed that about 5% of the SIA

objects formed after the 20 keV cascades have this C15 structure (either perfect or with defects in it). Due to their geometries, these clusters were predicted to be immobile. In a more recent study, Alexander et al. also shown that the C15 structure is the most stable for size lower than 51 [74]. This kind of structure was also observed experimentally [75]. According to Arakawa, the C15 structure plays the role of a precursor for the formation of loops and that above a certain size, the C15 structure turns into a loop one. The presence of these clusters should have an impact on the microstructure evolution because of their lack of mobility. Further investigations for taking them into account into atomistic models may thus improve the predictions of those models.

1.5 Conclusion

Important results from the literature have been exposed in this chapter. Firstly, the behavior of the vacancies formed under irradiation has been presented. In pure iron, vacancy clusters are observed by PAS. The mean size of these clusters increases with the dose. Simulation results highlight the fact that impurities such as carbon are responsible for this damage accumulation. In model binary systems, it has been shown that the nature of the solute atoms has a major effect on the vacancy population. Hence, the vacancy cluster density, mean size and thermal stability are affected by the affinity between the vacancy and the solute. Manganese appears to increase the density of vacancy objects. This observation has been reported in FeMn and FeMnNi model alloys. Point defect cluster kinetic properties also have an impact on the microstructure evolution. Since these properties are not accessible by experimental techniques (except for very large PD clusters), the importance of being able to calculate them to serve higher scale model has also been highlighted. Secondly, the solute clusters formed during the irradiation process have been discussed. Studying irradiated model alloys is a solid approach to understand the contribution of the different solutes in the nanostructure evolution. The copper case has been widely studied. The formation of Cu rich clusters is induced by the very low solubility limit of this element in the α iron matrix. This point is verified by thermal ageing of binary FeCu alloys. However, manganese, nickel and silicon atoms are major elements in the solute clusters formed under irradiation. In the presence of Cu, Mn-Ni-Si atoms segregate at the interface between the iron matrix and the copper precipitates. This observation has been reported in high copper RPV steels irradiated or thermal aged. In absence of Cu, the thermodynamic stability of these objects in absence of copper is still an open question. On the one hand, there is no experimental observation in low copper RPV steels of solute clusters under thermal ageing. Hence, some studies proposed a radiation induced formation mechanism for the MNS precipitates by segregation on SIA clusters. On the other hand, other studies based on empirical potentials and Metropolis Monte Carlo or on CALPHAD predict the thermodynamic stability of these clusters. Thirdly, SIA objects have been briefly introduced. Large SIA clusters form mobile loop. The mean size of the loops appears to be reduced when increasing the chemical complexity of the alloys increases. Recently, a new structure, called the C15, for the small SIA clusters has been proposed based on DFT calculations and later on observed experimentally. This structure is important because these objects are not likely to be mobile and must be taken into account in the future atomistic model development.

The next chapter will focus on numerical methods aiming to simulate the microstructure evolution under irradiation.

1.6 Bibliography

- [1] M. Eldrup and B. N. Singh, “Studies of defects and defect agglomerates by positron annihilation spectroscopy”, *Journal of Nuclear Materials*, vol. 251, pp. 132–138, Nov. 1997.
- [2] S. Takaki, J. Fuss, H. Kuglers, U. Dedek, and H. Schultz, “The resistivity recovery of high purity and carbon doped iron following low temperature electron irradiation”, *Radiation Effects*, vol. 79, no. 1, pp. 87–122, Aug. 1983.
- [3] M. Eldrup and B. N. Singh, “Study of defect annealing behaviour in neutron irradiated Cu and Fe using positron annihilation and electrical conductivity”, *Journal of Nuclear Materials*, vol. 276, no. 1, pp. 269–277, Jan. 2000.
- [4] M. Eldrup and B. N. Singh, “Accumulation of point defects and their complexes in irradiated metals as studied by the use of positron annihilation spectroscopy – a brief review”, *Journal of Nuclear Materials*, vol. 323, no. 2, pp. 346–353, Dec. 2003.
- [5] M. Eldrup, B. N. Singh, S. J. Zinkle, T. S. Byun, and K. Farrell, “Dose dependence of defect accumulation in neutron irradiated copper and iron”, *Journal of Nuclear Materials*, vol. 307, pp. 912–917, Dec. 2002.
- [6] E. Meslin, M. Lambrecht, M. Hernández-Mayoral, F. Bergner, L. Malerba, P. Pareige, B. Radiguet, A. Barbu, D. Gómez-Briceño, A. Ulbricht, and A. Almazouzi, “Characterization of neutron-irradiated ferritic model alloys and a RPV steel from combined APT, SANS, TEM and PAS analyses”, *Journal of Nuclear Materials*, vol. 406, no. 1, pp. 73–83, Nov. 2010.
- [7] C. Domain, C. S. Becquart, and L. Malerba, “Simulation of radiation damage in Fe alloys: an object kinetic Monte Carlo approach”, *Journal of Nuclear Materials*, vol. 335, no. 1, pp. 121–145, Oct. 2004.
- [8] V. Jansson, M. Chiapetto, and L. Malerba, “The nanostructure evolution in Fe-C systems under irradiation at 560K”, *Journal of Nuclear Materials*, vol. 442, no. 1, pp. 341–349, Nov. 2013.
- [9] C. Barouh, PhD thesis, “Modélisation multi-échelle de l'interaction entre les éléments d'alliages et les lacunes dans les aciers ferritiques”, Orléans University, 2015.
- [10] N. Castin, M. I. Pascuet, and L. Malerba, “Mobility and stability of large vacancy and vacancy-copper clusters in iron: An atomistic kinetic Monte Carlo study”, *Journal of Nuclear Materials*, vol. 429, no. 1, pp. 315–324, Oct. 2012.
- [11] M. J. Konstantinović and G. Bonny, “Thermal stability and the structure of vacancy–solute clusters in iron alloys”, *Acta Materialia*, vol. 85, pp. 107–111, Feb. 2015.
- [12] L. Messina, L. Malerba, and P. Olsson, “Stability and mobility of small vacancy–solute complexes in Fe–MnNi and dilute Fe–X alloys: A kinetic Monte Carlo study”, *Nuclear Instruments and Methods in Physics*, vol. 352, pp. 61–66, Dec. 2008.
- [13] S. C. Glade, B. D. Wirth, G. R. Odette, P. Asoka-Kumar, P. A. Sterne, and R. H. Howell, “Positron annihilation spectroscopy and small-angle neutron scattering characterization of the effect of Mn on the nanostructural features formed in irradiated Fe-Cu-Mn alloys”, *Philosophical Magazine*, vol. 85, no. 4, pp. 629–639, Jan. 2005.
- [14] M. Lambrecht and A. Almazouzi, “Positron annihilation study of neutron irradiated model alloys and of a reactor pressure vessel steel”, *Journal of Nuclear Materials*, vol. 385, no. 2, pp. 334–338, Mar. 2009.
- [15] K. Verheyen, M. Jardin, and A. Almazouzi, “Coincidence Doppler broadening spectroscopy in Fe, Fe–C and Fe–Cu after neutron irradiation”, *Journal of Nuclear Materials*, vol. 351, no. 1, pp. 209–215, Jun. 2006.
- [16] L. Chen, Z. C. Li, H. Schut, and N. Sekimura, “Positron annihilation study of Fe-ion irradiated reactor pressure vessel model alloys”, *J. Physics: Conference Series*, vol. 674, pp. 012012–8, Jan. 2016.
- [17] Y. Nagai, K. Takadate, Z. Tang, H. Ohkubo, H. Sunaga, H. Takizawa, and M. Hasegawa, “Positron annihilation study of vacancy-solute complex evolution in Fe-based alloys”, *Physical Review B*, vol. 67, no. 22, pp. 224202–6, Jun. 2003.
- [18] P. Olsson, T. P. C. Klaver, and C. Domain, “Ab initio study of solute transition-metal interactions with point defects in bcc Fe”, *Physical Review B*, vol. 81, no. 5, p. 054102, Feb. 2010.
- [19] R. Ngayam-Happy, PhD thesis, “Prévisions de l'évolution microstructurale sous irradiation d'alliages ferritiques par simulations numériques à l'échelle atomique”, Lille University, 2010.
- [20] K. Murakami, T. Iwai, H. Abe, N. Sekimura, Y. Katano, T. Iwata, and T. Onitsuka, “Role of nickel and manganese in recovery of resistivity in iron-based alloys after low-temperature proton

- irradiation”, *Philosophical Magazine*, vol. 95, no. 15, pp. 1680–1695, May 2015.
- [21] L. Messina, M. Nastar, T. Garnier, C. Domain, and P. Olsson, “Exact ab initio transport coefficients in bcc Fe-X (X=Cr, Cu, Mn, Ni, P, Si) dilute alloys”, *Physical Review B*, vol. 90, no. 1, p. 104203, Sep. 2014.
- [22] O. I. Gorbатов, A. H. Delandar, Y. N. Gornostyrev, A. V. Ruban, and P. A. Korzhavyi, “First-principles study of interactions between substitutional solutes in bcc iron”, *Journal of Nuclear Materials*, vol. 475, no. C, pp. 140–148, Jul. 2016.
- [23] E. Vincent, C. S. Becquart, and C. Domain, “Ab initio calculations of self-interstitial interaction and migration with solute atoms in bcc Fe”, *Journal of Nuclear Materials*, vol. 359, no. 3, pp. 227–237, Dec. 2006.
- [24] K. Fujii, K. Fukuya, N. Nakata, K. Hono, Y. Nagai, and M. Hasegawa, “Hardening and microstructural evolution in A533B steels under high-dose electron irradiation”, *Journal of Nuclear Materials*, vol. 340, no. 2, pp. 247–258, Apr. 2005.
- [25] K. Fujii, H. Nakata, K. Fukuya, T. Ohkubo, K. Hono, Y. Nagai, M. Hasegawa, and T. Yoshiie, “Hardening and microstructural evolution in A533B steels under neutron irradiation and a direct comparison with electron irradiation”, *Journal of Nuclear Materials*, vol. 400, no. 1, pp. 46–55, May 2010.
- [26] T. Toyama, A. Kuramoto, Y. Nagai, K. Inoue, Y. Nozawa, Y. Shimizu, Y. Matsukawa, M. Hasegawa, and M. Valo, “Effects of post-irradiation annealing and re-irradiation on microstructure in surveillance test specimens of the Loviisa-1 reactor studied by atom probe tomography and positron annihilation”, *Journal of Nuclear Materials*, vol. 449, no. 1, pp. 207–212, Jun. 2014.
- [27] T. Toyama, Y. Nagai, Z. Tang, M. Hasegawa, A. Almazouzi, E. van Walle, and R. Gerard, “Nanostructural evolution in surveillance test specimens of a commercial nuclear reactor pressure vessel studied by three-dimensional atom probe and positron annihilation”, *Acta Materialia*, vol. 55, no. 20, pp. 6852–6860, Dec. 2007.
- [28] V. Slugeň, O. Gokhman, S. Pecko, S. Sojak, and F. Bergner, “JRQ and JPA irradiated and annealed reactor pressure vessel steels studied by positron annihilation”, *Radiation Effects and Defects in Solids*, vol. 171, no. 3, pp. 231–241, May 2016.
- [29] A. Kuramoto, T. Toyama, T. Takeuchi, Y. Nagai, M. Hasegawa, T. Yoshiie, and Y. Nishiyama, “Post-irradiation annealing behavior of microstructure and hardening of a reactor pressure vessel steel studied by positron annihilation and atom probe tomography”, *Journal of Nuclear Materials*, vol. 425, no. 1, pp. 65–70, Jun. 2012.
- [30] B. Radiguet, PhD thesis, “Etude de la formation d'amas diffus de solutés sous irradiation dans des alliages modèles ferritiques”, Rouen University, 2004.
- [31] E. A. Marquis and J. M. Hyde, “Applications of atom-probe tomography to the characterisation of solute behaviours”, *Materials Science and Engineering R*, vol. 69, no. 4, pp. 37–62, Dec. 2009.
- [32] J. E. Zelenty, “Understanding thermally induced embrittlement in low copper RPV steels utilising atom probe tomography”, *Materials Science and Technology*, vol. 31, no. 8, pp. 981–988, Nov. 2014.
- [33] E. Vincent, PhD thesis, “Simulation numérique à l'échelle atomique de l'évolution microstructurale sous irradiation d'alliages ferritiques”, Lille University, 2006.
- [34] M. H. Mathon, A. Barbu, F. Dunstetter, and F. Maury, “Experimental study and modelling of copper precipitation under electron irradiation in dilute FeCu binary alloys”, *Journal of Nuclear Materials*, vol. 245, no. 2, pp. 224–237, 1997.
- [35] F. Bergner, M. Lambrecht, A. Ulbricht, and A. Almazouzi, “Comparative small-angle neutron scattering study of neutron-irradiated Fe, Fe-based alloys and a pressure vessel steel”, *Journal of Nuclear Materials*, vol. 399, no. 2, pp. 129–136, Apr. 2010.
- [36] E. Meslin, B. Radiguet, P. Pareige, and A. Barbu, “Kinetic of solute clustering in neutron irradiated ferritic model alloys and a French pressure vessel steel investigated by atom probe tomography”, *Journal of Nuclear Materials*, vol. 399, no. 2, pp. 137–145, Apr. 2010.
- [37] R. Ngayam-Happy, C. S. Becquart, C. Domain, and L. Malerba, “Formation and evolution of MnNi clusters in neutron irradiated dilute Fe alloys modelled by a first principle-based AKMC method”, *Journal of Nuclear Materials*, vol. 426, no. 1, pp. 198–207, Jul. 2012.
- [38] G. Bonny, D. Terentyev, A. Bakaev, E. E. Zhurkin, M. Hou, D. Van Neck, and L. Malerba, “On the thermal stability of late blooming phases in reactor pressure vessel steels: An atomistic study”, *Journal of Nuclear Materials*, vol. 442, no. 1, pp. 282–291, Nov. 2013.
- [39] E. Meslin, B. Radiguet, P. Pareige, C. Toffolon, and A. Barbu, “Irradiation-Induced Solute

- Clustering in a Low Nickel FeMnNi Ferritic Alloy”, *Experimental Mechanics*, vol. 51, no. 9, pp. 1453–1458, Mar. 2011.
- [40] F. Bergner, A. Ulbricht, P. Lindner, U. Keiderling, and L. Malerba, “Post-irradiation annealing behavior of neutron-irradiated FeCu, FeMnNi and FeMnNiCu model alloys investigated by means of small-angle neutron scattering”, *Journal of Nuclear Materials*, vol. 454, no. 1, pp. 22–27, Nov. 2014.
- [41] E. Meslin, B. Radiguet, and M. Loyer-Prost, “Radiation-induced precipitation in a ferritic model alloy: An experimental and theoretical study”, *Acta Materialia*, vol. 61, no. 16, pp. 6246–6254, Sep. 2013.
- [42] P. D. Styman, J. M. Hyde, K. Wilford, A. Morley, and G. D. W. Smith, “Precipitation in long term thermally aged high copper, high nickel model RPV steel welds”, *Progress in Nuclear Energy*, vol. 57, pp. 86–92, May 2012.
- [43] P. Pareige, K. F. Russell, R. E. Stoller, and M. K. Miller, “Influence of long-term thermal aging on the microstructural evolution of nuclear reactor pressure vessel materials: An atom probe study”, *Journal of Nuclear Materials*, vol. 250, no. 2, pp. 176–183, 1997.
- [44] J. M. Hyde, G. Sha, E. A. Marquis, A. Morley, K. B. Wilford, and T. J. Williams, “A comparison of the structure of solute clusters formed during thermal ageing and irradiation”, *Ultramicroscopy*, vol. 111, no. 6, pp. 664–671, May 2011.
- [45] M. Perez, F. Perrard, V. Massardier, X. Kleber, A. Deschamps, H. de Monestrol, P. Pareige, and G. Covarel, “Low-temperature solubility of copper in iron: experimental study using thermoelectric power, small angle X-ray scattering and tomographic atom probe”, *Philosophical Magazine*, vol. 85, no. 20, pp. 2197–2210, Feb. 2007.
- [46] M. K. Miller, M. A. Sokolov, R. K. Nanstad, and K. F. Russell, “APT characterization of high nickel RPV steels”, *Journal of Nuclear Materials*, vol. 351, no. 1, pp. 187–196, Jun. 2006.
- [47] M. K. Miller, K. F. Russell, M. A. Sokolov, and R. K. Nanstad, “APT characterization of irradiated high nickel RPV steels”, *Journal of Nuclear Materials*, vol. 361, no. 2, pp. 248–261, Apr. 2007.
- [48] H. Huang, PhD thesis, “Influence de l’irradiation aux neutrons sur le vieillissement des aciers de cuves des réacteurs nucléaires à eau pressurisée”, Rouen University, 2012.
- [49] M. K. Miller, A. A. Chernobaeva, Y. I. Shtrombakh, K. F. Russell, R. K. Nanstad, D. Y. Erak, and O. O. Zabusov, “Evolution of the nanostructure of VVER-1000 RPV materials under neutron irradiation and post irradiation annealing”, *Journal of Nuclear Materials*, vol. 385, no. 3, pp. 615–622, Apr. 2009.
- [50] M. K. Miller, K. A. Powers, R. K. Nanstad, and P. Efsing, “Atom probe tomography characterizations of high nickel, low copper surveillance RPV welds irradiated to high fluences”, *Journal of Nuclear Materials*, vol. 437, no. 1, pp. 107–115, Jun. 2013.
- [51] P. B. Wells, T. Yamamoto, B. Miller, T. Milot, J. Cole, Y. Wu, and G. R. Odette, “Evolution of manganese–nickel–silicon-dominated phases in highly irradiated reactor pressure vessel steels”, *Acta Materialia*, vol. 80, pp. 205–219, Oct. 2014.
- [52] P. D. Styman, J. M. Hyde, D. Parfitt, K. Wilford, M. G. Burke, C. A. English, and P. Efsing, “Post-irradiation annealing of Ni–Mn–Si-enriched clusters in a neutron-irradiated RPV steel weld using Atom Probe Tomography”, *Journal of Nuclear Materials*, vol. 459, pp. 127–134, Mar. 2015.
- [53] W. Xiong, H. Ke, R. Krishnamurthy, P. Wells, L. Barnard, G. R. Odette, and D. Morgan, “Thermodynamic models of low-temperature Mn–Ni–Si precipitation in reactor pressure vessel steels”, *MRS Communications*, pp. 1–5, Aug. 2014.
- [54] P. B. Wells, PhD thesis, “The Character, Stability and Consequences of Mn-Ni-Si Precipitates in Irradiated Reactor Pressure Vessel Steels”, University of California, Jul. 2016.
- [55] A. Wagner, F. Bergner, A. Ulbricht, and C. D. Dewhurst, “Small-angle neutron scattering of low-Cu RPV steels neutron-irradiated at 255 °C and post-irradiation annealed at 290 °C”, *Journal of Nuclear Materials*, vol. 441, no. 1, pp. 487–492, Sep. 2013.
- [56] G. R. Odette, “Radiation Induced Microstructural Evolution in Reactor Pressure Vessel Steels”, *MRS Online Proceedings Library Archive*, vol. 373, Jan. 1994.
- [57] P. D. Styman, J. M. Hyde, K. Wilford, D. Parfitt, N. Riddle, and G. D. W. Smith, “Characterisation of interfacial segregation to Cu-enriched precipitates in two thermally aged reactor pressure vessel steel welds”, *Ultramicroscopy*, pp. 1–7, Jun. 2015.
- [58] P. D. Edmondson, M. K. Miller, K. A. Powers, and R. K. Nanstad, “Atom probe tomography characterization of neutron irradiated surveillance samples from the R. E. Ginna reactor pressure vessel”, *Journal of Nuclear Materials*, vol. 470, pp. 147–154, Mar. 2016.

- [59] D. J. Sprouster, J. Sinsheimer, E. Dooryhee, S. K. Ghose, P. Wells, T. Stan, N. Almirall, G. R. Odette, and L. E. Ecker, “Structural characterization of nanoscale intermetallic precipitates in highly neutron irradiated reactor pressure vessel steels”, *Scripta Materialia*, vol. 113, pp. 18–22, Mar. 2016.
- [60] M. Chiapetto, L. Malerba, and C. S. Becquart, “Nanostructure evolution under irradiation in FeMnNi alloys: A ‘grey alloy’ object kinetic Monte Carlo model”, *Journal of Nuclear Materials*, vol. 462, pp. 91–99, Jun. 2015.
- [61] L. Messina, PhD thesis, “Multiscale modeling of atomic transport phenomena in ferritic steels”, KTH University, 2015.
- [62] C. Domain and C. S. Becquart, “Ab initio calculations of defects in Fe and dilute Fe-Cu alloys”, *Physical Review B*, vol. 65, no. 2, p. 024103, Jan. 2002.
- [63] R. A. Johnson, “Interstitials and Vacancies in α Iron”, *Physical Review*, vol. 134, no. 5, pp. 1329–1336, Jun. 1964.
- [64] F. Maury, A. Lucasson, P. Lucasson, Y. Loreaux, and P. Moser, “Interstitial mobility in FeNi, FeCo and FeMn dilute alloys”, *Journal of Physics F: Metal Physics*, vol. 16, no. 5, pp. 523–541, May 1986.
- [65] F. Maury, A. Lucasson, P. Lucasson, P. Moser, and F. Faudot, “Interstitial migration in irradiated iron and iron-based dilute alloys. II. Interstitial migration and solute transport in FeNi, FeMn and FeCu dilute alloys”, *Journal of Physics: Condensed Matter*, vol. 2, no. 47, pp. 9291–9307, Nov. 1990.
- [66] M. Hernández-Mayoral and D. Gómez-Briceño, “Transmission electron microscopy study on neutron irradiated pure iron and RPV model alloys”, *Journal of Nuclear Materials*, vol. 399, no. 2, pp. 146–153, Apr. 2010.
- [67] J. Marian, B. D. Wirth, A. Caro, B. Sadigh, G. R. Odette, J. M. Perlado, and T. Diaz de la Rubia, “Dynamics of self-interstitial cluster migration in pure α -Fe and Fe-Cu alloys”, *Physical Review B*, vol. 65, no. 14, pp. 144102–11, Mar. 2002.
- [68] H. Xu, R. E. Stoller, Y. N. Osetsky, and D. Terentyev, “Solving the Puzzle of $\{100\}$ Interstitial Loop Formation in bcc Iron”, *Physical Review Letters*, vol. 110, no. 26, p. 265503, Jun. 2013.
- [69] H. Xu, Y. N. Osetsky, and R. E. Stoller, “Self-evolving atomistic kinetic Monte Carlo: fundamentals and applications”, *Journal of Physics: Condensed Matter*, vol. 24, no. 37, pp. 375402–11, Aug. 2012.
- [70] H. Xu, Y. N. Osetsky, and R. E. Stoller, “Simulating complex atomistic processes: On-the-fly kinetic Monte Carlo scheme with selective active volumes”, *Physical Review B*, vol. 84, no. 13, p. 132103, Oct. 2011.
- [71] F. Gao, D. J. Bacon, Y. N. Osetsky, and P. Flewitt, “Properties and evolution of sessile interstitial clusters produced by displacement cascades in α -iron”, *Journal of Nuclear Materials*, 2000.
- [72] D. J. Bacon, F. Gao, and Y. N. Osetsky, “The primary damage state in fcc, bcc and hcp metals as seen in molecular dynamics simulations”, *Journal of Nuclear Materials*, vol. 276, no. 1, pp. 1–12, 2000.
- [73] M. C. Marinica, F. Willaime, and J. P. Crocombette, “Irradiation-Induced Formation of Nanocrystallites with C15 Laves Phase Structure in bcc Iron”, *Physical Review Letters*, vol. 108, no. 2, p. 25501, Jan. 2012.
- [74] R. Alexander, M. C. Marinica, L. Proville, F. Willaime, K. Arakawa, M. R. Gilbert, and S. L. Dudarev, “Ab initio scaling laws for the formation energy of nanosized interstitial defect clusters in iron, tungsten, and vanadium”, *Physical Review B*, vol. 94, no. 2, p. 024103, Jul. 2016.
- [75] K. Arakawa, private communication, 2016.

Chapter 2. Simulation methods and models

2.1	Introduction	33
2.2	Atomic jump processes	34
2.2.1	Uncorrelated random walk	35
2.2.2	Correlated random walk	35
2.2.3	Transport coefficients.....	36
2.2.4	Energetic considerations.....	36
2.3	Cohesive models	37
2.3.1	The ab-initio method	37
2.3.1.1	Generalities	37
2.3.1.2	Variational principle	38
2.3.1.3	The Hartree-Fock approximation.....	38
2.3.1.4	Density functional theory (DFT).....	39
2.3.1.5	DFT Code and methodology.....	40
2.3.2	The cluster expansion model.....	41
2.3.3	Concentration dependent model.....	42
2.4	Migration energy and prefactor	42
2.5	The Monte Carlo method	44
2.5.1	Generalities.....	44
2.5.2	The Metropolis algorithm.....	45
2.6	The Kinetic Monte Carlo method	45
2.6.1	Generalities.....	45
2.6.2	The AKMC approach retained	48
2.6.2.1	The energetic model.....	48
2.6.2.2	The migration model.....	50
2.6.3	Simulated versus physical time	51
2.6.4	The irradiation model	52
2.6.5	The grain boundary model.....	52
2.6.6	Analysis of the AKMC results	52
2.7	The Object Kinetic Monte Carlo method	52
2.8	AKMC acceleration methods	53
2.8.1	Temperature Accelerated Dynamics	54
2.8.2	Parallel Kinetic Monte Carlo.....	54
2.8.3	First passage KMC	55
2.8.4	The energy basin finding algorithm	55
2.8.5	Hybrid AKMC/OKMC.....	56
2.8.6	Coarse-grained KMC.....	56
2.9	Conclusion	57
2.10	Bibliography	57

2.1 Introduction

The simulation of the microstructure evolution under irradiation is performed by simulating the motion of point defects. To do so, different methods and models are required. This chapter will present them. Some important results from the random walk theory will first be exposed. This introduction will highlight the necessity to describe the total energy of the system as well as the migration energies. These two points are going to be the subject of the next sections. Then, numerical method such as the Monte Carlo method as well as the Kinetic Monte Carlo method will be presented. The focus will also be made on the on-lattice AKMC model developed during the last decade to simulate the RPV steels evolution under irradiation. To conclude this chapter, AKMC acceleration techniques from the literature will be exposed.

2.2 Atomic jump processes

Diffusion of substitutional atoms in metals is usually allowed by the migration of point defects. At equilibrium, this migration can occur for instance by exchanging the position of a vacancy with an atom present in the local atomic environment (LAE). Figure 2-1 illustrates this mechanism as well as the activation energy required to perform the exchange.

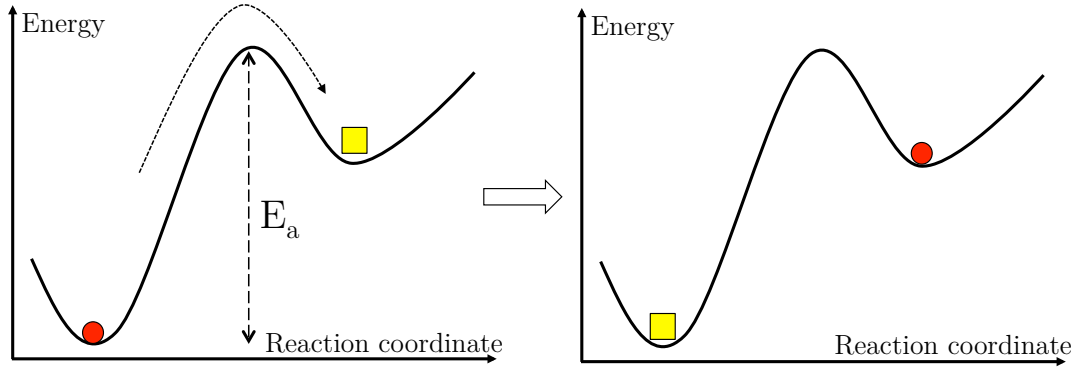


Figure 2-1: Illustration of an exchange between a vacancy (yellow square) and an atom (red circle). The activation energy E_a required to cross over the potential energy barrier is also represented.

A frequency of occurrence can be attached to that jump. For a thermally activated process such as point defect diffusion, the jump frequency is given by:

$$\Gamma = \nu e^{-\frac{E_a}{k_b T}} \quad \text{Equation 2-1}$$

Where ν denotes the attempt frequency and E_a corresponds to the activation energy of the process.

According to harmonic transition state theory [1], the attempt frequency can be expressed as:

$$\nu = \frac{\prod_{j=1}^{3N-3} \nu_j}{\prod_{j=1}^{3N-4} \nu_j^*} \quad \text{Equation 2-2}$$

Where ν_j and ν_j^* are the normal frequencies for vibrations at the local minimum and saddle states respectively and N is the number of atoms.

From the motion of atoms and point defects, several properties can be obtained. Since, KMC is all about transition rates, the relation between diffusion coefficient and jump frequency needs to be specified. Starting from a stochastic trajectory composed of elementary displacements \vec{r}_i , the total displacement of a particle after n moves is expressed by:

$$\vec{R} = \sum_{i=1}^n \vec{r}_i \quad \text{Equation 2-3}$$

Hence, the mean squared displacement is given by:

$$\langle \vec{R}^2 \rangle = \sum_{i=1}^n \langle \vec{r}_i^2 \rangle + 2 \sum_{i=1}^{n-1} \sum_{j=i+1}^n \langle \vec{r}_i \vec{r}_j \rangle \quad \text{Equation 2-4}$$

Using the diffusion theory, the mean squared displacement is connected to the diffusion coefficient (in a 3D random walk) by:

$$\langle R^2 \rangle = 6Dt \quad \text{Equation 2-5}$$

where t corresponds to the time.

2.2.1 Uncorrelated random walk

Now assuming that the diffusion process follows an uncorrelated random walk¹, the second term of Eq. (Equation 2-4) is null. This equation can be re-expressed as:

$$\langle R^2 \rangle = \langle n \rangle d^2 \quad \text{Equation 2-6}$$

where n corresponds to the number of jumps of a d distance. Using n , the jump frequency Γ is defined as:

$$\Gamma = \frac{\langle n \rangle}{Zt} \quad \text{Equation 2-7}$$

where Z is the number of neighboring sites available for a jump. Hence, injecting this definition into Eq. (Equation 2-6) leads to:

$$\langle R^2 \rangle = \Gamma Z d^2 t \quad \text{Equation 2-8}$$

Using Eq. (Equation 2-5) and (Equation 2-8), the jump frequency is related to D by:

$$\Gamma = \frac{6D}{d^2 Z} \quad \text{Equation 2-9}$$

In the case of the BCC system where $Z=8$ and $d = \frac{\sqrt{3}a_0}{2}$ (where a_0 is the lattice parameter), it becomes:

$$\Gamma = \frac{D}{a_0^2} \quad \text{Equation 2-10}$$

This formula is the one employed for the 3D migration of an object in the Object Kinetic Monte Carlo method that will be presented in 2.7.

2.2.2 Correlated random walk

In the case of a correlated random walk, the second term in Eq. (Equation 2-4) is not null. It can be the case of a tracer migrating through vacancy mechanism. In this system, the probability of the tracer to jump is higher if it already experienced a jump during the last states (possible back-jump) than if it is not the case. The effect is called positional memory effects. To take into account this correlation, the correlation factor is introduced as:

$$f = 1 + 2 \lim_{n \rightarrow \infty} \frac{\sum_{i=1}^{n-1} \sum_{j=i+1}^n \langle \vec{r}_i \vec{r}_j \rangle}{\sum_{i=1}^n \langle \vec{r}_i^2 \rangle} \quad \text{Equation 2-11}$$

Now taking into account this effect, Eq. (Equation 2-9) becomes:

¹ An uncorrelated random walk corresponds to a Markovian process. This means that the system in a state j will change to a state k regardless of the state i (the system is memory free).

$$\Gamma = \frac{6D}{fa^2Z} \quad \text{Equation 2-12}$$

And for the BCC system (where $f = 0.72$):

$$\Gamma = \frac{D}{fa_0^2} \quad \text{Equation 2-13}$$

2.2.3 Transport coefficients

From the trajectory of the atoms during the diffusion process, it is possible to evaluate the transport coefficients L_{ij} from the Onsager matrix. These coefficients can be calculated with the Kudo-Green formula [2] using the total displacement of the x specie $\Delta\vec{R}_x$:

$$L_{ij} = \frac{\Delta\vec{R}_i \cdot \Delta\vec{R}_j}{6Vt} \quad \text{Equation 2-14}$$

From these coefficients, several properties can be calculated [3]. Those used in this thesis are:

- The wind factor of a solute X in Fe which is equal to $-(1 + \frac{L_{FeX}^V}{L_{XX}^V})$. This quantity is positive if the vacancy drags the solute, otherwise it is negative.
- In the case of the interstitial diffusion mechanism, the partial diffusion coefficient ratio $\frac{L_{XI}^I}{L_{FeI}^I}$ (equal to $\frac{c_{Fe}}{c_X} \frac{L_{FeX}^I + L_{XX}^I}{L_{FeFe}^I + L_{FeX}^I}$) is greater than 1 if the dumbbell transports the solute.

These properties are important since they govern the non-equilibrium flux coupling that occurs under irradiation. Hence, an accurate description of these quantities is an important element in order to simulation the microstructure evolution of ferritic alloys under irradiation.

2.2.4 Energetic considerations

Equilibrium properties of a N particle system are accessible if its total energy can be computed. This is the thermodynamic aspect of the problem. To do so, a cohesive model that describes the interactions between the particles is required. Additionally, kinetic simulations such as AKMC require the knowledge of the transition rates (e.g. the migration energies). This is the kinetic aspect of the problem. Figure 2-2 illustrates these two aspects.

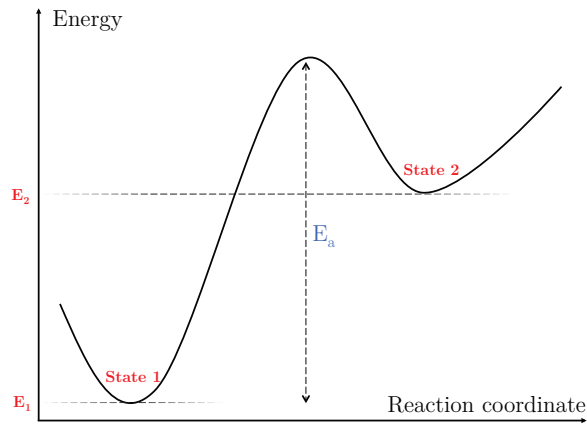


Figure 2-2: Representation of two distinct states the system can reach. The red values refer to the thermodynamic aspect while the blue one corresponds to the kinetic aspect.

Section 2.3 will introduce different cohesive models that are commonly used. Section 2.4 will present the kinetic aspects.

2.3 Cohesive models

In order to determine the properties of an atomic system, it is necessary to be able to calculate its energy. Accordingly, the interactions between the particles have to be described. Two different approaches are possible:

- The ab initio method is based on quantum mechanic laws and is adapted to compute the fundamental properties of a small set of particles. However, the computational resources required are large and the number of atoms that can be simulated small (typically few thousands of atoms).
- The empirical cohesive models are often less accurate but they allow the simulation of millions of atoms. On the one hand, there are interatomic potentials that provide mathematical expression of the potential energy of an atom according to the position of the neighboring atoms in the system (for any position of the atoms) for example EAM potentials for metals (up to few millions of atoms). On the other hand, interatomic potential on a rigid lattice, such as pair interaction models or more complex models based on the cluster expansion method that provides the energies of the atomic configurations. This approach will be described in the section concerning the Kinetic Monte Carlo method. Note that other intermediary cohesive models such as tight binding also exist.

2.3.1 The ab-initio method

2.3.1.1 Generalities

Most of the physical properties of a solid system depend on the behavior of its electrons. Describing such a system can only be done in the context of quantum mechanics (QM). Usually, the objective of QM methods is to approach the solution of the Schrödinger's time-independent equation:

$$\hat{H}\Psi(\vec{x}_1, \vec{x}_2, \dots, \vec{x}_N, \vec{R}_1, \vec{R}_2, \dots, \vec{R}_M) = E\Psi(\vec{x}_1, \vec{x}_2, \dots, \vec{x}_N, \vec{R}_1, \vec{R}_2, \dots, \vec{R}_M) \quad \text{Equation 2-15}$$

where \hat{H} is the Hamiltonian of the system composed by N electrons and M nucleus of M_x mass and Z_x charge. For simplicity reasons, the spin is omitted in (Equation 2-15) and the equations are given in atomic units. The Hamiltonian is defined as follows:

$$\hat{H} = -\frac{1}{2} \sum_{i=1}^N \nabla_i^2 - \frac{1}{2} \sum_{A=1}^M \frac{1}{M_A} \nabla_A^2 - \sum_{i=1}^N \sum_{A=1}^M \frac{Z_A}{r_{iA}} + \sum_{i=1}^N \sum_{j>l}^N \frac{1}{r_{ij}} + \sum_{A=1}^M \sum_{B>A}^M \frac{Z_A Z_B}{R_{AB}} \quad \text{Equation 2-16}$$

Equation 2-16 can be simplified using Born-Oppenheimer's approximation which decouples the motion of electrons from the one of the nucleus. The electrons are then moving in a static field induced by the fixed nucleus. This Hamiltonian is called the electronic Hamiltonian. Thereafter, only this Hamiltonian will be considered:

$$\hat{H}_{elec} = -\frac{1}{2} \sum_{i=1}^N \nabla_i^2 - \sum_{i=1}^N \sum_{A=1}^M \frac{Z_A}{r_{iA}} + \sum_{i=1}^N \sum_{j>i}^N \frac{1}{r_{ij}} = \hat{T} + \hat{V}_{Ne} + \hat{V}_{ee} \quad \text{Equation 2-17}$$

The objective is therefore to solve $\hat{H}_{elec} \Psi_{elec} = E_{elec} \Psi_{elec}$. In practice, it is not possible to solve this equation for a N electrons system (with $N>2$). It is then necessary to resort to other approximations.

2.3.1.2 Variational principle

The variational principle allows approximating the wave function of the ground state Ψ_0 . For that, it is necessary to test all the wave functions Ψ_{trial} satisfying the antisymmetrical property of the wave function as well as the fact that it must be normalized. The computed energy using Ψ_{trial} is then higher than E_0 (the energy of the ground state) for $\Psi_{trial} \neq \Psi_0$.

$$\langle \Psi_{trial} | \hat{H} | \Psi_{trial} \rangle = E_{trial} \geq E_0 = \langle \Psi_0 | \hat{H} | \Psi_0 \rangle \quad \text{Equation 2-18}$$

At this stage, it is important to notice that the notion of functional² has been introduced. Indeed, the energy described in Equation 2-18 is a functional of Ψ_{trial} . Then, the goal is to find:

$$E_0 = \min E[\Psi_{trial}] = \min \langle \Psi_{trial} | \hat{T} + \hat{V}_{Ne} + \hat{V}_{ee} | \Psi_{trial} \rangle \quad \text{Equation 2-19}$$

Obviously, it is not possible to search among all eligible functions. The Hartree-Fock approximation allows restricting the research domain.

2.3.1.3 The Hartree-Fock approximation

As a first approximation, the Hartree's approach was to express the global wave function of the N electrons system as the produce of N mono-electronic functions $\Psi(\vec{x}_1, \vec{x}_2, \dots, \vec{x}_N) = \psi_1(\vec{x}_1) \psi_2(\vec{x}_2) \dots \psi_N(\vec{x}_N)$. This approximation greatly simplifies the N electrons problem. However, it remains incomplete. The exchange interaction expressing the asymmetrical property of the wave function is not taken into account. The antisymmetrical property of the wave function is described:

$$\Psi(\vec{x}_1, \dots, \vec{x}_a, \dots, \vec{x}_b, \dots, \vec{x}_N) = -\Psi(\vec{x}_1, \dots, \vec{x}_b, \dots, \vec{x}_a, \dots, \vec{x}_N) \quad \text{Equation 2-20}$$

In order to take this property into account, the wave function (in the Hartree-Fock approximation) is put under the form of a Slater determinant. The motion of same spin electron pairs must indeed be correlated.

² Functional: It is an application that takes as an argument a function and returns a scalar such as $f(x) \xrightarrow{F[f(x)]} y$. For example, the functional $F[f(x)] = \int_0^1 f(x) dx$ returns the value $\frac{1}{3}$ for $f(x) = x^2$.

$$\Psi_0 = \frac{1}{\sqrt{N!}} \begin{vmatrix} \chi_1(\vec{x}_1) & \chi_2(\vec{x}_1) & \dots & \chi_N(\vec{x}_1) \\ \chi_1(\vec{x}_2) & \chi_2(\vec{x}_2) & \dots & \chi_N(\vec{x}_2) \\ \vdots & \vdots & \ddots & \vdots \\ \chi_1(\vec{x}_N) & \chi_2(\vec{x}_N) & \dots & \chi_N(\vec{x}_N) \end{vmatrix} \quad \text{Equation 2-21}$$

where $\chi_N(\vec{x})$ is the mono electronic wave function which is composed of an orbital $\phi(\vec{r})$ and of one of the two spin-eigenfunctions (α or β). $\chi(\vec{x})$ can be rewritten as $\chi(\vec{x}) = \phi(\vec{r})\sigma$ with $\sigma = \alpha, \beta$.

In order to completely satisfy the Pauli principle, it is necessary to add the exchange operator. Nevertheless, same spin electron pairs and opposite spin electron pairs are treated in a asymmetric manner. Thus, correlations are badly taking into account. The correlation energy E_{corr} is introduced as:

$$E_{corr} = E_{exact} - E_{HF} \quad \text{Equation 2-22}$$

The Hartree energy $E_{Hartree}$ describe the system without taking into account the exchange energy E_{exch} and the correlation energy E_{corr} . The sum of these two contributions is related to the exchange and correlation energy E_{XC} in such way that:

$$E_{exact} = E_{Hartree} + E_{XC} \quad \text{Equation 2-23}$$

Considering that the variable is the electronic density $\rho(\vec{r})$, the energy formulation as it is described in the density functional theory (DFT) is given by:

$$E_{exact}[\rho(\vec{r})] = E_{Hartree}[\rho(\vec{r})] + E_{XC}[\rho(\vec{r})] \quad \text{Equation 2-24}$$

It is then necessary to determine the best functional to reflect the exchange and correlation energy $E_{XC}[\rho(\vec{r})]$.

2.3.1.4 Density functional theory (DFT)

The employment of the electronic density $\rho(\vec{r})$ as a fundamental variable of the system reduces the complex N body problem into a one-body problem in an effective field V_{eff} ³ which takes into account all these interactions. The interest being that the electronic density only depends on the 3 spatial coordinates (6 if the spin is taken into account).

Theorem 1: For a given external potential, the total energy of the ground state E_0 is a unique functional of the electronic density $\rho(\vec{r})$.

Thus, a variable of the external potential induces a variation of the electronic density. The total energy of the system is then written:

$$E[\rho(\vec{r})] = T[\rho(\vec{r})] + \frac{1}{2} \int \int \frac{\rho(\vec{r})\rho(\vec{r}')}{|\vec{r} - \vec{r}'|} d^3\vec{r} d^3\vec{r}' + E_{XC}[\rho(\vec{r})] + \int \rho(\vec{r})V_{ext}(\vec{r})d^3\vec{r} \quad \text{Equation 2-25}$$

In this expression, only $E_{XC}[\rho(\vec{r})]$ cannot be computed exactly. The quantity $E_{XC}[\rho(\vec{r})]$ represents all the multibody contributions of the problem. Although small in comparison to the total energy of the system, $E_{XC}[\rho(\vec{r})]$ contains all the information needed for a good description of the interactions. Its evaluation is the foundation of the modern ab initio methods. The determination of $E_{XC}[\rho(\vec{r})]$ is difficult. This quantity is therefore approximated and can be calculated by quantum Monte Carlo for example.

³ V_{eff} is equal to the sum of the potentials $V_{Ne}(\vec{r})$ and $V_{ee}(\vec{r}_1, \vec{r}_2)$ explained in the Equation 2-16.

Theorem 2: A universal functional $E[n]$ of the total energy (independent of all external potential) exists for all many particles system and has a minimum corresponding to the minimal value of the ground state density and to the ground state energy of the system.

This theorem underlines the importance of the variational principle in DFT methods (just as in the Hartree-Fock method). In this context, the mono electronic wave functions are written:

$$\left[-\frac{1}{2}\nabla^2 + V_{eff}(\vec{r}) - \epsilon_i\right]\psi_i(\vec{r}) = 0 \quad \text{Equation 2-26}$$

with:

$$V_{eff}(\vec{r}) = V_{ext}(\vec{r}) + \int \frac{1}{|\vec{r}_i - \vec{r}_j|} \rho(\vec{r}_j) + V_{xc}(\vec{r}) \quad \text{Equation 2-27}$$

The effective Kohn and Sham Hamiltonian is thus written [4]:

$$h^{KS}[\rho(\vec{r})] = -\frac{1}{2}\nabla^2 + V_{ext}(\vec{r}) + \int \frac{1}{|\vec{r}_i - \vec{r}_j|} \rho(\vec{r}_j) + V_{xc}(\vec{r}) \quad \text{Equation 2-28}$$

And the electronic density $\rho(\vec{r})$ is noted:

$$\rho(\vec{r}) = 2 \sum_i f_i |\psi_i(\vec{r})|^2 \quad \text{Equation 2-29}$$

where f_i is a partial occupation function of the orbital ($0 \leq f_i \leq 1$). The 2 factor allows to take into account the double occupation of each orbital induced by the spin degeneracy.

The exchange and correlation potential is expressed as:

$$V_{xc}[\rho(\vec{r})] = \frac{\delta E_{xc}[\rho]}{\delta \rho(\vec{r})} \quad \text{Equation 2-30}$$

The fact that the effective potential V_{eff} depends on the electronic density $\rho(\vec{r})$ (itself depending on Ψ_i) reflects that the problem to treat is self-consistent. This process is called Self-Consistent Field calculation) and it applies to DFT and HF methods.

While DFT is an appropriate tool to compute fundamental properties of a static system, it is also widely employed to estimate kinetic properties such as migration barriers.

2.3.1.5 DFT Code and methodology

The DFT code used in this study (as well as Vincent and Ngayam-Happy thesis) is VASP (Vienna Ab initio Simulation Package) [5], [6]. The exchange and correlation functional is described by the Generalized Gradient Approximation (GGA) from Perdew et al. [7]. This approximation is known to provide a better description of iron than the LDA (Local Density Approximation). Since all-electron calculations are very resources demanding, the VASP code provides pseudo potentials to describe the electron-ion interactions. The library of pseudo-potentials provides two kinds of pseudo-potentials: the Ultra Soft Pseudo-Potential (USPP) and the Projector Augmented Wave (PAW).

Since computed properties can change depending on the pseudo-potential employed, the results from DFT calculations presented in this manuscript will refer to the pseudo-potential employed.

All the calculations are spin polarized. The supercells considered are from 250 and 1024 atoms, with periodic boundary conditions. All the configurations have been relaxed at constant volume. The k-points mesh are

respectively $3 \times 3 \times 3$ and $1 \times 1 \times 1$ for 250 and 1024 atom supercells. The energy cutoff is 300 eV for the PAW calculations.

2.3.2 The cluster expansion model

The cluster expansion approach is a simple model on rigid lattice that aims at overcoming the absence of interatomic potential when the chemical complexity of a system is too high. Using this approach, the total energy of a system is written as a sum of n-uplet interactions⁴.

$$E_{tot} = \sum_i \varepsilon_i + \sum_i \sum_{j<i} \varepsilon_{ij} + \sum_i \sum_{j<i} \sum_{k<j} \varepsilon_{ijk} + \sum_i \sum_{j<i} \sum_{k<j} \sum_{l<k} \varepsilon_{ijkl} + \dots$$

Usually these n-uplet interactions are pairs but they can be triplets ε_{ijk} or even quadruplets ε_{ijkl} . Figure 2-3 shows some simple interactions (from pair to quadruplet) that can be chosen.

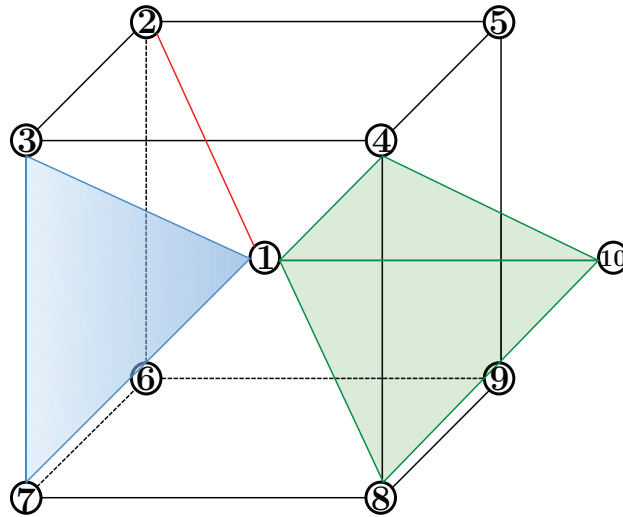


Figure 2-3: Illustration of possible pair interaction ε_{1-2} (red), triplet interaction ε_{1-3-7} (blue) and a quadruplet interaction $\varepsilon_{1-4-8-10}$.

Using the on-lattice Hamiltonian with a pair interaction approximation, the total energy of a N particles system can be written as:

$$E_{tot} = \sum_{k=1}^M \sum_{i=1}^N \sum_{j \neq i}^N \varepsilon_{i,j}^k \tag{Equation 2-31}$$

where $\varepsilon_{i,j}$ denotes the pair interactions between site i and j . M denotes the range of the pair interaction employed in the model.

⁴ The $\varepsilon_{\{i,j,\dots\}}$ depends on the element on sites $\{i, j, \dots\}$.

2.3.3 Concentration dependent model

An interesting way to overcome the limitation of pair interactions described above (which remain constant no matter the local atomic environments) was proposed by Senninger during her thesis [8]. A model was developed to simulate the FeCr system. Due to the necessity of the model to reproduce the asymmetrical mixing energies of the Fe-Cr alloys, the author introduced a dependence on the local Cr concentration in the Fe-Cr pair interactions. In this model, the pair interactions are defined as:

$$\epsilon_{Fe-Cr}^{(n)}(c) = \frac{1}{2} \left(\epsilon_{Fe-Cr}^{(n)}(c_{Fe}) + \epsilon_{Fe-Cr}^{(n)}(c_{Cr}) \right) \quad \text{Equation 2-32}$$

where the local concentration c (in the BCC lattice) is:

$$c_x = \frac{N_{Cr}^X(1) + N_{Cr}^X(2) + \delta_{XCr}}{15} \quad \text{Equation 2-33}$$

Here, $N_{Cr}^X(1)$ corresponds to the number of Cr atoms around the X atom at 1NN distance, $N_{Cr}^X(2)$ corresponds to the number of Cr atoms around the X atom at 2NN distance and δ_{XCr} is the Kronecker symbol (equal to 1 if the X site is occupied by a Cr atom).

2.4 Migration energy and prefactor

Now that the thermodynamic aspect has been exposed by means of the cohesive model description, the last aspect that needs to be presented, in order to simulate the temporal evolution of a system is the kinetic properties. The transition frequencies directly rule the probability of an event to happen. Several methods exist to evaluate the activation energy as well as the attempt frequency (presented in section 2.2). These methods can be divided into two groups. Those employing the on-lattice approximation and the others off-lattice. First, the methods that are not related to the on-lattice approximation are exposed.

In order to evaluate the activation energy of a process, the nudged elastic-band method (NEB) is commonly used to compute the migration activation energy. From the initial and the final state of the system, this method is able to find the minimum energy path. To do so, a sequence of different images of the system is built. This sequence corresponds to a path between the initial state and the final state. Each state is connected to its successor by a spring. Then, all states are relaxed at the same time. Using the NEB method, the force applied in a system is composed of two contributions. The first one is applied to the system (independently of the neighbor images). Only the component perpendicular to the local tangent of the band is retained. The second one is the force applied by the spring force component along the tangent. Then, the goal is to minimize the sum of the energy provided by DFT and the elastic energy.

Unlike the NEB [9], [10], the dimer method [11] is an open-ended technique that allows finding possible transition states. Two images of the system (which are close to each other on the potential energy surface) form the “dimer”. To find the transition states, the dimer climbs the potential energy surface from its starting position. Additionally, the dimer rotates to find the direction of the lowest curvature. A more recent way to evaluate the migration parameters has been proposed by the Activation-Relaxation Technique (ART) (which is also an open-ended technique). This method is able to define on-the-fly events in a given energy landscape [12].

When it comes to perform kinetic simulations, methods exist to find the transitions on the fly. Coupled with a KMC algorithm, these methods allow simulating the time evolution of a system without knowledge of possible events. One of these methods is the kART method (the “k” standing for kinetic) [13]. Basically, kART is a combination between ART and the KMC method. It is employed to simulate mechanisms that could not be observed by the mean of molecular dynamic [14] but its computation demands are high (the number of AKMC steps reachable is of the order of 10^4). Moreover, an equilibrium cohesive model (to have

forces on atoms) is required (making the employment of this technique for the simulation of complex alloys difficult). Another method based on the same idea is the SEAKMC method [15]. Like kART, this method is powerful to study complex elementary mechanisms involving several atoms such as the loop interactions exposed in chapter 1 paragraph 1.4.4.1, but not to simulate the whole evolution of a microstructure because the method is not fast enough to perform these types of simulation. To overcome the performance limitations of the one the fly KMC simulations, Rehman et al. [16] recently proposed a method that uses a cluster expansion approach to predict the activation barrier. The cluster expansion is built on the fly during the simulation from the barriers computed by the NEB method. Once the cluster expansion is trained, the authors found that the KMC simulation of the diffusion of Ag on a (100) Ag surface was orders of magnitude faster than standard KMC.

Concerning the evaluation of the activation energy in the on-lattice approximation, the broken bond model is a commonly used approximation that can be found in the literature. In this approximation, the migration energy explicitly depend on the local environment of the jumping atom at the saddle point. The "broken bond" terms come from the pair interactions between the jumping atom / vacancy that are broken after the jump. Hence, the migration energy for an atom A by means of the vacancy V is given by:

$$E_a^{i \rightarrow j} = e_A^{sp} - \sum_{i,n} \epsilon_{A-i}^n - \sum_{j,n} \epsilon_{j-V}^n \quad \text{Equation 2-34}$$

The Σ terms represent the pair interactions lost after the jump (which depend on the range n of the cohesive model). Concerning the e_A^{sp} , its definition varies from one author to another:

- It can be constant (e.g. no dependency on the environment at the saddle point [17])
- It can also correspond to the binding energy between A and the system when A is at the saddle point, described by a sum of effective pair interactions between the atom at the saddle point and its first nearest neighbors [18], [19].

The limitation of this migration model comes from the chemical complexity of the RPV alloys. The number of local configurations around the saddle-point grows as N_{species}^6 . Since the vacancy is a specie in our on-site KMC model, the number of configurations is equal to 117649 (without symmetry considerations). Nowadays, computing the binding energy between the vacancy and its first neighbors at the saddle point by means of DFT calculations is very difficult due to the combinatorial explosion. Thus, this migration model was not retained in E. Vincent PhD work for the simulation of the complex alloys [20]. The model chosen in this study is the Final-Initial System Energy model (usually called FISE). Theoretical foundations of this model involving the energy variation in the saddle point energy estimation can be found in [21]. In the FISE model, the saddle-point energy is estimated by:

$$E_a^{i \rightarrow j} = E_{a_0} + \frac{E_j - E_i}{2} = E_{a_0} + \frac{\Delta E}{2} \quad \text{Equation 2-35}$$

This energy is the sum of two contributions. The reference migration energy E_{a_0} is, in our model, a constant only depending on the type of jump performed (in the case of vacancies, it refers to the atom that permutes its position with the vacancy); ΔE represents the energy difference between final and initial state, which is assume to be impact on the saddle-point energy.

2.5 The Monte Carlo method

2.5.1 Generalities

The Monte Carlo method is commonly used to compute mean properties of a system at equilibrium.

The mean equilibrium value of a quantity $\langle A \rangle$ is given in the canonical ensemble by:

$$\langle A \rangle_{NVT} = \int A \frac{e^{-\frac{\mathcal{H}}{k_b T}}}{Z} d\Gamma \quad \text{Equation 2-36}$$

where Γ is the volume of the state space and \mathcal{H} is the Hamiltonian of the system.

In practice, it is impossible to determine directly the partition function of a N particle system. However, the means of a physical quantity $\langle A \rangle$ can still be calculated. To do this, it is necessary to generate microstates $\{r^N\}_i$ distributed by the density probability ρ of the statistical ensemble considered. A Markov chain is built, that is to say that each state explicitly depends on the previous state and belongs to a finite set of states (e.g. the state space). The order in which the states succeed to each other has no physical meaning. The challenge is to find a way where each state has been produced with the good probability at the end of the simulation (i.e. at equilibrium).

$$\{r^N\}_i \xrightarrow{\Pi_{ij}} \{r^N\}_j \quad \text{Equation 2-37}$$

The Π_{ij} matrix (called transition matrix) has to be stochastic ($\sum_j \Pi_{ij} = 1$) and ergodic ($\rho\Pi = \rho$), where ρ is the limit distribution of the Markov chain.

The ρ vector is known and its elements ρ_i are given by the probability density of the statistical ensemble considered. In the canonical ensemble ρ_i is given by:

$$\rho_i = \frac{e^{-\beta\mathcal{H}(\{r^N\}_i)}}{Z} \quad \text{Equation 2-38}$$

where Z is the partition function and \mathcal{H} the Hamiltonian and β corresponds to $k_b T$.

The ergodicity condition is quite important because it allows the equilibrium not to be destroyed when it is established. To make the Markov chain ergodic the detailed balance condition is usually employed:

At equilibrium, the average number of moves allowed from any state i to any state j is exactly equal to the average number of reverse movements. This is the microscopic reversibility condition (or detailed balance).

This condition can be rewritten in a mathematical way as:

$$\rho_i \Pi_{ij} = \rho_j \Pi_{ji} \quad \text{Equation 2-39}$$

To move from a given state i to a state j , the underlying matrix of the Markov chain α is introduced. Its element α_{ij} correspond to the attempt $i \rightarrow j$. α is chosen symmetric ($\alpha_{ij} = \alpha_{ji}$). The probability of accepting the move is written P_{ij} and Π_{ij} can be re-expressed as:

$$\Pi_{ij} = \alpha_{ij} P_{ij} \quad \text{Equation 2-40}$$

And from the detailed balance equation (Equation 2-39):

$$\rho_i \alpha_{ij} P_{ij} = \rho_j \alpha_{ji} P_{ji} \quad \text{Equation 2-41}$$

Which leads to this property that does not imply the partition function:

$$\frac{P_{ij}}{P_{ji}} = \frac{\rho_j}{\rho_i} = \frac{e^{-\beta U_j}/Z}{e^{-\beta U_i}/Z} = e^{-\beta \Delta U_{ij}} \quad \text{Equation 2-42}$$

2.5.2 The Metropolis algorithm

The Metropolis algorithm [22], [23] is a numerical method that allows to compute several properties of a system at the equilibrium. The algorithm of the method can be written as:

$$\begin{aligned} \text{if } \rho_j < \rho_i & \quad P_{ij} = \frac{\rho_j}{\rho_i} \text{ and } P_{ji} = 1, & \quad \Pi_{ij} = \alpha_{ij} \frac{\rho_j}{\rho_i} \text{ and } \Pi_{ji} = \alpha_{ij} = \alpha_{ji} \\ \text{if } \rho_j \geq \rho_i & \quad P_{ij} = 1 \text{ and } P_{ji} = \frac{\rho_i}{\rho_j}, & \quad \Pi_{ij} = \alpha_{ij} = \alpha_{ji} \text{ and } \Pi_{ji} = \alpha_{ji} \frac{\rho_i}{\rho_j} \end{aligned}$$

To decide if the attempt has to be accepted when $P_{ij} \neq 1$, a random number ξ in the interval $[0,1]$ is generated from a uniform distribution. If $\xi \leq P_{ij}$ the attempt is accepted. In the other case, it is refused and another proposition is made.

2.6 The Kinetic Monte Carlo method

2.6.1 Generalities

The “infrequent event problem” is one of the main issues when it comes to investigate the long-term evolution of an atomistic system. The “infrequent” term here is used to qualify a process whose occurring frequency is much lower than the typical vibrational frequencies of the particles. Generally, such events are not observable through Molecular Dynamics (MD) simulations because of the small time step required for the integration of the equations of motion. The Atomic Kinetic Monte Carlo (AKMC) is a suitable method to overcome this limitation. In order to achieve this, a list of all relevant event’s transition frequencies is built. The knowledge of all transition frequencies allows making the system evolve from state-to-state without describing the particles oscillations. Figure 2-4 illustrates these different points. The succession of states is temporally connected using the residence-time algorithm [24]. Nowadays, the AKMC is a widely used simulation method in a large spectrum of scientific fields.

Unlike the Metropolis algorithm, the mean-residence-time algorithm allows to simulate the time evolution of Poisson type processes occurring at known rates. This method provides a numerical solution of the Master equation:

$$\frac{\partial P(i, t)}{\partial t} = - \sum_{j \neq i} \omega(i \rightarrow j) P(i, t) + \sum_{j \neq i} \omega(j \rightarrow i) P(j, t) \quad \text{Equation 2-43}$$

the $\omega(a \rightarrow b)$ is the probability per unit time for the system to make the transition from state a to state b and $P(a, t)$ is the probability for the system to be in state a at time t .

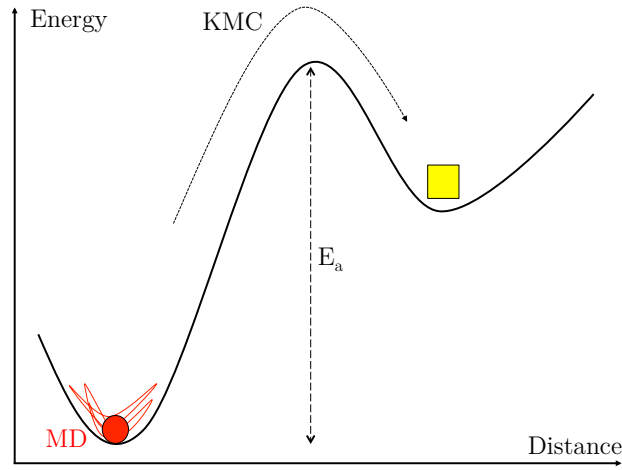


Figure 2-4: Schematic representation of a one-dimensional diffusion of an atom (circle) through a vacancy (square) mechanism. If the activation energy E_a is too high, only oscillations of the atom (red lines) will be observed by MD simulations. The KMC can overcome this limitation if the activation energy as well as the attempt frequency related to the transition are known. In this case, the discrete transition can be performed (solid line).

As in the Metropolis Monte Carlo method, the detailed-balance criterion is used to let the system reach and maintain equilibrium. At equilibrium, the Master equation can therefore be rewritten as:

$$\frac{\partial P(i, t)}{\partial t} = 0 \quad \text{Equation 2-44}$$

The first step of this rejection-free KMC algorithm (usually called residence-time algorithm) is to generate a configuration of the system complying with the input parameters (solute concentration, number of vacancies, etc). From this configuration, the total energy of the system and the jump frequencies of all possible jumps are calculated. $\Gamma_{j,k}$ represents the jump frequency of the k jump of the j diffusing specie. A random number ξ between 0 and $\sum_{j,k} \Gamma_{j,k}$ is then generated. The jump chosen m of the diffusing specie l between all the jumps available is the one corresponding to:

$$\sum_{j=1}^l \sum_{k=1}^{m-1} \Gamma_{j,k} < \xi \leq \sum_{j=1}^l \sum_{k=1}^m \Gamma_{j,k} \quad \text{Equation 2-45}$$

The probability associated with this jump is:

$$P_{l,m} = \frac{\Gamma_{l,m}}{\sum_{j,k} \Gamma_{j,k}} \quad \text{Equation 2-46}$$

Once the selected jump is executed, the time is increased by the mean time step according to:

$$\Delta t = \frac{-\ln(\xi')}{\sum_{j,k} \Gamma_{j,k}} \quad \text{Equation 2-47}$$

Where ξ' is a random number uniformly distributed between 0 and 1.

Taking into account this new configuration, the list of all available transitions is updated and the next jump is chosen. Figure 2-5 presents the algorithm in a schematic way.

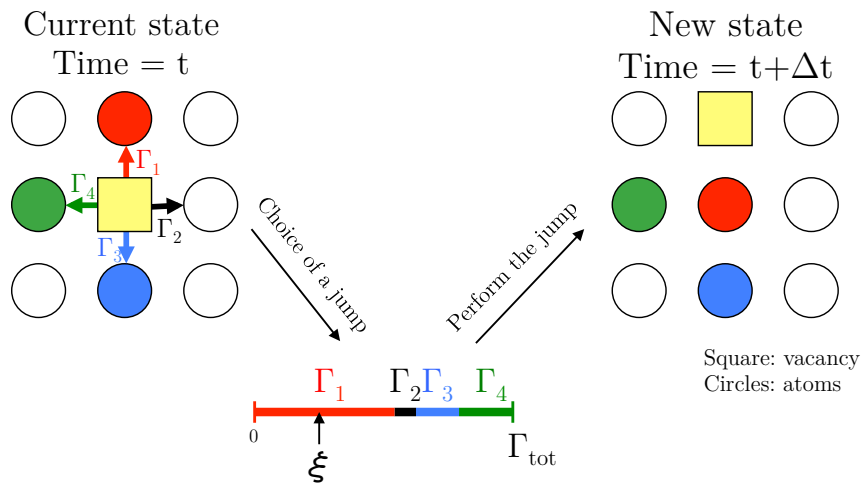


Figure 2-5: Representation of the KMC algorithm on a 2D square lattice with one vacancy performing a transition with one of its first nearest neighbors (1NN transition).

A global representation of the algorithm used to perform the KMC simulation is presented in Figure 2-6.

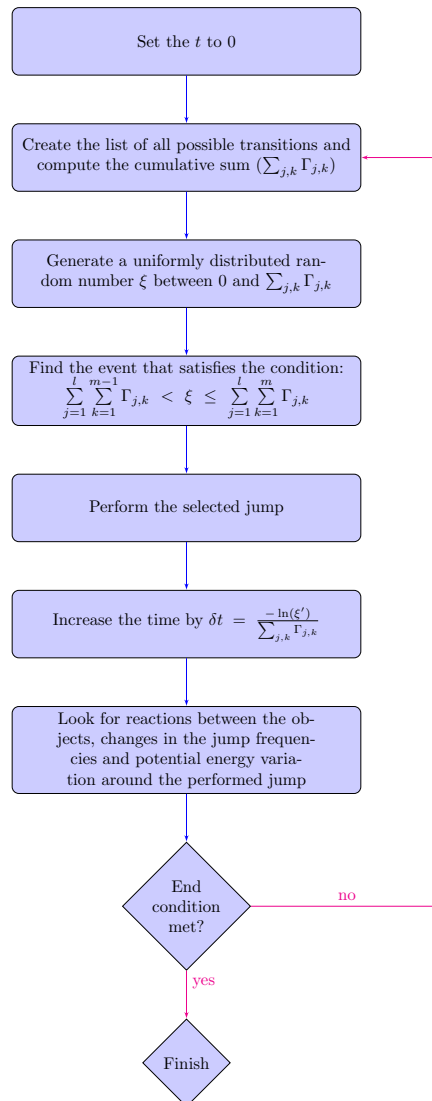


Figure 2-6: Flowchart representing the different steps for performing a KMC simulation.

Now that the KMC method has been introduced, some comments have to be made. First, this algorithm is a serial algorithm (succession of jumps) this property makes its parallelization a non-trivial subject if the species are not homogeneously distributed. Secondly, this algorithm does not include rejection. Each step a move is performed. To finish, the higher $\sum_{j,k} \Gamma_{j,k}$, the lower Δt . This leads, for example, to a slow time elapse when the number of possible jump is large (e.g. under irradiation where the number of diffusive species is typically higher than 100).

To conclude this section, it is important to note that the KMC code LAKIMOCA performs on-lattice KMC calculation. This means that particles are fixed on an atomic lattice. Jumps are performed between first nearest neighbor sites. The atoms do not move around the perfect crystal lattice and no lattice relaxation can be done. However, the cohesive model takes into account the energetic impact of lattice relaxation from the ab initio calculations which have been done for the parameterization of the model.

2.6.2 The AKMC approach retained

2.6.2.1 The energetic model

Because of the chemical complexity of the targeted system (the RPV steel), there is no interatomic potential available. Thus, the choice was made to use pairs-interactions (ϵ) for describing the energy of the system. It presents the advantage of being fast for performing variation of the total energy. In the present model, only interactions until the second nearest neighbors are taken into account.

In the context of this model, the total energy of the system can be written as:

$$E_{tot} = \sum_{k=1}^2 \sum_{i=1}^N \sum_{j \neq i}^N \epsilon_{i,j}^k + E_{dumb} + E_{FIA} \quad \text{Equation 2-48}$$

Where the first term denotes the interactions between on-site particles, E_{dumb} and E_{FIA} denote the dumbbell energy and the foreign interstitial atoms energy (e.g. carbon).

All these pair interactions have been parameterized during two PhD thesis for our Fe-CuNiMnSiP-C system [20], [25]. This parameterization will be denoted ‘‘Pair2NN-Vincent’’ parameterization in the rest of the manuscript.

From this pair interaction model, several thermodynamic properties can be computed. The cohesive energy can be written as:

$$E_{coh}(X - X) = 4\epsilon_{X-X}^{1nn} + 3\epsilon_{X-X}^{2nn} \quad \text{Equation 2-49}$$

The mixing energy is given by:

$$E_{mix}(X/Y) = -4\epsilon_{X-X}^{1nn} - 3\epsilon_{X-X}^{2nn} + 8\epsilon_{X-Y}^{1nn} + 6\epsilon_{X-Y}^{2nn} - 4\epsilon_{Y-Y}^{1nn} - 3\epsilon_{Y-Y}^{2nn} \quad \text{Equation 2-50}$$

The iNN binding energies can be expressed by:

$$E_b^i(X - Y) = \epsilon_{Fe-X}^i + \epsilon_{Fe-Y}^i - \epsilon_{Fe-Fe}^i + \epsilon_{X-Y}^i \quad \text{Equation 2-51}$$

The vacancy formation energy in X is:

$$E_{for}(Vac/X) = 8\epsilon_{Vac-X}^{1nn} + 6\epsilon_{Vac-X}^{2nn} - 4\epsilon_{X-X}^{1nn} - 3\epsilon_{X-X}^{2nn} \quad \text{Equation 2-52}$$

Since the previous equations do not allow determining ϵ_{Fe-Fe}^{2nn} , ϵ_{Vac-Fe}^{2nn} and ϵ_{X-X}^{2nn} , the choice was made to assume simple linear relations:

$$\begin{aligned}\epsilon_{X-X}^{1nn} &= \gamma_X \epsilon_{Fe-Fe}^{2nn} \\ \epsilon_{Fe-Fe}^{1nn} &= \alpha \epsilon_{Fe-Fe}^{2nn} \\ \epsilon_{Vac-X}^{1nn} &= \beta \epsilon_{Vac-X}^{2nn}\end{aligned}\quad \text{Equation 2-53}$$

In the “Pair2NN-Vincent” parameterization, α , β and γ_X are equal to 1.

Concerning the E_{dumb} terms, other parameters are employed in the cohesive model, since SIAs are more complex than on site species:

- E_b^{comp} represents the binding energy between one atom in the dumbbell and one atom b in a compressive position;
- E_b^{tens} represents the binding energy between the dumbbell and one atom on a tensile position;
- $E_b^{SIA-SIA}$ is the binding energy between two SIAs;
- E_b^{self} is the binding energy between the two atoms in the dumbbell.

Figure 2-7 illustrates these interactions.

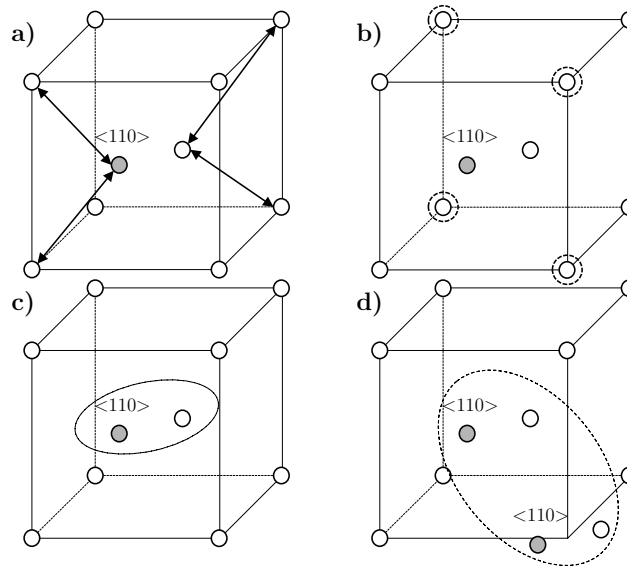


Figure 2-7: a) E_b^{comp} terms illustrated by the double arrows. b) Tensile position highlighted by the dashed circles. c) Self binding energy of the atoms in the dumbbell (E_b^{self}). d) SIA-SIA binding energies ($E_b^{SIA-SIA}$).

Using these interactions, the E_{dumb} is given by:

$$\begin{aligned}E_{dumb} = \sum_i \left(E_f^{<110>} + \sum_j E_b^{comp}(dumb_i - X_j) + \sum_j E_b^{tens}(X_j) + \sum_{i,j} E_b^{self}(X_j - X_k) \right. \\ \left. + \sum_j E_b^{SIA-SIA}(dumb - dumb) \right)\end{aligned}\quad \text{Equation 2-54}$$

2.6.2.2 The migration model

The migration model retained by Vincent was the FISE model (presented in section 2.4).

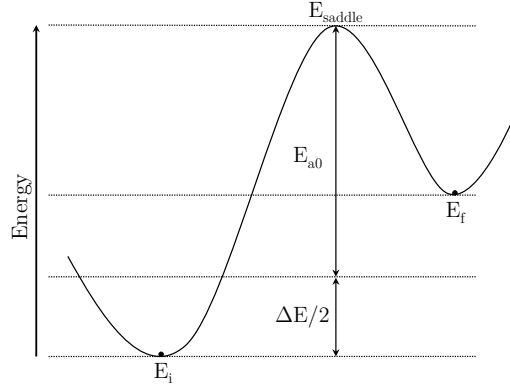


Figure 2-8: Schematic representation of the two terms composing the FISE model.

Using pair interaction models, it is not possible to compute on-the-fly the attempt frequency and the activation energy of a particular transition. Thus, assumptions have to be done. The first one is to consider the attempt frequency as a constant. Its value is chosen to be equal to $6 \times 10^{12} \text{ s}^{-1}$ which is of the order of the Debye's frequency. This commonly used assumption is based on the fact that small variations of the activation energy are more likely to have greater impact than those of the attempt frequency on the occurring frequency of a transition (because of its exponential dependency). While this assumption can have effects on the hierarchy of rates [26], it still remains an acceptable first order hypothesis. This migration energy model is compatible with the detailed balance conditions (see Equation 2-44):

$$\omega(i \rightarrow j)P(i) = \omega(j \rightarrow i)P(j) \quad \text{Equation 2-55}$$

By replacing the $\omega(x \rightarrow y)$ terms and the $P(x)$ (the probability for being in the x state), the previous expression can be written as:

$$\nu e^{-\frac{E_a^{i \rightarrow j}}{k_b T}} e^{-\frac{E^i}{k_b T}} = \nu e^{-\frac{E_a^{j \rightarrow i}}{k_b T}} e^{-\frac{E^j}{k_b T}} \quad \text{Equation 2-56}$$

Where Z is the partition function. Since ν is supposed constant, some simplifications can be done:

$$e^{-\frac{E_a^{i \rightarrow j}}{k_b T}} e^{-\frac{E^i}{k_b T}} = e^{-\frac{E_a^{j \rightarrow i}}{k_b T}} e^{-\frac{E^j}{k_b T}} \quad \text{Equation 2-57}$$

By replacing the $E_a^{x \rightarrow y}$ by $E_{a_0}^{x \rightarrow y} + \frac{E_y - E_x}{2}$, the final expression can be obtained:

$$e^{-\frac{E_{a_0}^{i \rightarrow j}}{k_b T}} e^{-\frac{E^i - E^j}{k_b T}} = e^{-\frac{E_{a_0}^{j \rightarrow i}}{k_b T}} e^{-\frac{E^i - E^j}{k_b T}} \quad \text{Equation 2-58}$$

The jumping atom going from state i to state j and from state j to state i is necessarily the same. Since the E_{a_0} term only depends on the jumping atom, the latter condition is always true ($E_{a_0}^{i \rightarrow j} = E_{a_0}^{j \rightarrow i}$).

All the AKMC simulations presented in this manuscript were performed with the FISE model. The list of the E_{a_0} is given in Table 2-1.

X	Fe	Cu	Si	Mn	Ni	P
USPP E_{a0} (X) (eV) [20]	0.62	0.54	0.42	1.03	0.68	0.41
PAW E_{a0} (X) (eV) [27]	0.70	0.51	0.51	0.42	0.63	0.40

Table 2-1: E_{a0} employed for the vacancy migration in the FISE model. These results come from DFT calculations.

Concerning the interstitial migration model, the E_{a0} refers to the atom in the dumbbell that will move from one site to another. Table 2-2 shows the values used in this study.

X	Fe	Cu	Si	Mn	Ni	P
E_{a0} (X) (eV)	0.31	0.32	0.52	0.40	0.45	0.20

Table 2-2: E_{a0} from USPP DFT calculations which are employed for the interstitial migration in the FISE model [25] for Fe, Cu, Si, Mn and Ni. The value for P comes from PAW DFT calculations.

2.6.3 Simulated versus physical time

To avoid the generally unwanted presence of free surfaces at the boundaries of the simulated volume⁵, periodic boundary conditions (also called Born–von Karman boundary conditions) are commonly applied in atomistic simulations. Assuming a vacancy formation energy (E_f) of 1.6 eV in the α iron, the associated vacancy concentration is about 2 per 10^{13} atoms at 600 K. Nowadays, this enormous quantity of constituents is unreachable in the atomistic simulations (mainly because of memory limitations). Hence, even with only one vacancy in the simulation box, the system experiences a vacancy oversaturation. As a consequence, the simulated time provided by the mean-residence-time algorithm has to be re-scaled. A simple approach can be applied when the simulated system does not contain solute atoms. In this condition, the physical time can be rescaled using:

$$t_{real} = \frac{C_v^{kmc}}{C_v^{eq}} t_{kmc} \quad \text{Equation 2-59}$$

Where C_v^{kmc} is the vacancy concentration in the simulation box, C_v^{eq} is the equilibrium vacancy concentration ($C_v^{eq} = e^{-E_f/k_bT}$) and t_{kmc} is the time provided by the mean-residence-time algorithm [20].

In a binary system, as well as in a multinary system, the vacancy formation energy is usually unknown. In the case of the FeCu system, the vacancy formation energy is lower in Cu than in Fe. One possible method for rescaling the time is to introduce a factor related to the time spent in the matrix in the C_v^{kmc} expression [18]:

$$C_v^{kmc} = \frac{f_v^{kmc}(Fe)}{X_{Fe}^{vol} L^3} \quad \text{Equation 2-60}$$

Where $f_v^{kmc}(Fe)$ is the fraction of time that the vacancy spent in the matrix, X_{Fe}^{vol} is the iron volume fraction and L^3 is the volume of the simulation box.

For more complex alloys (ternary, quaternary and above), the rescaling of the time is made empirically from experimental results on one reference condition. However, this approach has not been used in this work.

⁵ Free surfaces are usually not desired at the edge of the simulation box because of the too important surface/volume ratio when comparing the simulated box size to a typical grain.

2.6.4 The irradiation model

AKMC neutron irradiation simulations are performed by introducing cascade debris obtained, for instance, by MD calculations. The cascades used in this work were computed by Stoller et al. using 20 keV and 100 keV PKA energy [28]. A probability is associated to the cascade introduction and is accounted for during the event selection. This probability is related to the cascade introduction frequency (which corresponds to a neutron flux provided by the user). The cascade introduction frequency is added to the sum of all jump frequencies. Hence, at every step, a probability to select the cascade introduction event exists. When a vacancy is placed on a lattice site, it is possible that it replaces a solute atom. If it is the case, the solute atom is placed in a reservoir. When a SIA is introduced in the simulation box, the atom on the lattice site remains unchanged and will be part of the dumbbell. A solute atom is placed as the second atom of the dumbbell if the reservoir is not empty. Otherwise, the second atom in the dumbbell will be an iron. This mechanism ensures the solute concentration to remain constant during the simulation⁶.

2.6.5 The grain boundary model

In order to simulate large sinks (such as grain boundaries), absorbing surfaces are employed in irradiation simulations using LAKIMOCA [20], [25]. These absorbing surfaces are placed along the z axis on both sides of the box. When a defect reaches the surface, it disappears. In the case of the SIA, the potential solute in the dumbbell is also placed in the reservoir. Concerning the recombination distance between a vacancy and a self-interstitial atom, it is set to a 2NN distance (2.85 Å) which corresponds to the α iron lattice parameter.

2.6.6 Analysis of the AKMC results

To compare the results obtained in the AKMC simulations with experimental data, one needs to define what a cluster is. In our simulations, we consider species which are within 1NN distant to belong to the same cluster. Furthermore, we introduce a cutoff as follows:

If a cluster has a size below the given cutoff, it is not counted in the evaluation of the property (e.g. density, mean composition, volume fraction). The idea behind this treatment is to somehow assess the resolution limits of the experimental techniques.

Note that this cutoff is different from the cutoff used to decide if a cluster of given size will be treated as an object in the hybrid AKMC (see section 3.3.1 of the third chapter). The later will be referred to as the object cutoff.

2.7 The Object Kinetic Monte Carlo method

Despite success in modeling material behavior, the AKMC method encounters another type of “infrequent event problem”. In this case, “infrequent” refers to rare state transitions in comparison with much more frequent transitions that may not make the system evolve much. These phenomena can be experienced in systems having a wide range of transition frequencies. This problem is called the “low barriers problem”.

⁶ Note for the reader: The "reservoir" term might be confusing. It has nothing to do with the grand canonical ensemble. This mechanism is just present to let the steel composition unchanged during the simulation. Alternatively, randomly choosing the nature of the second atom in the dumbbell depending on the input composition would also do the trick.

In comparison with the AKMC, the OKMC method introduces a higher level of abstraction for the elementary events leading to the microstructure evolution. In this model, the system is no longer seen as an assembly of atoms but as a collection of objects. Properties such as migration/emission are allocated to these objects with a frequency of occurrence. Objects are also characterized by type, size, shape, position and volume of interaction. Figure 2-9 illustrates the possible events. The benefit of this approach is quite easy to guess: the reachable time-scale is higher than the one from the atomic point of view. For example, the multiple elementary jumps making the whole point-defect cluster move are replaced by a global translation. However, the details concerning the cluster structure are lost. Furthermore, the explicit treatment of the solute in the OKMC method is difficult to implement.

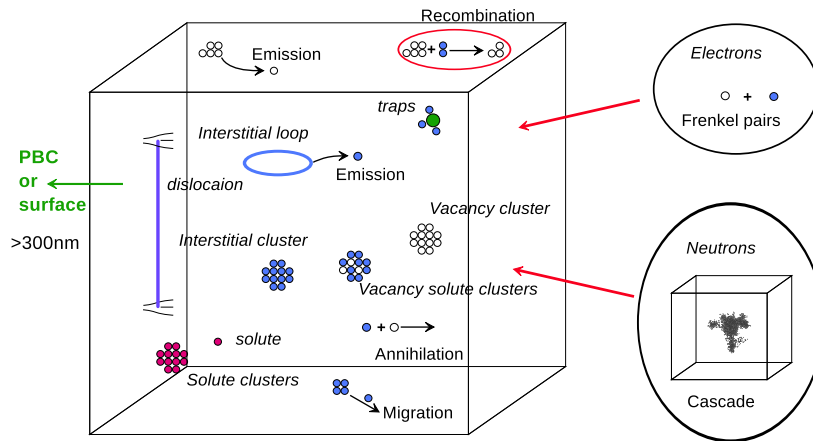


Figure 2-9: Schematic representation of the objects and events in an OKMC simulation [29].

Concerning the emission rates, a common approximation to extrapolate values for large sizes is to employ the well know capillary law. In this model, the point-defect cluster is associated to a spherical object. This assumption is required to establish a proportional relation between the formation energy of the defect and its surface. The binding energy between an atom/point-defect to an $(n-1)$ size object is given by:

$$E_b(n) = E_f(n-1) + E_f(1) - E_f(n) \quad \text{Equation 2-61}$$

In the capillarity model, this binding energy can be expressed as:

$$E_b(n) = E_f(1) + \frac{E_b(2) - E_f(1)}{2^{2/3} - 1} (n^{2/3} - (n-1)^{2/3}) \quad \text{Equation 2-62}$$

The energy required for the emission to happen is usually assumed to be the sum of the migration energy of the monomer in the pure matrix and the binding energy E_b presented above.

Concerning the mobilities of the objects, they are often computed by means of the AKMC method (for different sizes of PD cluster).

2.8 AKMC acceleration methods

For now, it remains difficult to perform simulations of irradiation similar to those in reactor conditions. This limitation comes from the length of simulations that can typically last three months to achieve doses of the order of 30 mdpa (whereas the target dose is 0.1 dpa). Also note that the ratio between flux simulated and real flux is of the order of 10^5 to 10^6 and that a decrease of the simulated flux result in an increase in the duration of simulations. Acceleration of LAKIMOCA code is necessary. For this, it is important to avoid hopping sequences that do not contribute to microstructure evolution (“useless” jumps) due to the trapping of the diffusive species when they are in clusters form or too strongly bound to solutes.

Literature is quite rich in methods to accelerate KMC simulations. Unfortunately, a specific system is usually associated with a suitable acceleration method. The different acceleration methods available are presented in the next paragraphs.

2.8.1 Temperature Accelerated Dynamics

Initially developed by Voter et al. [30] for molecular dynamics (MD), the idea of this method is based on an artificial increase of the temperature in order to increase frequencies of choosing infrequent events. The authors are interested in systems where the potential energy surface consists of basins separated by barriers that are high compared to the thermal energy $k_B T$. The system spends a long time vibrating in a state before escaping to another state by an infrequent thermal fluctuation. In order to make rare transitions observable by MD method, the authors proposed to use an artificial increase of the temperature. Hence, the essence of the Temperature accelerated Dynamics (TAD) method is to raise the temperature and correct for the temperature-induced bias by filtering out some of the transitions and allowing only those transitions that should occur at the original temperature. This procedure is allowed because the harmonic Transition State Theory provides an Arrhenius relation between the rate and the temperature. Hence, the escape-time t_{ref} at the reference temperature T_{ref} can be extrapolated at a higher temperature T_{TAD} by this simple relation:

$$\delta t_{ref} = \delta t_{TAD} e^{-Em(\frac{1}{k_B T_{ref}} - \frac{1}{k_B T_{TAD}})} \quad \text{Equation 2-63}$$

where t_{TAD} is the escape time at the T_{TAD} temperature.

Using this method, the speedup expected is up to 100.

2.8.2 Parallel Kinetic Monte Carlo

With the emergence of multicore systems, the use of multiple processors in order to accelerate calculations is possible. However, the parallelization of KMC simulations remains a non-trivial task and it is still under active development. Parallel KMC is usually done by dividing the simulation box into domains containing subdomains [31]-[34]. Each of these domains runs an independent KMC simulation. Communication between cores is imperative to ensure the passage of a diffusing species from one domain to another. In addition, the simulated time flows differently from one domain to another. This forces the domain whose time flows faster to "wait" for those whose time runs slower. This is why a NULL event is commonly used in these types of simulations thereby causing a decrease in performance. The following list is an example of a parallel KMC algorithm using subdomain decomposition to avoid boundary conflicts:

- At the beginning of a cycle, each processor's local time is initialized to zero.
- One of the subdomain is then randomly selected so that all processors operate on the same subdomain during that cycle.
- Each processor then simultaneously and independently carries out KMC events in the selected subdomain until the time of the next event exceeds the time interval T.
- Each processor then communicates the events occurring at the boundary with its neighboring processors, updates its event rates, and moves on to the next cycle using a new randomly chosen subdomain.

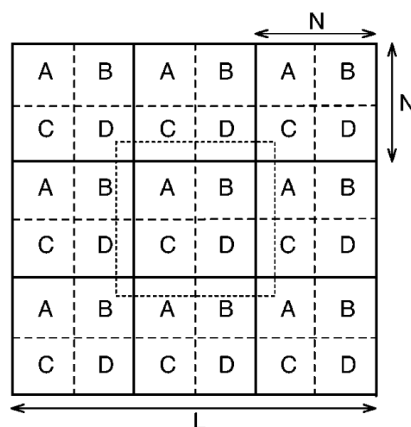


Figure 2-10: Decomposition of processor's domain into subdomain A, B, C, D (from [34]).

The main problem with this method is that diffusive species have to be homogeneously distributed in the simulation box to really observe an increase of the KMC performances. With our system where the point defect spatial distribution is not homogeneous, parallel KMC seems not to be a good optimization axis.

2.8.3 First passage KMC

The method relies on time dependent Green's functions to propagate the walkers over long distances in a single KMC step [35], [36]. The space is partitioned into non-overlapping "protective domains" (PDs), each containing one walker, and then using appropriate first-passage Green's functions to propagate walkers to the boundaries of their respective PDs, one walker at a time. Thus, numerous diffusive hops are replaced by large "super-hops" guaranteeing that the statistics of random walks remains unaltered.

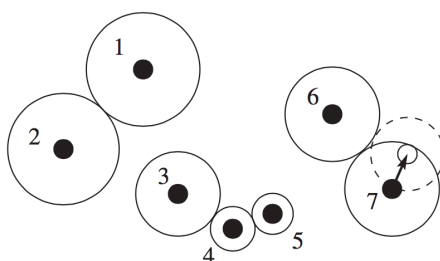


Figure 2-11: Illustration of the protection zone around each walker (from [35]).

This method has been notably used for irradiation simulation of pure iron. The authors reached a simulated dose of 3 dpa in one day of calculation on one CPU for low flux simulation ($\approx 10^{-9}$ dpa.s⁻¹). Unfortunately, the method's practical applicability is severely limited when the density of particles or walkers is high. In this condition, the protective zone becomes very small and the computational efficiency decreases in a radical way.

2.8.4 The energy basin finding algorithm

This algorithm determines if a diffusing species is trapped in a potential well (typically a diffusing species in a cluster) using the potential surface around the diffusing species. The potential well is called a basin and the authors proposed an algorithm to identify them. Once a basin has been identified, the escape time of the diffusing species is generally provided by a first passage method. This method has been used in a 2D binary

system (Si-As system) and a speedup of 10^3 as been obtained [37]. The acceleration of computing time for 3D and more complex systems is still questionable.

Athènes et al. have developed an analytical based model to exit basin, applied for the precipitation of Cu in FeCu with a speedup of about 2 orders of magnitude and 8 orders of magnitude respectively at 473 K and 273 K [38]. However, during the agglomeration regime, the speed-up tends to decrease. Using this model to simulate complex alloy under irradiation is currently a very complex task.

2.8.5 Hybrid AKMC/OKMC

The Hybrid AKMC/OKMC method consists of considering clusters whose dimensions are large as objects and assigned to these objects various properties. Castin et al. have employed this method to accelerate KMC simulations of α Fe-Cu systems [39]. In this study, Cu clusters above 15 atoms are considered as objects, for which migration and dissociation events are defined, based on specific, size-dependent, and thermally activated frequencies. Matching between the fully atomistic and the coarse-grained approach is achieved by using a neural network. The artificial neural network (ANN) has been used to predict the migration energy of a vacancy depending on its LAE in the FeCu system. The artificial neural network was trained on a database of vacancy migration energies provided by an interatomic potential using the NEB method. Using the prediction of the ANN, Castin performed kinetic simulations that provide a large number of stability and mobility parameters for V-Cu_N clusters.

Once a vacancy (v) has been absorbed by a Cu_N cluster object, the latter becomes a vCu_N object, and new events are defined in replacement of the vacancy migration in the regular AKMC algorithm:

- Dissociation of the cluster, with a frequency denoted as Γ_{diss} . Two dissociation mechanisms are possible: (i) emission of the vacancy from the cluster or (ii) emission of a vCu₁ pair, as in OKMC simulations.
- Migration of the cluster, with a frequency denoted as Γ_{mig} → Jumps of the central atom of the cluster (dragging the whole cluster) to any of the eight possible 1nn lattice sites (in bcc). After the migration is completed, Cu atoms within an absorption range are added to the cluster.
- Coalescence of clusters when, after a migration event is chosen, the absorption range of the vCu_N cluster overlaps with the absorption range of another Cu_N cluster.

This method is interesting and provides an acceleration of several orders of magnitude according to the author. Nevertheless, the studied system by Castin was binary and not subject to a supersaturation of point defects (i.e. not in irradiation conditions).

2.8.6 Coarse-grained KMC

Garnier et al. recently proposed to use a coarse-grained master equation built from the atomic version (Equation 2-43) [40]. In this formalism, the whole system is divided into a certain number of cells. An occupancy vector describes the state of the system. Each element of this vector corresponds to a cell. This means that the spatial information within the cell is lost. Hence, the master equation no longer involves transition rates between atomistic microstates; it involves the transitions between the occupancy vector. In order to describe the energetic of the system, an effective Hamiltonian at the coarse-grained scale is used. Using the Onsager matrix, the “jump frequencies” between one state to another are accessible. The method has been applied to the binary FeCu system. A direct comparison between AKMC and Coarse-grained KMC was performed and the results were in good agreement. The acceleration coefficient was of the order of 10^3 . However, the implicit local equilibrium hypothesis which is inherent to this method is a limiting factor to simulate microstructure evolution under irradiation.

2.9 Conclusion

Simulation techniques as well as the different models used or evoked in the manuscript were presented. Several acceleration techniques from the literature to speed-up the AKMC simulations were also exposed. It turns out that there is no universal way to speed-up AKMC simulation. For each system, depending on its dimensionality, complexity and homogeneity, corresponds an adapted acceleration method. For the RPV target material and irradiation conditions, the cohesive model should remain simple enough in order to have a limited number of parameters, and the method able to treat a large number of point defects and solutes in a system inhomogeneous in time (i.e. large range of jump frequencies) and in space (isolated defects and solutes and mixed point defect – solute clusters). Thus the possible methods to accelerate are limited, and an hybrid AKMC/OKMC method seems to be a good compromise. In the next chapter, the hybrid AKMC/OKMC method developed during this thesis will be exposed as well as the improvements of the model that were required regarding the prediction of the model at high doses.

2.10 Bibliography

- [1] G. Vineyard, “Frequency factors and isotope effects in solid state rate processes”, *Journal of Physics and Chemistry of Solids*, vol. 3, no. 1, pp. 121–127, 1957.
- [2] A. R. Allnatt and E. L. Allnatt, “Computer simulation of phenomenological coefficients for atom transport in a random alloy”, *Philosophical Magazine A*, vol. 49, no. 5, pp. 625–635, Sep. 2006.
- [3] L. Messina, PhD thesis, “Multiscale modeling of atomic transport phenomena in ferritic steels”, KTH University, 2015.
- [4] W. Kohn and L. J. Sham, “Self-Consistent Equations Including Exchange and Correlation Effects”, *Physical Review*, vol. 140, no. 4, pp. A1133–A1138, 1965.
- [5] G. Kresse and J. Hafner, “Ab initio molecular dynamics for liquid metals”, *Physical Review B*, vol. 47, no. 1, pp. 558–561, Jan. 1993.
- [6] G. Kresse and J. Furthmüller, “Self-interaction correction to density functional approximation for many electron systems”, *Physical Review B*, vol. 54, 1996.
- [7] J. Perdew, J. Chevary, S. Vosko, K. Jackson, M. Pederson, D. Singh, and C. Fiolhais, “Atoms, molecules, solids, and surfaces: Applications of the generalized gradient approximation for exchange and correlation”, *Physical Review B*, vol. 46, no. 11, pp. 6671–6687, Sep. 1992.
- [8] O. Senninger, PhD thesis, “Ségrégation et précipitation dans les alliages fer-chrome hors et sous irradiation”, Grenoble University, 2013.
- [9] G. Henkelman, B. P. Uberuaga, and H. Jónsson, “A climbing image nudged elastic band method for finding saddle points and minimum energy paths”, *Journal of Chemical Physics*, vol. 113, no. 2, pp. 9901–9904, Dec. 2000.
- [10] G. Henkelman and H. Jónsson, “Improved tangent estimate in the nudged elastic band method for finding minimum energy paths and saddle points”, *Journal of Chemical Physics*, vol. 113, no. 2, pp. 9978–9985, Dec. 2000.
- [11] G. Henkelman and H. Jónsson, “A dimer method for finding saddle points on high dimensional potential surfaces using only first derivatives”, *Journal of Chemical Physics*, vol. 111, no. 15, pp. 7010–7022, 1999.
- [12] N. Mousseau and G. T. Barkema, “Traveling through potential energy landscapes of disordered materials: The activation-relaxation technique”, *Physical Review E*, vol. 57, no. 2, pp. 2419–2424, Feb. 1998.
- [13] F. El-Mellouhi, N. Mousseau, and L. J. Lewis, “Kinetic activation-relaxation technique: An off-lattice self-learning kinetic Monte Carlo algorithm”, *Physical Review B*, vol. 78, no. 15, pp. 153202–4, Oct. 2008.
- [14] P. Brommer, L. K. Béland, J.-F. Joly, and N. Mousseau, “Understanding long-time vacancy aggregation in iron: a kinetic activation-relaxation technique study”, *Physical Review B*, vol. 90, no. 13, pp. 134109, 2014.
- [15] H. Xu, Y. N. Osetsky, and R. E. Stoller, “Self-evolving atomistic kinetic Monte Carlo: fundamentals and applications”, *Journal of Physics: Condensed Matter*, vol. 24, no. 37, pp. 375402, Aug. 2012.
- [16] T. Rehman, M. Jaipal, and A. Chatterjee, “A cluster expansion model for predicting activation

- barrier of atomic processes”, *Journal of Computational Physics*, vol. 243, pp. 244–259, Jun. 2013.
- [17] F. Soisson and G. Martin, “Monte Carlo simulations of the decomposition of metastable solid solutions: Transient and steady-state nucleation kinetics”, *Physical Review B*, vol. 62, no. 1, pp. 203–214, Jul. 2000.
- [18] Y. L. Bouar and F. Soisson, “Kinetic pathways from embedded-atom-method potentials: Influence of the activation barriers”, *Physical Review B*, vol. 65, no. 9, pp. 094103, Mar. 2002.
- [19] F. Soisson and C.-C. Fu, “Cu-precipitation kinetics in α -Fe from atomistic simulations: Vacancy-trapping effects and Cu-cluster mobility”, *Physical Review B*, vol. 76, no. 2, pp. 214102, Dec. 2007.
- [20] E. Vincent, PhD thesis, “Simulation numérique à l'échelle atomique de l'évolution microstructurale sous irradiation d'alliages ferritiques”, Lille University, 2006.
- [21] H. C. Kang and W. H. Weinberg, “Dynamic Monte Carlo with a proper energy barrier: Surface diffusion and two-dimensional domain ordering”, *Journal of Chemical Physics*, vol. 90, no. 5, pp. 2824–8, 1989.
- [22] N. Metropolis, A. W. Rosenbluth, M. N. Rosenbluth, A. H. Teller, and E. Teller, “Equation of State Calculations by Fast Computing Machines”, *Journal of Chemical Physics*, vol. 21, no. 6, pp. 1087–1092, Jun. 1953.
- [23] N. Metropolis and S. Ulam, “The monte carlo method”, *Journal of the American Statistical Association*, vol. 44, no. 247, pp. 335–341, 1949.
- [24] A. B. Bortz, M. H. Kalos, and J. L. Lebowitz, “A new algorithm for Monte Carlo simulation of Ising spin systems”, *Journal of Computational Physics*, vol. 17, no. 1, pp. 10–18, 1975.
- [25] R. Ngayam-Happy, PhD thesis, “Prévisions de l'évolution microstructurale sous irradiation d'alliages ferritiques par simulations numériques à l'échelle atomique”, Lille University, 2010.
- [26] T. Lazauskas, S. D. Kenny, and R. Smith, “Influence of the prefactor to defect motion in α -Iron during long time scale simulations”, *Journal of Physics: Condensed Matter*, vol. 26, no. 39, pp. 395007–395007, Sep. 2014.
- [27] L. Messina, M. Nastar, T. Garnier, C. Domain, and P. Olsson, “Exact ab initio transport coefficients in bcc Fe-X (X=Cr, Cu, Mn, Ni, P, Si) dilute alloys”, *Physical Review B*, vol. 90, no. 1, pp. 104203, Sep. 2014.
- [28] R. E. Stoller, “The effect of free surfaces on cascade damage production in iron”, *Journal of Nuclear Materials*, vol. 307, pp. 935–940, Dec. 2002.
- [29] C. Domain, C. S. Becquart, and L. Malerba, “Simulation of radiation damage in Fe alloys: an object kinetic Monte Carlo approach”, *Journal of Nuclear Materials*, vol. 335, no. 1, pp. 121–145, Oct. 2004.
- [30] M. R. Sørensen and A. F. Voter, “Temperature-accelerated dynamics for simulation of infrequent events”, *Journal of Chemical Physics*, vol. 112, no. 21, pp. 9599, 2000.
- [31] G. Arampatzis, M. A. Katsoulakis, P. Plecháč, M. Taufer, and L. Xu, “Hierarchical fractional-step approximations and parallel kinetic Monte Carlo algorithms”, *Journal of Computational Physics*, vol. 231, no. 2, pp. 7795–7814, Oct. 2012.
- [32] E. Martínez, J. Marian, M. H. Kalos, and J. M. Perlado, “Synchronous parallel kinetic Monte Carlo for continuum diffusion-reaction systems”, *Journal of Computational Physics*, vol. 227, no. 8, pp. 3804–3823, Apr. 2008.
- [33] E. Martínez, P. R. Monasterio, and J. Marian, “Billion-atom synchronous parallel kinetic Monte Carlo simulations of critical 3D Ising systems”, *Journal of Computational Physics*, vol. 230, no. 4, pp. 1359–1369, Feb. 2011.
- [34] Y. Shim and J. G. Amar, “Semirigorous synchronous sublattice algorithm for parallel kinetic Monte Carlo simulations of thin film growth”, *Physical Review B*, vol. 71, no. 12, pp. 125432–13, Mar. 2005.
- [35] T. Opplestrup, V. V. Bulatov, G. H. Gilmer, M. H. Kalos, and B. Sadigh, “First-Passage Monte Carlo Algorithm: Diffusion without All the Hops”, *Physical Review Letters*, vol. 97, no. 23, pp. 230602–4, Dec. 2006.
- [36] A. Donev, V. V. Bulatov, T. Opplestrup, G. H. Gilmer, B. Sadigh, and M. H. Kalos, “A First-Passage Kinetic Monte Carlo algorithm for complex diffusion–reaction systems”, *Journal of Computational Physics*, vol. 229, no. 9, pp. 3214–3236, May 2010.
- [37] B. Puchala, M. L. Falk, and K. Garikipati, “An energy basin finding algorithm for kinetic Monte Carlo acceleration”, *Journal of Chemical Physics*, vol. 132, no. 13, pp. 134104, Apr. 2010.
- [38] M. Athènes and V. V. Bulatov, “Path factorization approach to stochastic simulations.”, *Physical Review Letters*, vol. 113, no. 23, pp. 230601, Dec. 2014.

- [39] N. Castin, M. I. Pascuet, and L. Malerba, “Mobility and stability of large vacancy and vacancy-copper clusters in iron: An atomistic kinetic Monte Carlo study”, *Journal of Nuclear Materials*, vol. 429, no. 1, pp. 315–324, Oct. 2012.
- [40] T. Garnier and M. Nastar, “Coarse-grained kinetic Monte Carlo simulation of diffusion in alloys”, *Physical Review B*, vol. 88, no. 1, pp. 134207, Oct. 2013.

Chapter 3. Improvements of the AKMC model

3.1	Introduction	61
3.2	Algorithmic optimization of the code	62
3.2.1	Generalities.....	62
3.2.2	Jump frequency calculation.....	63
3.2.3	Jump selection algorithm.....	65
3.2.4	Back-jump algorithm.....	67
3.2.5	Other optimizations.....	67
3.2.6	LAKIMOCA restructuration.....	68
3.3	The hybrid AKMC/OKMC method	68
3.3.1	The model in pure iron.....	68
3.3.1.1	Point defect cluster's diffusion.....	70
3.3.1.2	Point defect cluster's emission.....	70
3.3.2	Parameterization of the hybrid method for the pure iron system.....	71
3.3.2.1	AKMC study of point defect cluster properties.....	71
3.3.2.2	Validation of the parameterization.....	74
3.3.3	Pure iron under irradiation.....	74
3.3.4	Model with solute treatment.....	76
3.3.5	Parameterization.....	77
3.3.5.1	The FeCu system.....	77
3.3.5.2	Properties of the vacancy-Mn/Ni clusters.....	80
3.3.5.3	Properties of the vacancy-Si clusters.....	80
3.3.5.4	Outcomes of the hybrid AKMC/OKMC method with solutes.....	82
3.3.6	The hybrid method in the RPV system.....	82
3.4	Features for grain microstructure modeling	89
3.4.1	The grain boundary model.....	89
3.4.1.1	Probabilistic absorbing surfaces.....	89
3.4.1.2	The absorber model.....	90
3.4.1.3	Comparing absorbing surfaces and the absorber model.....	90
3.4.2	Traps in the AKMC.....	94
3.4.2.1	The model.....	94
3.4.2.2	Parameterization.....	95
3.4.2.3	Results.....	97
3.5	Conclusion	98
3.6	Bibliography	100

3.1 Introduction

This chapter concerns all improvements of the AKMC model that have been introduced. These improvements can be purely algorithmic or modification of the model. Firstly, algorithmic optimizations of the AKMC code are presented. Secondly, the hybrid AKMC/OKMC method is exposed. Thirdly, new features that have been developed to improve the AKMC model are discussed.

3.2 Algorithmic optimization of the code

3.2.1 Generalities

Optimizing the routines consuming the most computation time was the first step of the AKMC acceleration. Before providing details about the optimization performed, let us remind the LAKIMOCA implementation of the algorithm used to perform the KMC simulation. Figure 3-1 shows all steps of an AKMC sequence.

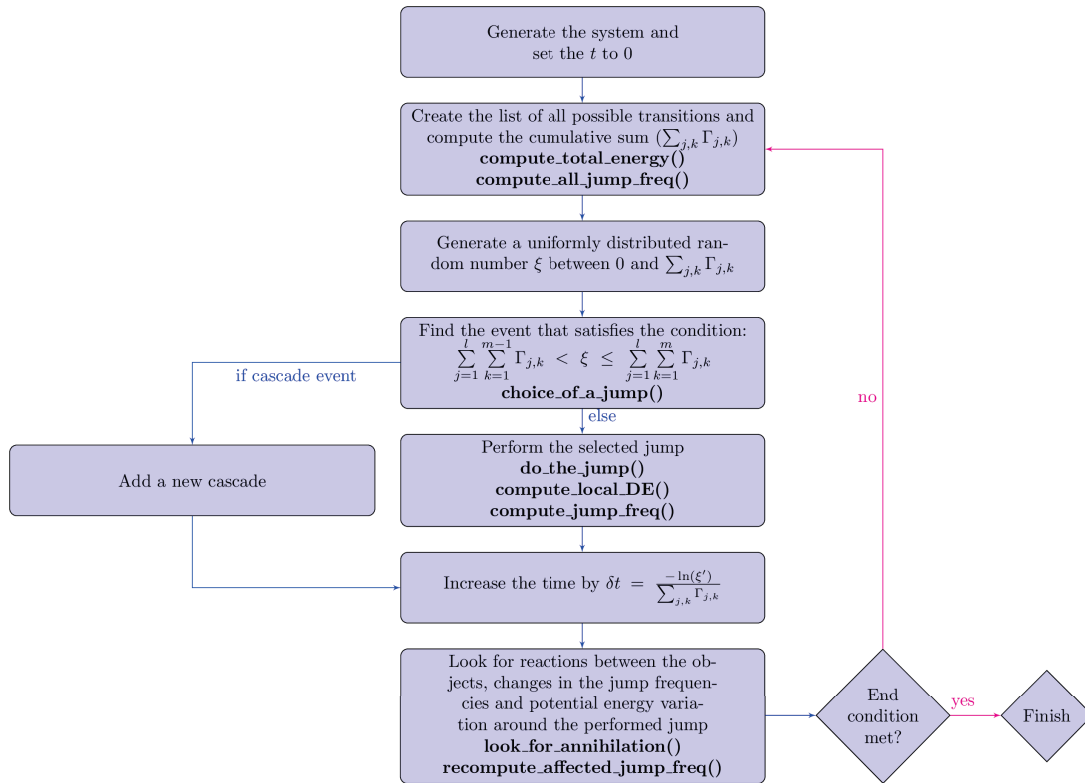


Figure 3-1: LAKIMOCA flowchart of the different steps required to perform an AKMC simulation. Text in bold represents the associated functions.

According to Figure 3-1, several functions are required:

- `compute_total_energy()`: Compute the total energy of the initial system (depending on the cohesive model used).
- `compute_all_jump_freq()`: Compute the jump frequencies of all point defects present in the simulation box.
- `choice_of_a_jump()`: Find the selected jump according to the ζ random number.
- `do_the_jump()`: Perform the selected jump.
- `compute_local_DE()`: Update the site's energy around the performed jump.
- `compute_jump_freq()`: Compute the new jump frequency after the jump (one version for the vacancies and one version for the interstitial).
- `look_for_annihilation()`: Check around the point defect that has jumped if it is likely to recombine with another point defect.
- `recompute_affected_jump_freq()`: Look around the point defect that jumped if it has affected other point defect jump frequencies. If so, recompute these jump frequencies using `compute_jump_freq()`.

The last six routines presented above need to be well optimized since they are called each AKMC step. Hence, the first part of this work has been to find the most penalizing routines. In order to find them, profiling of simulations under irradiation conditions was performed. These profilings are presented in Annex I.

3.2.2 Jump frequency calculation

The first function identified as the most penalizing routine is the one responsible for the computation of the vacancy migration frequency (the vacancy version of `compute_jump_freq()`). This function was found to consume more than half the computation time.

A first attempt to speed-up the calculation of the vacancy jump frequencies was performed by parallelizing the different calls to this function. Instead of computing the eight frequencies in a sequential way, we have tried to distribute these calculations on several processors. This parallelization has been done using the OpenMP library, which is an open source library for shared memory parallel programming. This parallelization method provides automatic parallelization based on directive commands introduced in the program. The commands basically just mention which part of the code has to be parallelized and which are the parallel variables and arrays. The initial algorithm should be simple enough to allow the compiler to build an efficient parallel executable [1]. We have used the `#pragma` directive to send the succession of calls to the `compute_jump_freq()` function on several cores. Unfortunately, it doesn't make the computation faster. The parallelization efficiency has been obtained for one vacancy diffusing in pure Fe. The overall runtime is ~10 times slower on two processors than serial calculation and ~50 times slower on 4 processors. This reduction in performance is due to communications between processors. Hence, the serial algorithm had to be accelerated.

The reason of this large slowing down of the overall execution comes from the fact that the number of pair interaction calculations was not reduced to the minimum, we have thus changed the function. Figure 3-2 shows a visual support for a better understanding on how the old and new functions work.

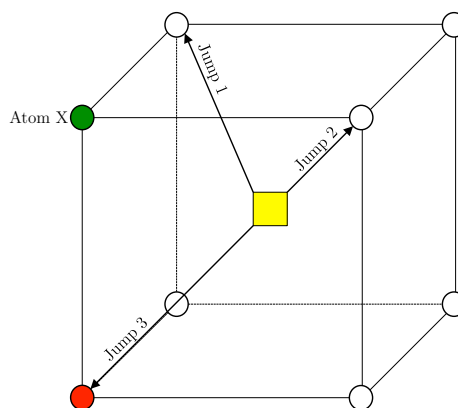


Figure 3-2: Illustration of different jumps for a vacancy in BCC iron.

For the three jumps represented in Figure 3-2, the vacancy will respectively lose and gain, inter alia, one 1NN pair interaction Vac-X and one 2NN pair interaction Vac-X. In order to get the corresponding pair interaction, it is necessary to access to the nature of the atom X that is stored in a 3D array representing the crystal. However, the access to elements in a large array is a time consuming task. Using the old method, each jump frequency is computed separately. Thus, in the present example, it was necessary to access the X atom nature 3 times (one for each jump illustrated in Figure 3-2).

Using the new method, the local atomic environment is analyzed just one time. This means that all atoms involved in the jump process are stored in local variables. The result of this local environment analysis is used for the eight jump frequency calculations. Hence, all jump frequencies are computed in one function call and the number of calls to the large array representing the crystal is reduced to its minimum. Figure 3-3 illustrates the difference between the old and the new method in a schematic way.

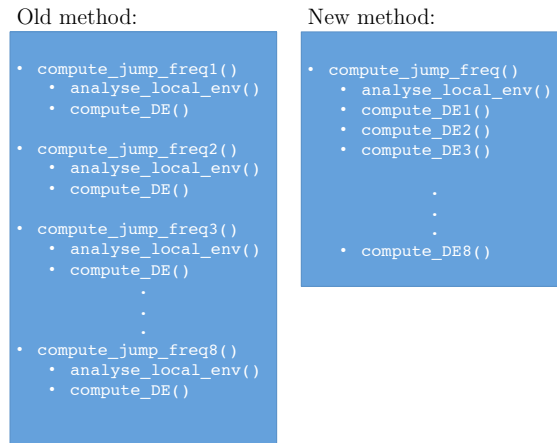


Figure 3-3: Algorithmic differences between the old method in charge of the vacancy jump frequency calculations and the new one. Using the old method, the local analysis around the jump is called several times. It is performed only once using the new method.

Exploiting the symmetries of the crystal also allowed us to reduce the number of operations (several jumps share the same loss or the gain of pair interactions). The new function developed limits the number of pair interactions calculation to its minimum. The results obtained are rigorously the same as the ones obtained with the old method. The acceleration obtained for the overall execution of the code with the employment of this new function has been tested for different systems (Table 3-1) using the “Pair2NN-Vincent” parameterization in a $60 \times 60 \times 60$ simulation box:

- System A: one cluster containing 10 point-defects in Fe-0.18Cu at.% at 600 K
- System B: 1 point-defect in pure iron at 600 K
- System C: 20 point-defects placed randomly in a RPV type model alloy

	System A	System B	System C
Acceleration (for 5.10^7 steps)	6.5	3.6	2.9

Table 3-1: Acceleration obtained for the overall execution of LAKIMOCA employing the algorithmic optimization for the jump frequency calculation of vacancies.

The most favorable case appears to be the vacancy cluster case. This can be explained by the fact that one jump of a vacancy in a vacancy cluster can affect the jump frequencies of the other vacancies close to it. Hence, the mean number of vacancy jump frequency calculations per KMC step is higher in this case than in the others. Profilings for System C are provided in Annex I. These profilings indicate that the part of the code responsible for the jump frequency calculations has been accelerated by a factor of 11.

The method used in order to accelerate vacancy jump frequency calculations has also been applied to the treatment of the interstitials and the results presented in Table 3-2.

	System A	System B	System C
Acceleration (for 1.10^8 steps)	1.6	1.2	1.4

Table 3-2: Acceleration obtained for the overall execution of LAKIMOCA employing the algorithmic optimization for the jump frequency calculation of the interstitials.

The acceleration is always lower than it is for the vacancy treatment since the old subroutine for the treatment of the interstitials had already been optimized at the beginning of this work.

While the acceleration obtained is rather modest compared to the targeted one, these optimizations represent a non-negligible improvement especially for the calculation of point-defect cluster properties (such as diffusion and emission).

Other algorithmic optimizations have been developed in a model AKMC code. Sections 3.2.3, 3.2.4 and 3.2.5 present these optimizations.

3.2.3 Jump selection algorithm

The first algorithm concerns the selection of the event. This part of the AKMC algorithm is done by the `choice_of_a_jump()` routine. This process is performed every KMC step and is done by a linear search in LAKIMOCA. When the number of events becomes too large, the algorithm becomes inefficient. Employing a binary tree (BT) data structure limits this effect [2]. The algorithm is rather easy to implement and the average run-time complexity¹ for searching in this data type structure is $\Theta(\log n)$ versus $\Theta(n)$ for the linear search where n is the total number of events. Figure 3-4 illustrates this data structure.

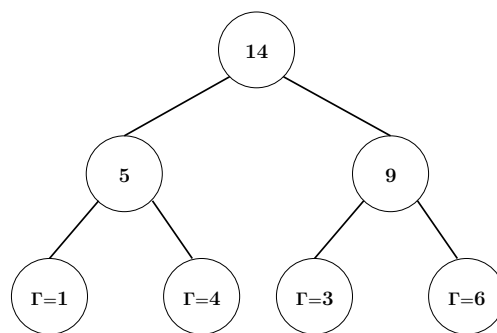


Figure 3-4: Illustration of the binary tree in the context of the KMC event selection. Nodes at the bottom of the tree represent the values of the occurring frequencies of the events. These nodes are connected to top-level nodes that contain the sum of the two jump frequencies. The top of the tree corresponds to the sum of all the event frequencies available in the system.

¹ Average run-time complexity: average amount of time for an algorithm to perform a task depending of the size of the problem.

Using this data structure, searching the event selected by the ξ random number generated between 0 and the sum of the frequencies is performed as follows:

1. Starting from the top of the tree, ξ is compared to the two nodes below.
2. If ξ is lower (or equal) than (to) the left node content, the algorithm will take the left path. Otherwise, the value associated to the left node is subtracted from ξ and the algorithm will take the right path.
3. Repeat the second operation until reaching the roots of the tree.

A schematic example for a given ξ is shown in Figure 3-5:

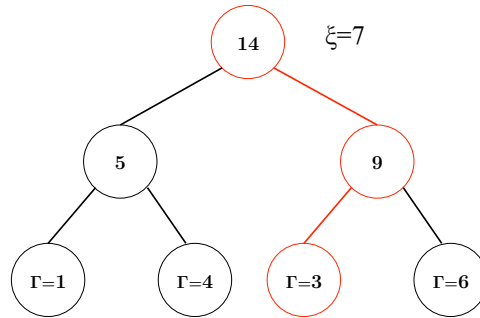


Figure 3-5: Path (in red) taken by the algorithm from the top of the tree to its root with $\xi=7$. At the beginning, ξ is higher than 5 so ξ takes the value 2 ($7-5$) and the right node is chosen. After the previous step, ξ is lower than 3 leading to the choice of the left path. Thus, the selected event is the third one (from left to right).

Since every change in the jump frequencies has to be propagated from bottom to top every KMC steps, the binary tree search can be less efficient than the linear search when the number of defects is too low. Figure 3-6 presents the acceleration obtained on the overall execution of the code as a function of the number of vacancies in the system.

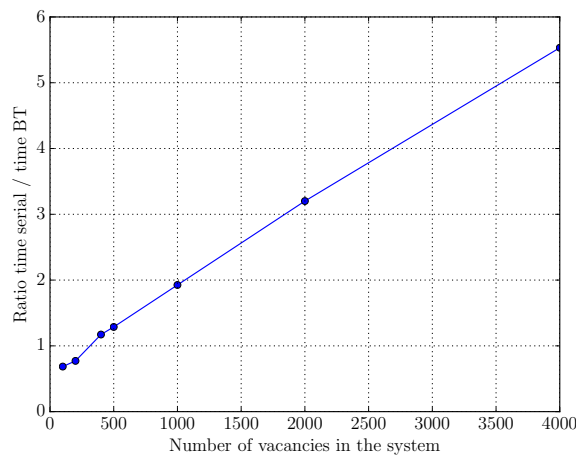


Figure 3-6: Total acceleration for 10^8 akmc steps provided by the binary-tree (BT) as a function of the number of vacancies in the system. The system was Fe-0.18Cu-0.69Ni-1.38Mn-0.47Si-0.01P with PBC at 600 K.

It appears that the binary tree search algorithm becomes advantageous above ~ 400 vacancies (or more generally ~ 400 PD). The switch between the two algorithms for the selection of an event is performed on-the-fly during the simulation, depending on the number of defects present in the system. This takes advantage of both algorithms. Note that it could also be interesting to use the binary tree in the OKMC version of LAKIMOCA as the number of defects can be high.

3.2.4 Back-jump algorithm

During a simulation, it can happen that a point defect oscillates between two positions near a point-defect cluster. In this situation, a certain number of point-defect jump frequencies are affected by the jump. The system can spend a large number of AKMC steps in this two states alternation by performing a long sequence of back-jumps. While this phenomenon can be physical, it leads to several calls to the function computing the jump frequencies. Hence, optimizations have been introduced to reduce the computation time. Figure 3-7 illustrates the back-jump process.

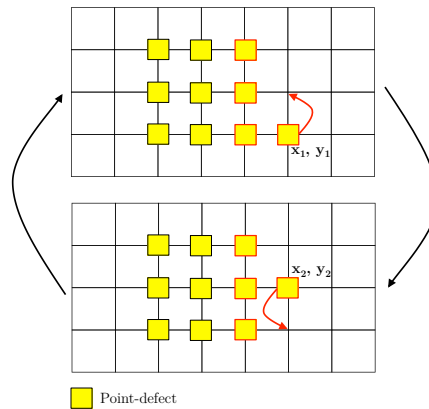


Figure 3-7: Two states alternation for a point defect at the interface of a point defect cluster. Assuming a 2NN interaction model and using the FISE barrier model, jump frequencies associated to the point defects colored in red have to be updated after every jump.

A simple approach to solve this problem is to store the affected jump frequencies before the jump. At a given AKMC step N , a point defect performs the $(x_1, y_1) \rightarrow (x_2, y_2)$ jump. When a new jump occurs at step $(N+1)$, if the point defect that jumps is the same as the one at step N and its direction corresponds to $(x_2, y_2) \rightarrow (x_1, y_1)$, the previously stored jump frequencies are applied to the associated point defects. This process is repeated until the back-jump sequence is broken.

This method makes these oscillations less penalizing. For the simulation of a neutron irradiation of a typical RPV model alloy (using the “Pair2NN-Vincent” parameterization), the number of jump frequency calculations saved is about 7 times the number of AKMC steps.

3.2.5 Other optimizations

The other algorithmic optimizations made in the model code are listed below:

- Implementation of the Linked-Cells. This improves the distance analysis (for example to know if a jump modified other jump frequencies around). This implementation is used in `look_for_annihilation()` and `recompute_affected_jump_freq()`.
- All the jump frequencies (corresponding to activation energies ranging from -3 eV to 3 eV with a step of 10^{-3} eV) are computed at the beginning of the simulation and stored in an array. This avoids using (every AKMC step) the exponential function, which is quite heavy in terms of computation time. This saves 7% of the overall execution time in a typical simulation of a RPV model alloy under irradiation.

All these improvements allow a reduction of the runtime by a factor of 7 (in terms of number of AKMC steps performed per day) in a typical simulation of a RPV model alloy under neutron irradiation.

3.2.6 LAKIMOCA restructuration

An important restructuration of the LAKIMOCA code has also been done based on the AKMC model code. The modifications are given below:

- Functions have been put in different files according to their purpose (the main source file was drastically cleaned).
- Header files (*.h) have been created for every source file (*.c). This greatly reduces the source of bugs. The compilation procedure is also safer using this method.
- Structures for vacancies and interstitials have been implemented. This makes the manipulation of these objects safer than before (especially for the annihilation case). An example for the vacancy case is given in the following code block:

```
/**
 * Properties related to the vacancy object */
struct _Vacancy
{
    /** id of the vacancy (from 1 to nv) */
    int id;
    /** Position of the vac */
    int x, y, z;
    /** State of the vac (0:akmc; 1:okmc) */
    short int state;
    /** jump frequencies of the vac */
    double jump_freq[8];
    /** Total jump frequency of the vac */
    double total_jump_freq;
    /** Sub-lattice associated to the vacancy */
    int sub_lattice;
    /** id of the object the vacancy belongs to */
    int object_id;
};
```

According to our tests, the code runs well for the BCC systems and MMC, AKMC, irradiation, isochronal annealing simulations. This new form of the LAKIMOCA code will make future development faster and safer.

3.3 The hybrid AKMC/OKMC method

3.3.1 The model in pure iron

Despite all the improvements presented in the first part of this chapter, we found the acceleration of LAKIMOCA not to be sufficient. We thus have decided to develop an hybrid model between the AKMC and the OKMC. This choice was motivated by the fact that a large proportion of the AKMC steps are performed on large and quasi-immobile point defect clusters. Let us remember that the LAKIMOCA software consists of two codes: an “atomic” code and an “object” one. The hybrid model had to be implemented in the atomic version of LAKIMOCA since the “atomic” version of the code is completely distinct from the “object” one. A schematic description of the method is presented in Figure 3-8.

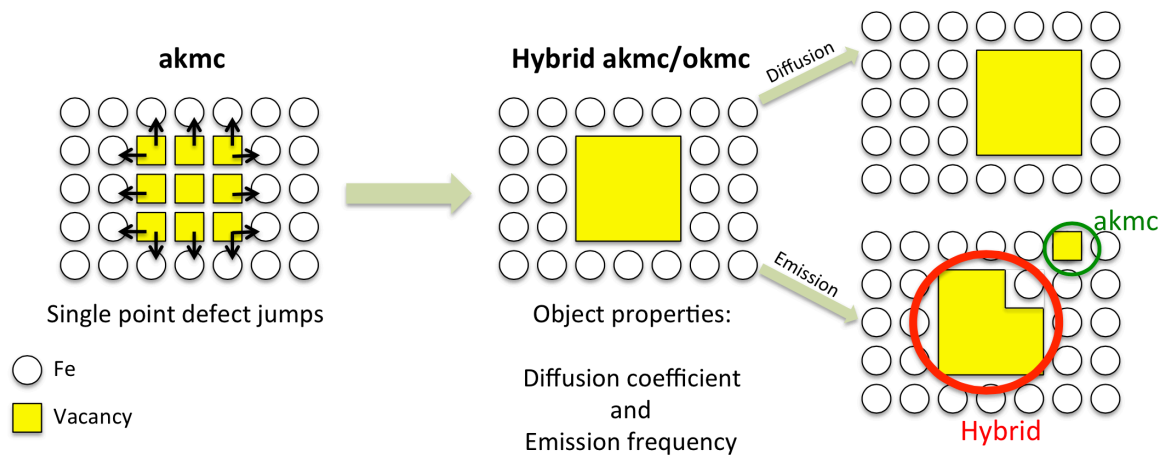


Figure 3-8: Illustration of the hybrid AKMC/OKMC method

The assumption behind this approach is that large point defect cluster motion does not impact much the microstructure evolution and more precisely the formation of solute-rich clusters. Hence, losing details concerning the description of this type of object might not drastically change the stochastic trajectory of the simulation. However, a rigorous description of small and mobile objects needs to be kept.

The following section provides information about it.

In the case of pure iron, when a group of 1NN point defects has a size (in number of point defects) higher than the object cutoff, all these point defects are considered as one object. The individual jump frequencies of the point defects associated to an object are null. Frequencies for migration and emission are associated with each object. The migration is performed through the whole cluster translation of a 1NN distance. For the emission, the point defect is sent in a random direction near the object. When the size of an object changes, the object returns to the AKMC state. This AKMC relaxation is required because it allows the objects to return to an energetically more favorable configuration rather than being stuck in an atypical geometry. Figure 3-9 presents vacancy cluster geometries obtained if the AKMC relaxation is not allowed.

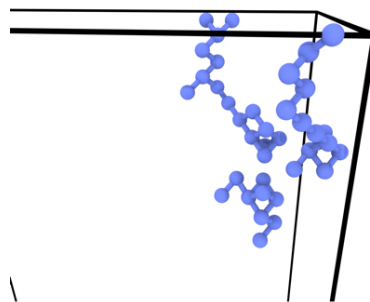


Figure 3-9: Vacancy cluster geometries observed when there is no AKMC relaxation of the objects allowed. Usually our AKMC model predicts spherical type vacancy clusters.

Every n AKMC steps, all the objects are rebuilt (see Annex IV to get the command related to this function).

3.3.1.1 Point defect cluster's diffusion

Diffusion consists of a $\frac{a\sqrt{3}}{2}$ jump of all the PD constituting the cluster in a randomly chosen (111) direction (between the eight possible directions). A simple 1D example of the method is given Figure 3-10:

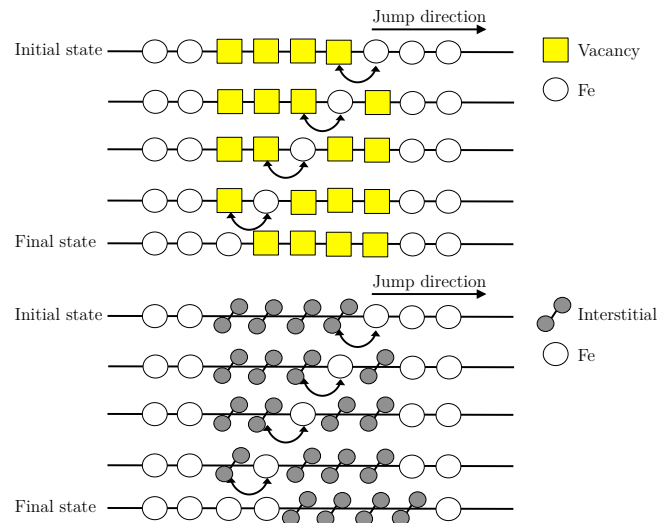


Figure 3-10: Diffusion method employed for performing a 1NN global translation of a vacancy or interstitial object.

The first step of the algorithm is to find all the elements constituting the clusters that have a 1NN iron in the randomly selected direction of the jump. Then, the method illustrated in Figure 3-10 is employed until the iron that has been introduced in the PD cluster meet another iron. It is important to note that the dumbbell orientation does not change during the jump. Once translation has happened, a local cluster analysis is performed on the cluster to take into account possible size changes.

3.3.1.2 Point defect cluster's emission

The subroutine in charge of cluster's emission chooses a PD at the interface and sends it in a random direction near the cluster. The algorithm searches iteratively a site occupied by an iron up to a 2NN distance. When this site is found, the iron atom at the spot where the PD is placed moves to the initial position of the PD (see Figure 3-11).

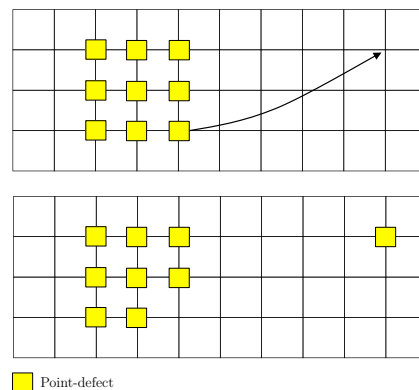


Figure 3-11: Schematic illustration of an emission from a PD cluster.

This choice of a local emission has been made in order to keep the possibility for the emitted PD to return into the cluster.

3.3.2 Parameterization of the hybrid method for the pure iron system

3.3.2.1 AKMC study of point defect cluster properties

The hybrid method has been first tested for the simulation of the pure iron system. Since the OKMC part of the hybrid method requires the mobility as well as the stability data of the objects, AKMC simulations have been performed to determine them. Multiple runs are required to extract a meaningful average value. To achieve this, starting from the same cluster configuration, 500 simulations per object size and per temperature have been launched in a $30 \times 30 \times 30 a_0$ simulation box with periodic boundary conditions. The temperature has been set up to 600, 700 and 800 K. The subroutine in charge of the emission detection was called every 20-100 AKMC steps (depending on the size of the object). This has allowed us to obtain the emission frequency as well as the diffusion coefficient by using the well-known Einstein relation:

$$D = \frac{\langle R^2 \rangle}{6t} \quad \text{Equation 3-1}$$

Where $\langle R^2 \rangle$ is the mean squared displacement and t is the time.

These calculations have been performed using two different AKMC parameterizations. The first one is the “Pair2NN-Vincent” parameterization. It corresponds to the parameterization developed during the PhD work of Vincent [3]. The second is called “Pair2NN-PAW”. In this parameterization, the pair interactions are adjusted to describe the 1NN and 2NN binding energies of the di-vacancy cluster predicted by PAW DFT [4].

Figure 3-12 presents the results obtained in the case of vacancy clusters.

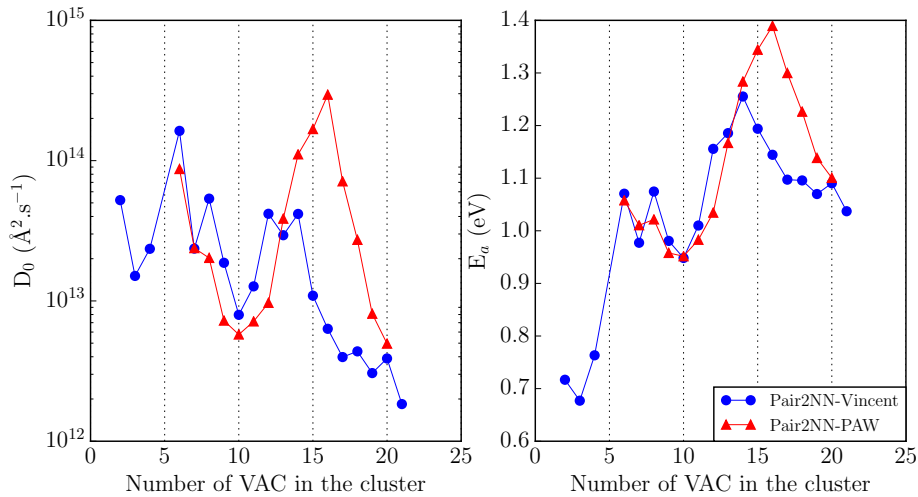


Figure 3-12: Evolution of the diffusion prefactor as well as the associated activation energy as a function of the number of vacancies in the cluster.

The results suggest that important geometry effects affect the cluster mobility. According to the different conformations accessible to the cluster, its mobility can be greatly affected by adding (or removing) just one vacancy. Both parameterizations provide the same tendencies up to size 14. Above this size, differences are observed (higher D_0 and E_a for the “Pair2NN-PAW” parameterization). The same behavior is observed for the emission frequencies (see Figure 3-13):

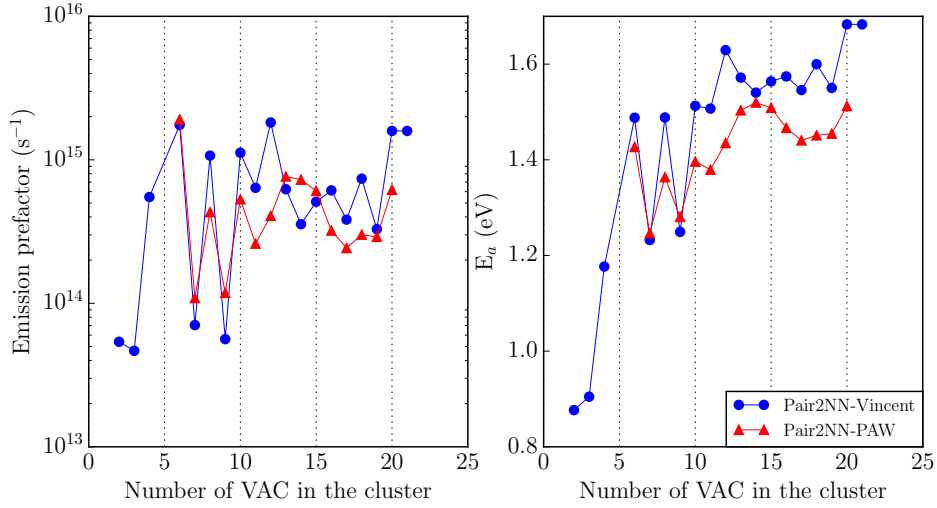


Figure 3-13: Evolution of the emission attempt frequency as well as the associated activation energy as a function of the number of vacancies in the cluster.

One interesting way to probe the dynamics of vacancy clusters is to plot the ratio between the migration frequency and the emission frequency. Figure 3-14 presents this ratio at 573 K for our calculations and compares with data found in the literature.

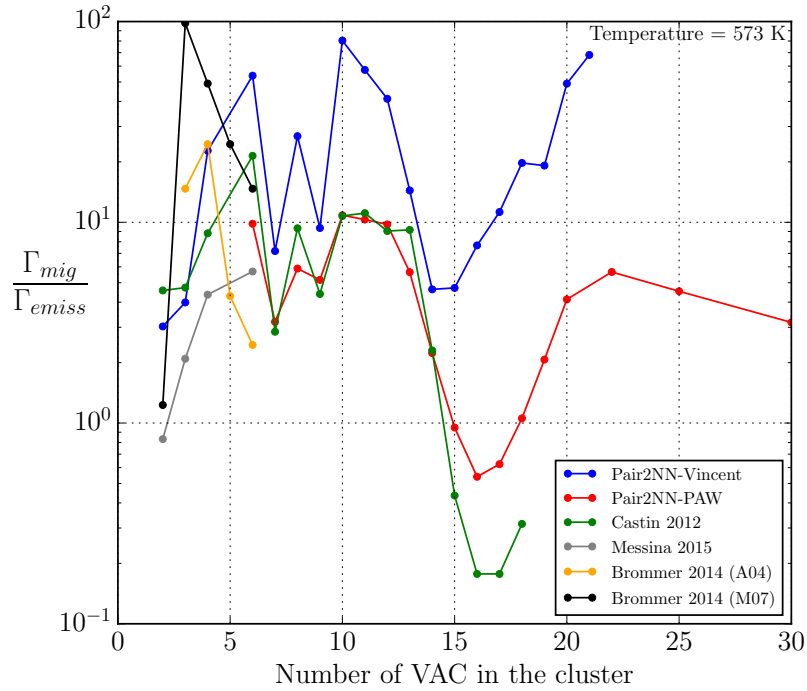


Figure 3-14: Evolution of the ratio between the migration frequency and the emission frequency as a function of the number of vacancies in the cluster at 573 K. Results extracted from the literature come from Castin [5] (the calculations were performed using an interatomic potential), Messina [6] (the calculations were performed using pair interactions) and Brommer [7] (using two different interatomic potentials with the k-ART method).

Our results suggest that a vacancy cluster performs between 10 and 100 1NN distance jumps before emission happens when using the “Pair2NN-Vincent” parameterization. For midsize vacancy clusters, the results are in good agreement with the ones obtained by Castin with an interatomic potential [5]. It is especially the case for the “Pair2NN-PAW” parameterization. The model predicts the same geometry effects (adding or

removing one vacancy can have a large impact on the object properties). Concerning the small vacancy cluster behavior, our model is known for wrongly reproduce their motions. Indeed the barrier estimation in our model does not describe very well the low barriers that can be encountered in such clusters (for example the V_3 is known to diffuse faster than the mono-vacancy [7], [8], and our model fails to reproduce this behavior). Note that differences exist between the EAM empirical potentials A04 and M07 tested by Brommer on small vacancy clusters. Differences are also observed for the largest vacancy clusters studied. The pair interaction model predicts objects that still migrate before emission happens while the interatomic potential predicts a regime where the emission is dominant.

Using the same AKMC approach, SIA clusters have also been studied. The conditions used were the same as in the case of vacancies. For an equivalent size, the SIA clusters were found to be less mobile than the vacancy clusters (to our knowledge, there is no experimental result that can validate/invalidate this observation). Moreover, no emission was observed at the temperature of interest (600 K). For clusters containing more than 15 SIAs and after three days of calculations, it was not possible to determine a diffusion coefficient since the objects were immobile. Figure 3-15 presents the results for the SIA cluster mobility.

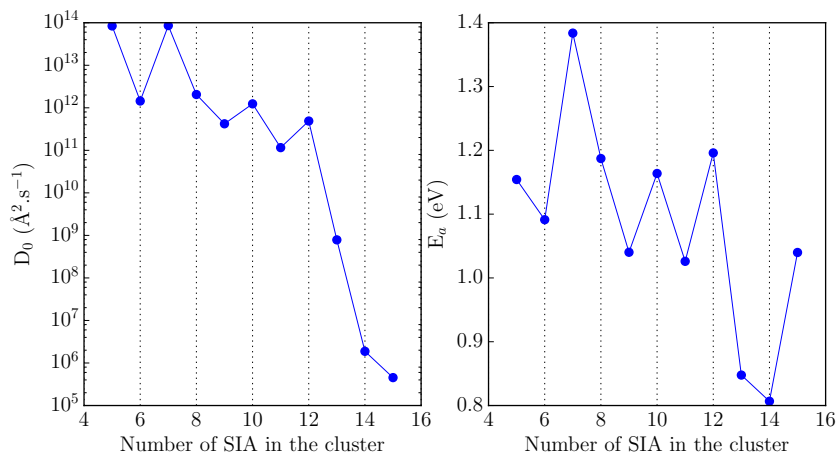


Figure 3-15: Evolution of the diffusion prefactor as well as the associated activation energy as a function of the number of SIA in the cluster.

In order to illustrate the competition between vacancy and interstitial cluster migration, Figure 3-16 presents the ratio between the vacancy cluster migration frequency and the SIA cluster migration frequency.

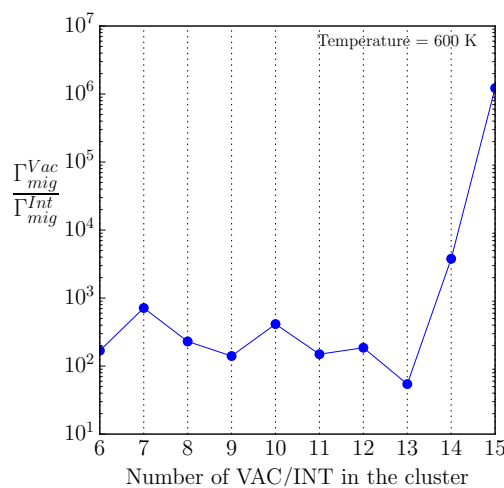


Figure 3-16: Ratio between the vacancy cluster migration frequency and the SIA cluster migration frequency at 600 K.

For a given size, the model predicts vacancy clusters that are much more mobile than SIA clusters. Above size 13, SIA clusters appear to be almost immobile from the vacancy cluster perspective.

3.3.2.2 Validation of the parameterization

In order to validate our hybrid AKMC/OKMC model and parameterization, isochronal annealing simulations have been performed. Isochronal annealing experiments consist in a low temperature electron irradiation followed by a heating of the sample according to a specific temperature ramp. Hence, thermally activated processes are unlocked one after the other. In our simulations, the irradiation is performed by introducing the appropriate number of point defects, then, the temperature in the simulation box is increased every Δt seconds. The population of defects is tracked during the whole simulation. Results can be compared to the experimental isochronal annealing experiments (see chapter 1 section 1.2.1). Previous results have shown a good agreement between the AKMC model and the experimental results [9]. In our work, the isochronal annealing simulations have been performed in a $120 \times 120 \times 120 a_0$ box irradiated at 0.2 mdpa (i.e. by the introduction of 750 Frenkel pairs) at 70 K. Periodic boundary conditions have been applied in all directions and the increment of the temperature has been set to 3 K every 300 s. The object cutoff has been set to 6 for both vacancy and interstitial clusters. Figure 3-17 shows the results obtained using the standard AKMC method and the hybrid method. Each plot represents the mean over three runs.

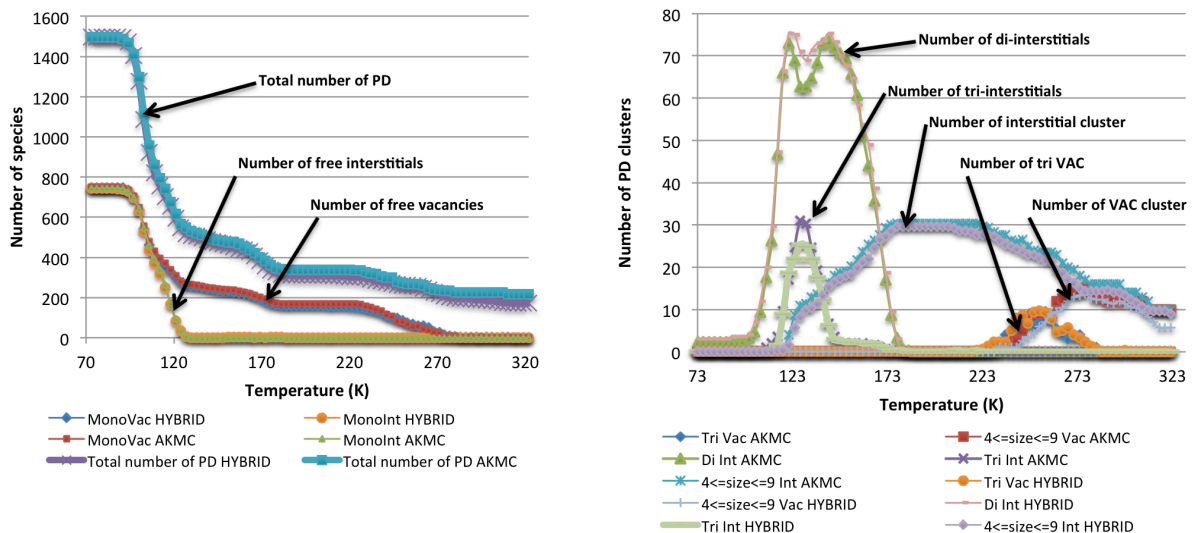


Figure 3-17: Evolution of the population of defects as a function of temperature for the AKMC and the Hybrid method.

The agreement between the two methods is good. Using the hybrid method, the evolution of the vacancy/interstitial population agrees with the standard AKMC results. Even when looking at more complex defect populations (such as V_2 , V_3 , interstitial clusters etc.), the agreement remains good. The acceleration factor is high (>200) since the calculations lasted ~ 48 hours with the standard AKMC method versus 10 min for the hybrid method. These results confirm the validity of the approach as well as its potential for long-term irradiation simulations.

3.3.3 Pure iron under irradiation

In the case of irradiation, the hybrid method also allows reaching high irradiation doses in much lower flux conditions for pure Fe. Simulations have been performed in a $60 \times 60 \times 120 a_0$ and $60 \times 60 \times 240 a_0$ boxes with absorbing surfaces along the z axis. The temperature has been set to 573 K and various flux have been employed (from $5 \cdot 10^{-5}$ to $5 \cdot 10^{-7}$ dpa/s with 20-100 keV displacement cascades). The object cutoff has been set

to 6 for both vacancy and interstitial clusters. The SIA cluster density and mean sizes obtained are represented in Figure 3-18.

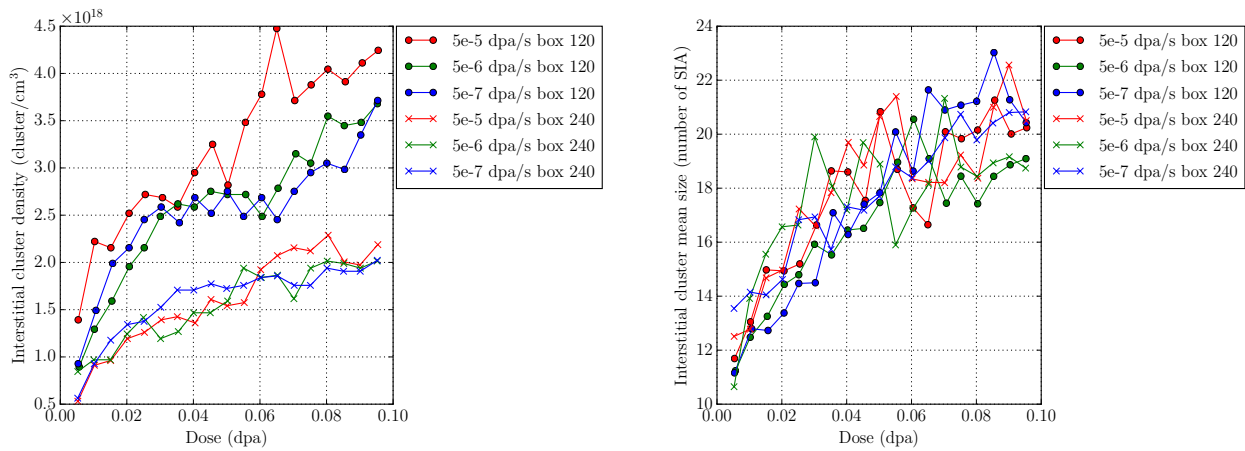


Figure 3-18: Evolution of the SIA cluster density and mean size as a function of the dose. Each plot is the mean of three simulations.

The first observation one can make is that no vacancy clusters remain in the simulation box before the introduction of a new displacement cascade. Because vacancy clusters are quite mobile, according to our model, they quickly annihilate on the absorbing surfaces. This is a problem because experimental results show that vacancy clusters are present in pure iron under irradiation. Since simulations performed in pure iron with absorbing surfaces seem to overestimate surface effects, the same simulations were launched in the same conditions but using periodic boundary conditions in all directions. With this method, all point defects recombine before the introduction of a new cascade. This is not in agreement with the point-defect accumulation observed experimentally. These results indicate that a better treatment for the absorbing surfaces needs to be developed (or that vacancy clusters are too mobile).

Another problem highlighted by these simulations is that for the SIA clusters, there is no obvious effect of the flux/size of the box on the evolution of the microstructure (except for the smallest box with the highest flux). Doubling the simulation box volume simply divides the SIA cluster density by two. It appears thus that our model will not be able to describe flux effects (except in the case of very high fluxes). In fact, as presented above, vacancies are likely to be quickly suppressed from the simulation boxes. In this state, only quasi-immobile SIA clusters are present in the system. During this phase, the simulation spends more or less time (depending on the flux) before a new cascade is introduced. As a consequence, a reduction of the flux has no effect on the final microstructure (which is an unexpected issue of the model).

Among all the SIA clusters in our different simulation boxes, only one (in one of the largest boxes) would be observable in a TEM. This single cluster corresponds to a density of 10^{16} m^{-3} whereas the experimental loop density in pure iron at 0.1 dpa is of the order of 10^{15} m^{-3} [10].

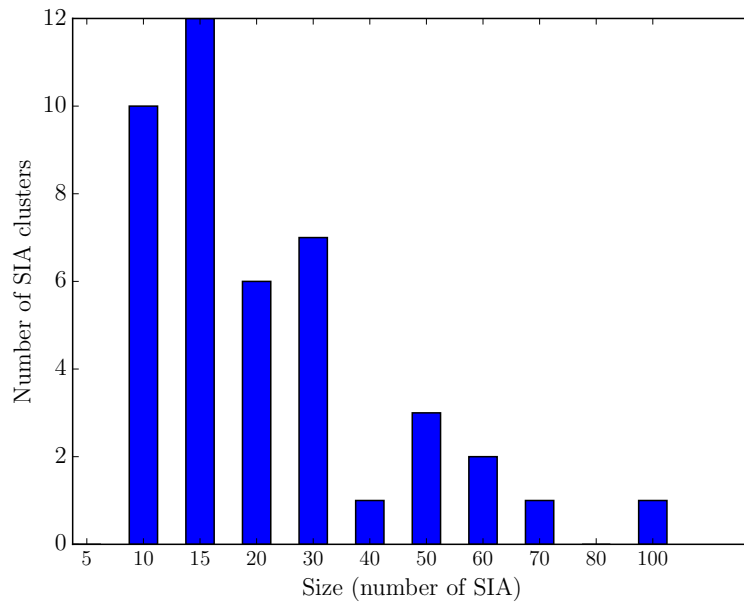


Figure 3-19: Size distribution of the SIA clusters in the largest simulation box at 573 K with the lowest flux at 0.1 dpa. One cluster corresponds to a density of $5 \times 10^{22} \text{ m}^{-3}$.

3.3.4 Model with solute treatment

The presence of solutes in the objects has also been implemented in the hybrid method. The general concept remains the same as it is in the case of pure iron except that the point defect clusters can transport solutes and another event associated with these new types of objects has been added. Indeed, the objects can “emit” a solute (this is necessary in order to mimic a solute transported that can dissociate from the cluster while the cluster diffuses). Figure 3-20 presents the hybrid method applied in the case of the FeCu alloy.

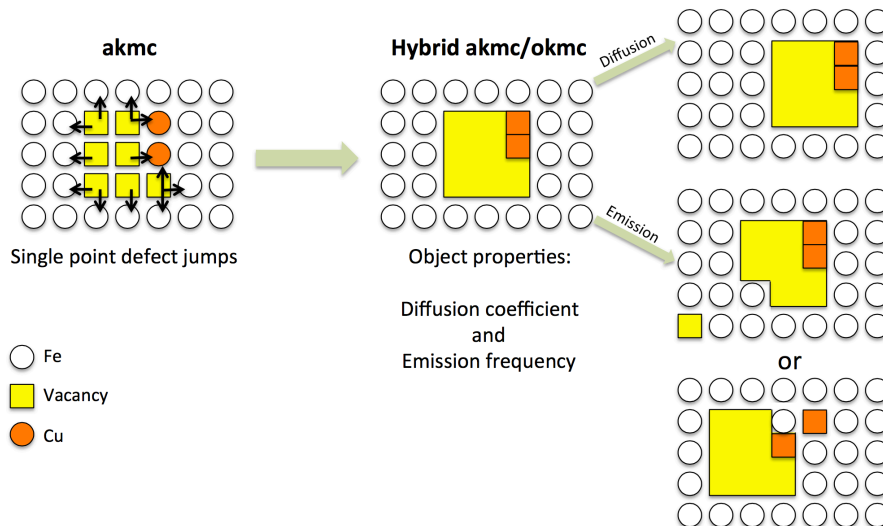


Figure 3-20: Illustration of the hybrid method in the presence of solutes.

The diffusion model in presence of solutes is presented in Figure 3-21. Basically, the method behaves the same way as the one presented for pure iron (section 3.3.1.1). However, the first step of the algorithm is to find a solute (or a point defect) constituting the cluster that has a 1NN iron atom in the direction of the jump.

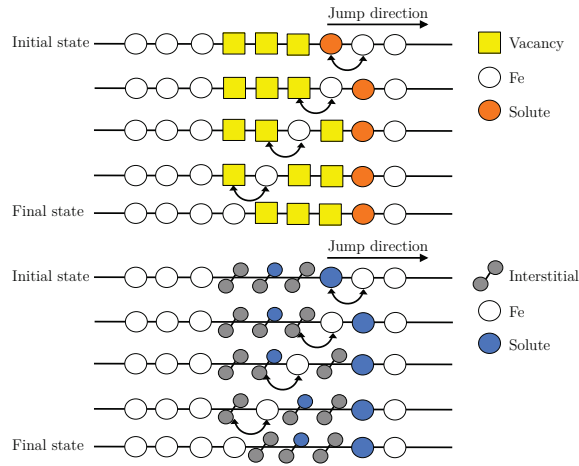


Figure 3-21: Diffusion method employed to perform a 1NN global translation of a vacancy or interstitial object in the presence of solutes.

The hybrid method with the solute treatment has first been tested on the FeCu system. The next section presents the results.

3.3.5 Parameterization

3.3.5.1 The FeCu system

The parameterization of the hybrid method in the FeCu system has been adjusted on AKMC calculations of V-Cu type cluster motions. At the beginning of the simulation, one vacancy cluster decorated with a variable number of Cu is introduced in the simulation box. The cluster introduced is built in a deterministic way (e.g. for a given cluster composition, the initial geometry of the cluster is always the same). Every 20 AKMC steps, a cluster analysis is performed. If a vacancy or a Cu atom is more than 2NN distant from the cluster, it is considered that emission has happened and the simulation stops. The AKMC simulations have been performed at 600, 700, and 800 K (500 simulations per case) in a $30 \times 30 \times 30 a_0$ simulation box with periodic boundary conditions. The results are presented in Figure 3-22.

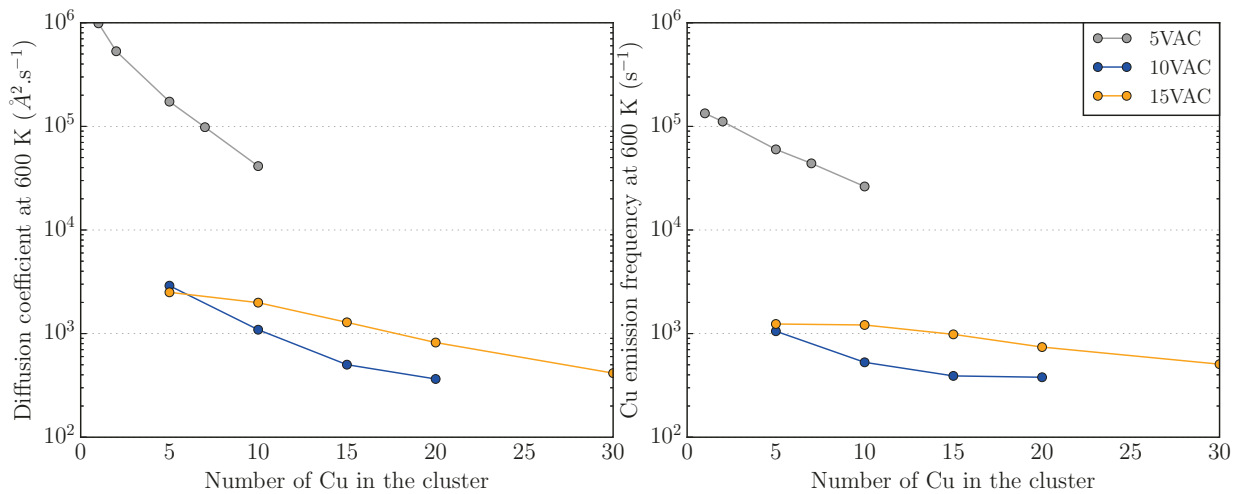


Figure 3-22 : (left) Diffusion coefficient at 600 K for different vacancy clusters as a function of the number of Cu in the cluster. (right) Evolution of the copper emission frequency at 600 K for different vacancy clusters as a function of the number of Cu in the cluster at 600 K.

The main mechanism leading to a size change of the Vac-Cu cluster is a loss of Cu. Vacancy emissions are less frequent (~5% of the first emission at 600 K) and no emission of a Vac-Cu complex has been observed. For a given number of vacancies in the cluster, the copper emission frequency and the mobility decrease when the number of Cu atoms in the cluster increases.

According to the results presented in Figure 3-23, the diffusion coefficient at 600 K of a Vac-Cu clusters by can be fitted using:

$$D(N_{vac}, N_{Cu}) = 7.10^6 e^{-0.556N_{vac}} e^{-(0.71e^{-0.154N_{vac}})N_{Cu}} \text{ (\AA}^2/\text{s)}$$

In the same manner, the copper emission frequency at 600 K can be fitted by:

$$\Gamma_{Emiss_{Cu}}(N_{vac}, N_{Cu}) = 10^8 N_{vac}^{-4.33} e^{(0.0144N_{vac}-0.2617)N_{Cu}} \text{ (s}^{-1}\text{)}$$

The model predicts a decrease of the mobility/emission frequency when adding Cu atoms in the cluster (for a given number of vacancies). Adding vacancies (for a given number of Cu in the cluster) produces the same effect.

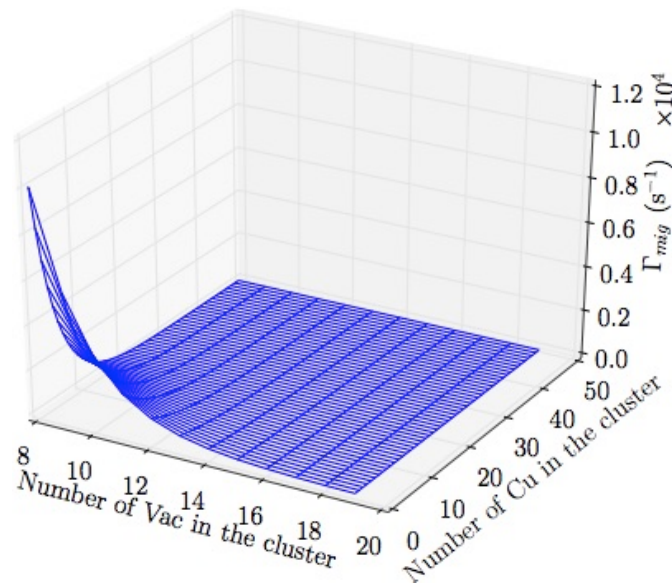


Figure 3-23: Evolution of the whole cluster jump frequency at 600 K as a function of the N_{vac} and N_{Cu} in the cluster (according to the previous fit).

Using the previous Vac-Cu object parameterization, neutron irradiation has been simulated in a Fe-0.8Cu (at.%) system at 600 K. The size box has been set to $60 \times 60 \times 120 a_0$ with absorbing surfaces along the z axis. The flux employed was $\sim 10^{-5} \text{ dpa.s}^{-1}$. The 20-100 keV cascades used come from Stoller et al. simulations [11]. The hybrid AKMC/OKMC introduces a bias in comparison with standard AKMC results (as illustrated by the difference in the mean cluster size evolution between standard AKMC and Hybrid AKMC/OKMC simulations in Figure 3-24). The cluster density evolution with the dose is in good agreement for the two methods. However, the mean size of the Cu clusters is lower in the case of the hybrid method. In order to determine the mechanisms leading to this difference, several simulations have been performed using the hybrid method with different object cutoffs for the object treatment of the vacancies (i.e. the object cutoff value presented in section IV under the keyword `vac/int_obj_size_cutoff`).

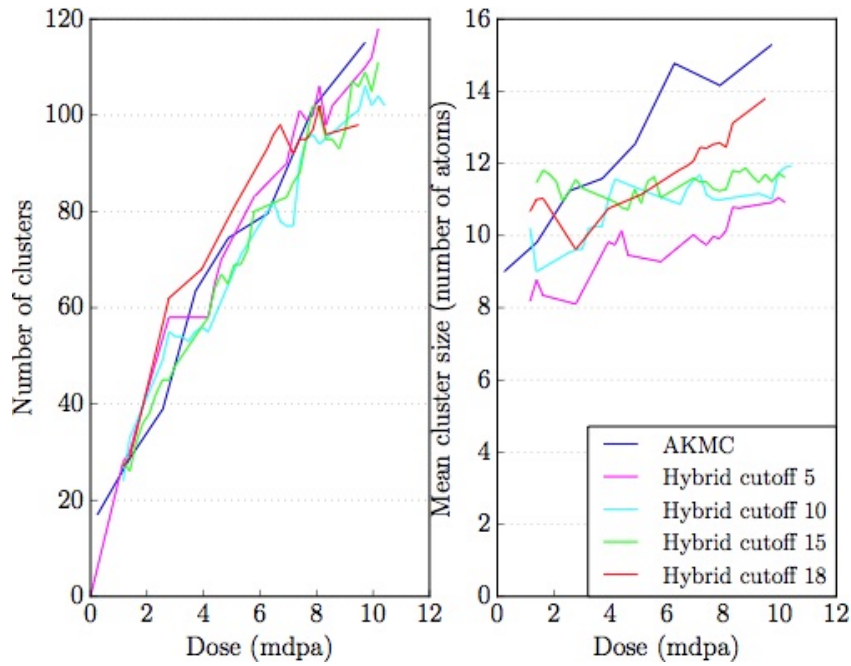


Figure 3-24: Evolution of the number of Cu clusters (left) and of the mean cluster size (right) as a function of the dose for different object cutoff values (presented in 3.3.1).

It seems that increasing the cutoff value leads to mean cluster sizes closer to those observed in AKMC at the expense of longer simulation time. However, even for a cutoff value equal to 18, differences remain. This indicates that the bias is probably introduced by a bad description of large vacancy cluster properties or when the number of copper in the Vac-Cu cluster is too high. Hence, with this parameterization approach, we will have to remain with the standard AKMC treatment for vacancy. This treatment will remain valid for the rest of this chapter.

Since an accurate treatment of the Vac-Cu objects appears too complex, other optimization methods have been tried to accelerate the simulations. As in the case of pure iron, the vacancy population disappears before the introduction of a new cascade. In this state, the system spends a lot of computation time dealing with quasi-immobile SIA clusters. We proposed an optimization that consists in introducing a cascade as soon as all vacancies have been annihilated. This approximation is termed the NO-VAC approximation. Another and stronger approximation has been made for the treatment of SIA clusters. For a SIA_n -solute_p cluster, we have chosen to consider it as immobile for $p \geq 2$ and $n \geq 6$. This choice is motivated by the fact that SIA_n -solute_p clusters are even less mobile than in the case of pure iron (making their studies quite difficult using the AKMC method). It is especially the case when Cu is present. This approximation is called OBJ-INT and it includes the NO-VAC approximation.

Using NO-VAC as well as the OBJ-INT approximations, the simulations are quite accelerated, and the target dose is reached using the OBJ-INT approximation. Figure 3-25 presents the simulated evolution of the microstructure for a Fe-0.8Cu (at.%) system irradiated with neutrons at 600 K. The size box has been set to $60 \times 60 \times 120 a_0$ with absorbing surfaces on z. The flux employed was $\sim 10^{-5} \text{ dpa.s}^{-1}$. For the low dose regime (the only regime accessible with AKMC), there is not much difference between the NO-VAC/OBJ-INT and the standard AKMC run. The acceleration is in the order of 100.

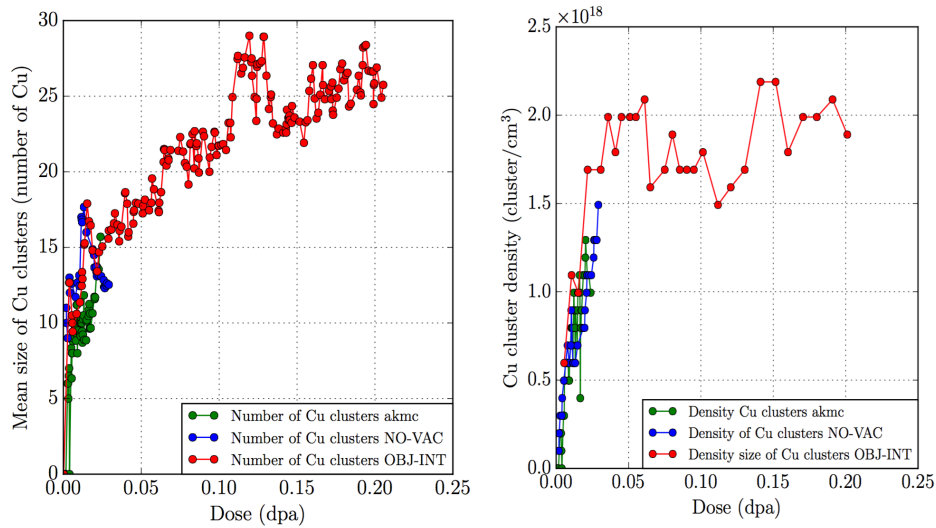


Figure 3-25: Evolution of the mean size Cu clusters (left) and Cu cluster density (right) as function of the dose. The cluster size criterion was set to 5 species.

The results suggest that the OBJ-INT approximation does not introduce a bias in the trajectory of the simulation (at least at the low dose regime observable by the AKMC and NO-VAC simulations).

3.3.5.2 Properties of the vacancy-Mn/Ni clusters

The effect of Mn and Ni on the mobility of the vacancy clusters appears difficult to determine. In fact (in the case of the “Pair2NN-Vincent” parameterization), the Vac-Mn and Vac-Ni binding energies are low and they are even repulsive in the case of Mn-Mn and Ni-Ni. In these conditions, the vacancies quickly move away from the solutes (see Figure 3-26) making the determination of a diffusion coefficient for these clusters meaningless.

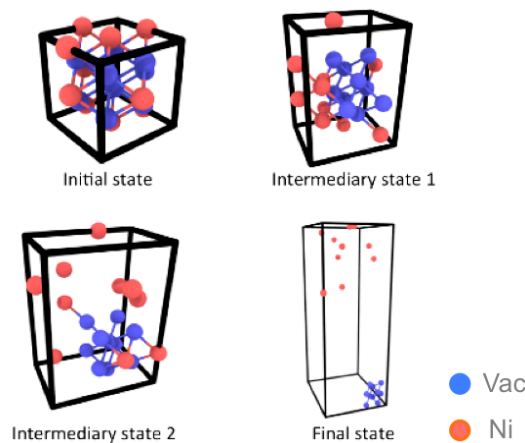


Figure 3-26: Illustration of the behavior of a vacancy cluster in presence of Ni (the same phenomenon is observed in the case of Mn).

3.3.5.3 Properties of the vacancy-Si clusters

Because vacancies with Si and Si bind strongly, the effect of Si content on a vacancy cluster has been investigated. The AKMC simulations have been performed at 600, 700, and 800 K (500 simulations per case) in a $30 \times 30 \times 30 a_0$ simulation box with periodic boundary conditions. Figure 3-27 presents the results concerning the mobility of these objects.

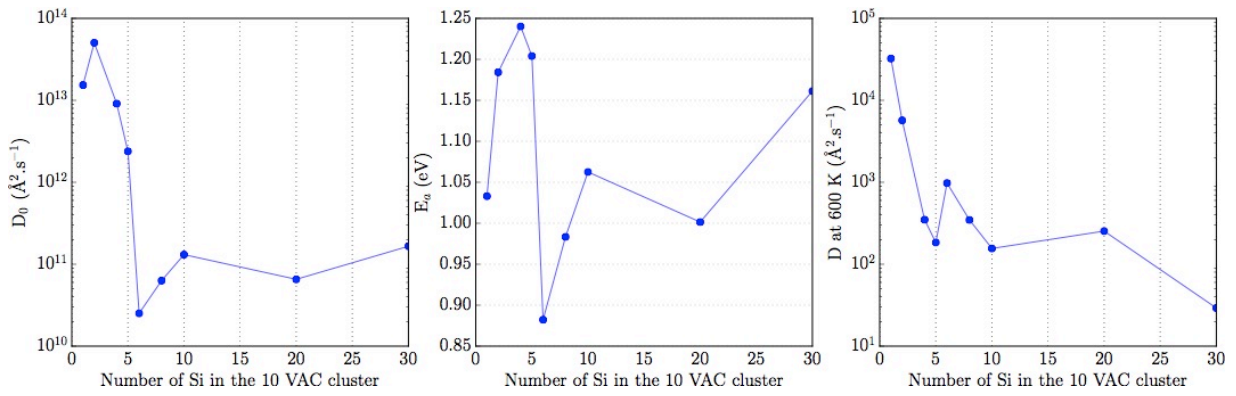


Figure 3-27: Diffusion prefactor, activation energy and diffusion coefficient as a function of the number of Si in the 10 VAC cluster.

Similar to the Vac-Cu case, the mobility of a vacancy object is reduced when the number of Si constituting the cluster increases. The emission case is more complex because of the absence of a single predominant emission mechanism when increasing the solute content. Figure 3-28 shows the evolution of the proportion of “Si emission” as a function of the vacancy cluster composition.

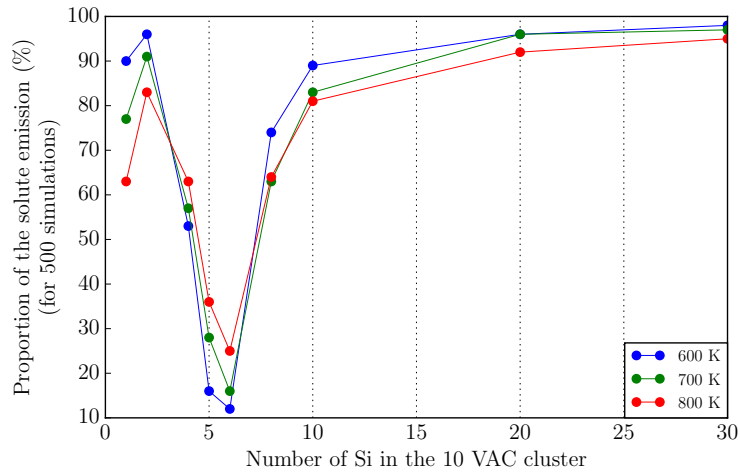


Figure 3-28: Proportion of Si emission as a function of the number of Si in the 10 VAC cluster.

According to these AKMC calculations, the predominant emission mechanism changes as a function of the vacancy cluster Si content. This effect was not observed when investigating the Vac-Cu object properties. These emission properties are presented in Figure 3-29. This effect might be caused by the constant cluster geometry at the beginning of the simulation.

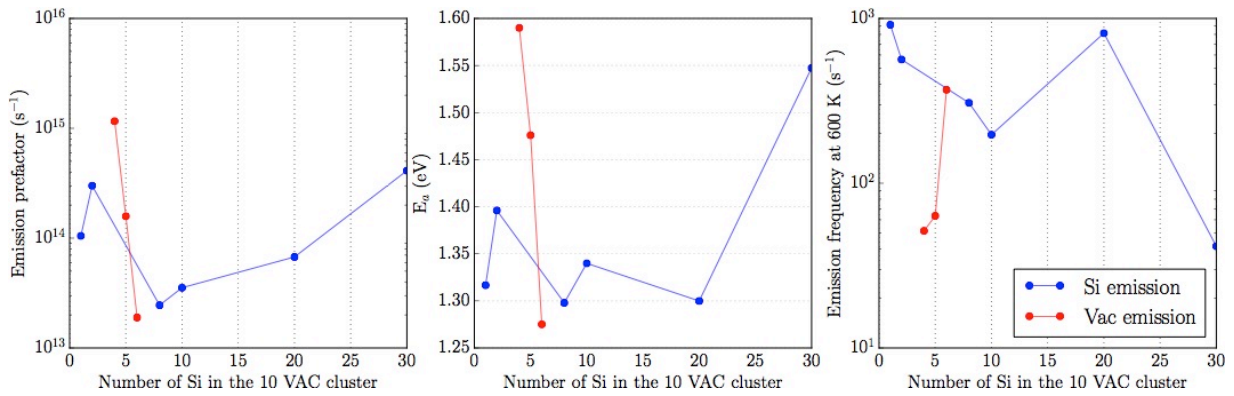


Figure 3-29: Emission prefactor, activation energy and emission frequency as a function of the number of Si in the 10 VAC cluster.

3.3.5.4 Outcomes of the hybrid AKMC/OKMC method with solutes

Different simulations have been performed in order to study the properties of vacancy objects in presence of solutes (Cu, Mn, Ni and Si). Building simple laws to predict the properties of a vacancy object as a function of its solute content turns out to be challenging. Even in the FeCu binary system, the hybrid method introduces a large bias in the simulation trajectory. Moreover, the variety of behaviors (from dissociation in the Mn/Ni case to the varying dominant emission mechanism in the Si case) makes the study of multinary vacancy clusters even more difficult. Note as well that this type of calculations is very resource demanding and that the combinatorics is an important limiting factor for the study of chemically complex objects. However, considering the SIA clusters as immobile above a certain size (the OBJ-INT approximation) has successfully accelerated the simulation for the FeCu system under irradiation making the target dose reachable. Hence this approximation will be used on more complex systems and no assumption on the vacancy object properties will be made.

3.3.6 The hybrid method in the RPV system

Considering SIA_n-solute_p clusters immobile for $p \geq 2$ and $n \geq 6$ cluster (OBJ-INT approximation), makes high doses reachable for the simulation of RPV model alloys. The two following sections presents the results for a high and a low RPV model alloy. In the analysis of the data, only clusters containing n species or more are taken into account. n is referred to as the cluster criterion in the manuscript.

High copper RPV model alloy:

First, the Fe-0.18Cu-1.38Mn-0.69Ni-0.47Si-0.01P at.% material simulated in the thesis of Ngayam Happy [9] is discussed. The simulation has been performed in a $60 \times 60 \times 120 a_0$ box with absorbing surfaces along the z axis. The temperature has been set to 600 K and the flux employed was $\sim 10^{-5}$ dpa/s using 20-100 keV cascades.

A comparison has been made between the standard AKMC run and the hybrid method with the OBJ-INT hypothesis. Figure 3-30 presents the two microstructures obtained at 21 mdpa. This dose has been chosen because it is the dose the standard AKMC was able to reach in a reasonable time (~ 1 week of calculations).

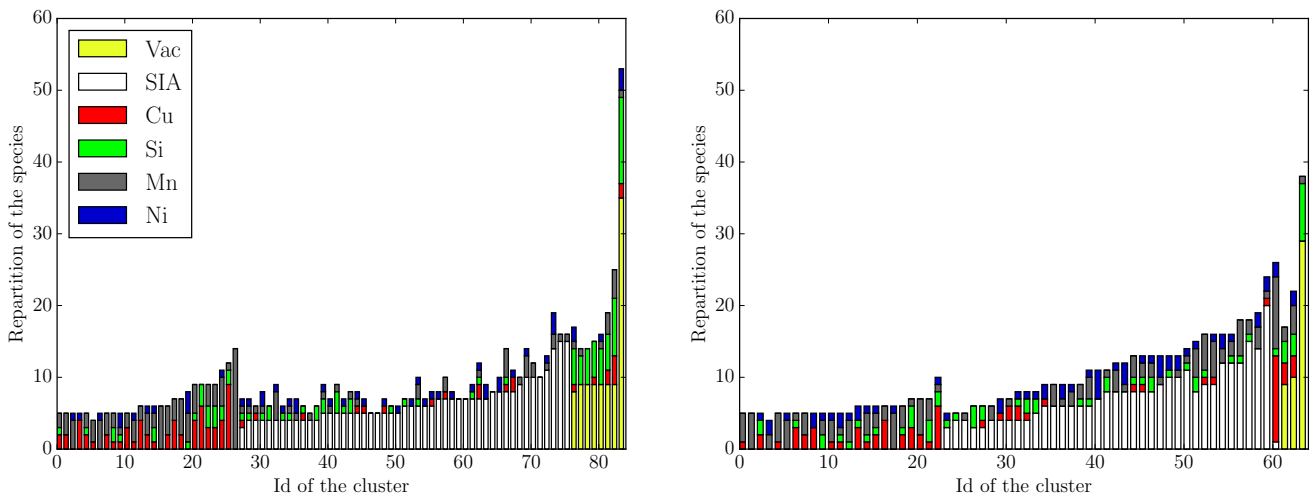


Figure 3-30: Microstructure obtained at 21 mdpa for the standard AKMC (left) and for the hybrid method (right) for the Fe-0.18Cu-1.38Mn-0.69Ni-0.47Si-0.01P at.% alloy. The cluster size criterion was set to 5 species.

There is not much difference between the two microstructures. The pure solute cluster density is equivalent between the two methods. They are more enriched in copper than the clusters associated with SIAs. As concerns SIA clusters, the hybrid method predicts a lower density than standard AKMC. A similar comparison for vacancy clusters is not pertinent because their population fluctuates a lot during the simulation as already discussed in section 3.3.3 and also because obtaining a picture of the average vacancy cluster population cluster is not a trivial task. During the simulation, the total number of vacancies usually reaches zero before the introduction of a new cascade. As in the pure iron system, the effect of a reduction of the flux is difficult to study because of the overestimation of surface effects. Figure 3-31 and Figure 3-32 present the microstructure obtained at 150 mdpa using the hybrid method.

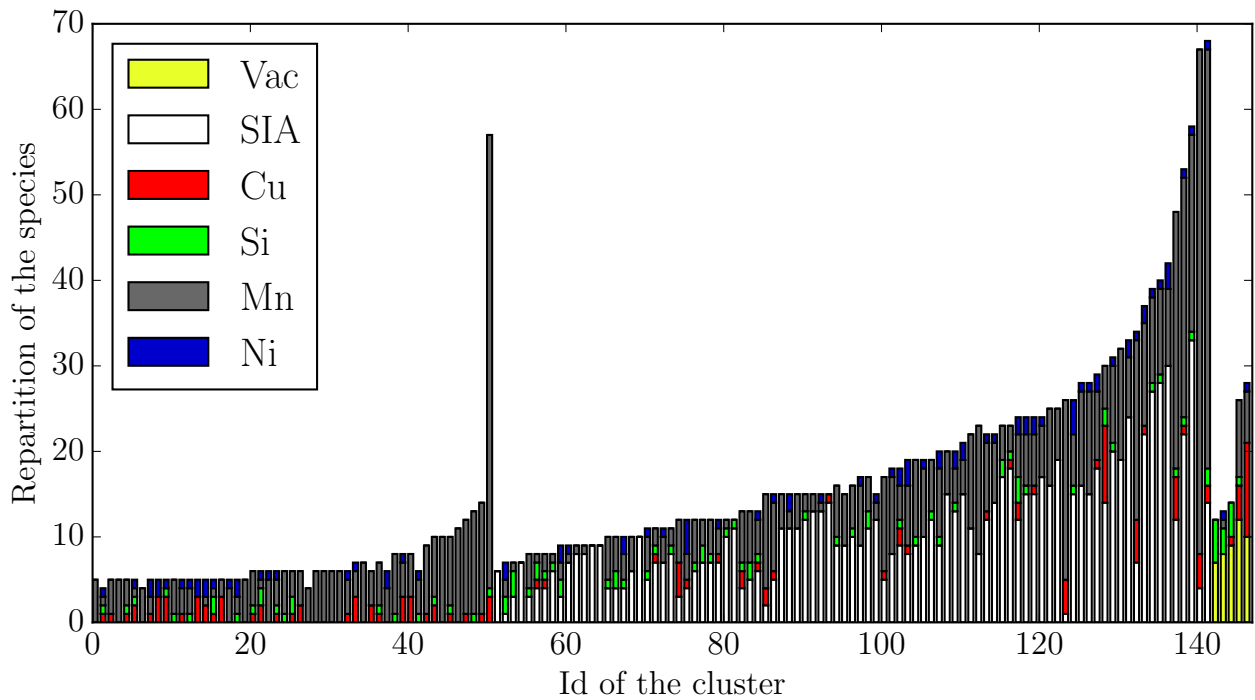


Figure 3-31: Microstructure obtained using the hybrid method for the simulation of the Fe-0.18Cu-1.38Mn-0.69Ni-0.47Si-0.01P at.% alloy irradiated at 150 mdpa. The cluster size criterion was set to 5 species. One bar corresponds to one cluster.

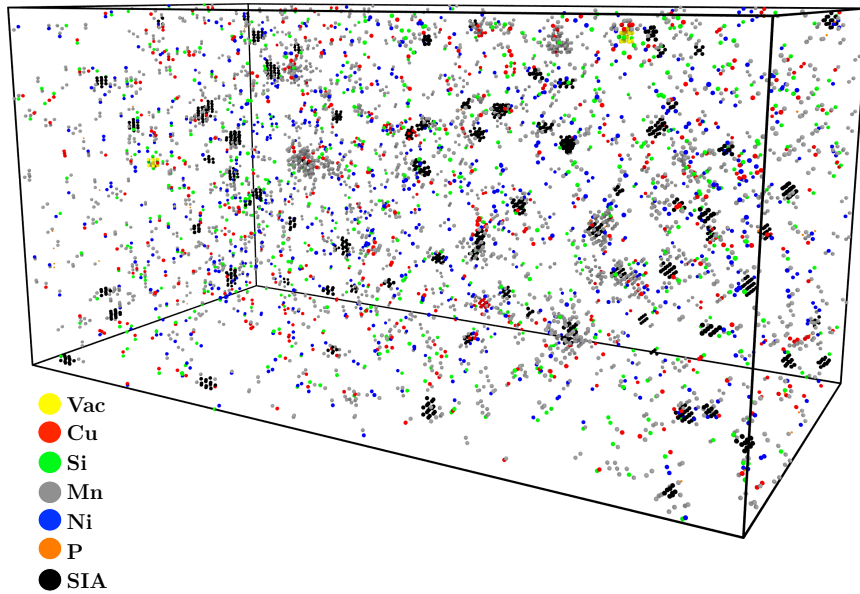


Figure 3-32: Microstructure obtained using the hybrid method for the simulation of the Fe-0.18Cu-1.38Mn-0.69Ni-0.47Si-0.01P at.% alloy irradiated at 150 mdpa. Species fully surrounded by 1NN irons are not displayed. The size box is 17.1×17.1×34.2 nm.

The results for the high dose simulation suggest that the observations made at 21 mdpa remain valid at 150 mdpa. The clusters mainly enriched in copper are not associated with point defects while Mn/Ni rich clusters are still associated with SIA. Solute clusters that are not associated with point defects are rather small (size < 10 solute atoms for a large proportion of them). For the microstructure obtained at 150 mdpa, we applied the cutoff treatment presented in section 2.6.6 of the second chapter. Several cutoffs have been applied to check the impact of the cutoff radii on the mean composition of the objects. These results are presented in Figure 3-33. The mean solute composition does not vary significantly with the cutoff considered. Independently of their sizes, the clusters are mainly enriched in Mn.

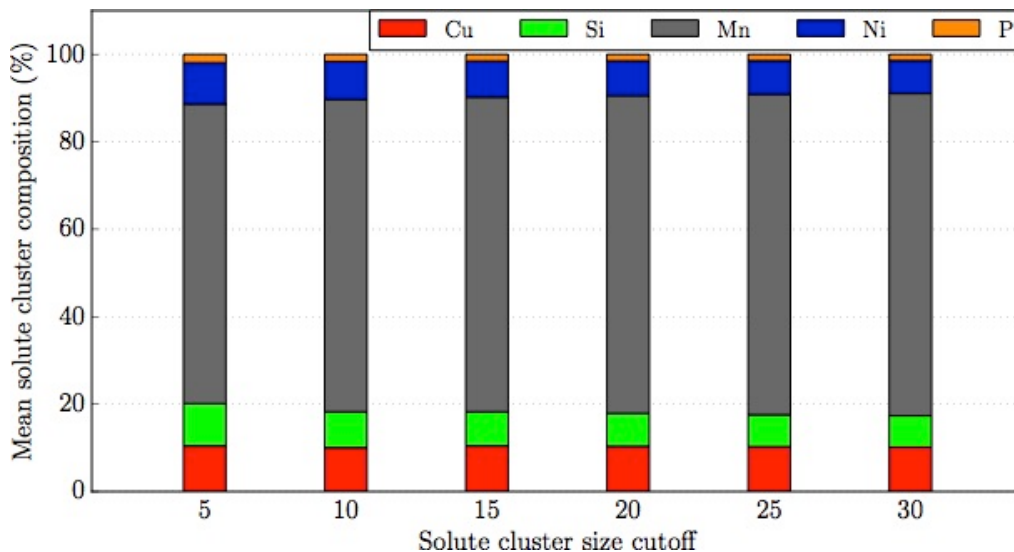


Figure 3-33: Evolution of the mean solute cluster composition as a function of the cluster criterion (in number of atoms) for the simulation of the Fe-0.18Cu-1.38Mn-0.69Ni-0.47Si-0.01P at.% alloy at 150 mdpa.

Figure 3-34 presents the evolution of the solute cluster density simulated as a function of the cutoff. Since the experimental solute cluster density is between $1 \times 10^{23} \text{ m}^{-3}$ and $3 \times 10^{23} \text{ m}^{-3}$ [10], [12], it can be seen that the solute cluster density is overestimated below a cutoff of 35 solute atoms in the cluster. The largest solute cluster observed, at 150 mdpa, contains 64 solute atoms.

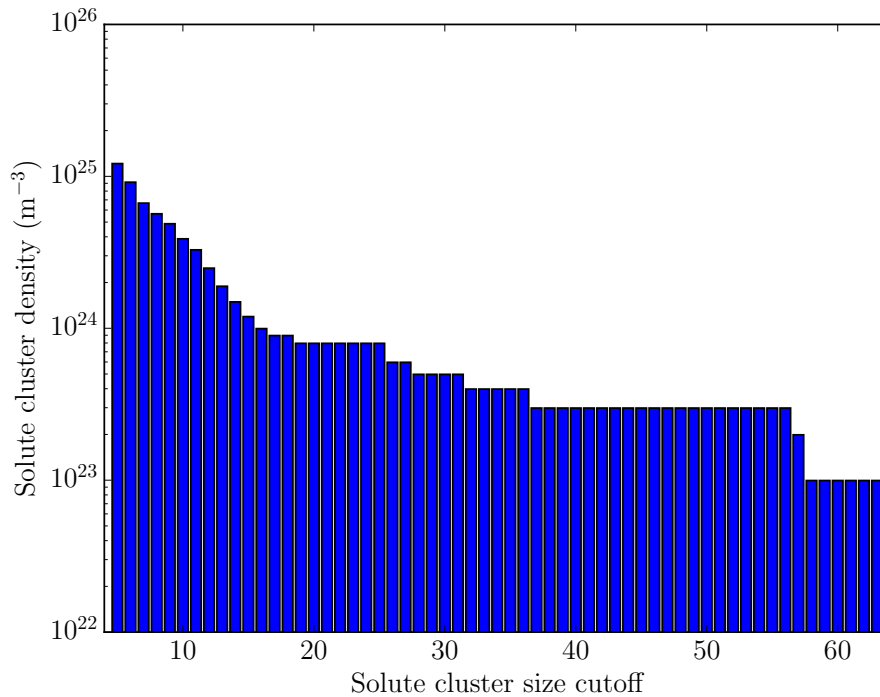


Figure 3-34: Solute cluster density as a function of the cluster size criterion (in number of atoms) for the microstructure simulated at 150 mdpa in the Fe-0.18Cu-1.38Mn-0.69Ni-0.47Si-0.01P at.% system.

Concerning the effect of dose, Figure 3-35 presents the evolution of the number of clusters per categories (vacancy, SIA or solute cluster) as well as the mean size evolution during the irradiation. \overline{N}_X^Y corresponds to the mean number of X species in the Y type cluster.

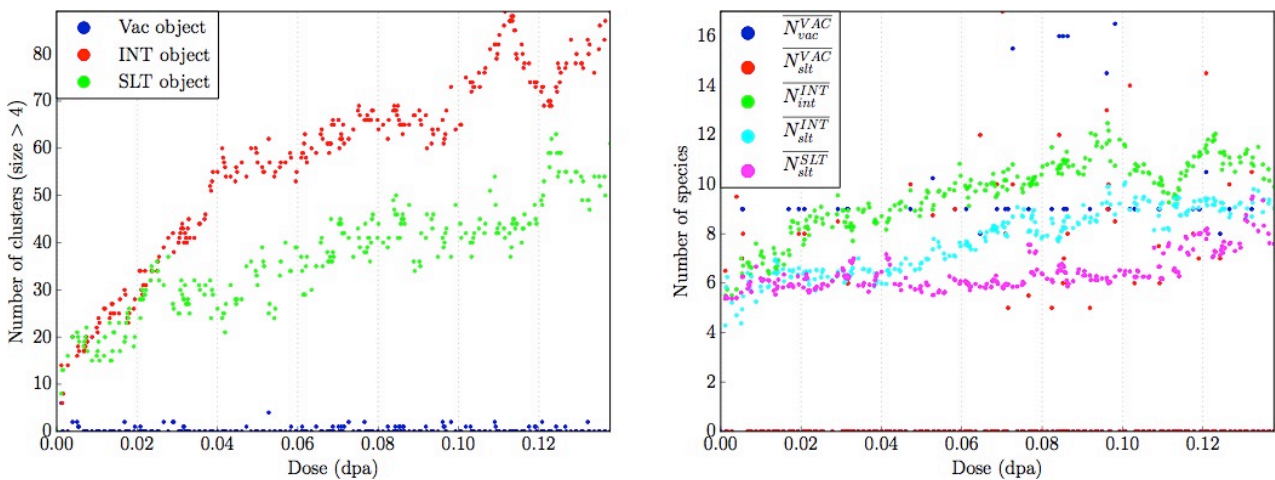


Figure 3-35: Evolution of the number of objects (depending on their type) as a function of the dose simulated for the Fe-0.18Cu-1.38Mn-0.69Ni-0.47Si-0.01P at.% alloy. The cluster criterion was set to 5 species. One cluster corresponds to a density of $\sim 10^{23} \text{ m}^{-3}$.

The solute and SIA cluster density increase with the dose. According to our parameterization, vacancy clusters are quite mobile in the RPV model alloy. Due to their tendency to annihilate on the absorbing surfaces, the number of vacancy clusters reaches zero several times during the whole simulation. The number of SIA and the number of solutes in the SIA clusters increase with the dose. The number of solute atoms in the solute clusters also slightly increases with the dose. These results illustrate the fact that large vacancy clusters formed during the simulation (size>30) are mobile enough to annihilate on surfaces.

Figure 3-36 shows the mean composition of these objects. Results concerning the vacancy clusters show large fluctuations but they are clearly mostly enriched in Si. For the SIA clusters, their Mn content increases with the dose and saturates at 80% after ~80 mdpa. The solute clusters that are not associated to point defect are mainly enriched in Mn and Cu (respectively 75% and 20%).

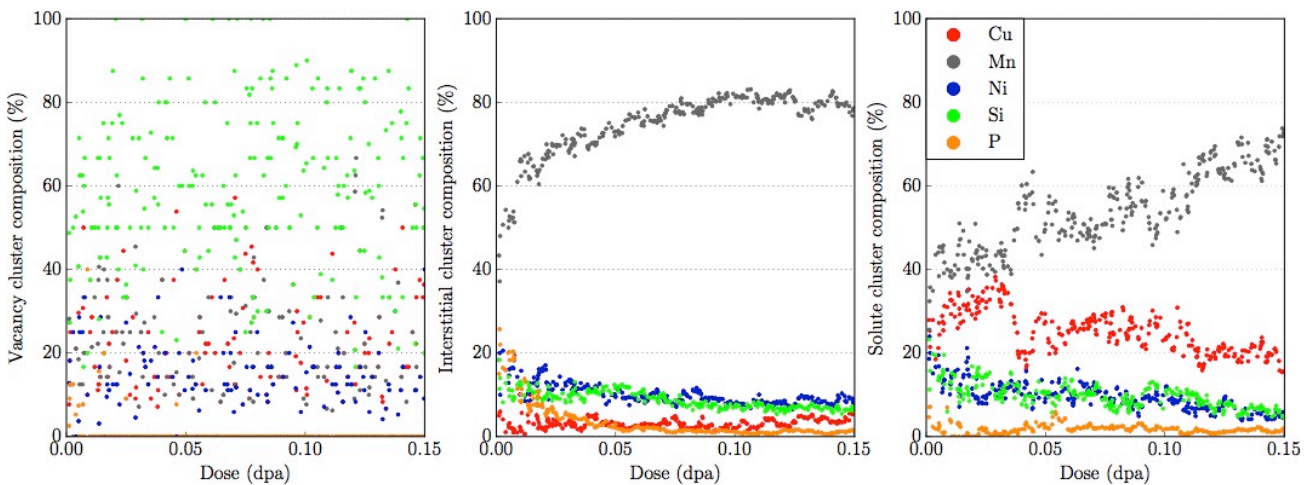


Figure 3-36: Evolution of the mean solute composition for different classes of nanofeatures as a function of dose for the Fe-0.18Cu-1.38Mn-0.69Ni-0.47Si-0.01P at.% alloy.

In his PhD work, Ngayam Happy showed that the parameterization of the AKMC model predicts radiation-induced segregation of solutes (especially Mn) on SIA clusters [9]. Our simulation confirms Ngayam Happy's observation in the high dose regime.

Low copper RPV alloy:

The Fe-0.05Cu-1.38Mn-0.69Ni-0.47Si-0.01P at.% alloy has also been simulated using the hybrid method. The simulation has been performed in a $60 \times 60 \times 120 a_0$ box with absorbing surfaces along the z axis. The temperature has been set to 600 K and the flux employed was $\sim 10^{-5}$ dpa/s using 20-100 keV cascades. Figure 3-37 presents the evolution of the number of cluster for each categories (vacancy, SIA or solute cluster) as well as the mean size evolution with dose. The SIA cluster density saturates for a dose higher than 60 mdpa. For the solute cluster density, it linearly increases with the dose. This observation is in agreement with experimental results. It can be noticed that the solute cluster density is lower in the case of the low copper RPV alloy than in the high copper case. As in the high copper material, the vacancy population regularly reaches zero during irradiation. As concerns the mean size of the objects, the quantities that grow with the dose are the mean number of SIA in the SIA clusters and the mean number of solute clusters in the interstitial clusters. Hence, the solute rich cluster formation mechanism consisting in radiation-induced segregation of solutes on SIA clusters is still valid in the low Cu case. The vacancy cluster mean size is not described due to the statistical noise. The solute cluster mean size remains constant during the simulation (~6 atoms in the clusters).

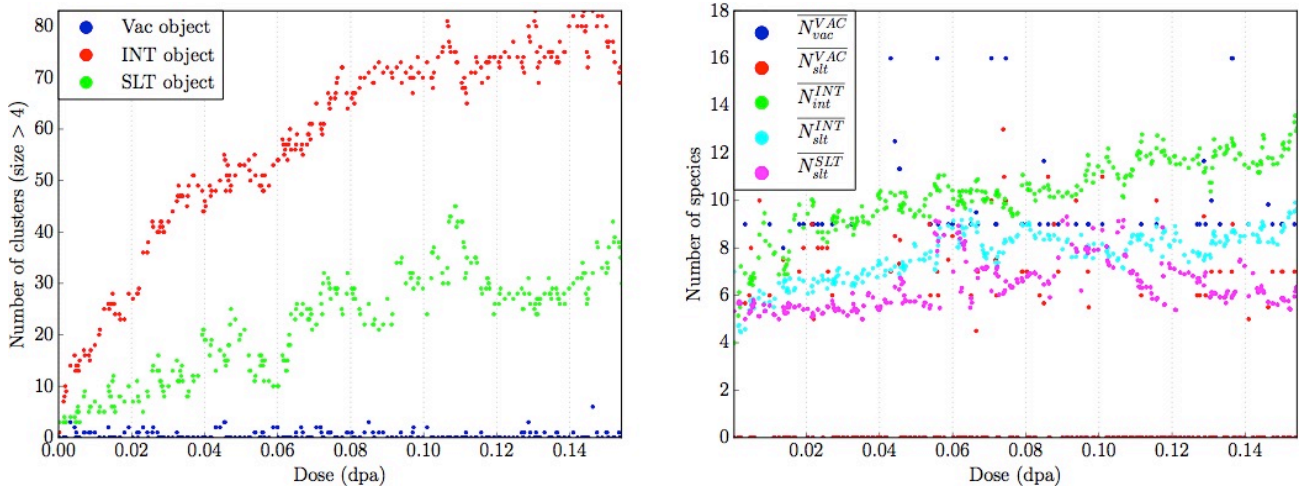


Figure 3-37: Evolution of the number of the object classes predicted in the simulation box as a function of the dose (left) and evolution of the mean number of species in the different types of clusters as a function of the dose (right) for the Fe-0.05Cu-1.38Mn-0.69Ni-0.47Si-0.01P at.% alloy. One cluster corresponds to a density of $\sim 10^{23} \text{ m}^{-3}$. The cluster criterion was set to 5 species.

Figure 3-38 presents the results concerning the mean composition of these objects. The mean solute composition of the vacancy clusters still shows large fluctuations, however vacancy clusters are still mainly enriched in Si. As in the high copper case, the SIA clusters are mainly enriched in Mn. In this low copper case, the solute cluster mean composition is comparable to the SIA clusters mean composition.

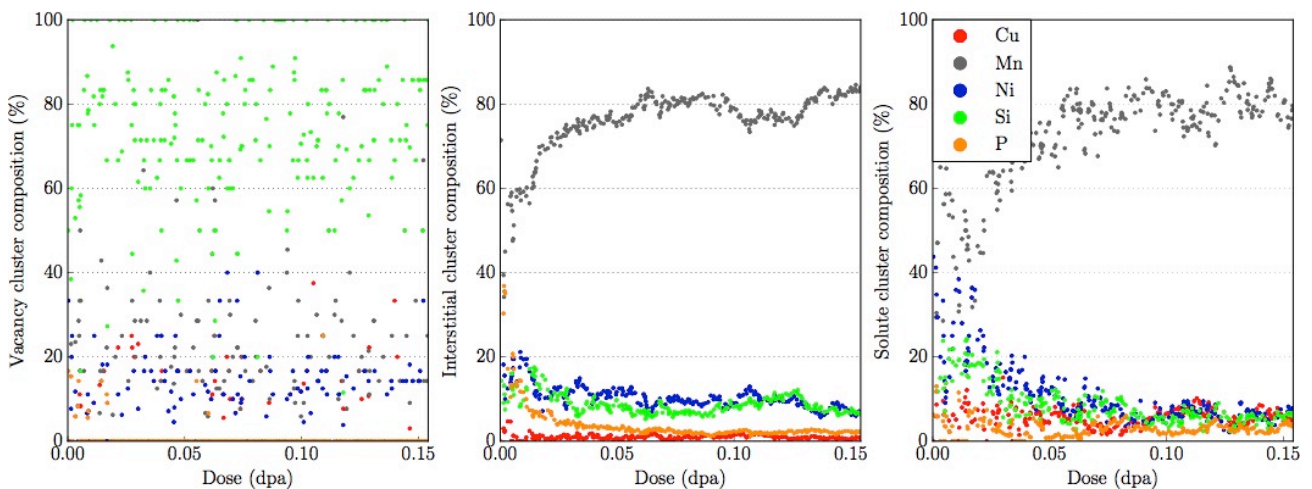


Figure 3-38: Evolution of the mean solute composition for different classes of nanofeatures as a function of the dose for the Fe-0.05Cu-1.38Mn-0.69Ni-0.47Si-0.01P at.% alloy.

Figure 3-39 presents the microstructure obtained at 150 mdpa. As in the high copper case, the predominant class of clusters is the SIA cluster. As previously mentioned, the number of solute clusters that are not associated to point defects is lower than in the high copper case.

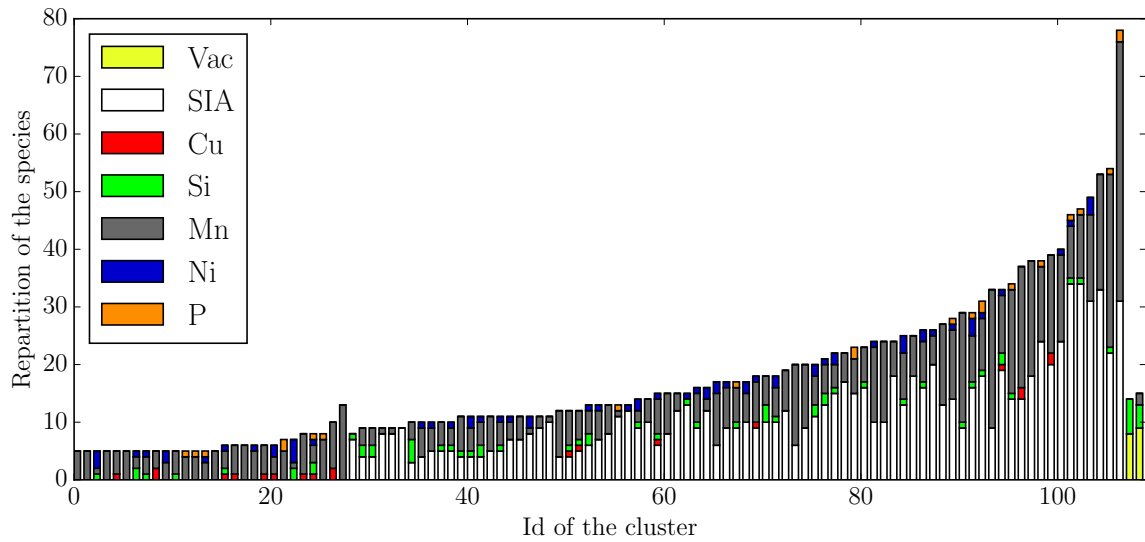


Figure 3-39: Microstructure obtained using the hybrid method for the Fe-0.05Cu-1.38Mn-0.69Ni-0.47Si-0.01P at.% irradiated alloy at 150 mdpa. The cluster size criterion was set to 5 species.

Figure 3-40 presents the solute cluster density as a function of the cutoff. In order to obtain a solute cluster density comparable to the one observed by APT, the cutoff has to be equal to ~25. Assuming APT has a detection efficiency of 60%, it leads to a minimum of 15 solutes atoms observed by APT.

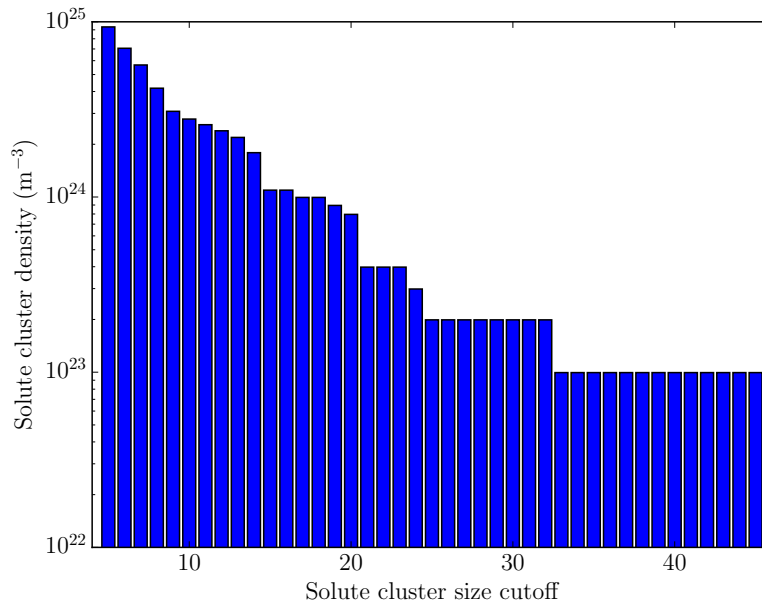


Figure 3-40: Solute cluster density as a function of the cluster criterion for the Fe-0.05Cu-1.38Mn-0.69Ni-0.47Si-0.01P at.% material.

Concerning the mean composition of solute-rich clusters, Figure 3-41 presents the results compared to results extracted from the literature [12].

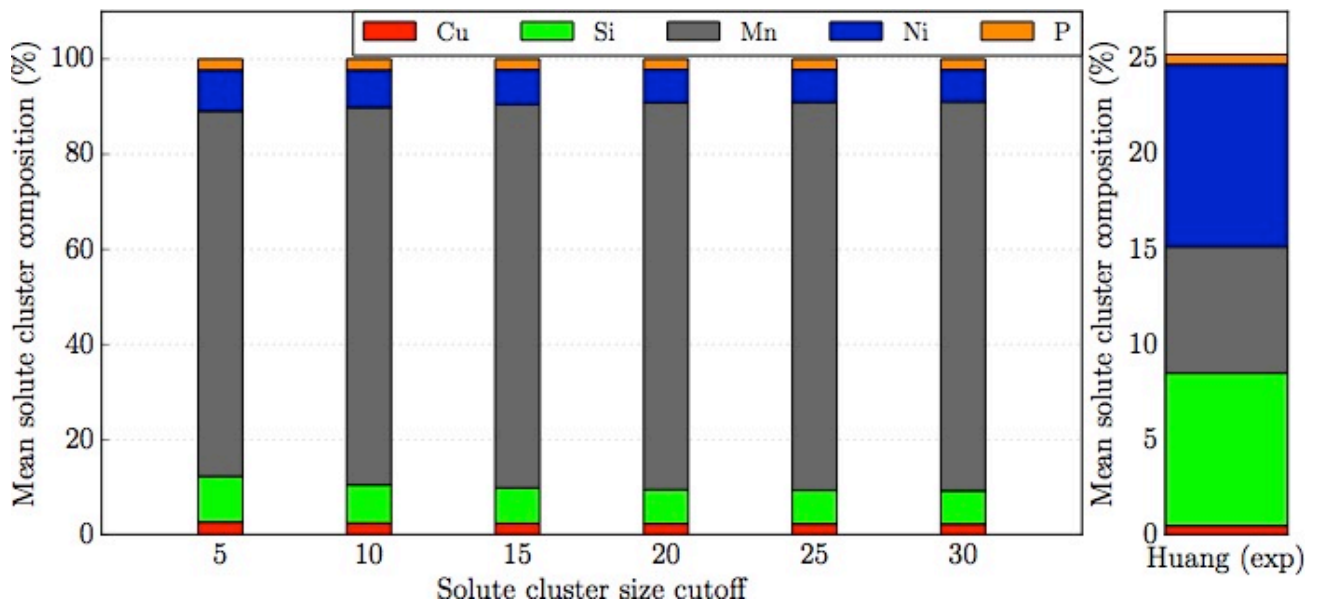


Figure 3-41: Evolution of the mean solute cluster composition observed experimentally on the Fe-0.038Cu-1.36Mn-0.68Ni-0.53Si-0.01P-0.66C at.% [12] compared to simulation results at 150 mdpa for different cluster criteria. The experimental fluence is $7.6 \times 10^{23} \text{ n.m}^{-2}$ which corresponds to 60 years of service irradiation (150 mdpa).

From these results, it appears that the mean solute cluster composition does not change that much when increasing the cutoff. When comparing the simulated microstructure to the experimental one, the predicted manganese content is overestimated while the Ni/Si content is pretty low.

3.4 Features for grain microstructure modeling

Real steels exhibit heterogeneities such as grain boundaries, dislocations and impurities. Grain boundaries and dislocations act as sinks for the point defects and therefore are very important. Impurities such as carbon can trap point defects. Since these “nanofeatures” can have an impact on the microstructure evolution under irradiation, they have been “modeled” in AKMC.

3.4.1 The grain boundary model

3.4.1.1 Probabilistic absorbing surfaces

Simulation results from section 3.3.3 have shown that employing absorbing surfaces in the AKMC model is detrimental to reproduce the flux effect. This is due to the overestimation of the surface/volume ratio in the simulation box compared to reality.

The first approach used to solve this issue was to implement probabilistic absorbing surfaces. In this model, when a defect reaches the surface, it has a probability (specified by the user) to be absorbed. Since point-defect cluster motion is ruled by a large number of elementary jumps, large point-defect clusters can also be absorbed at the surfaces with this feature. Hence, given an absorbing probability of a single defect, the probability for a DP cluster to be absorbed depends on its size. As a result, microstructures simulated with probabilistic absorbing surfaces were similar to those with the absorbing surfaces. This motivated the choice of another method to reduce the sink strength. Employing an absorber that presents a realistic sink strength compared to the one of a grain appeared to be an acceptable solution.

3.4.1.2 The absorber model

Calculating the sink strength of grain boundaries or thin foils is not trivial as it depends on other sinks within the material. However, a simple expression has been derived for the two limiting cases: high importance of internal sink losses or dominant effect of the surfaces [13].

Assuming a spherical geometry, and assuming that the internal sink losses are small compared to the grain boundary losses, the sink strength of a grain with a radius r_{gb} of 1 μm is equal to [13]:

$$k_{gb}^2 = \frac{14.4}{r_{gb}^2} = 1.44 \times 10^{13} \text{ m}^{-2}$$

In our simulation with surfaces in the z direction (typically in a $60 \times 60 \times 120 a_0$ box), which corresponds to a thin foil, the sink strength as a function of the thickness of the foil l is given by [13]:

$$k_{thin\ foil}^2 = \frac{2}{l^2} = 1.70 \times 10^{15} \text{ m}^{-2}$$

if we assume that losses on the surfaces are predominant over the internal losses.

Hence the absorbing surface model tends to overestimate the sink strength of a grain with a radius equal to 1 μm (by about two orders of magnitude). The approach employed to overcome this limitation is to use an absorber. The absorber is a site on the lattice characterized by two capture radii (one for the vacancies and one for the interstitials). When the distance between a point defect and the absorber is smaller than or equal to the capture radius, the defect is absorbed.

The sink strength of such an absorber is given by:

$$k_{trap}^2 = 4\pi n r_{trap}$$

Where n represents the density of traps and r_{trap} is the radius of the trap.

Using this approach, the sink strength of a $200 \times 200 \times 200 a_0$ in presence of one sink with a capture radius corresponding to a 2NN distance is equal to $1.9 \times 10^{13} \text{ m}^{-2}$. This value is comparable to the sink strength of a grain with a radius equal to 1 μm and agrees better than the one for the absorbing surfaces.

Concerning the bias, the one induced by a grain boundary between the vacancy / interstitial absorption is very small, it is not possible to introduce it in a typical AKMC simulation box (the difference between the capture radius is smaller than a 1NN distance). Thus, the capture radius for the vacancy and interstitial is supposed to be equal.

When compared to the sink strength of the absorbing surfaces, the new approach represents an improvement and will lead to more realistic simulations.

3.4.1.3 Comparing absorbing surfaces and the absorber model

In order to compare the use of absorbing surfaces on Z, PBC in all directions and the absorber model, different simulations have been performed on a model RPV. They will be referred to as the absorbing surface case, the absorber case and the PBC case. The simulations have been performed on a Fe-0.18Cu-1.38Mn-0.69Ni-0.47Si-0.01P at.% alloy in a $60 \times 60 \times 120 a_0$ box. The temperature has been set to 563 K and the flux employed was $\sim 10^{-5}$ dpa/s using 20-100 keV cascades. SIA cluster larger than 6 SIAs are set immobile while no assumption is made about the vacancy cluster mobility.

The absorbing surface case:

Figure 3-42 presents the evolution of the number of clusters per category (vacancy, SIA or solute clusters) as well as the mean size evolution with dose. As previously mentioned in section 3.3.6, the number of vacancy clusters is very low and it frequently reaches zero during the simulation. Hence, vacancies tend to annihilate periodically on surfaces (since the SIA cluster population increases). On the contrary, the number of interstitial clusters as well as the number of solute clusters increases linearly with the dose. The apparent increase in the mean number of vacancies/solute in the vacancy clusters is due to the presence of a large vacancy cluster ($V_{\sim 50}$). For the interstitial objects, the associated mean size grows slowly with the dose.

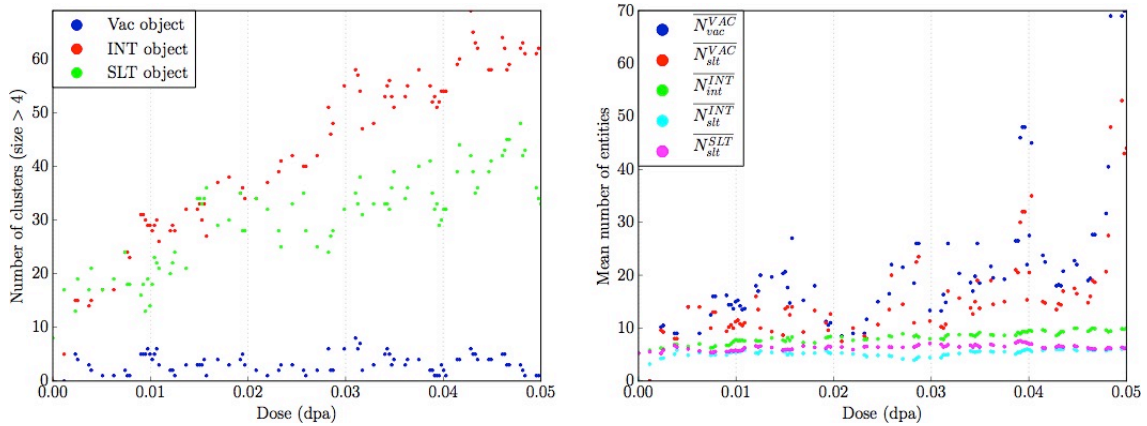


Figure 3-42: Evolution of the number of the object classes predicted in the Fe-0.18Cu-1.38Mn-0.69Ni-0.47Si-0.01P at.% material with the dose (left) and evolution of the mean number of species in different type of clusters as a function of the dose (right). One cluster corresponds to a density of $\sim 10^{23} \text{ m}^{-3}$. In this simulation, the absorbing surfaces were employed. The cluster criterion was set to 5 species.

Regarding the composition of these objects, Figure 3-43 shows that vacancy clusters are mainly enriched in Si. This is consistent with the “Pair2NN-Vincent” parameterization since the highest 1NN Vac-X binding energy in this cohesive model is the vacancy-Si pair. The vacancy clusters are also decorated with Cu and Mn. The Ni and P content is negligible. For the interstitial clusters, Mn is the predominant solute associated. This can be explained by the binding energies as well as the stability of the Mn in the mixed dumbbell. As for the solute clusters, they are mainly enriched in Cu and Mn.

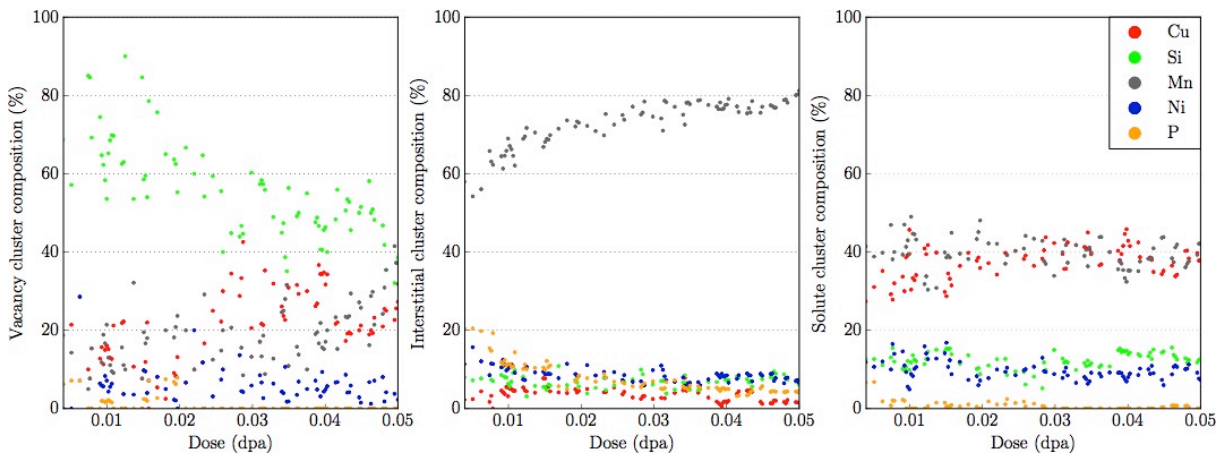


Figure 3-43: Evolution of the mean solute composition for different classes of nanofeatures as a function of the dose for the Fe-0.18Cu-1.38Mn-0.69Ni-0.47Si-0.01P at.% material. In this simulation, the absorbing surfaces were employed.

The absorber case:

Employing an absorber with a capture radius equal to a 2NN distance induces longer computing time than absorbing surfaces to reach similar doses and therefore the reachable dose is decreased. It also has impacts on the microstructure simulated. Figure 3-44 and Figure 3-45 present the results.

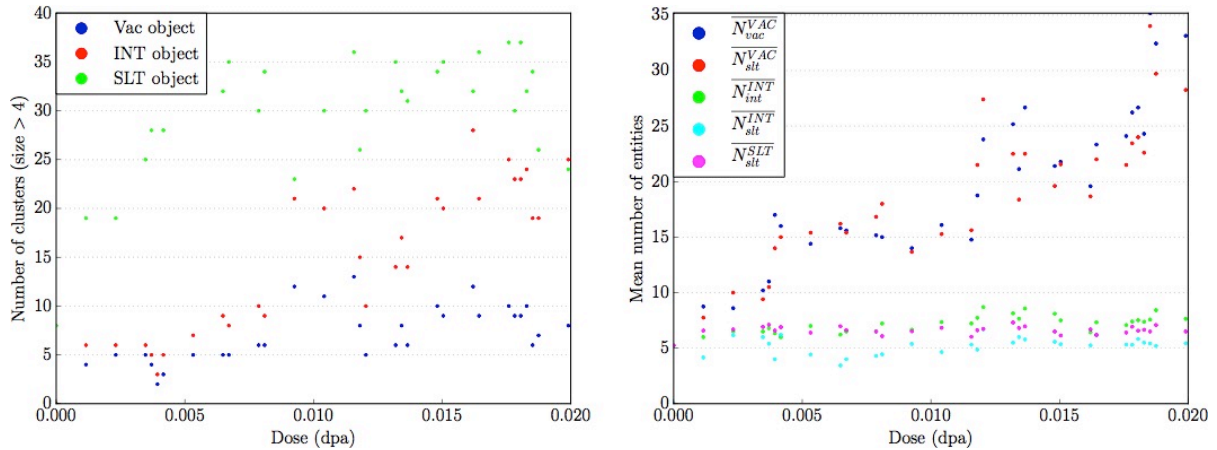


Figure 3-44: Evolution with the dose of the number of the object (left) and of the mean number of species in different type of clusters (right) for the Fe-0.18Cu-1.38Mn-0.69Ni-0.47Si-0.01P at.% alloy. One cluster corresponds to a density of $\sim 10^{23} \text{ m}^{-3}$. In this simulation, the absorber model has been employed. The cluster criterion has been set to 5 species.

The first difference between the absorber and the absorbing surface model one is that vacancy clusters tend to accumulate in the former. The interstitial cluster population still grows linearly with the dose. However, the number of interstitial is slightly lower than in the absorbing surface case. This is due to the fact that removing the absorbing surfaces forces reactions between the objects (aggregation and annihilation). The difference is the number of solute clusters that is slightly higher in the absorber case. Concerning the mean size of the different objects, there is not much difference between both cases. The solute content in vacancy clusters is slightly higher in the absorber case.

The composition of formed objects are presented in Figure 3-45. They are quantitatively similar to those of the absorbing surface model: SIA clusters are mainly enriched in Mn while the solute clusters are enriched in Mn/Cu. The only difference arises from the Si content in the vacancy clusters. It is much lower in the absorber case. This can be explained by the previously mentioned higher solute content in vacancy clusters in the absorber case. Since vacancies have a higher lifetime in the absence of absorbing surfaces, they induce a more pronounced accumulation of solutes around them. Moreover, since vacancies explore the simulated volume for a longer time, the encounter between a vacancy and a P is more probable. The P atom is known to bind strongly with the vacancy and it also tends to trap it (due to the low $E_{a0}(P)$ in the FISE model).

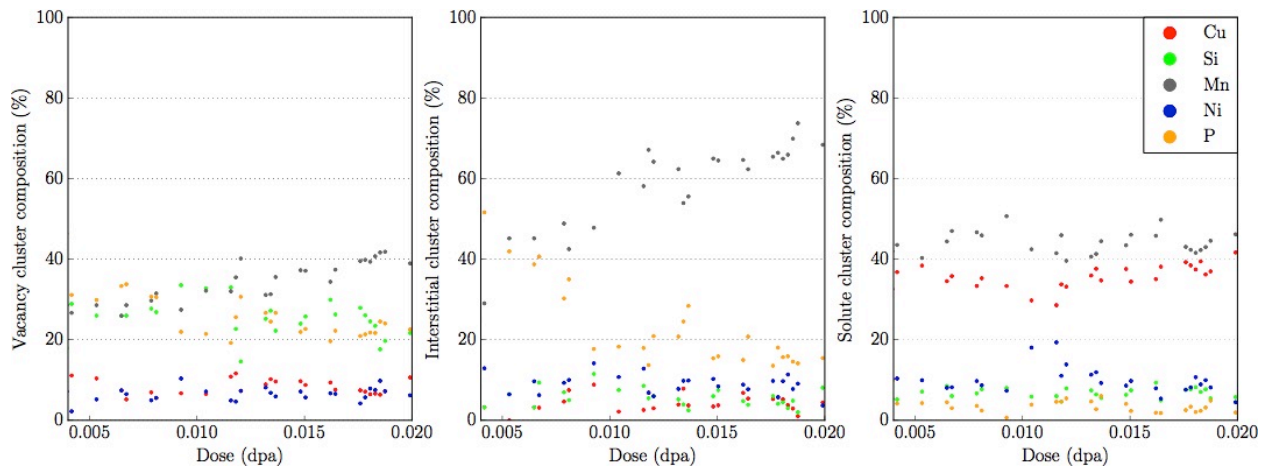


Figure 3-45: Evolution with the dose of the mean solute composition for different classes of nanofeatures for the Fe–0.18Cu–1.38Mn–0.69Ni–0.47Si–0.01P at.% alloy. In this simulation, the absorber model was employed.

The PBC case:

Using the PBC treatment, the results are equivalent to those obtained with the absorber. As shown in Figure 3-46, the accumulation of interstitials and vacancies in the simulation box still happen in the PBC case.

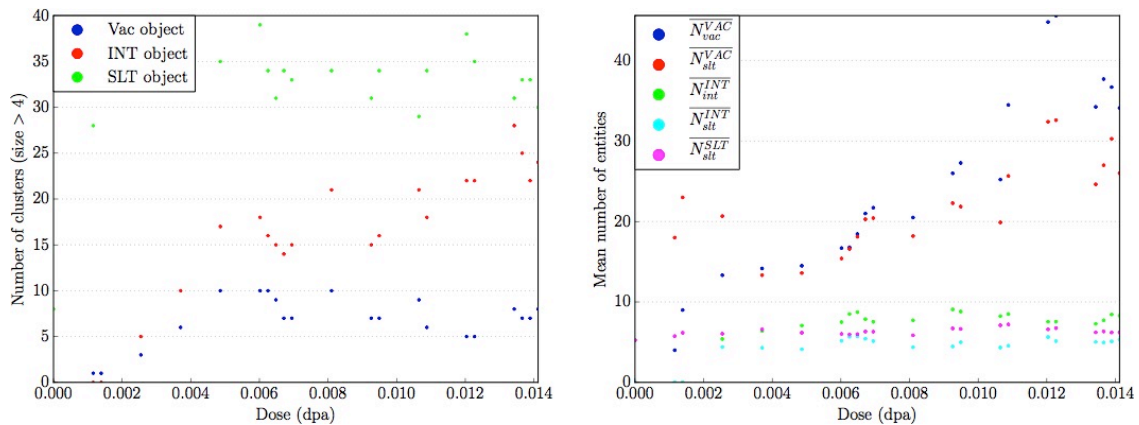


Figure 3-46: Evolution with the dose of the number of the object (left) and of the mean number of species in the different types of clusters (right) for the Fe–0.18Cu–1.38Mn–0.69Ni–0.47Si–0.01P at.% alloy. One cluster corresponds to a density of $\sim 10^{23} \text{ m}^{-3}$. In this simulation, a PBC treatment has been employed. The cluster criterion was set to 5 species.

The tendency for the vacancy cluster to contain P atoms that was observed in the absorber case has also been found in the PBC case (as shown in Figure 3-47). SIA clusters are still mainly enriched in Mn and solute clusters in Mn and Cu.

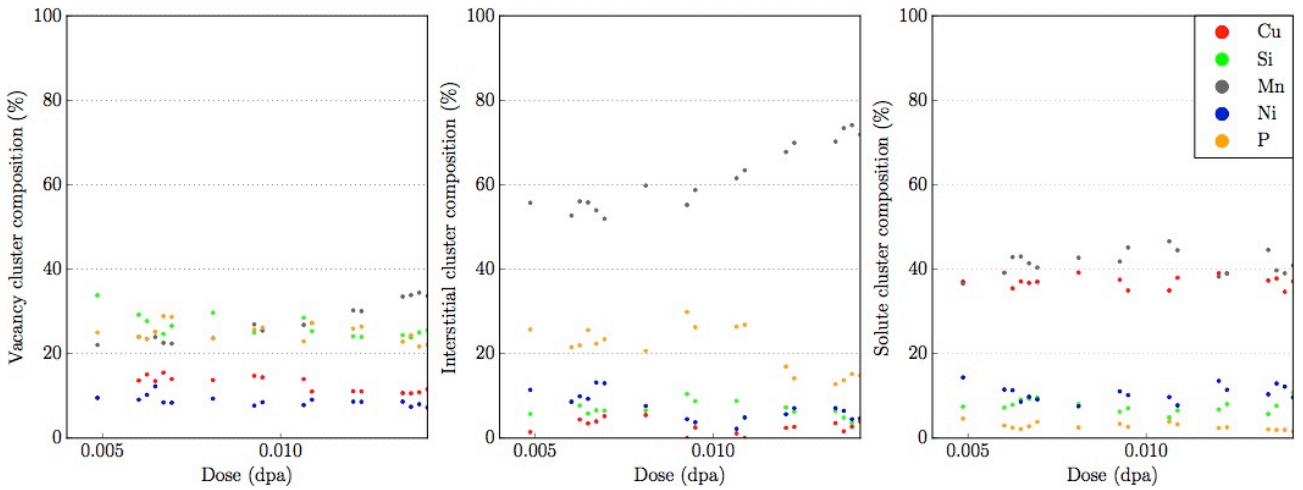


Figure 3-47: Evolution with the dose of the mean solute composition for different classes of nanofeatures as a function for the Fe-0.18Cu-1.38Mn-0.69Ni-0.47Si-0.01P at.% alloy. In this simulation, a PBC treatment has been employed.

This collection of simulations highlights the fact that adding an absorber in our AKMC simulation does not have an important impact on the microstructure as compared to the PBC case. In these conditions, the PD objects are more likely to react and the presence of the absorber does not affect that much the trajectory of the system. In terms of reachable doses, removing the surfaces makes the target dose no longer accessible. However, performing simulation without absorbing surfaces has a positive effect on the vacancy population (since vacancies are observed experimentally in the irradiated RPV model alloys).

3.4.2 Traps in the AKMC

3.4.2.1 The model

Impurities such as carbon can always be found even in very pure iron. The carbon is known to bind strongly with vacancies and trap them. As a consequence, impurities have an impact on the microstructure evolution under irradiation.

Taking advantage of the traps model in the OKMC, a simple implementation of traps has been introduced in LAKIMOCA. The role of these traps is to simulate the presence of a small amount of impurity, such as carbon atoms, in the system. In the atomic framework, traps are described as on-site species associated with pair interactions. Traps only interact with point defects. The reference migration energy E_{a0} in the FISE model (presented in the third section of chapter 2) has been set to 10 eV for both vacancies and interstitials. This ensures that traps will be immobile during the whole simulation. Binding energies E_b (trap-Vac) and E_b (trap-SIA) have been respectively set to 1.0 eV and 0.4 eV to agree with [14]. The range of these interactions corresponds to a 1NN distance. From the OKMC point of view, once an object is built, its mobility is set to zero and its emission frequency is supposed not to be perturbed by the presence of the trap.

Another important aspect of the trap model is the un-trapping process. This is basically done in the “standard OKMC” method by adding a trapping energy to the cluster migration energy to obtain the dissociation energy. This method was used in our AKMC model and the mobility of a trapped cluster is expressed:

$$\Gamma_{mig}(size) = \Gamma_{mig0}(size) e^{\frac{-(E_{mig}(size)+E_{trap}(size))}{k_b T}}$$

To do so, a new file trap.in has been added. The E_{trap} terms can be specified for each type (vacancy or interstitial) and for all cluster sizes. More details are provided in Annex IV.

Since the extraction of a point defect cluster from a trap is a complex mechanism, the choice was made to un-trap the cluster by sending the trap in a random location in the simulation box instead of moving the cluster. Because the carbon is known to be mobile ($E_m \sim 0.8$ eV [9]) in α iron, this assumption was supposed as acceptable.

3.4.2.2 Parameterization

Another important point for long-term irradiation simulation in iron is that large SIA clusters are known to be mobile. However, our current cohesive model predicts immobile SIA objects for size above 13 SIA in the object. The hybrid AKMC/OKMC method can overcome this limitation. In the previous irradiation simulation in iron (section 3.3.3), our hybrid AKMC/OKMC simulations were performed assuming that the SIA clusters above size 13 were immobile. The SIA mobilities employed were the ones from the OKMC model developed by Chiapetto [15] for the simulation of the FeMnNi system under irradiation. These mobilities were originally used to simulate the FeC system. In this model, the prefactor of the migration process evolve as:

$$v = \frac{c}{n^{0.8}}$$

where n is the number of SIAs in the cluster and c is a constant equal to $8.11 \times 10^{12} \text{ s}^{-1}$.

The activation energy for migration is presented in Table 3-3:

Number of SIA	E_a (eV)	Number of SIA	E_a (eV)
1	0.31	7	0.20
2	0.42	8	0.20
3	0.42	9	0.20
4	0.80	10-N	0.20
5	0.10	N<	0.90
6	0.20		

Table 3-3: Activation energies for the SIA migration used in Chiapetto OKMC [15]. With N chosen as 90.

Concerning the vacancy objects, the results from the AKMC simulations obtained in section 3.3.2.1 for pure iron have been used and extrapolated. Figure 3-48 presents the parameterization obtained.

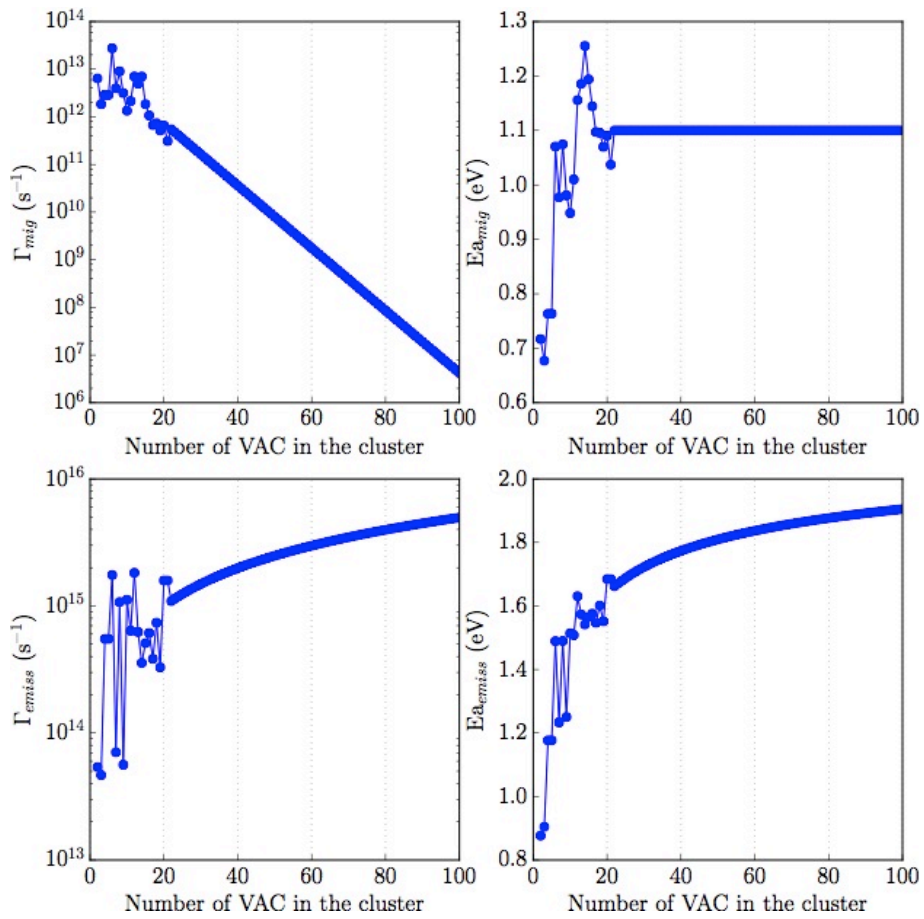


Figure 3-48: OKMC parameterization used for the properties of the vacancy objects depending on their sizes.

Concerning the parameterization of the traps, the binding energies used are given in Table 3-4.

Number of PD	E_b (Trap-SIA) (eV)	E_b (Trap-Vac) (eV)
1	0.17	0.65
2	0.28	1.1
3	0.36	0.93
4	0.34	0.96
5	0.6	1.23
6	0.6	1.2
7-N	0.6	0.4
N <	1.1	0.4

Table 3-4: Binding energies between traps and point defect clusters used in the hybrid AKMC/OKMC with traps. N has been set to 90.

3.4.2.3 Results

Irradiation simulations have been performed at 563 K in a $100 \times 100 \times 100 a_0$ simulation box containing one absorber. Its capture radius corresponds to a 1NN distance. Two traps concentration have been used (0.013 and 0.026 at.%). These quantities of traps represent a sink strength of 4.0×10^{16} and $8.0 \times 10^{16} \text{ m}^{-2}$ (the sink strength employed in the Chiapetto OKMC was $\sim 4.0 \times 10^{16} \text{ m}^{-2}$). The flux was set to $2 \times 10^{-5} \text{ dpa.s}^{-1}$. Figure 3-49 shows the evolution of the microstructure with the dose.

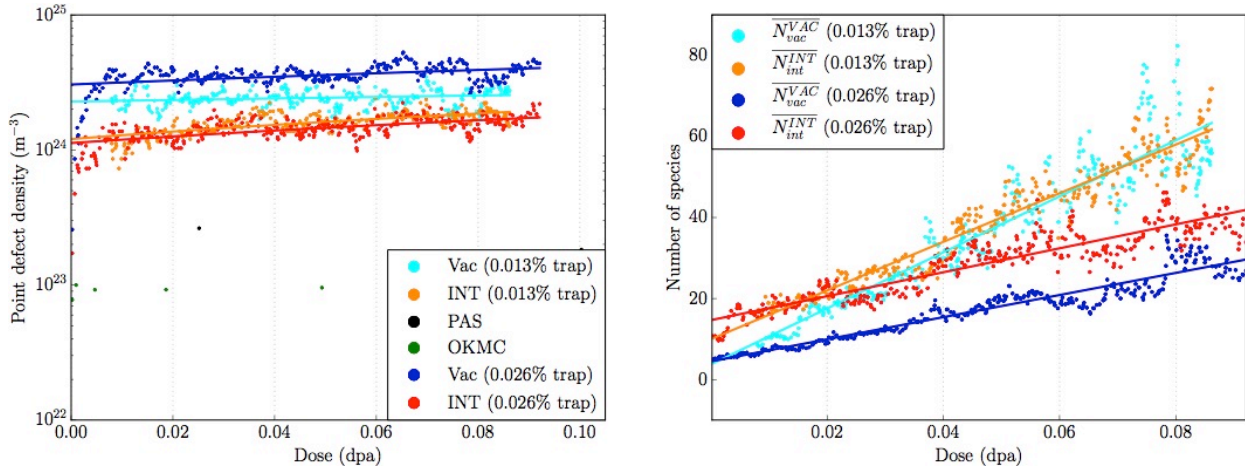


Figure 3-49: Evolution with the dose of the vacancy cluster density. OKMC results come from Jansson OKMC [14] and PAS results from REVE experiments [16] (left). Evolution with the dose of the mean size of the vacancy and interstitial clusters (right).

According to Figure 3-49, our hybrid model tends to overestimate the vacancy cluster density. It is also observed that increasing the concentration of traps increases the vacancy cluster density. However, the results suggest that introducing traps, for the concentrations we have explored, does not have a strong impact on the SIA cluster density. This is in agreement with the fact that we use lower binding energies between traps and SIA clusters than between traps and vacancy clusters. Concerning the mean size of the point defect clusters, it increases for both vacancies and interstitials for the two trap concentrations. In the 0.013% trap case, the mean size of the vacancy and interstitial is comparable. For 0.026% of trap, the mean size of clusters is lower than in the simulation containing less traps. Hence, while the traps have no impact on the SIA cluster density, it has one on their mean size.

Concerning the proportion of traps associated to the point defects, Figure 3-50 shows that traps are more likely to be associated with vacancies. When increasing the number of traps in the simulation box, the proportion of traps associated to vacancies also increases. This observation is in agreement with the increase of the vacancy cluster density when increasing the trap concentration. The proportion of traps associated to SIA clusters remains almost constant during irradiation and no effect of the trap concentration is observed on this quantity.

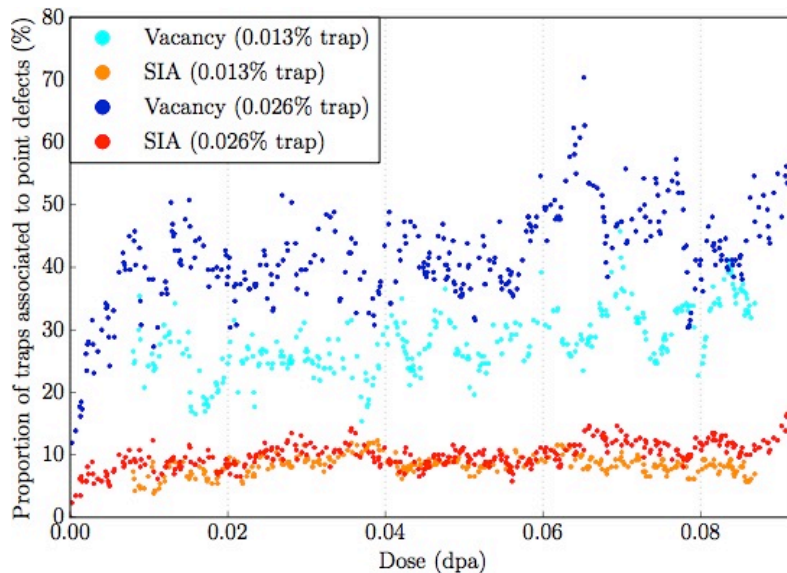


Figure 3-50: Evolution with the dose of the proportion of traps associated to vacancies or SIA.

These simulations show that reproducing an OKMC simulation from an hybrid AKMC model remains difficult. The main issue comes from the accessible volume in AKMC versus OKMC. As a result of this, too small object densities are not observable. Moreover, the object sink strengths are not directly comparable between the two approaches. However, traps have highlighted an important impact on the predicted microstructure. Their use in AKMC could be envisaged.

3.5 Conclusion

Several algorithmic optimizations of the AKMC code have been presented. These optimizations lead to an acceleration by factor up to 6 on the overall execution of the code when point defect clusters form. This acceleration has been particularly useful for the investigation of point defect cluster mobilities and emission frequencies. Additional optimizations have also been tested on a model code. Some of these optimizations could be used in both AKMC and OKMC versions of LAKIMOCA to improve its global performance.

An hybrid AKMC/OKMC approach has been developed in the LAKIMOCA code. The efforts made to parameterize the OKMC part of the hybrid model allowed us having a better understanding of the rates governing the model. It clearly appears that the model predicts SIA clusters as immobile objects above size 13. In the case of the pure iron system, the hybrid approach has been parameterized on a large number of AKMC simulations. The validation of the parameterization has been achieved on post-irradiation isochronal annealing. The results are in very good agreement with AKMC simulations and the acceleration on the runtime is about 200. This allows reaching the target dose in the Fe system. The simulated microstructure presents however differences when compared to the experimental observations. First, almost all vacancies annihilate on absorbing surfaces, which aim at describing grain boundaries. Since vacancies are observed in this system under irradiation by PAS, the first limitation highlighted concern the overestimation of the “grain boundary” effects. The second limitation concerns the inability of the model to describe flux effects in pure iron.

To overcome these limitations, absorbers and traps have been introduced in LAKIMOCA. The absorber model has been developed in order to obtain a sink strength comparable to that of 1 μm grain in our simulations. However, removing the absorbing surfaces leads to an important decrease of the dose that can be reached in a reasonable amount of computing time. While a flux effect might exist in the simulated RPV model alloy without the absorbing surfaces, the calculations are too slow to observe it. The trap model has

been introduced to take into account the presence of impurities such as carbon into our simulations. The results of simulations using the trap model show that transferring an OKMC parameterization to an AKMC model is a difficult task. This is mainly due to the smaller box size used in AKMC.

Concerning the solute treatment in the hybrid model, an attempt to simulate the FeCu under irradiation has been achieved. Unfortunately, the parameterization of this system is too computation demanding. The variety of macro-event frequencies is too large to properly describe them. Hence, using the object FeCu parameterization, the hybrid method introduces a bias in the simulation trajectory. However, taking advantage of the predicted immobility of the large SIA clusters allowed us reaching the target dose (in the FeCu system as well as in a RPV type model alloy). Unfortunately the microstructures simulated did not agree fully with the APT observations. The “Pair2NN-Vincent” parameterization tends to overestimate the solute cluster density and underestimate their size. The Ni and Si content in the solute clusters are also underestimated. For these reasons, it has been decided to build a new cohesive model that takes into account recent DFT results. This is the subject of the next chapter.

3.6 Bibliography

- [1] L. Dagum and R. Menon, “OpenMP: an industry standard API for shared-memory programming”, *IEEE computational science and engineering*, vol. 5, no. 1, pp. 46–55, 1998.
- [2] D. Knuth, “The Art of Computer Programming 1: Fundamental Algorithms”, *MA: Addison-Wesley*, 1968.
- [3] E. Vincent, PhD thesis, “Simulation numérique à l'échelle atomique de l'évolution microstructurale sous irradiation d'alliages ferritiques”, Lille University, 2006.
- [4] P. Olsson, T. P. C. Klaver, and C. Domain, “Ab initio study of solute transition-metal interactions with point defects in bcc Fe”, *Physical Review B*, vol. 81, no. 5, pp. 054102, Feb. 2010.
- [5] N. Castin, M. I. Pascuet, and L. Malerba, “Mobility and stability of large vacancy and vacancy-copper clusters in iron: An atomistic kinetic Monte Carlo study”, *Journal of Nuclear Materials*, vol. 429, no. 1, pp. 315–324, Oct. 2012.
- [6] L. Messina, L. Malerba, and P. Olsson, “Stability and mobility of small vacancy–solute complexes in Fe–MnNi and dilute Fe–X alloys: A kinetic Monte Carlo study”, *Nuclear Instruments and Methods in Physics*, vol. 352, pp. 61–66, Dec. 2008.
- [7] P. Brommer, L. K. Béland, J.-F. Joly, and N. Mousseau, “Understanding long-time vacancy aggregation in iron: a kinetic activation-relaxation technique study”, *Physical Review B*, vol. 90, no. 13, pp. 134109, 2014.
- [8] F. G. Djurabekova, L. Malerba, C. Domain, and C. S. Becquart, “Stability and mobility of small vacancy and copper-vacancy clusters in bcc-Fe: An atomistic kinetic Monte Carlo study”, *Nuclear Instruments and Methods in Physics Research Section B: Beam Interactions with Materials and Atoms*, vol. 255, no. 1, pp. 47–51, Feb. 2007.
- [9] R. Ngayam-Happy, PhD thesis, “Prévisions de l'évolution microstructurale sous irradiation d'alliages ferritiques par simulations numériques à l'échelle atomique”, Lille University, 2010.
- [10] E. Meslin, M. Lambrecht, M. Hernández-Mayoral, F. Bergner, L. Malerba, P. Pareige, B. Radiguet, A. Barbu, D. Gómez-Briceño, A. Ulbricht, and A. Almazouzi, “Characterization of neutron-irradiated ferritic model alloys and a RPV steel from combined APT, SANS, TEM and PAS analyses”, *Journal of Nuclear Materials*, vol. 406, no. 1, pp. 73–83, Nov. 2010.
- [11] R. E. Stoller, “The effect of free surfaces on cascade damage production in iron”, *Journal of Nuclear Materials*, vol. 307, pp. 935–940, Dec. 2002.
- [12] H. Huang, PhD thesis, “Influence de l'irradiation aux neutrons sur le vieillissement des aciers de cuves des réacteurs nucléaires à eau pressurisée”, Rouen University, 2012.
- [13] R. Bullough, M. R. Hayns, and M. H. Wood, “Sink strengths for thin film surfaces and grain boundaries”, *Journal of Nuclear Materials*, vol. 90, no. 1, pp. 44–59, May 1980.
- [14] V. Jansson, M. Chiapetto, and L. Malerba, “The nanostructure evolution in Fe-C systems under irradiation at 560K”, *Journal of Nuclear Materials*, vol. 442, no. 1, pp. 341–349, Nov. 2013.
- [15] M. Chiapetto, L. Malerba, and C. S. Becquart, “Nanostructure evolution under irradiation in FeMnNi alloys: A ‘grey alloy’ object kinetic Monte Carlo model”, *Journal of Nuclear Materials*, vol. 462, pp. 91–99, Jun. 2015.
- [16] E. Meslin, M. Lambrecht, M. Hernández-Mayoral, F. Bergner, L. Malerba, P. Pareige, B. Radiguet, A. Barbu, D. Gómez-Briceño, A. Ulbricht, and A. Almazouzi, “Characterization of neutron-irradiated ferritic model alloys and a RPV steel from combined APT, SANS, TEM and PAS analyses”, *Journal of Nuclear Materials*, vol. 406, no. 1, pp. 73–83, Nov. 2010.

Chapter 4. Concentration dependent cohesive model: parameterization development and irradiation results

4.1	Introduction	101
4.2	Comparison of the parameterizations found in the literature	102
4.2.1	Thermodynamic aspects	103
4.2.2	Metropolis Monte Carlo simulations.....	104
4.2.3	Kinetic aspects.....	105
4.2.4	Transport through a vacancy mechanism	106
4.2.5	Transport through a SIA mechanism.....	107
4.2.6	Outcome of the parameterization comparison.....	109
4.3	Development of a concentration dependent parameterization	110
4.3.1	Principle of the CDP type approach	111
4.3.2	Parameterization strategies	114
4.3.3	Parameterization of the binary systems	117
4.3.3.1	The FeCu system.....	117
4.3.3.2	The FeMn, FeNi and FeSi systems	119
4.3.4	Parameterization of the ternary/ quaternary systems.....	122
4.3.5	Parameterization of the vacancies	125
4.3.6	Parameterization validation	128
4.3.7	Monte Carlo simulations on RPV model alloy.....	130
4.3.8	Kinetic properties	131
4.4	Simulations of irradiation	133
4.4.1	Comparison between CDP and “Pair2NN-Vincent” at low dose.....	133
4.4.2	Coupling the CDP model with the hybrid AKMC/OKMC	137
4.4.3	Vacancy object parameterization effects.....	138
4.4.4	Flux and temperature effects	141
4.4.5	Copper effects.....	143
4.4.6	Synthesis of the irradiation simulations with the hybrid CDP model	149
4.5	Conclusion	150
4.6	Bibliography	150

4.1 Introduction

Due to the deviation observed between simulated and experimental microstructure at high dose obtained in the previous chapter, improving the parameterization is a necessity. The objective of the first section is to perform a comparison between AKMC parameterizations we have tested for the simulation of the RPV model alloy. The second section will be dedicated to the development of a concentration dependent cohesive model. Then, irradiated microstructures obtained using this cohesive model will be presented.

4.2 Comparison of the parameterizations found in the literature

Due to the deviation between the predictions of the AKMC model and the experimental observations that have been reported in chapter 3, a comparison between some parameterizations found present in the literature have been done. The first on-lattice parameterization proposed for RPV steel simulations comes from Liu et al. [1]. It has been developed to perform lattice Metropolis Monte Carlo simulations using 1NN pair interactions. The parameters come from binary alloys mixing energies. A second parameterization has been developed during Vincent PhD thesis [2] in order to perform Kinetic Monte Carlo simulation. Many properties have been collected from USPP ab initio calculations. These input parameters have then been adjusted to reproduce thermal ageing experiments on model alloys (from FeCu to FeCuMnNiSi). It is important to note that a big effort has been made to reproduce the FeCu binary system. The parameterization of the Mn, Ni and Si has been achieved based on two observations. The first one corresponds to the absence of Mn, Ni and Si precipitation in the binary matrix due to the high solubility limit of these solutes in iron. The second one is the influence of the solutes on Cu precipitation [3-5].

The last set of parameters (ϵ_{ij}) has been inspired by Messina PhD work [6]. The purpose of that work was to compute solute transport through vacancy/interstitial mechanism. To achieve this, all relevant barriers for the one vacancy – one solute system have been computed using PAW PW91 DFT calculations. The results have been compared to the prediction of the FISE model (often used to predict barriers when the chemical complexity of the system increases). It turned out that the FISE model coupled with the binding energies from ab initio calculations reproduced the tendencies described by the SCMF analytical model [6].

The denomination used to refer to these parameterizations is as follows:

- **Pair2NN-Vincent**: Original Vincent parameterization (adjusted on USPP ab initio calculations) [2].
- **Pair1NN-Liu97**: Solution enthalpies are those used in Liu's parameterization (from the binary mixing energies) and determine Slt-Slt pair interactions [1]. For kinetic simulations, the pair interactions Vac-Slt are those used in Vincent's parameterization. Cohesive energy used to get the ϵ_{i-j} interactions as well as migration energies have also been extracted from Vincent's parameterization. All 2NN pair interactions are null.
- **Pair2NN-PAW**: Parameterization fully based on pair binding energies from PAW PW91 DFT.

In the following section, these parameterizations will be compared from thermodynamic and kinetic points of view.

4.2.1 Thermodynamic aspects

Thermodynamic properties such as binding energies and mixing energies have an important impact on the microstructure evolution. Figure 4-1 compares the different properties predicted by the parameterizations.

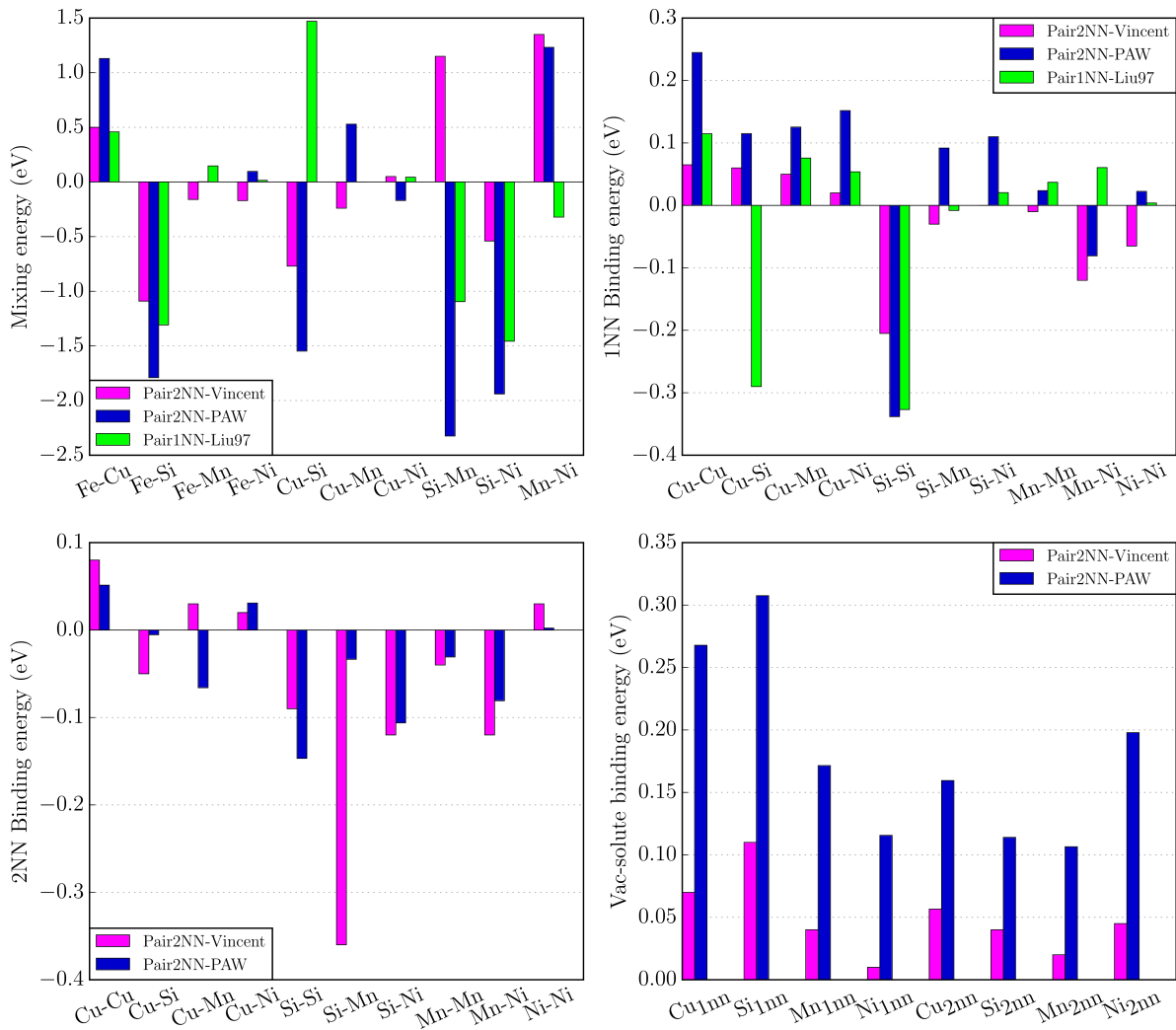


Figure 4-1: Enthalpy solution, 1NN solute-solute binding energies, 2NN solute-solute binding energies and vacancy-solute binding energies for different parameterizations.

The main differences between the parameterizations are given below:

- The “Pair1NN-Liu97” parameterization induces the formation of Mn-Ni clusters.
- The 1NN solute-solute binding energies are often lower with the “Pair2NN-Vincent” parameterization compared with the “Pair2NN-PAW” parameterization. Concerning the “Pair1NN-Liu97” version, the binding energies are usually between “Pair2NN-Vincent” and “Pair2NN-PAW” parameterizations (except for the $E_{b_{Cu-Si}}$ which become repulsive and for $E_{b_{Mn-Ni}}$ which become attractive).
- The 2NN solute-solute binding energies are often higher than the “Pair2NN-Vincent” parameterization compared with the “Pair2NN-PAW” parameterization.
- The Vac-Slt binding energies are always lower than the “Pair2NN-Vincent” parameterization.

4.2.2 Metropolis Monte Carlo simulations

In order to study the influence of the different parameterizations on the simulated microstructures, Metropolis Monte Carlo (MMC) simulations have been performed. The purpose was to compare the MMC results to the experimental results from Styman et al. [7]. In the study, a Fe-0.44Cu-1.66Ni-1.38Mn-0.75Si (at.%) steel thermally aged during 90000 hours at 638 K has been studied by APT. The simulations were performed under the same conditions. The box size was set to $60 \times 60 \times 60 a_0$ with PBC. At the end of all simulations, one cluster remains in the simulation box. Figure 4-2 presents the results and Figure 4-3 presents the shape of the clusters formed.

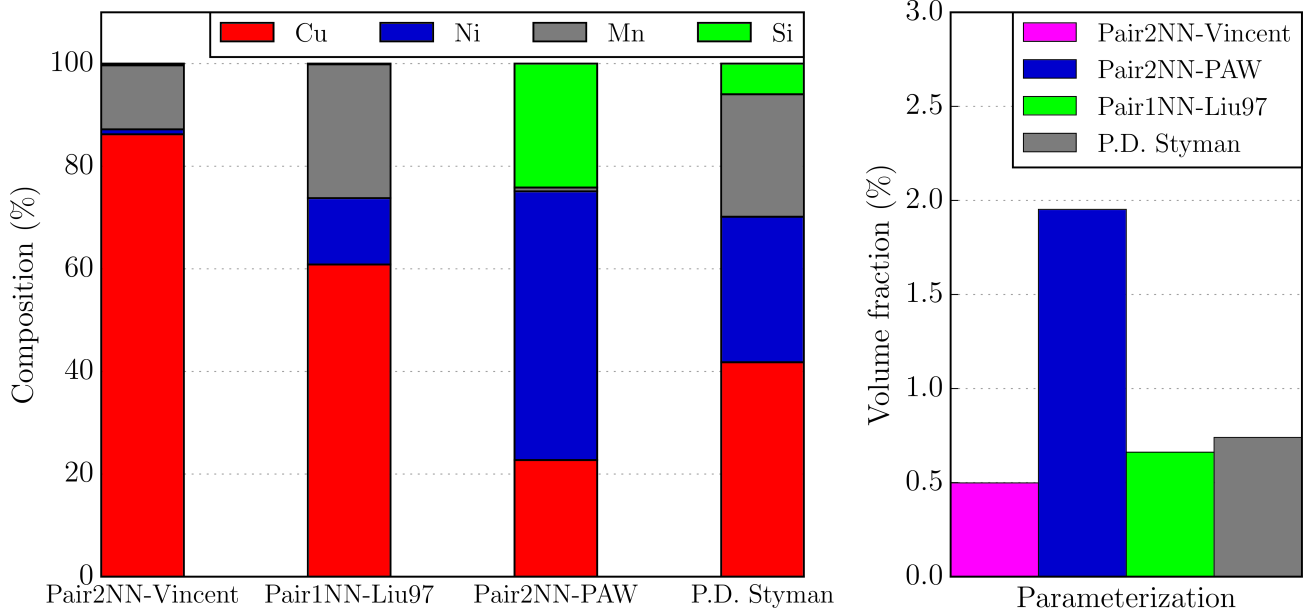


Figure 4-2: (left) Mean cluster composition obtained through MMC simulations using the different parameterizations. These results are compared to Styman et al. results [7]. (right) Volume fraction obtained using the different parameterizations.

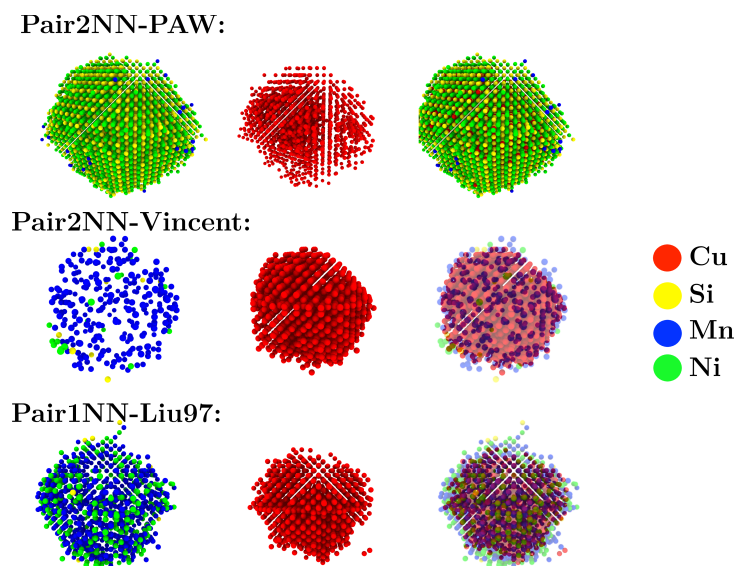


Figure 4-3: Shape of the cluster formed under MMC simulation on a Fe-0.44Cu-1.66Ni-1.38Mn-0.75Si (at.%) system at 638 K for the different parameterizations.

Observations made from these MMC simulations are listed below:

- The “Pair2NN-Vincent” parameterization underestimates the Si, Mn, and Ni contents of the cluster formed while it overestimates the Cu content.
- The “Pair1NN-Liu97” parameterization produces results that are closer to the experimental ones.
- The “Pair2NN-PAW” parameterization is the only parameterization that does not reproduce the Cu-core, Mn-Ni-Si –shell commonly mentioned in the literature for high copper RPV alloys (reported in section 1.3.4.2 of the first chapter).
- None of these parameterizations reproduce correctly the Si content of the cluster formed.

4.2.3 Kinetic aspects

To complete the previous MMC calculations, thermal ageing using the AKMC method has been performed under the same conditions. The thermal ageing simulation consists of placing one vacancy in the simulation box at a given temperature. The composition of the simulated material was Fe-0.44Cu-1.66Ni-1.38Mn-0.75Si (at.%) and the temperature has been fixed at 638 K. The vacancy formation energy used to adapt the KMC time was 1.6 eV using equation 2-59 presented in the second chapter. For the “Pair2NN-Vincent” and “Pair1NN-Liu97” parameterizations, the E_{a0} terms have been obtained using USPP DFT calculations. For the “Pair2NN-PAW” parameterization the E_{a0} terms have been obtained using PAW DFT calculations. These E_{a0} terms are presented in section 2.6.2.2 of the second chapter. Figure 4-4 and Figure 4-5 present the results.

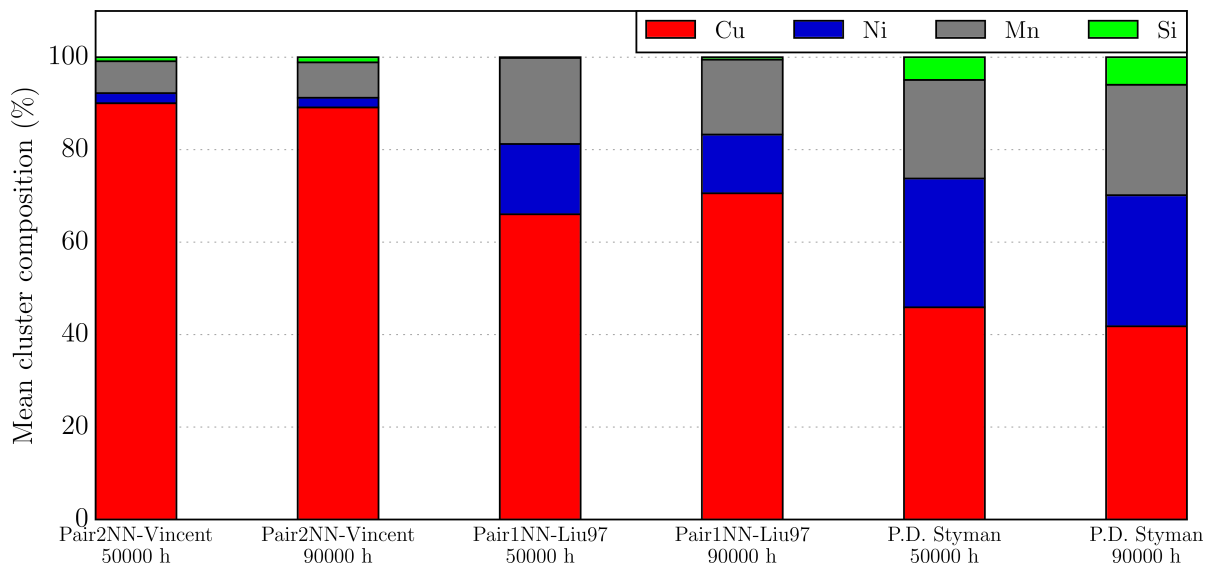


Figure 4-4: Mean cluster composition after thermal ageing for the different parameterizations. Experimental results from Styman et al. are also shown [7].

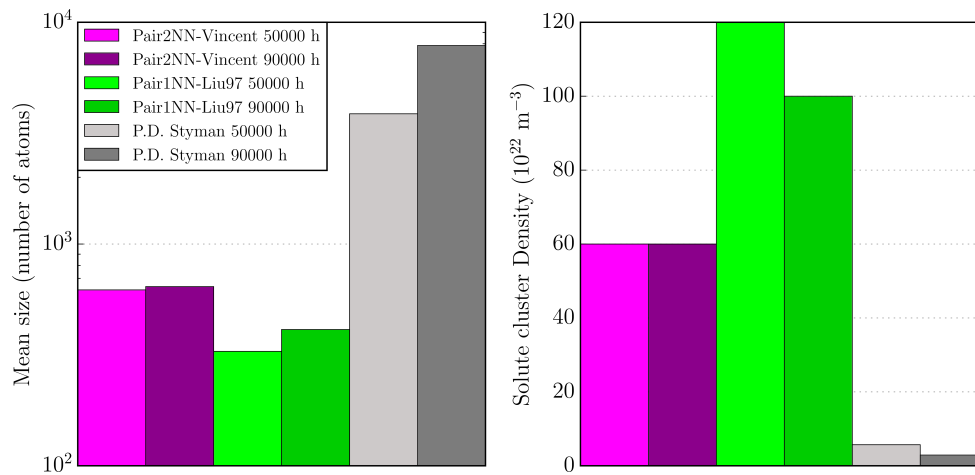


Figure 4-5: Mean cluster size (in number of atoms) and cluster density after thermal ageing for the different parameterizations. Experimental results are also provided [7].

The main observations are:

- Concerning the cluster compositions, the tendencies observed with AKMC are the same as the ones observed in the MMC simulations. The “Pair1NN-Liu97” parameterization provides the cluster compositions closest to the experimental ones.
- All the parameterizations overestimate the cluster density (by 1 or 2 orders of magnitude).
- All the parameterizations underestimate the mean size of the clusters.
- The “Pair2NN-PAW” parameterization does not allow observing the formation of solute-rich clusters (even after 90000 simulated hours). Indeed, the vacancy is quickly trapped by the surrounding solutes. In this state, the system no longer evolves.

4.2.4 Transport through vacancy mechanism

In his PhD thesis, Messina provides a direct comparison between the “Pair2NN-PAW” and the “Pair2NN-Vincent” parameterization for the transport of solutes via vacancy mechanism. The results suggest that drag occurs at 600 K only in the case of the “Pair2NN-PAW” parameterization and not for the “Pair2NN-Vincent” parameterization.

A direct comparison of migration energies predicted by DFT and the FISE model using “Pair2NN-Vincent” and “Pair2NN-PAW” is presented in Figure 4-6.

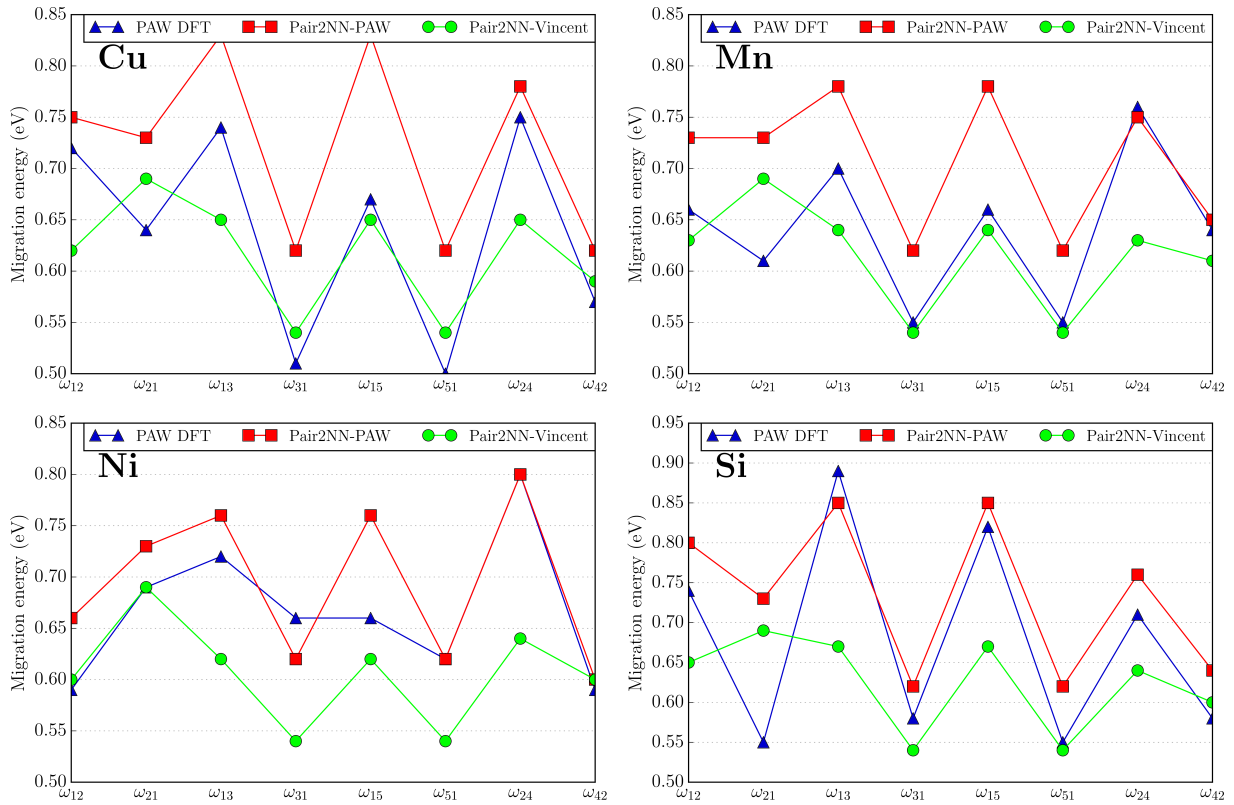


Figure 4-6: Migration energies predicted by the “Pair2NN-Vincent” and “Pair2NN-PAW” compared to the PAW DFT values. ω_{ij} corresponds to the migration of the vacancy from a i NN to a j NN distance from the solute.

Comparing the two AKMC parameterizations is difficult. In some cases, the “Pair2NN-Vincent” parameterization provides results closer to the DFT predictions. In other cases, the “Pair2NN-PAW” is closer. However, according to Messina et al. [6], the “Pair2NN-PAW” parameterization coupled with the FISE model is the only one that reproduces the tendencies given by the SCMF calculations [8]. Thus, this parameterization seems to be the most appropriate between the two.

4.2.5 Transport through SIA mechanism

Using the SCMF approach, L. Messina also investigated solute transport through interstitial mechanisms. Results from Messina et al. suggest that P and (to a lesser extent) Mn are transported by SIA. In order to compare our model to the analytical SCMF model, these types of calculations have been performed by AKMC using the “Pair2NN-Vincent” parameterization.

The partial diffusion coefficient ratios presented in chapter 2 were computed for the different solute atoms. One SIA and one solute atom are introduced in a $6 \times 6 \times 6$ a_0 Fe matrix with PBC. Non-overlapping moving averages have been computed to obtain the partial diffusion coefficient using n Means number of AKMC sequences containing n Steps AKMC steps. The moving average is computed on the fly. To get converged results, the n Steps and n Means parameters are adjusted and they depend on the solute. These two parameters are presented in Table 4-1 for the different solute atoms investigated.

	Cu		Si		Mn		Ni	
Temperature	nSteps	nMeans	nSteps	nMeans	nSteps	nMeans	nSteps	nMeans
600	5×10^3	4×10^6	5×10^3	2×10^6	2×10^5	1×10^5	5×10^3	2×10^6
900	5×10^3	4×10^6	5×10^3	2×10^6	2×10^5	1×10^5	5×10^3	2×10^6
1200	5×10^3	4×10^6	5×10^3	2×10^6	2×10^5	1×10^5	5×10^3	2×10^6
1600	5×10^3	4×10^6	5×10^3	2×10^6	2×10^5	1×10^5	5×10^3	2×10^6

Table 4-1: Number of AKMC step in a sequence (nSteps) and number of sequences (nMeans) performed to obtain a converged value for the partial diffusion coefficients.

Figure 4-7 presents the comparison between the AKMC and the analytical models.

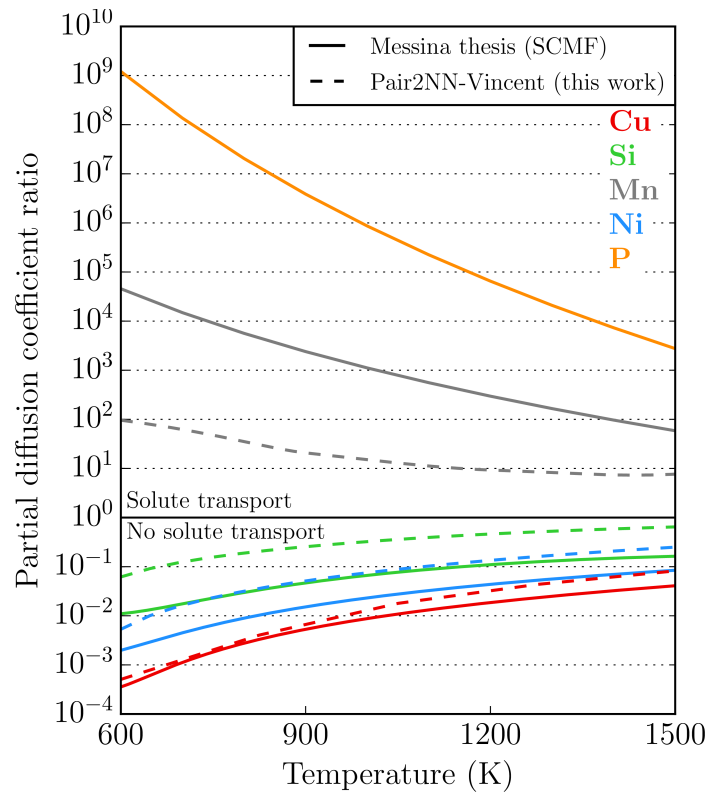


Figure 4-7: Partial diffusion coefficient ratio as a function of the temperature for different solutes.

For Cu, Ni and Si, neither SCMF nor AKMC predict transport through SIA mechanism. While differences exist between the two models, the relative order for the different partial diffusion coefficient ratios is reproduced. In agreement with the analytical model, the Mn solute is transported by the SIA but AKMC underestimates its efficiency in compared to SCMF. For P, the evaluation of the partial diffusion coefficient ratio was not possible by means of AKMC. The P atom always remained in the dumbbell. Hence, the L_{FeI}^I term in the partial diffusion coefficient ratio expression (e.g. $\frac{L_{XI}^I}{L_{FeI}^I}$) is null. This makes the calculation way too long to get a meaningful mean value. However, it is possible to conclude that the transport of the P atom through SIA is very efficient and that its partial diffusion coefficient ratio is much higher than the one of manganese.

4.2.6 Outcome of the parameterization comparison

All the results presented before indicate that the parameterization of the AKMC model remains an issue. Improving the prediction of a property is done by losing accuracy on another property. Indeed, it was shown in previous sections (4.2.2 and 4.2.3) that a pair model purely based on mixing energies (“Pair1NN-Liu97” parameterization) predicts realistic mean solute cluster composition as compared to the experiments. However, the solute cluster density is highly overestimated. Moreover, directly adding the binding energies from PAW DFT calculations (“Pair2NN-PAW” parameterization) prevents microstructure evolution while it allows describing the solute transport through vacancy mechanism. This is due to high trapping effects between the vacancy and the solutes. This shows that the “Pair2NN-PAW” parameterization is not suitable for thermal ageing simulations (in FeCu as well as RPV model alloys) in agreement with the experiments. Despite the kinetic limitations of the “Pair2NN-PAW” parameterization, an efficient transport of the solutes through vacancy mechanism might be an important element to improve the prediction of the AKMC model.

The main issue is the transferability of DFT results to a 2NN pair interaction model. The total binding energy of a configuration (e.g. a cluster) is a suitable quantity to compare the stability of different objects. For a configuration containing A_i objects the binding energy is written as [9]:

$$E_b^{tot}(A_1, A_2, \dots, A_n) = [E(\sum A_i) + (n - 1)E_{ref}] - \sum_i^n E(A_i) \quad \text{Equation 4-1}$$

where E_{ref} corresponds to the energy of the supercell without any objects, $E(A_i)$ is the energy of the supercell containing only the object A_i and $E(\sum A_i)$ is the energy of the supercell containing all the interacting objects.

Figure 4-8 shows the evolution of the total binding energy for several Cu cluster sizes in iron. PAW DFT predictions are compared to those of the “Pair2NN-PAW” parameterization.

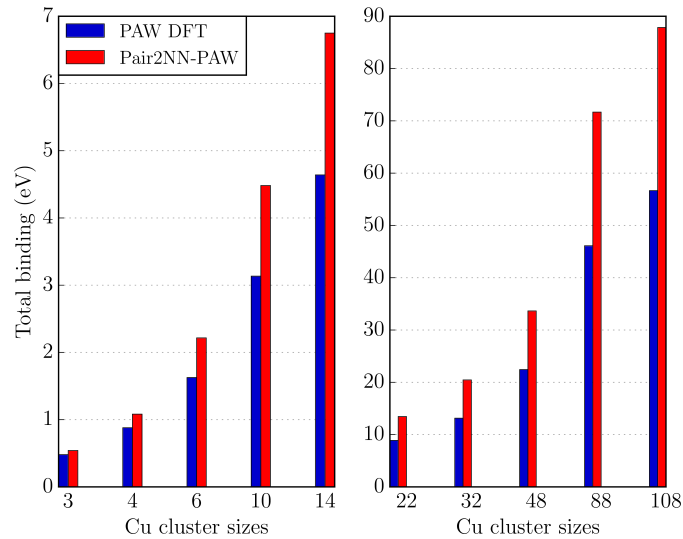


Figure 4-8: Evolution of the total binding energy for different sizes of Cu clusters using PAW DFT and the “Pair2NN-PAW” parameterization.

While the Cu-Cu pair binding energies are strictly equal for the two models, the larger the cluster size, the more the “Pair2NN-PAW” parameterization overestimates the total binding energies (. It appears thus that the current formalism for the pair interaction model has reached its limits. A natural attempt to solve this problem is to go beyond “pairs”. Using triplets (presented in section 2.3.2 of the second chapter) would seem to be a

good choice and we have tested this. Figure 4-9 presents a comparison between PAW DFT, “Pair2NN-PAW” parameterization and a triplet model from the cluster stability point of view.

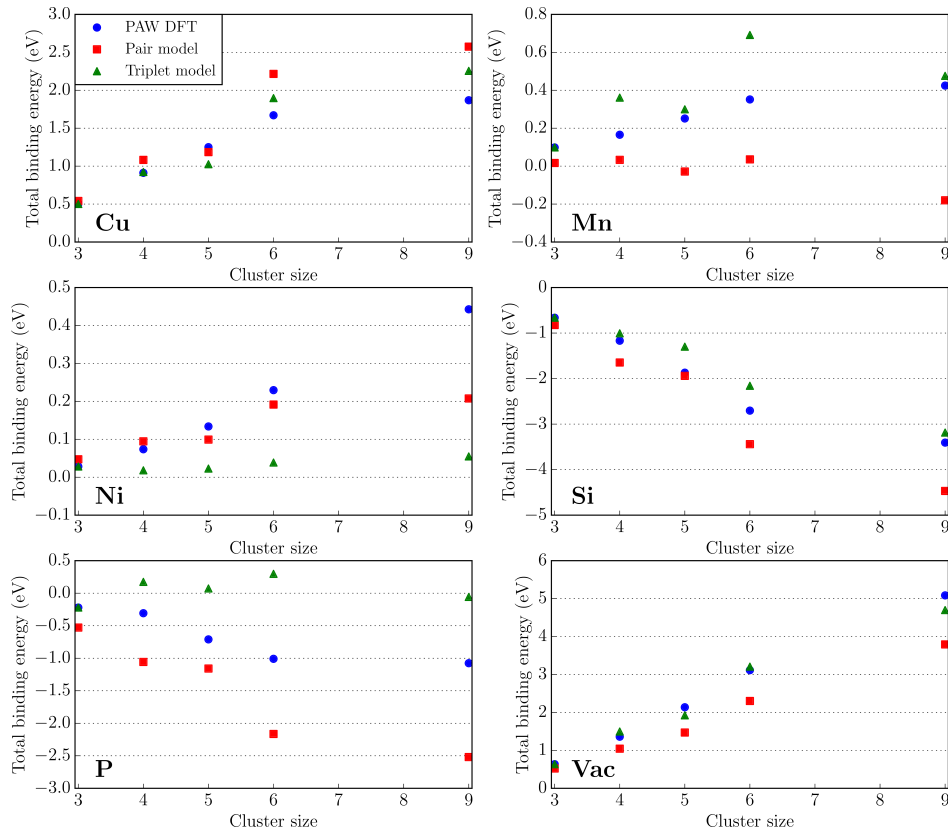


Figure 4-9: Total binding energies predicted by different cohesive models for different pure clusters in iron.

For Cu clusters, using triplet interactions instead of pair interactions gives results closer to those predicted by PAW DFT. As concerns Mn clusters, the situation is more complex. Triplets tend to overestimate the stability of these clusters while pairs underestimate it. Pairs also appear to provide a better description of Ni clusters. For the Si and vacancy clusters, both models predict the good tendencies. Finally, the pair interaction model provides tendencies closer to PAW DFT in the case of P clusters.

As a conclusion, the assessment of this pair/triplet interaction comparison is not trivial and the superiority of a triplet interaction model over a pair interaction model is not that clear. Furthermore, going beyond triplet might be too complex since it requires hundreds of parameters. Hence, a new formalism for the pair interaction model has been developed.

4.3 Development of a concentration dependent parameterization

The new parameterization has been developed in order to improve the following two points:

- Reproduce the transport mechanism through a vacancy mechanism predicted by PAW DFT calculations.
- Allow for the formation of Manganese-Nickel precipitates (MNPs).

This new model is inspired by the model employed in Senninger PhD work [10] for the study of the Fe-Cr system. Our new model is named “Concentration Dependent Pairs” (CDP).

4.3.1 Principle of the CDP approach

The main idea is to make the pair interactions v_{ij} dependent on the surrounding environment of the species i and j . To do so, two sets of 2NN pair interaction parameters are used for the two limiting cases called the dilute and concentrated cases. At this stage, two main parameters are introduced in the model:

- v_{ij}^{Dilute} corresponds to the set of pair interaction in the dilute case
- $v_{ij}^{Cluster}$ corresponds to the set of pair interaction in the concentrated case

The v_{ij}^{Dilute} parameters are used to provide pair binding energies that are comparable to those computed with DFT. The $v_{ij}^{Cluster}$ parameters are used to avoid the overestimation of the cluster binding energies when increasing the size and are adjusted on cluster stabilities predicted by PAW DFT. The last parameter that is required is a mathematical expression that connects the dilute and the concentrated case. It depends on the local concentration α_{ij} . A new parameter called β is introduced. It allows defining the shape of the curve used to extrapolate values between the two limiting cases using the following formula:

$$\varepsilon_{ij} = (v_{ij}^{Cluster} - v_{ij}^{Dilute})\alpha_{ij}^{\beta} + v_{ij}^{Dilute} \quad \text{Equation 4-2}$$

$\alpha \in [0,1]$ and represents the local concentration, $v_{ij}^{Cluster}$ corresponds to the targeted pair interaction in the concentrated case (when $\alpha=1$) and v_{ij}^{Dilute} corresponds to the pair interaction in the dilute case (when $\alpha=0$).

Hence, the energy of site i can be expressed as follows:

$$E_i = \frac{1}{2} \sum_{j=1}^8 (v_{ij}^{Cluster_{1nn}} - v_{ij}^{Dilute_{1nn}}) \alpha_{ij}^{\beta} + v_{ij}^{Dilute_{1nn}} + \frac{1}{2} \sum_{j=1}^6 (v_{ij}^{Cluster_{2nn}} - v_{ij}^{Dilute_{2nn}}) \alpha_{ij}^{\beta} + v_{ij}^{Dilute_{2nn}} \quad \text{Equation 4-3}$$

For simplicity, we chose $\beta=1$. The energy of site i can be re-expressed as:

$$E_i = \frac{1}{2} \sum_{j=1}^8 v_{ij}^{Dilute_{1nn}} (1 - \alpha) + v_{ij}^{Cluster_{1nn}} \alpha + \frac{1}{2} \sum_{j=1}^6 v_{ij}^{Dilute_{2nn}} (1 - \alpha) + v_{ij}^{Cluster_{2nn}} \alpha \quad \text{Equation 4-4}$$

Figure 4-10 illustrates the principle of the CDP method in the case of binding energies.

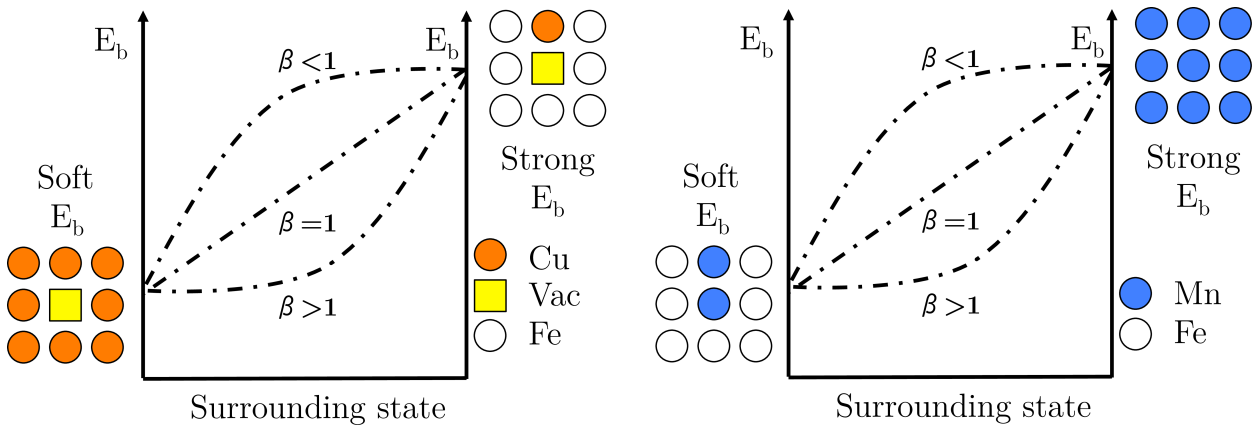


Figure 4-10: Evolution of the binding energies Vac-Cu (left) and Mn-Mn (right) depending on the local environment. Several shape of curves are proposed to link the two limiting cases.

Since there is not one universal method to define a concentration, choices have to be made. In the CDP model, α is defined as the concentration around the i - j pair, hence, similar to a “bound” approach (since the concentration is defined around two sites). It is also important to note that the atoms constituting the pair are not counted in the α calculation. A convenient way to define α is:

$$\alpha_{ij} = 1 - \frac{(13 - Coord_i) + (13 - Coord_j)}{26} \quad \text{Equation 4-5}$$

where $Coord_i$ is the number of 1NN+2NN solute atoms and point defects around i (excluding j).

In this formula, any species (excluding i or j) that is not Fe contribute to 1 in the $Coord_x$ calculation. This is the case regardless of the type of the solute atom/PD on site i/j . This expression is convenient because it simplifies the parameterization adjustments. Figure 4-11 presents the evolution of the binding energies for this approach.

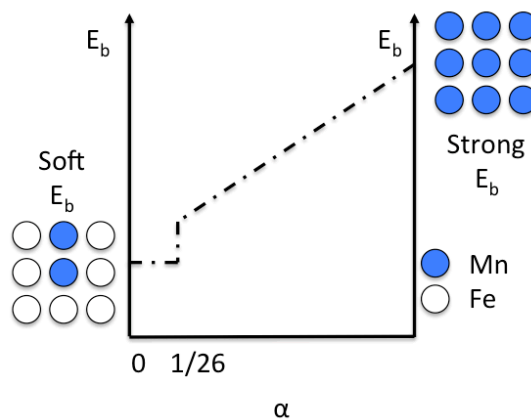


Figure 4-11: Schematic diagram for the CDP approach.

The main problem with this definition of α is that it induces “double counting” of some atomic sites. Figure 4-12 presents the sites that are counted twice around a 1NN and 2NN pair.

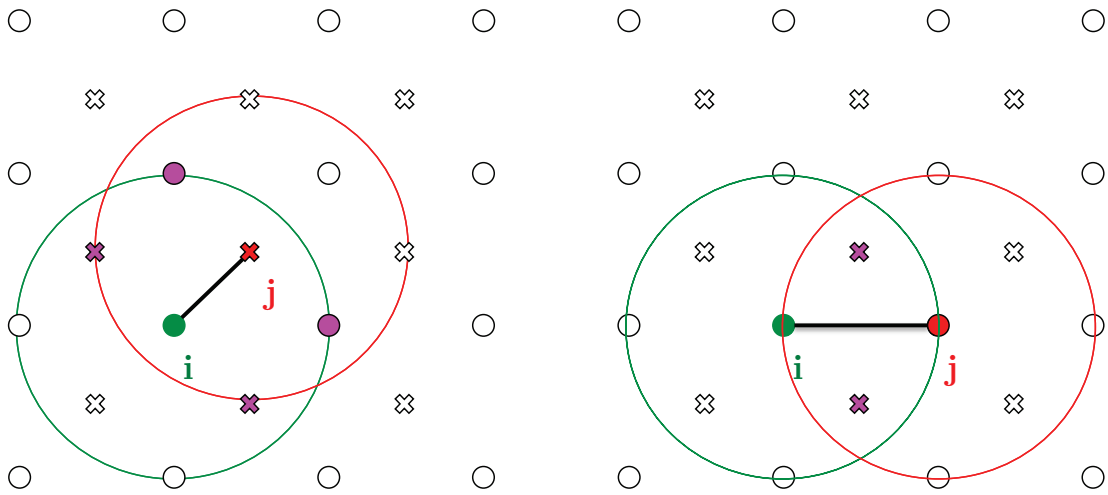


Figure 4-12: 1NN+2NN sites around the ij pair in a BCC lattice (1nn pair on the left and 2nn pair on the right). The colored circles correspond to the 2NN distance range. Sites that are counted twice are displayed in magenta.

It turns out that this “double counting” has little impact on the results and the method is acceptable to estimate the versatility/flexibility of the new model. Figure 4-13 presents the different α associated with each pair in the case of an interface. Two counting methods are compared: the “double counting” method and the true number of solutes around the pairs (excluding the pair itself).

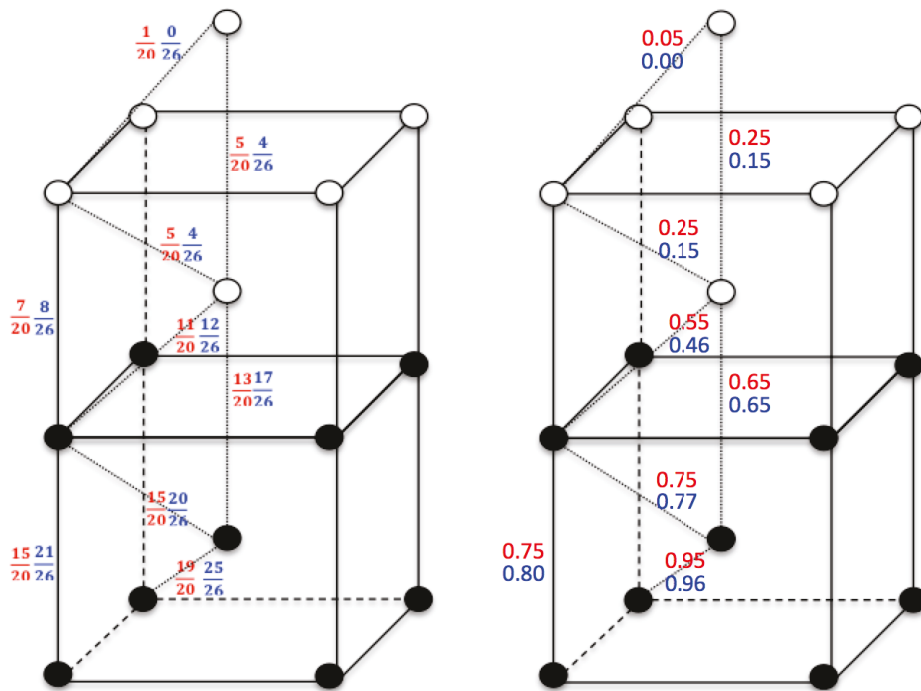


Figure 4-13: Concentration (α) with the double counting method (blue) and the true number of solutes around pairs (red). Fractional form is presented on the left and decimal form on the right. The numbers are placed near i - j pairs.

As Figure 4-13 shows, the double counting method does not introduce large bias. For this reason, it has been employed with the CDP model and all the results produced in this thesis with the CDP model have been obtained with this approach.

Using this new cohesive model, the formation energy of the vacancy in X (with $X \neq \text{Fe}$) is given by:

$$E_f(\text{Vac} - X) = 8\epsilon_{X-\text{Vac}}^{1nn}(1) + 6\epsilon_{X-\text{Vac}}^{2nn}(1) - 4\epsilon_{X-X}^{1nn}(1) + 3\epsilon_{X-X}^{2nn}(1) \quad \text{Equation 4-6}$$

where values in brackets correspond to values of α (ϵ being a function of α as shown in Equation 4-2).

The cohesive energy is:

$$E_{coh}(X \neq \text{Fe}) = 4\epsilon_{X-X}^{1nn}(1) + 3\epsilon_{X-X}^{2nn}(1) \quad \text{Equation 4-7}$$

The mixing energy is:

$$E_{mix}(X - \text{Fe}) = 8\epsilon_{\text{Fe}-X}^{1nn}(0) + 6\epsilon_{\text{Fe}-X}^{2nn}(0) - 4\epsilon_{\text{Fe}-\text{Fe}}^{1nn}(0) - 3\epsilon_{\text{Fe}-\text{Fe}}^{2nn}(0) - 4\epsilon_{X-X}^{1nn}(1) - 3\epsilon_{X-X}^{2nn}(1) \quad \text{Equation 4-8}$$

The 1NN binding energy is:

$$Eb_{X-Y}^{1nn} = -\epsilon_{\text{Fe}-\text{Fe}}^{1nn}(0) - \epsilon_{X-Y}^{1nn}(0) + 4\epsilon_{\text{Fe}-X}^{1nn}(0) - 3\epsilon_{\text{Fe}-X}^{1nn}\left(\frac{1}{26}\right) + 3\epsilon_{\text{Fe}-X}^{2nn}(0) - 3\epsilon_{\text{Fe}-X}^{2nn}\left(\frac{1}{26}\right) + 4\epsilon_{\text{Fe}-Y}^{1nn}(0) - 3\epsilon_{\text{Fe}-Y}^{1nn}\left(\frac{1}{26}\right) + 3\epsilon_{\text{Fe}-Y}^{2nn}(0) - 3\epsilon_{\text{Fe}-Y}^{2nn}\left(\frac{1}{26}\right) \quad \text{Equation 4-9}$$

The 2NN binding energy is:

$$Eb_{X-Y}^{2nn} = -\epsilon_{\text{Fe}-\text{Fe}}^{2nn}(0) - \epsilon_{X-Y}^{2nn}(0) + 4\epsilon_{\text{Fe}-X}^{1nn}(0) - 4\epsilon_{\text{Fe}-X}^{1nn}\left(\frac{1}{26}\right) + 1\epsilon_{\text{Fe}-X}^{2nn}(0) + 4\epsilon_{\text{Fe}-Y}^{1nn}(0) - 4\epsilon_{\text{Fe}-Y}^{1nn}\left(\frac{1}{26}\right) + 1\epsilon_{\text{Fe}-Y}^{2nn}(0) \quad \text{Equation 4-10}$$

Comment:

In a more complex model, the way to count around site i could depend on the species on site i . For example, if site i corresponds to a manganese, the calculation of α could be done by counting only the number of Mn+Ni around i .

4.3.2 Parameterization strategies

Two approaches have been developed in order to parameterize the CDP model. The first one (called CDP- β) has been made to keep the adaptability of a “classic pair interaction model” (where adjustments can be made “by hand”). The second one corresponds to a numerical method developed in a library called *speed-check* (see Annex VI for more details).

“CDP- β ” parameterization:

Since the number of parameters is doubled using the CDP method, adjusting the parameterization “by hand” is quite complex. Figure 4-14 presents the procedure and the assumptions that have been made.

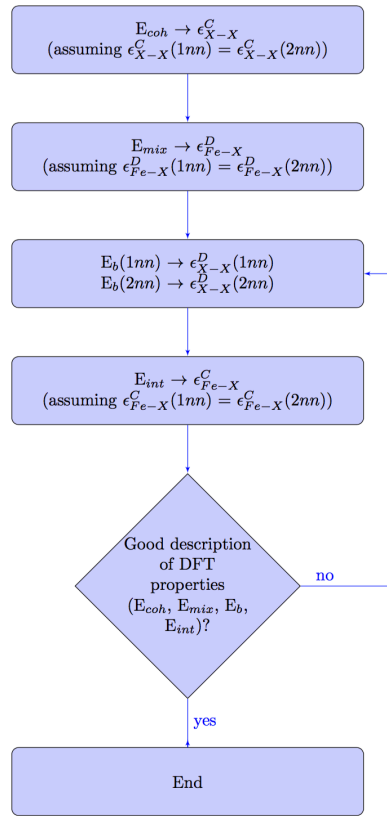


Figure 4-14: CDP- β procedure for the parameterization of the CDP cohesive model.

According to Figure 4-14, fixing E_{coh} , E_{mix} and E_b makes the parameterization approach simple. The only free parameters are indeed $\varepsilon_{\text{Fe-X}}^{\text{Cluster}_{1nn}}$, $\varepsilon_{\text{X-X}}^{\text{Dilute}_{1nn}}$ and $\varepsilon_{\text{X-X}}^{\text{Dilute}_{2nn}}$.

While this method leads to a major improvement (e.g. being able to choose E_{coh} , E_b , E_{int} and E_{mix}), MMC simulations lead to a microstructure that is not in agreement with the experimental observations since no solute atoms remain in the solid solution. Figure 4-15 presents this microstructure for the RPV type alloy (Fe-0.44Cu-1.66Ni-1.38Mn-0.75Si at.%) at 563 K simulated by MMC in a $60 \times 60 \times 60 a_0$ box with PBC.

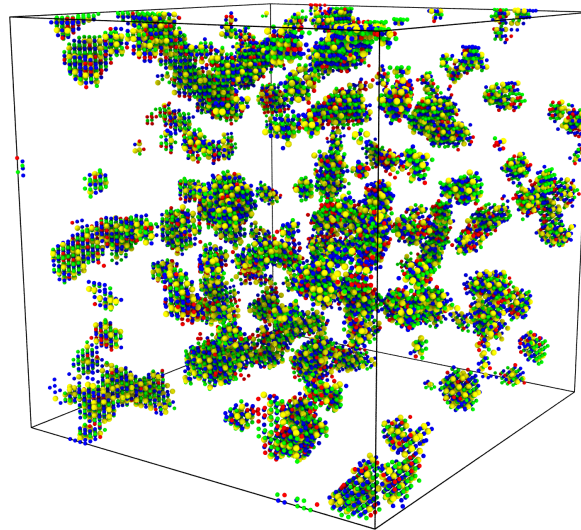


Figure 4-15: Simulated microstructure by MMC using the CDP- β parameterization on a Fe-0.44Cu-1.66Ni-1.38Mn-0.75Si at.% system at 563 K. Cu, Si, Mn and Ni atoms respectively correspond to the red, yellow, blue and green spheres.

Since the CDP- β strategy requires making some assumptions in order to reduce the large number of parameters, numerical methods that explore the parameter space may be advantageous. Moreover, a numerical tool can be used to match not only fundamental properties such as E_{coh} , E_{mix} , E_b and E_{int} but also solute cluster stabilities predicted by PAW DFT. Matching the solute cluster properties “by hand” was very difficult and this may explain the microstructure presented in Figure 4-15.

The numerical method developed is the subject of the following section. This parameterization will be referred to as CDP.

CDP parameterization:

Adjusting the CDP parameterization without numerical tools is difficult. Moreover it requires making several assumptions that restrict the number of degree of freedom of the model (the free parameters were only $\epsilon_{Fe-X}^{Cluster1nn}$, $\epsilon_{X-X}^{Dilute1nn}$ and $\epsilon_{X-X}^{Dilute2nn}$). Hence, a numerical way to explore the parameterization has been developed based on a brute-force search. First we focused on the binary systems (FeCu, FeMn and FeNi). The method relies on a grid exploration in the parameter space of our new cohesive model. The advantage of this method is that no assumption has to be made on the 1NN/2NN balance. The method behaves like this:

- Values for $E_{coh}(X \neq Fe)$, $E_{mix}(X - Fe)$, Eb_{X-X}^{1nn} and Eb_{X-X}^{2nn} are fixed. The $\epsilon_{Fe-Fe}^{1nn/2nn}(0)$ and $\epsilon_{Fe-Fe}^{1nn/2nn}(1)$ are supposed equal and correspond to the BCC iron cohesive energy.
- Since $E_{coh}(X \neq Fe)$ is fixed, giving a value to $\epsilon_{X-X}^{1nn}(1)$ automatically provides the $\epsilon_{X-X}^{2nn}(1)$ value.
- It is also valid for the $\epsilon_{Fe-X}^{2nn}(0)$ since the mixing energy is fixed.
- The free parameters are $\epsilon_{X-X}^{1nn}(1)$, $\epsilon_{Fe-X}^{1nn}(0)$, $\epsilon_{Fe-X}^{1nn}(1)$, $\epsilon_{Fe-X}^{2nn}(1)$.
- For given values of the free parameters, $\epsilon_{X-X}^{1nn}(0)$ and $\epsilon_{X-X}^{2nn}(0)$ are given by the fixed binding energies.

For the adjustment of free parameters, every set of combination of $\epsilon_{X-X}^{1nn}(1)$, $\epsilon_{Fe-X}^{1nn}(0)$, $\epsilon_{Fe-X}^{1nn}(1)$, $\epsilon_{Fe-X}^{2nn}(1)$ varying from -1 to 0 with a step of 0.02 have been tested (note that the step used for the $\epsilon_{X-X}^{1nn}(1)$ interactions has been set to 0.1). This corresponds to ~1 million parameterizations tested for each binary system.

This procedure leads to a large number of parameterizations that can satisfy the input values. The choice of the parameterization is then performed by comparing the binding energies (presented in section 4.2.6) of solute clusters predicted by the parameterization to PAW DFT results. Figure 4-16 presents the different cluster geometries used to choose the parameterization from the cluster stability point of view.

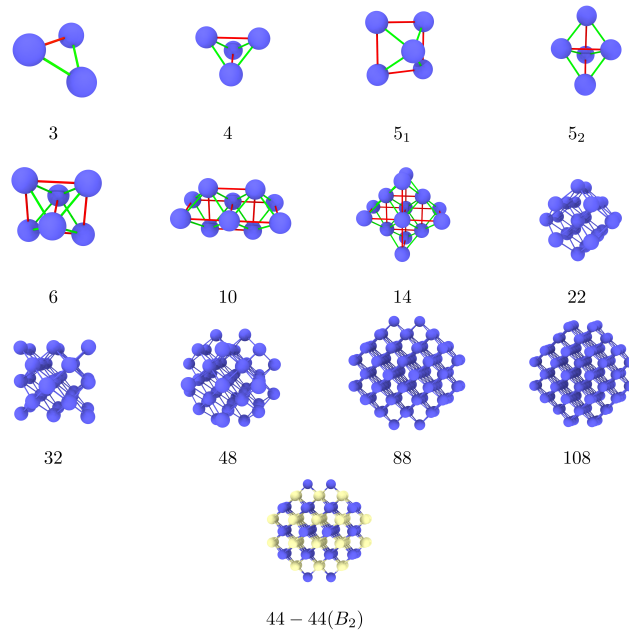


Figure 4-16: Nomenclature used for the different clusters studied. The number associated to the cluster corresponds to its size (in number of atoms) except for the B_2 cluster. When the number of atoms is not too high, the 1NN bonds are displayed in green while the 2NN bounds are in red. 44-44(B_2) stands for a mixed solute cluster that complies with the B_2 structure (the A atoms are displayed in blue while the B atoms are in yellow). In binary systems, this cluster stands for a “dilute” Fe-X cluster. This cluster is useful to adjust 2NN interactions (since there are only 2NN solute-solute interactions).

The following sections analyze the stabilities of the clusters obtained. These results are also compared to those obtained with “Pair2NN-Vincent”, “Pair2NN-PAW” and “Pair1NN-Liu97” parameterizations.

4.3.3 Parameterization of the binary systems

4.3.3.1 The FeCu system

First, the FeCu system parameterization is discussed. MMC simulations have been performed in a $60 \times 60 \times 60 a_0$ box on a Fe-0.44Cu (at.%) at 563 K using a parameterization obtained with the CDP procedure. The cluster geometries predicted were not spherical. Figure 4-17 illustrates these observations.

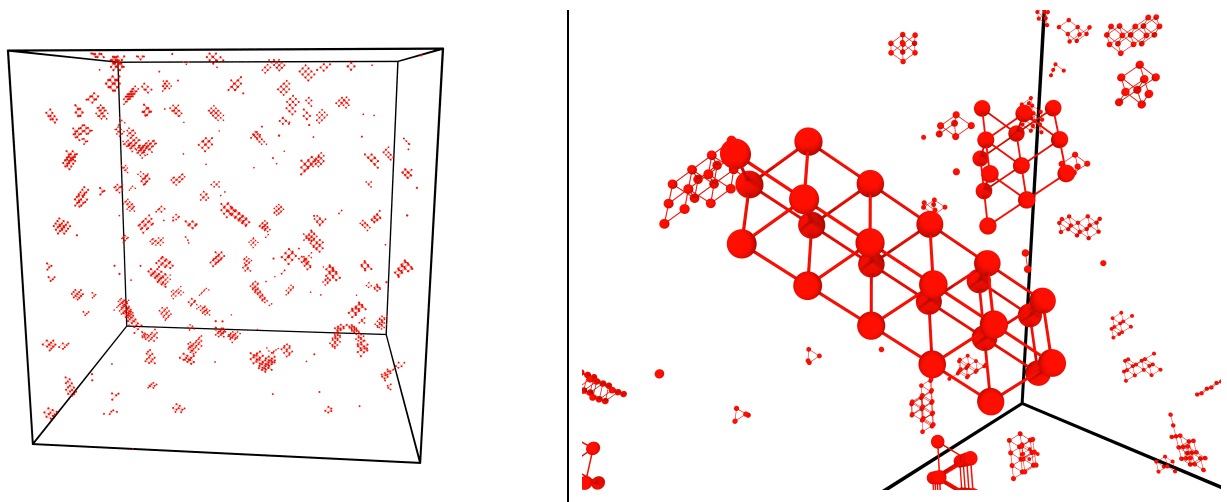


Figure 4-17: Typical microstructure observed with the CDP parameterization using MMC simulations in the FeCu system (left). Zoom on the not spherical Cu cluster geometries obtained (right).

The results obtained using the MMC simulations show that a refinement of the method is required. This suggests that the interface energy (110) needs to be employed to select a parameterization.

Taking into account that the (110) interface energy should be close to the (001) interface energy in the parameter selection, we obtain a parameterization, which predict spherical Cu clusters geometries. This issue has already been encountered by Vincent [2]. Figure 4-18 presents the microstructure obtained by MMC for the Fe-0.44Cu at.% system at 563 K. The predicted interface energies for the (001) and (110) orientation are respectively 295 and 285 mJ/m². According to USPP DFT calculations, these quantities are 370 (for the (100) interface) and 359 (for the (110) interface) mJ/m² [11]. Hence, the values predicted by the CDP model appear to be in agreement with DFT.

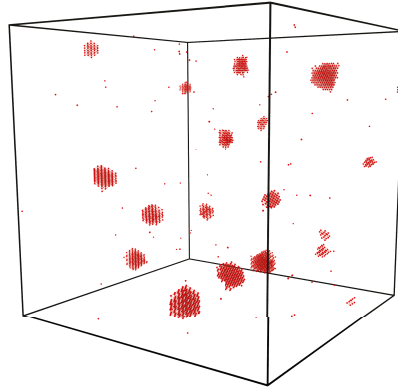


Figure 4-18: MMC simulated microstructure in the Fe-0.44Cu at.% system at 563 K when the parameterization takes the (110) interface energy into account.

Figure 4-19 presents the comparison between the different pair interaction models and the PAW DFT results.

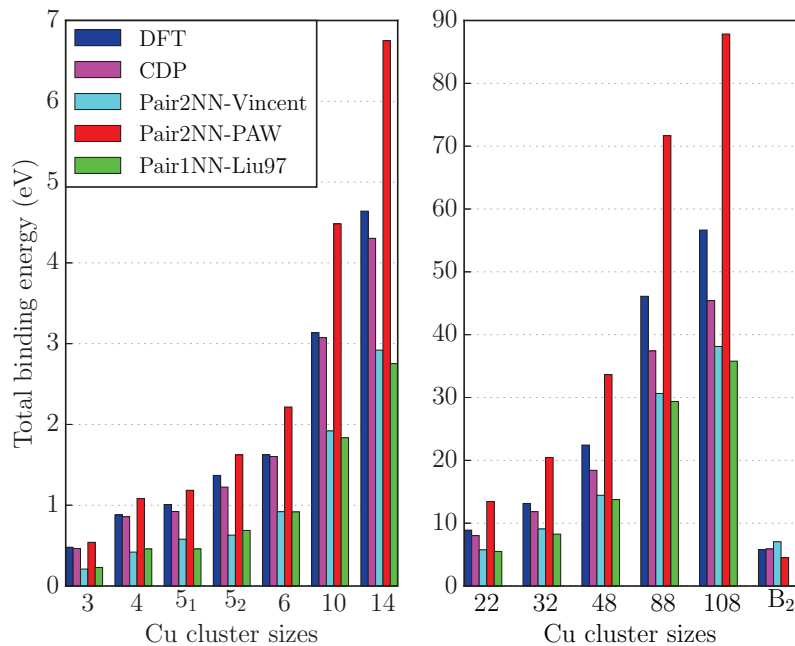


Figure 4-19: Total binding energies for different Cu cluster sizes. B₂ stands for the 44–44(B₂) cluster presented in Figure 4-16.

In comparison to PAW DFT calculations, the standard pair interaction model (“Pair2NN-Vincent”) tends to underestimate the stabilities of Cu clusters. This effect was predictable since the parameterization was made using USPP DFT calculations, which tend to be less binding than PAW DFT [2]. Using the PAW binding energies directly as the only input parameters (“Pair2NN-PAW”) leads to a large overestimation of the Cu cluster stability. The thermodynamic based parameterization (“Pair1NN-Liu97”) provides similar results to the “Pair2NN-Vincent” parameterization. The CDP model seems to improve the description of these objects by predicting the closest results to the PAW DFT for the small Cu clusters without becoming too binding on the largest objects. Since copper precipitation was well reproduced with the “Pair2NN-Vincent” parameterization, the choice has been made not to choose values too different in the CDP model.

4.3.3.2 The FeMn, FeNi and FeSi systems

MMC simulations at 600 K have also been used for the parameterization of the FeMn, FeNi and FeSi binary systems. The alloy contents of the binaries have been chosen to correspond to the typical content of the elements in the RPV type material (Fe-1.4Mn, Fe-0.7Ni and Fe-0.5Si at.%). For the FeMn and FeNi systems, the parameterization selected predicts the precipitation of the Mn/Ni in pure iron. Figure 4-20 illustrates this observation in the case of a low Mn alloy (pure Fe-0.4Mn at.% at 563 K).

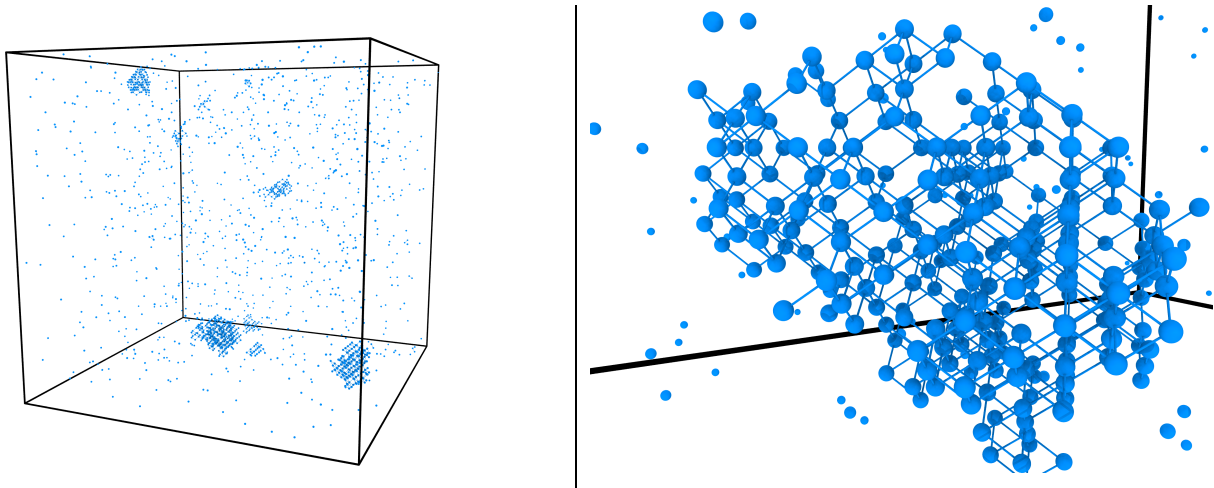


Figure 4-20: Equilibrium microstructure predicted by the MMC simulation in a $60 \times 60 \times 60 a_0$ box for the Fe-0.4Mn at.% alloy at 563 K (left) as well as the cluster structure observed (right).

The Mn clusters observed are “dilute” clusters (50%Mn and 50%Fe). The typical structure of these clusters is presented in Figure 4-21. We refer to this cluster structure as ‘diamond type’.

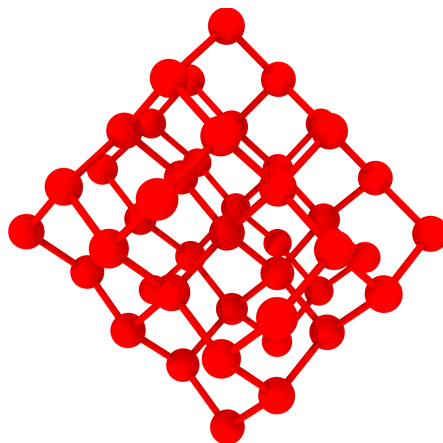


Figure 4-21: Typical structure predicted by the MMC simulation in in Fe-0.4Mn at.% at 563 K. Only solute atoms and 1NN bounds are displayed. The solute at the center of the structure has four 1NN solute atoms and six 2NN Fe atoms.

The same observation has been made in the case of the FeNi system. Those results are not in agreement with the phase diagram [12] and with PAW DFT calculations. According to PAW DFT, the total binding energies of the 44Fe-44Mn/Ni diamond type clusters are 2.54 and 2.47 eV respectively for the Mn and Ni. Hence, the diamond type structure of the clusters appears to be an artifact of the cohesive model. Thus, this structure has been removed from the numerical searching method. Excluding this structure, the parameterization selected predicts low total binding for the 80 Mn/Ni cluster in diamond type structure (-1.98 eV in the case of Mn and 0.74 eV for the Ni cluster). The only compromise that has to be done to predict reasonable stabilities of the clusters (in comparison with PAW DFT) was made on the (001) Fe/X interface energies (81 mJ/m² in the case of Mn and -36 mJ/m² for the Ni). This might not be an issue since the total binding energies of the clusters are well reproduced.

Figure 4-22 and Figure 4-23 present the predicted Mn/Ni cluster stabilities for different cohesive models.

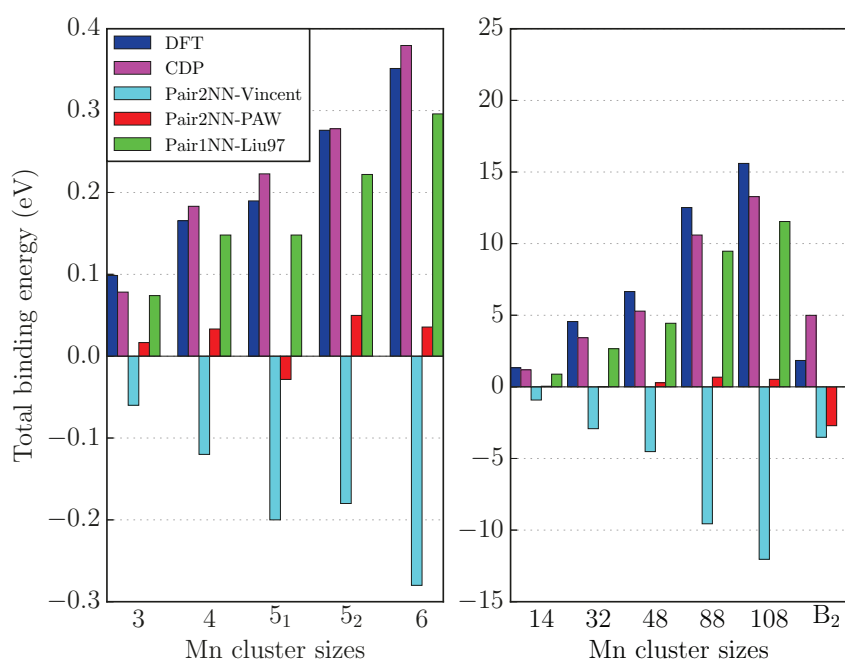


Figure 4-22: Total binding energies for different Mn cluster sizes. B₂ stands for the 44–44(B₂) cluster presented in Figure 4-16.

The standard pair interaction model (“Pair2NN-Vincent”) predicts that Mn clusters are unstable. This can be explained by the repulsive E_b used in this parameterization as well as the negative solution enthalpy. While the total binding energies are low in comparison with those obtained in the FeCu system, PAW DFT calculations predict Mn clusters to be stable. As in the case of Cu clusters, using directly the E_b from PAW DFT does not allow to reproduce well the stability of solute clusters. The “Pair1NN-Liu97” parameterization agrees well with the PAW DFT predictions. Concerning the CDP model, the choice has been made to slightly overestimate the stability of small Mn clusters (from size 4 to 6) in order to get a better description of the largest clusters.

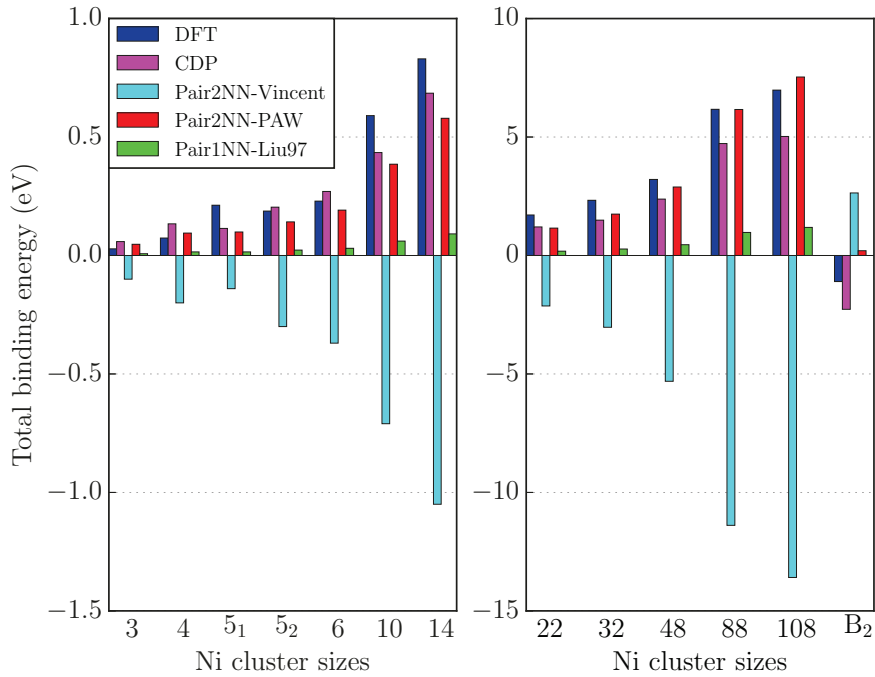


Figure 4-23: Total binding energies for different Ni cluster sizes. B₂ stands for the 44–44(B₂) cluster presented in Figure 4-16.

From the “Pair2NN-Vincent” parameterization point of view, the observations on the FeNi system are the same as for the FeMn system. However, in this case, the stability of the Ni clusters is underestimated using the “Pair1NN-Liu97” parameterization. In this system, the “Pair2NN-PAW” parameterization seems to be an acceptable approach. For the CDP parameterization, the choice has been made to slightly overestimate the stability of the small Ni clusters to improve the prediction on larger ones (like what has been done in the FeMn case).

Results concerning the Si in the CDP model are presented Figure 4-24. In this case, there is a global agreement between all the parameterizations. Si clusters are indeed always unstable and the Si atoms remain in solid solution during MMC simulation at 563 K in the Fe-0.5Si (at.%) system.

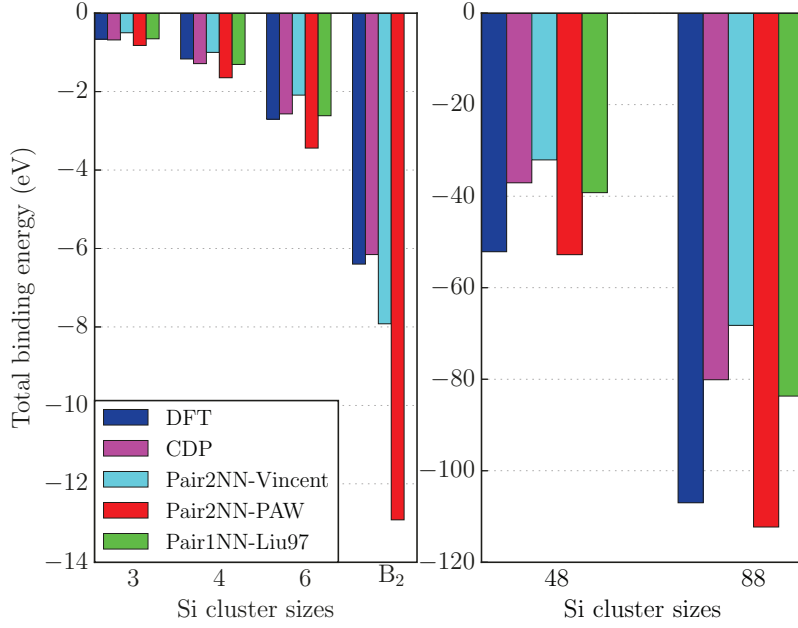


Figure 4-24: Total binding energies for different Si cluster sizes. B₂ stands for the 44–44(B₂) cluster presented in Figure 4-16.

4.3.4 Parameterization of the ternary/ quaternary systems

Selecting the set of parameters for the ternary system is easier more straightforward than in the binary case. There are only four parameters to fix: $\epsilon_{X-Y}^{1nn}(0)$, $\epsilon_{X-Y}^{2nn}(0)$, $\epsilon_{X-Y}^{1nn}(1)$ and $\epsilon_{X-Y}^{2nn}(1)$.

- The $\epsilon_{X-Y}^{1nn}(0)$ and $\epsilon_{X-Y}^{2nn}(0)$ parameters are provided by the PAW DFT pair binding energies.
- The $\epsilon_{X-Y}^{1nn}(1)$ and $\epsilon_{X-Y}^{2nn}(1)$ parameters are chosen to suit the targeted mixing energies (those employed in the “Pair1NN-Liu97” parameterization). The only free variable is the balance between the 1NN and 2NN interactions.

The E_b as well as the E_{mix} are fixed. The only free parameter is $\epsilon_{X-Y}^{1nn}(1)$ (because providing a value to $\epsilon_{X-Y}^{1nn}(1)$ directly gives a value to $\epsilon_{X-Y}^{2nn}(1)$ since the mixing energy is fixed). Around 1000 parameterizations have been tested. The value of $\epsilon_{X-Y}^{1nn}(1)$ that provided a realistic prediction of cluster stabilities corresponds to the chosen parameter. Figure 4-25 presents the different clusters geometries used to for the clusters in this step of the parameterization.

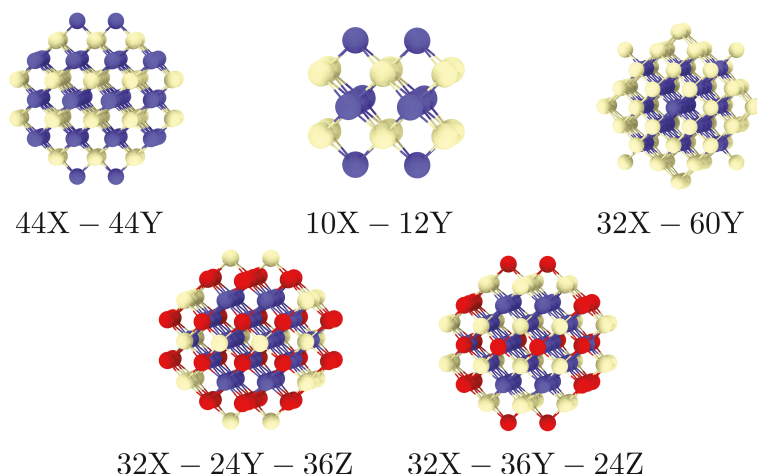


Figure 4-25: Clusters considered for the ternary/quaternary parameterization. X atoms are printed in blue, Y atoms in yellow, Z atoms in red.

The PAW DFT data for the ternary systems have been used to adjust the CDP set of parameters while values for the quaternary systems have been used to validate the set of parameters obtained. Figure 4-26 and Figure 4-27 present the results.

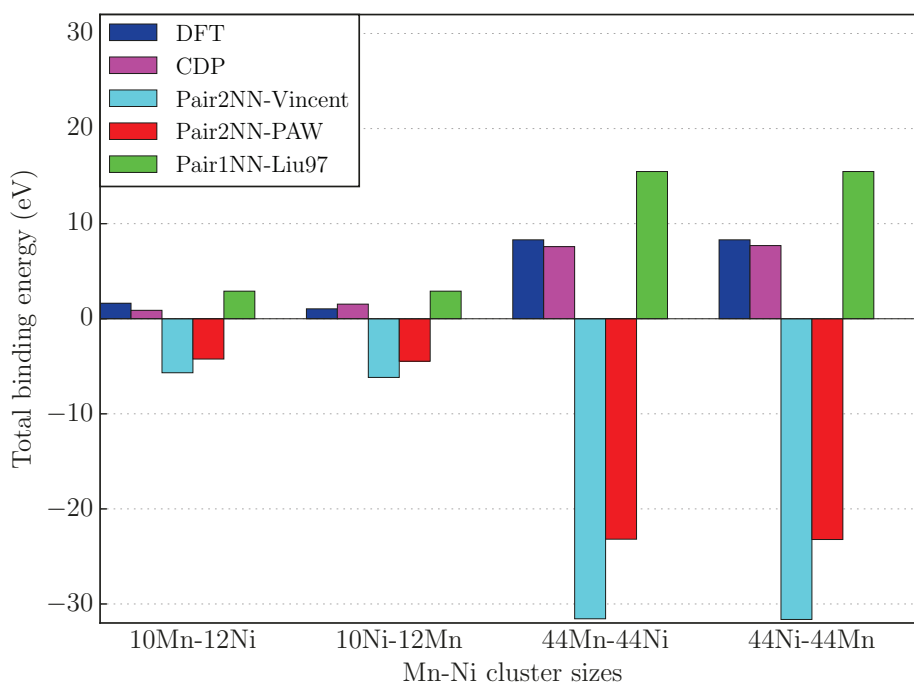


Figure 4-26: Total binding energy for different Mn-Ni clusters.

The CDP parameterization greatly improves the description of the Mn-Ni cluster. Due to the negative binding energies as well as the positive Mn-Ni solution enthalpy employed in the “Pair2NN-Vincent” and “Pair2NN-PAW” parameterization, the Mn-Ni clusters are predicted to be unstable (whereas PAW DFT predicts them to be slightly stable). The “Pair1NN-Liu97” parameterization overestimates the total binding energies of the B₂ type clusters because of its lack of 2NN interactions. The CDP parameterization predictions are in good agreement with the PAW DFT values.

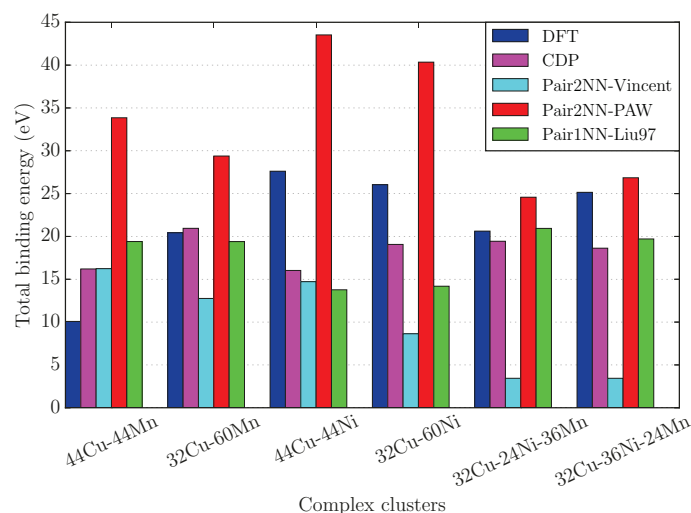


Figure 4-27: Total binding energies for different Cu/Mn-Ni and Cu-Mn-Ni clusters.

The CDP model also improves the Cu-Mn cluster descriptions. As seen before, the “Pair2NN-PAW” parameterization tends to overestimate the stability of solute clusters. For the B_2 type structure (44X–44Y), both “Pair2NN-Vincent” and “Pair1NN-Liu97” parameterization overestimate their stability. The numerical method for exploring the CDP set of parameters really makes sense on this type of cluster (e.g. adjusting the $\epsilon_{X-Y}^{1nn}(1)$ interactions). For the core-shell structure (32X–60Y), both “CDP” and “Pair1NN-Liu97” parameterization are in agreement with PAW DFT. For the Cu-Ni clusters, the observations are basically the same as in the Cu-Mn case. However, for this system, the B_2 structure is well reproduced by the “Pair1NN-Liu97” parameterization.

To validate this CDP parameterization, quaternary systems have been used. On these clusters, the “Pair2NN-Vincent” parameterization underestimates the total binding energy of the Cu-core Mn/Ni-shell structure. This can be explained by the difficulty to mix Mn and Ni together in this parameterization. The “Pair2NN-PAW” parameterization predictions are in agreement with the DFT values but only because of the large contribution of the Cu-core (which has been overestimated). On this complex system, the “Pair1NN-Liu97” parameterization provides the closest prediction to the DFT value. However, predictions of the CDP model remain acceptable. The effect of Si on the stability of Mn, Ni and MnNi clusters are presented in Figure 4-28.

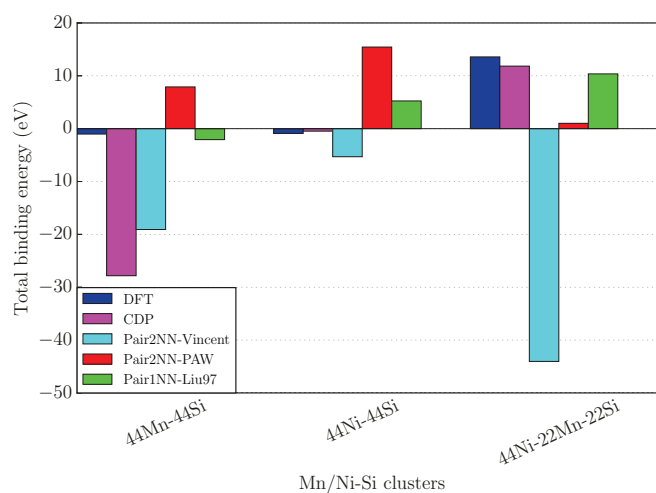


Figure 4-28: Total binding energies for large Si-/Mn/Ni complexes.

As in the previous section, the “Pair2NN-Vincent” parameterization fails to reproduce the stability of complex solute clusters in comparison with DFT predictions. This is an important issue since Mn-Ni-Si cluster (MNS cluster) formation mechanism is a central question for the understanding of RPV steels evolution under irradiation. The “Pair2NN-PAW” parameterization is also inadequate to treat these systems. The “Pair1NN-Liu97” parameterization predicts good results except in the case of Ni-Si cluster. Concerning the CDP model, the choice has been made to reduce the stability of the $44\text{Mn-}44\text{Si(B}_2\text{)}$ cluster. In fact, using the total binding energy predicted by the PAW DFT in the CDP model leads to the precipitation of Mn-Si in the iron matrix. The structure of the cluster observed is presented in Figure 4-29.

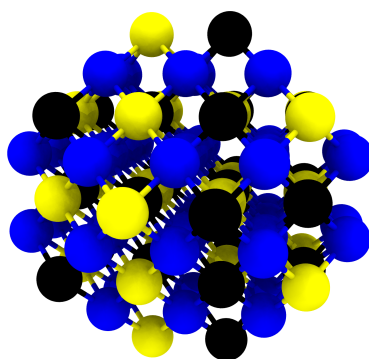


Figure 4-29: Typical “dilute” (i.e. containing iron) structure predicted by the MMC in presence of Mn and Si at 600 K when using the total binding energy of the $44\text{Mn-}44\text{Si(B}_2\text{)}$ cluster predicted by PAW DFT. Mn, Fe and Si atoms are respectively the blue, black and yellow spheres (1NN bounds are displayed).

The total binding energy of this structure is 7.3 eV according to PAW DFT. Without lowering the $44\text{Mn-}44\text{Si(B}_2\text{)}$ structure stability, the CDP model predicts a total binding energy of 15.6 eV. Hence the stability of the B_2 structure has been adjusted to comply with a “dilute” cluster structure. In this condition, the CDP model predicts a stability of 7.5 eV for the dilute structure and there is no formation of Mn-Si clusters at equilibrium at 600 K.

To conclude on this part about the solute-solute parameterization comparison, we have found that:

- The “Pair2NN-Vincent” parameterization failed in reproducing the large panel of different solute clusters (except in the case of pure Cu clusters).
- Employing the binding energies from PAW DFT as the unique parameters is usually not the right approach.
- The thermodynamic based parameterization (“Pair1NN-Liu97”) predictions are often remarkably in agreement with the PAW DFT values.
- From all the parameterizations available, the current CDP model is the one that, on average, provides the closest results to the DFT values.

4.3.5 Parameterization of the vacancies

Small vacancy-solute clusters have also been studied. Figure 4-30 shows the different clusters considered. A good description of these small objects is very important if one wants to be able to reproduce elementary mechanisms occurring under irradiation.

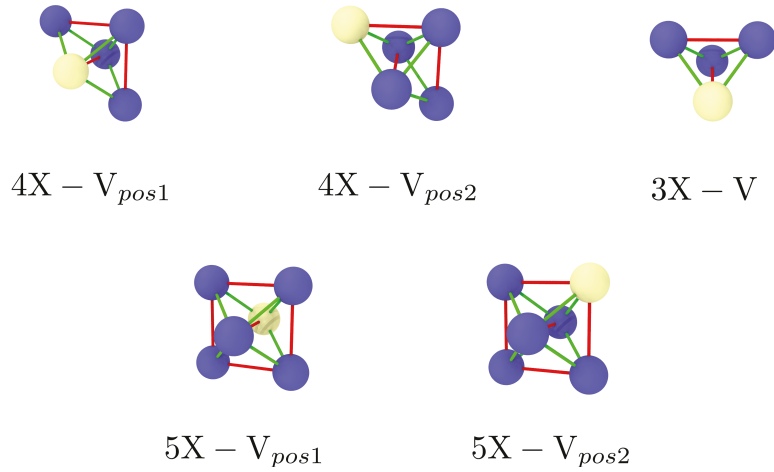


Figure 4-30: Small one vacancy – X solute clusters considered for the vacancy-solute interactions parameterization. Solute atoms are shown in blue while the vacancy color is yellow. 1NN bonds are displayed in green while the 2NN bounds are in red.

Figure 4-31 presents the results for the V-Mn/Ni clusters and Figure 4-32 presents the results for the V-Cu clusters.

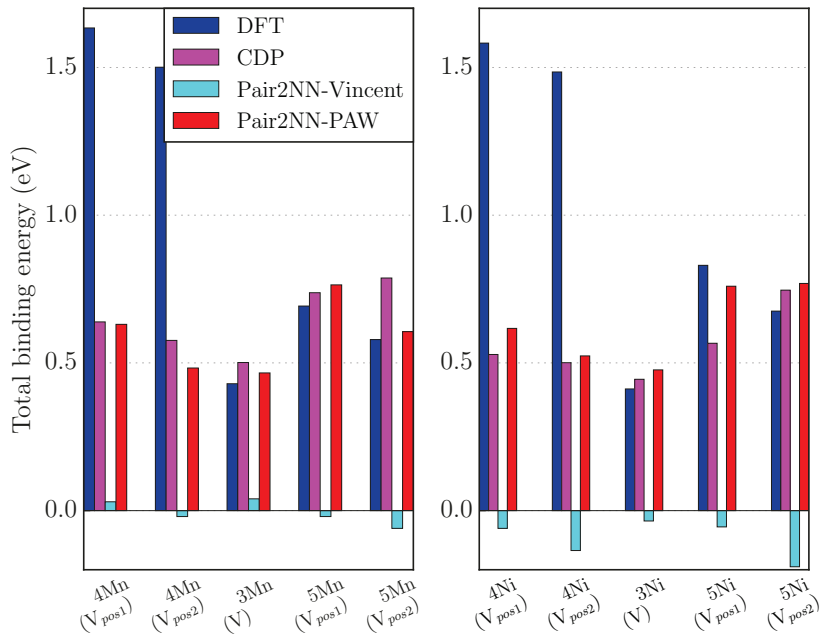


Figure 4-31: Total binding energies for small V-xMn/xNi complexes.

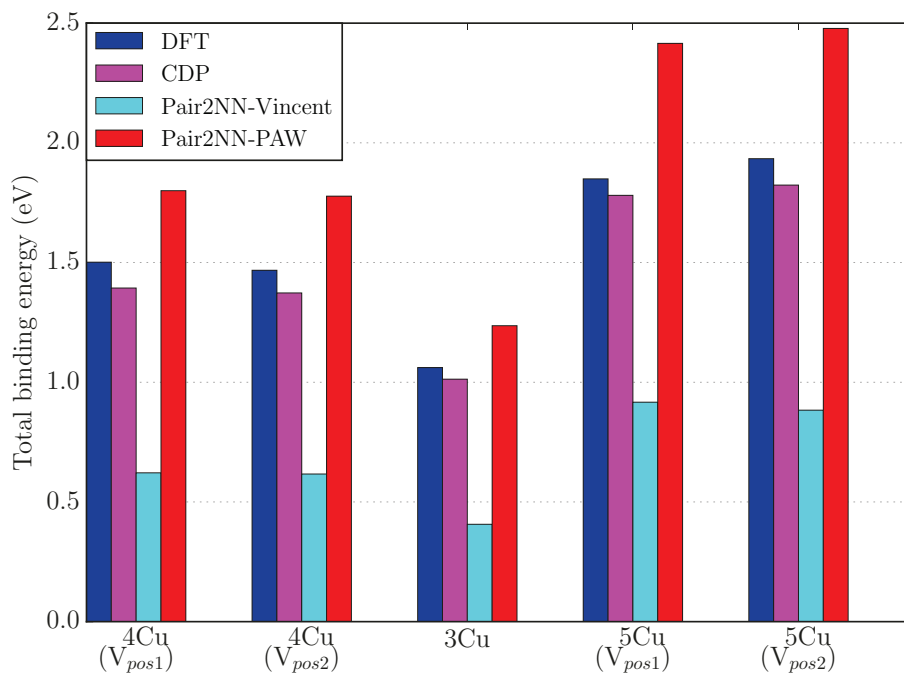


Figure 4-32: Total binding energies for small V-xCu complexes.

Since the ϵ_{ij} involved in a small cluster are close to the ϵ_{ij}^{dilute} interactions, the “CDP” and the “Pair2NN-PAW” parameterization often provide comparable results. As in the solute-solute case, the “Pair2NN-Vincent” parameterization does not agree with the PAW DFT values in the presence of Mn and Ni.

Figure 4-33 presents the results for the core-vacancy – solute-shell system (corresponding to the 32X-60Y structure presented in Figure 4-25).

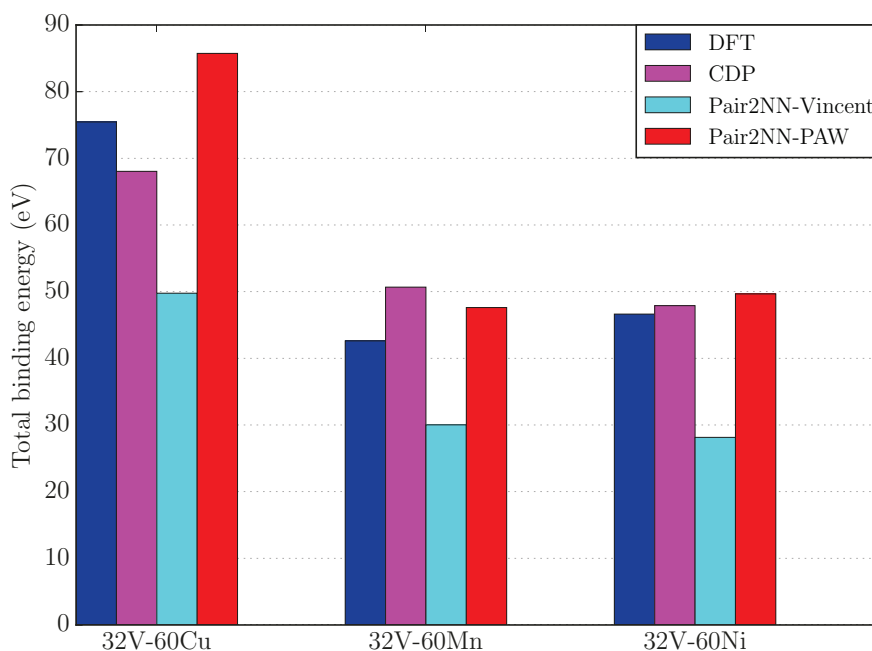


Figure 4-33: Total binding energies for large V-Cu/Mn/Ni complexes (vacancies surrounded by solutes).

Just as in the solute-solute case, the CDP model improves the description of V-solute complexes when compared to the “Pair2NN-Vincent” parameterization. The “Pair2NN-PAW” parameterization also provides results comparable to the PAW DFT predictions (at least for these small objects).

4.3.6 Parameterization validation

The CDP model has been parameterized on a large panel of objects. However, the chemical complexity of these objects is less than the one the system experiences during irradiation. We now proceed to the assessment of the predictions of the model. Due to combinatory limitations, only small clusters have been used to quantify the prediction of the new model when increasing the chemical complexity.

First, clusters of size 3 are discussed. The clusters are denoted X-Y-Z. X is first nearest neighbor to Y and Z. Y and Z are separated by a 2NN distance.

The results for binary clusters are presented in Figure 4-34. The clusters contain up to two different species (solute atoms or vacancies).

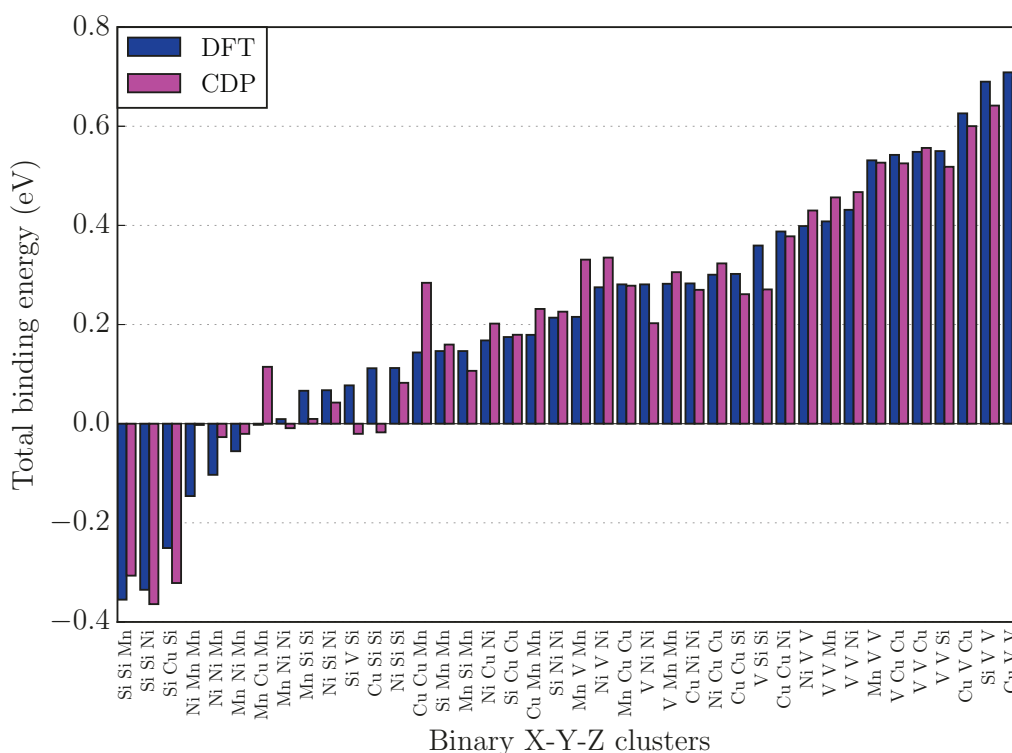


Figure 4-34: Total binding energies for the binary X-Y-Z clusters. The results are sorted from the less to the more stable cluster according to PAW DFT.

Small binary clusters are well reproduced by the CDP model. However, some configurations remain difficult to describe (especially those presenting low stabilities). This effect is more pronounced when the chemical complexity increases as shown for the ternary clusters in Figure 4-35.

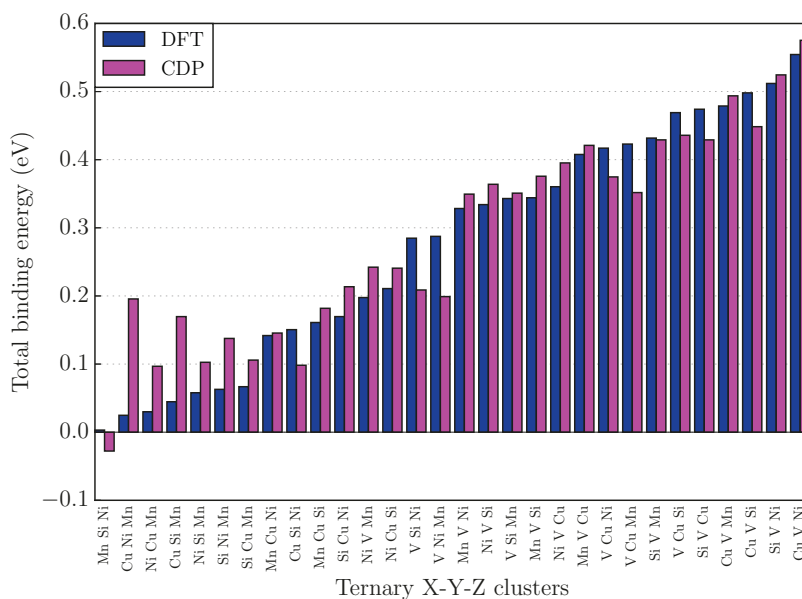


Figure 4-35: Total binding energies for the ternary X-Y-Z clusters. The results are sorted from the less to the more stable cluster according to PAW DFT.

When increasing the chemical complexity of the clusters, the CDP model tends to be overbinding (especially for the less stable clusters). More results concerning the X-Y-Z clusters are given in Annex VII. For medium size clusters (size 6), Figure 4-36 compares the binding energy between a specie and the 5 others in the cluster for the two parameterizations.

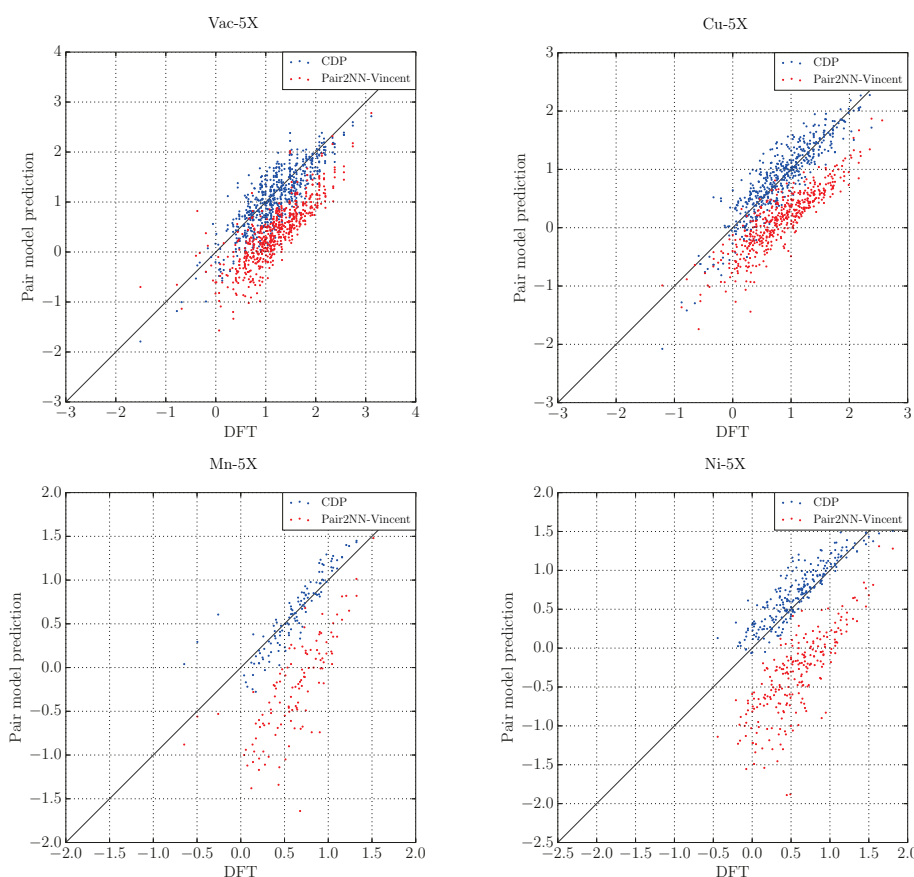


Figure 4-36: Binding energy between a specie Y and a cluster of size 5. Y can be Cu, Mn, Ni and Vac. The cluster of size 5 can be a mixed cluster or not (a pure or multinary cluster).

On the one hand, the “Pair2NN-Vincent” parameterization tends to underestimate the binding energies. On the other hand, the CDP model appears to slightly overestimate these energies (particularly in the Ni-5X case). The reason for that is because of the too small size of the cluster. In this condition, the $v_{ij}^{Cluster}$ “cluster” terms (in Equation 4-2) of the CDP model are not contributing that much to the pair interaction because of the too low local concentration. Hence, the model behaves more like the “Pair2NN-PAW”. This tendency can clearly be observed in the case of size 4 clusters as presented in Figure 4-37.

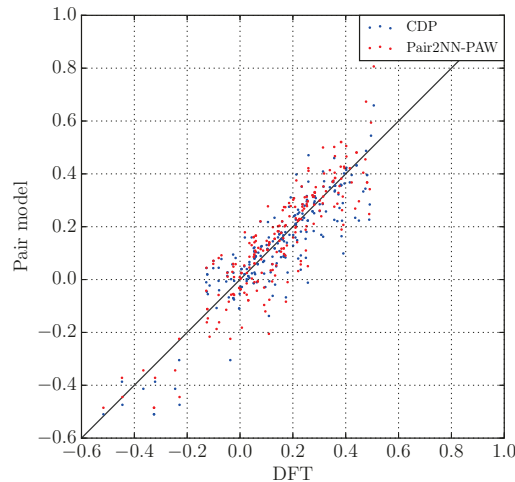


Figure 4-37: Total binding energy of size 4 cluster for the CDP model and the “Pair2NN-PAW” parameterization.

4.3.7 Monte Carlo simulations on RPV model alloy

The MMC simulations presented in section 4.2.2 to reproduce Styman experiments [7] have been performed using the CDP model. Figure 4-38 presents the results.

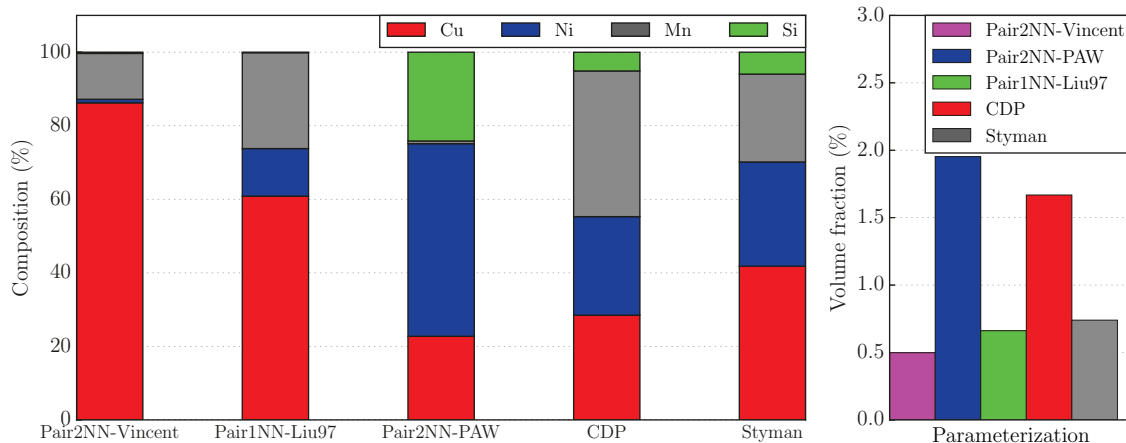


Figure 4-38: (left) Mean cluster composition obtained using MMC simulations with different parameterizations. These results are compared to Styman et al. results [7]. (right) Volume fraction obtained using the different parameterizations.

From cluster observed after the MMC simulation, it is possible to compare the CDP prediction to the experimental results from Styman. Results show that the CDP model tends to underestimate the Cu content of the cluster. It also overestimates the Mn content. However, the new cohesive model predicts the closest

results to the experiments compared to the other parameterizations. Concerning the volume fraction, the CDP model overestimates its value. This can be explained by the fact that the cluster formed during the simulation is larger than those observed with the other parameterizations. Figure 4-39 presents the structures of the clusters obtained in these simulations.

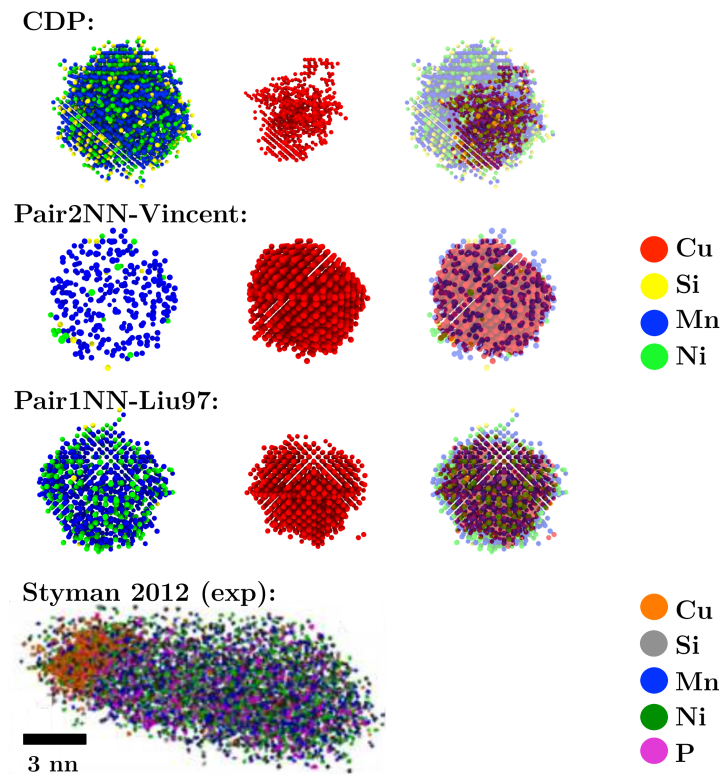


Figure 4-39: Structure of the clusters predicted by the different parameterizations. On the left, the Mn-Ni-Si shell is shown. At the center of the figure, the Cu core is present. On the right, the two previous images on the left are superposed. A precipitate observed by Styman is also presented [13].

The cluster structures are very different from one parameterization to another. One interesting point is that the CDP model is the only parameterization that allows for the formation of a multi-layer rich in Mn-Ni-Si around a Cu precipitate. This type of structure resembles the MNS phase growing on the Cu cluster observed experimentally under thermal ageing [13] (at a grain boundary) or under irradiation [14].

4.3.8 Kinetic properties

Improving solute transport through a vacancy mechanism was a key factor that motivated the development of the CDP model. The transport coefficients as well as the wind factor presented in chapter 2 section 2.2.3 have been computed using both the CDP model and the “Pair2NN-Vincent” parameterization. These results have also been compared to those obtained by Messina [8] using the explicit barrier obtained through DFT calculations and the “Pair2NN-Vincent” parameterization. These calculations have been performed in a $6 \times 6 \times 6 a_0$ simulation box with one solute and one vacancy in it. The transport coefficients have been sampled every 5000 AKMC steps until the mean values have converged (between 10^8 and 10^9 AKMC steps depending on the solute and the temperature). Figure 4-40 presents the results.

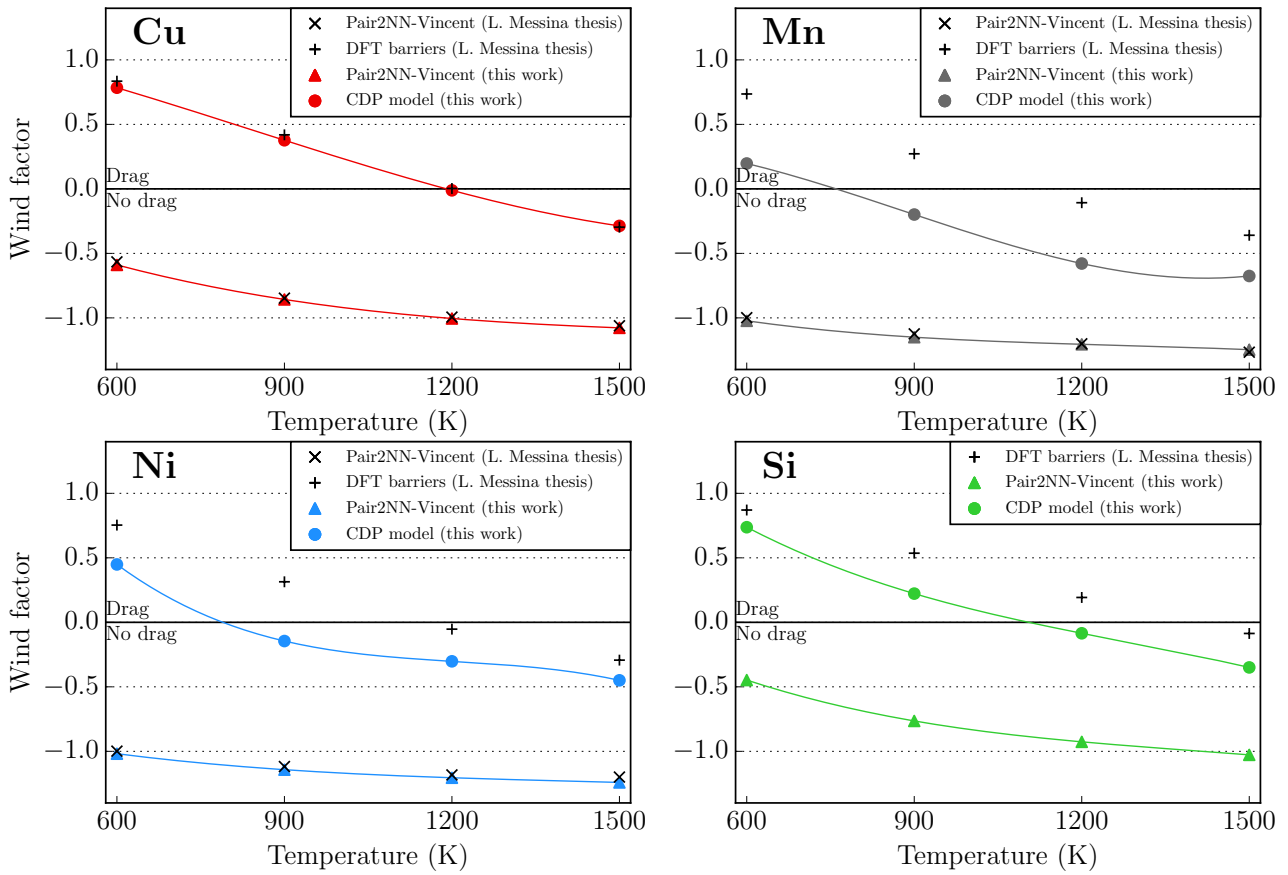


Figure 4-40: Wind factor as a function of the temperature for Cu, Si, Mn and Ni. When the wind factor is positive, drag occurs. Otherwise, there is no drag.

For all the solutes investigated in this study, the agreement is good between this work and the one of Messina using the “Pair2NN-Vincent” parameterization. Concerning the Cu atom, the CDP model is in very good agreement with the explicit DFT barrier model. The prediction of the FISE model with the “Pair2NN-Vincent” parameterization is not that good in the case of manganese. Concerning this case, the results presented as “Pair2NN-Vincent” and “Pair2NN-Vincent L. Messina thesis” correspond to the calculation performed using the reference migration energy equal to 0.42 eV. Employing the 1.03 eV value presented in section 2.6.2 of the second chapter leads to wind factors equal to -7.29, -3.06, -1.30 and -1.24 respectively at 600, 900, 1200 and 1500 K. Concerning the Ni and Si, the CDP model always underestimates the wind factor when compared to the explicit barrier model. However, for all solutes, the sign of the wind factor at the temperature of interest (600 K) is always the same as the one obtained in Messina’s work making the drag tendencies going in the same direction. These results concerning the CDP model are encouraging because it has been developed (among other goals) to increase the drag tendency of the solute atoms by a vacancy mechanism.

4.4 Simulations of irradiation

4.4.1 Comparison between CDP and “Pair2NN-Vincent” at low dose

Irradiation simulations have been performed using both CDP and “Pair2NN-Vincent” parameterizations. The temperature has been set to 573 K with a flux of 10^{-5} dpa/s. 20 and 100 keV cascades from Stoller have been used [15]. The simulation box was $60 \times 60 \times 120 a_0$ with absorbing surfaces on z. A cluster that contains more than 6 SIAs is treated as an immobile object. The vacancies are always treated in AKMC. In the data analysis, only clusters containing n (cluster criterion) species or more are taken into account.

The FeMnNi and FeCuMnNi model alloy compositions were chosen to be comparable to those of Meslin [16].

a) Fe-1.1Mn-0.68Ni (at.%):

First, the Fe-Mn-Ni ternary system is discussed. Figure 4-41 and Figure 4-42 present the results. \overline{N}_X^Y corresponds to the mean number of X species in the Y type cluster. These properties are also calculated for the size > 4 clusters.

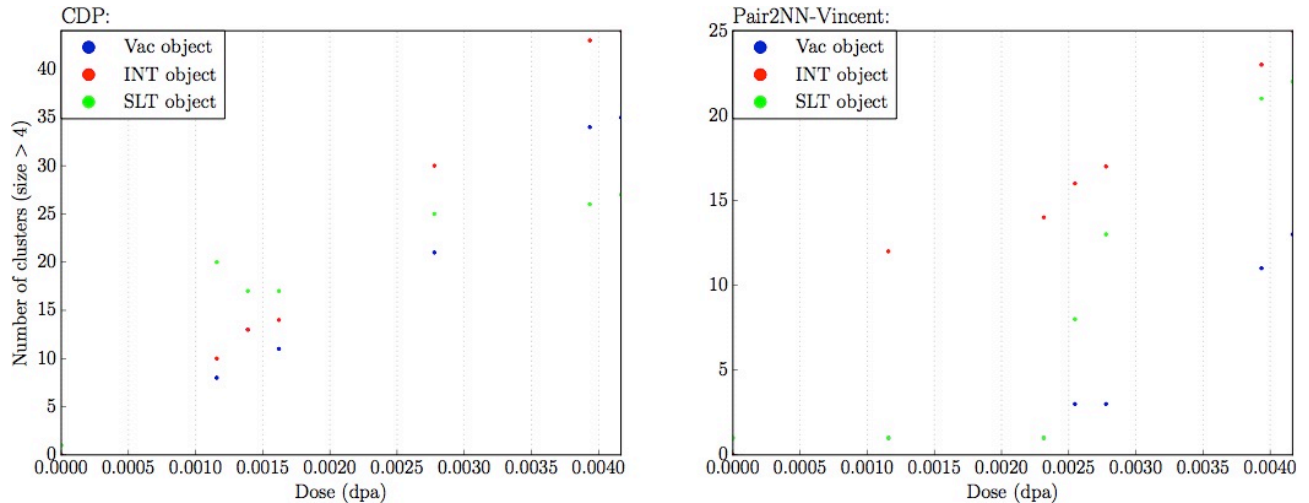


Figure 4-41: Evolution with the dose of the number of clusters. (left) CDP model, (right) “Pair2NN-Vincent” parameterization. The Vac object population corresponds to pure vacancy clusters and mixed vacancy-solute clusters. The same applies for the Int objects. Concerning the Solute object population, it corresponds to the defect-free clusters. The cluster criterion was set to 5 species.

Mn-Ni solute clusters are observed using both cohesive models. Concerning the vacancies, some vacancy clusters remain in the simulation box in the CDP case, whereas they tend to annihilate on the surfaces using the “Pair2NN-Vincent” model. This is due to the high mobility predicted by the “Pair2NN-Vincent” model. Hence, the density of vacancy objects is lower in the “Pair2NN-Vincent” parameterization than in the CDP model.

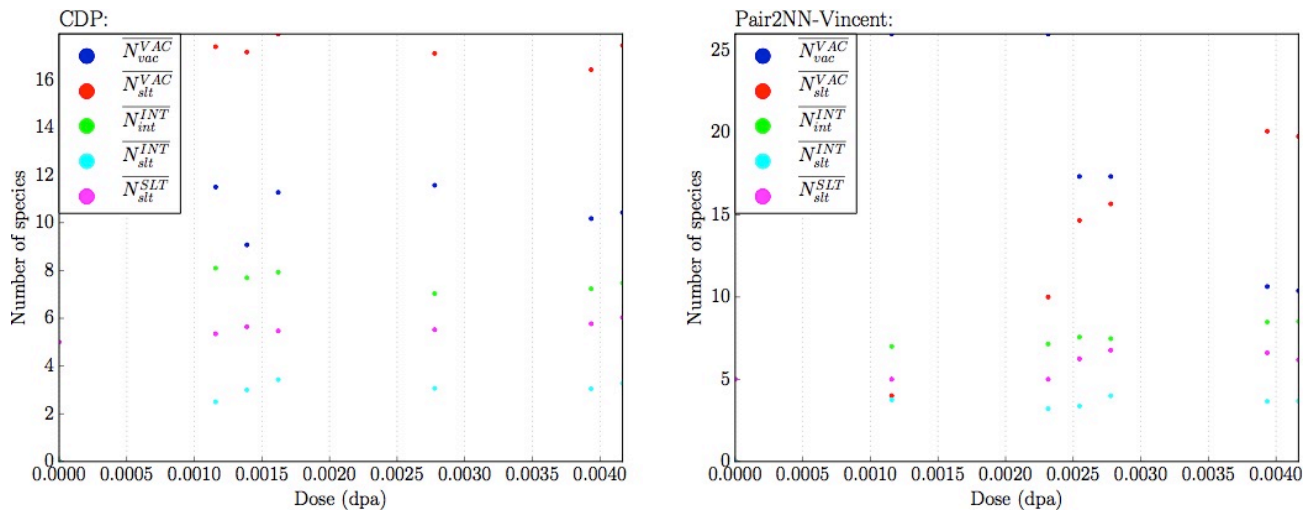


Figure 4-42: Evolution with the dose of the mean number of species in different types of clusters. (left) CDP model, (right) “Pair2NN-Vincent” parameterization.

The analysis of the number of species per object type also shows similarities between the two models. The mean number of SIA per SIA cluster as well as the mean number of solute in SIA clusters does not differ between the two models. Vacancy clusters appear to be enriched in solutes in both models. Concerning the composition of the objects, vacancies tend to be more enriched in Mn in the CDP model. For the other objects, the mean compositions are comparable as shown in Figure 4-43.

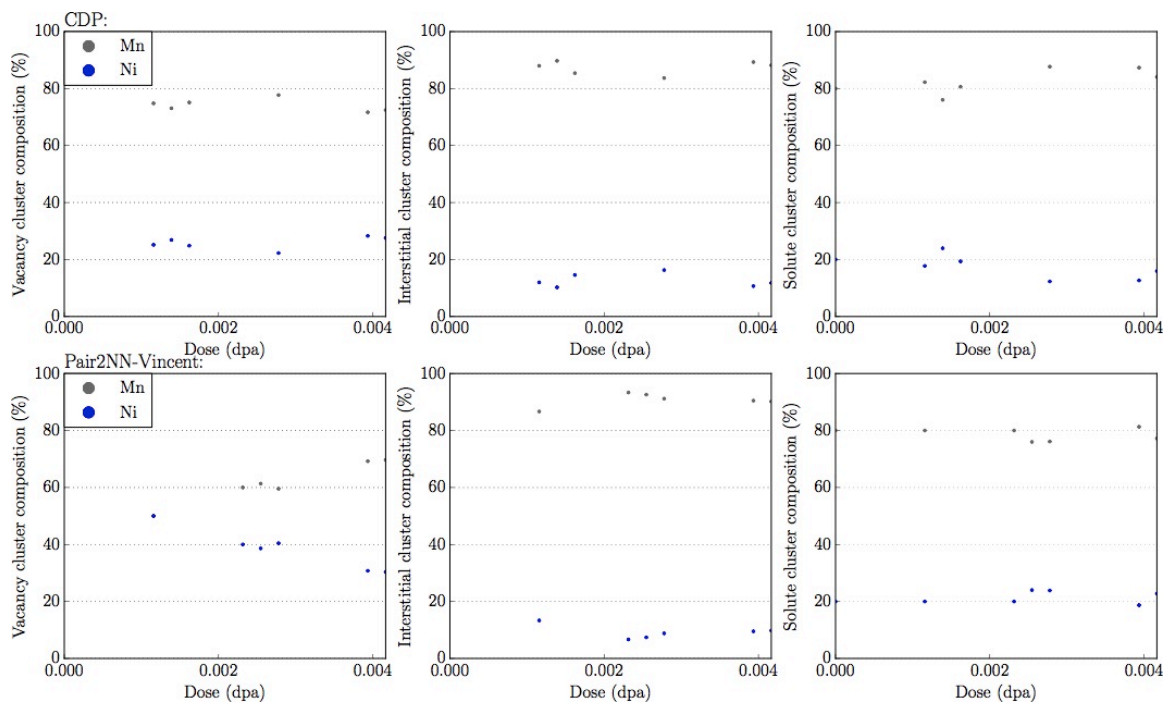


Figure 4-43: Evolution with the dose of the mean composition of the different types of clusters. (top) CDP model, (bottom) “Pair2NN-Vincent” parameterization.

At least in the low dose regime, results from the CDP model and the “Pair2NN-Vincent” parameterization are comparable. However, the distribution of the cluster shows some differences (see Figure 4-44).

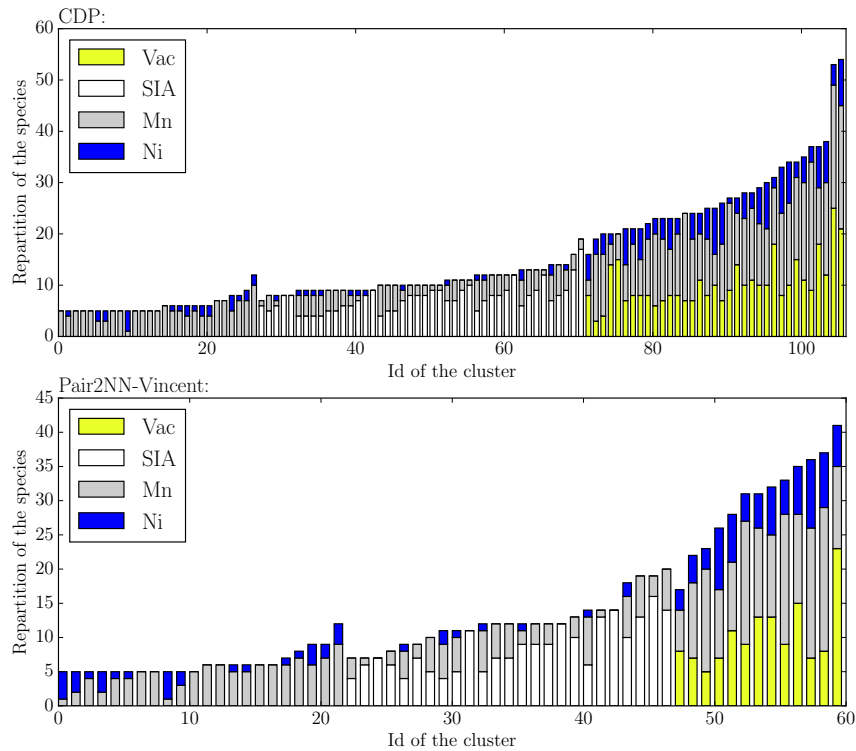


Figure 4-44: Microstructure obtained at 4 mdpa for the “Pair2NN-Vincent” and CDP parameterization. The cluster size criterion was set to 5 species.

The main difference comes from the number of vacancy and interstitial cluster. There are more vacancy and interstitial clusters that are formed in the CDP model. This can be explained by the lower mobility of the vacancy clusters which makes recombination mechanism less favored and the accumulation of PD clusters easier in the CDP.

b) Fe-0.09Cu-1.1Mn-0.68Ni (at.%):

In order to observe the effect of the addition of Cu, the FeCuMnNi system under irradiation has been simulated. The simulation parameters are the same as the ones used in the case of the FeMnNi alloy. The post-treatment performed is also identical. Figure 4-45 and Figure 4-46 present the results.

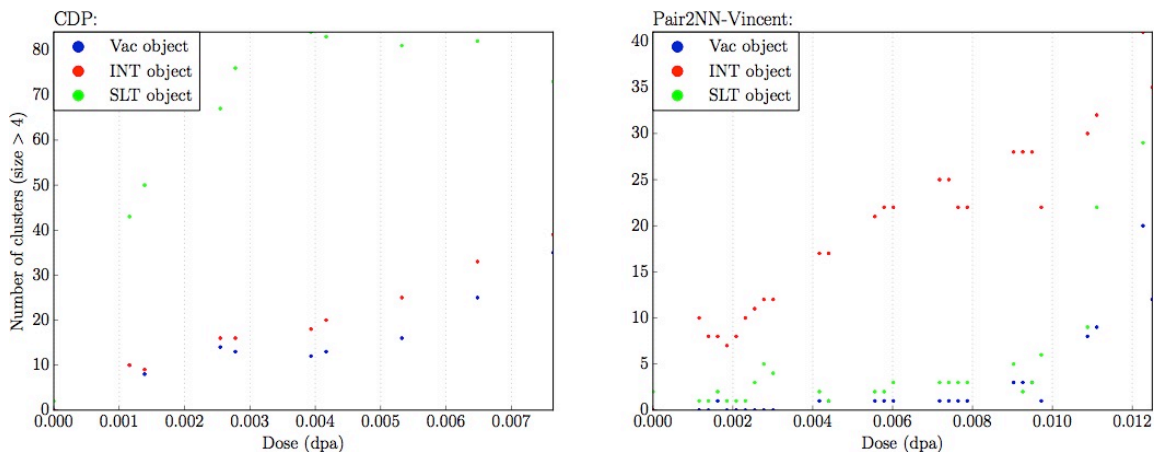


Figure 4-45: Evolution with the dose of the number of clusters. (left) CDP model, (right) “Pair2NN-Vincent” parameterization. The Vac object population corresponds to pure vacancy clusters and mixed vacancy-solute clusters. The same applies for the Int objects. Concerning the Solute object population, it corresponds to the defect-free clusters. The cluster size criterion was set to 5 species.

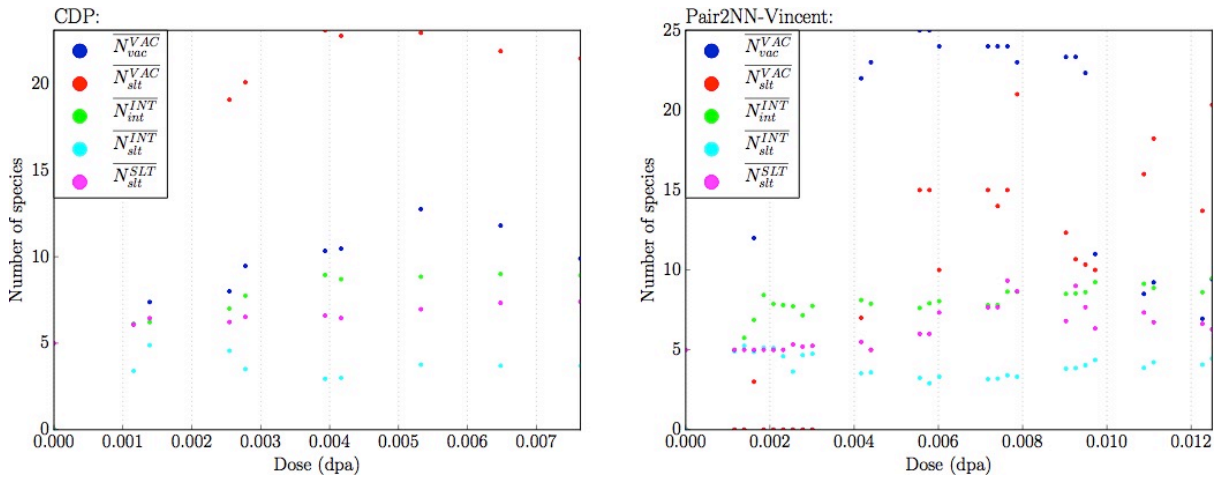


Figure 4-46: Evolution with the dose of the mean number of species in different types of clusters. (Top) CDP model, (Bottom) “Pair2NN-Vincent” parameterization.

A large number of solute clusters are formed using the CDP model and more clusters are formed than in the “Pair2NN-Vincent” model. The trends observed in the FeMnNi alloy concerning the vacancy population remain true in the FeCuMnNi system. The vacancy cluster density increases with the dose in the CDP model. In fact, the apparent increase of the $\overline{N_{vac}^{VAC}}$ quantity using the “Pair2NN-Vincent” model is due to the formation of a large vacancy cluster.

Using the CDP model, the solute cluster density is about two times higher in the FeCuMnNi alloy than in FeMnNi alloy. This is in agreement with the experimental observations. Indeed, according to [17], increasing the Cu content lead to an increase of the solute cluster density. Figure 4-47 presents the evolution of the mean composition of the objects.

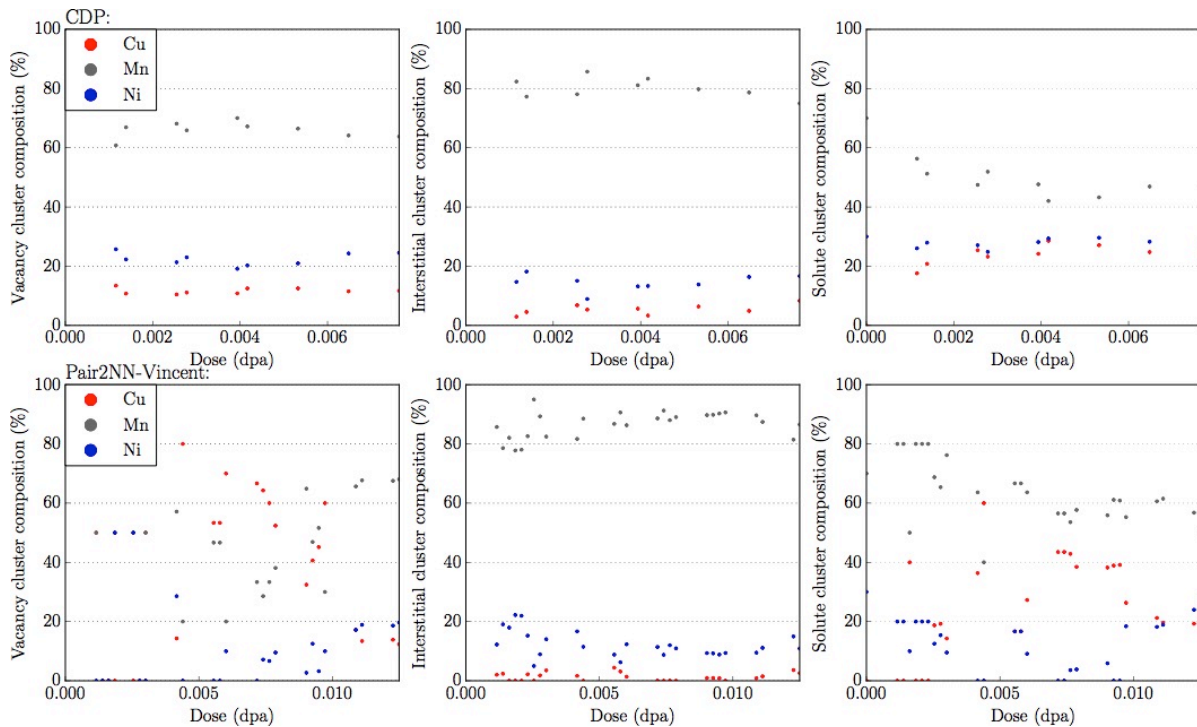


Figure 4-47: Evolution with the dose of the mean composition of the different types of clusters. (top) CDP model, (bottom) “Pair2NN-Vincent” parameterization.

Since the vacancy population obtained with the “Pair2NN-Vincent” model is “very noisy”, the mean composition presented is “noisy” too. Concerning the CDP model, the vacancy cluster are mainly enriched in Mn. Both models predict the same tendencies for the mean SIA cluster composition: they are mainly enriched in Mn.

The solute cluster populations present differences. The Ni content in these clusters tends to decrease for the “Pair2NN-Vincent” model: at 10 mdpa, the solute clusters formed are mainly composed of Cu and Mn. When the dose increases, the CDP model also predicts a decrease of the Mn content combined to an increase of the Cu content. However, the Ni content remains constant. This observation goes in the right direction since the CDP model has been developed to increase the stability of Mn-Ni-(Si) precipitates.

As in FeMnNi alloy, the distribution of the clusters presents some differences. Figure 4-48 shows that the clusters formed during irradiation are more numerous and larger in the CDP case than in the “Pair2NN-Vincent” case. The largest solute clusters are also found to be associated with vacancies using the CDP model.

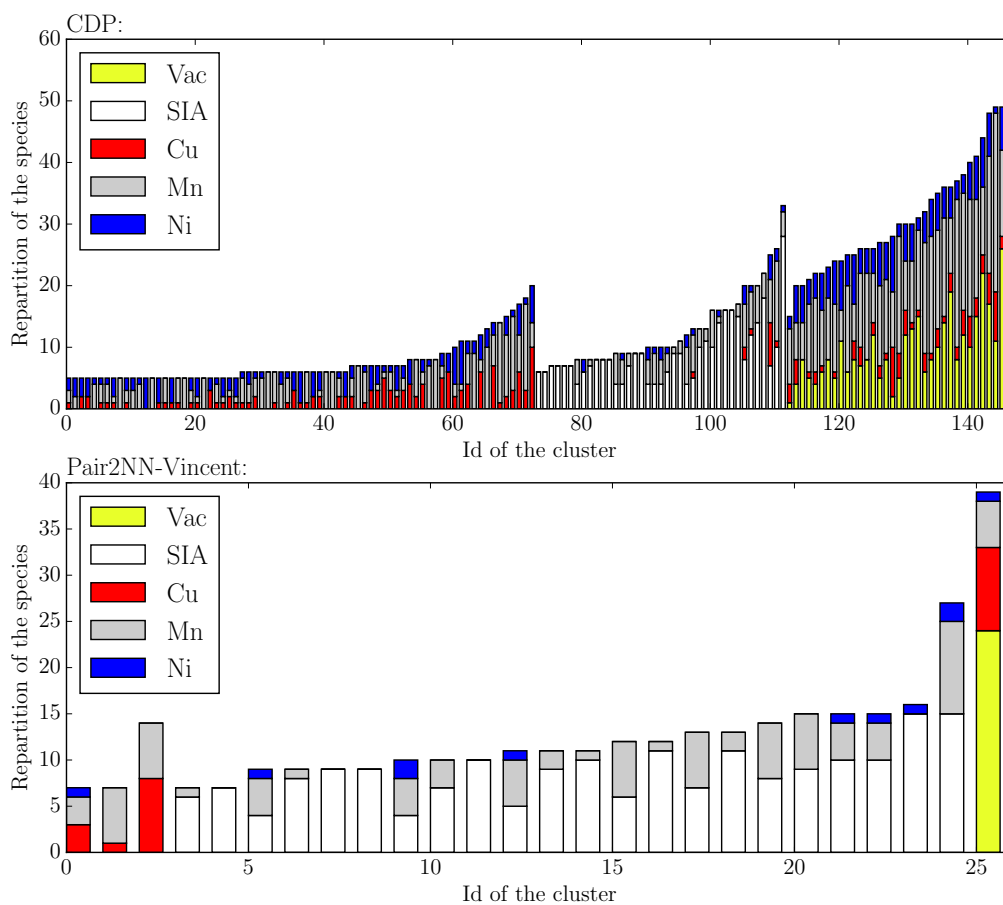


Figure 4-48: Microstructure obtained at 8 mdpa for the “Pair2NN-Vincent” and CDP parameterization. The cluster size criterion was set to 5 species.

4.4.2 Coupling the CDP model with the hybrid AKMC/OKMC

Simulations from the previous section show that simulating “medium” dose (~10 mdpa) irradiation is no longer possible with a full AKMC treatment of the vacancies. The CDP model runs about nine times slower than the “Pair2NN-Vincent” model in terms of number of AKMC steps per day (this is due to the increase of the model complexity presented in Annex III). Moreover, in this model, the vacancy clusters get trapped by the solute atoms. This leads to a large number of AKMC steps spent on quasi-immobile vacancy clusters (just

as it was the case for the SIA clusters in the “Pair2NN-Vincent” parameterization). An attempt to employ the hybrid AKMC/OKMC has thus been made.

Since the vacancy clusters are less mobile using the CDP model, the choice has been made to make them immobile above size 4. V_1 and V_2 are always treated in AKMC. Concerning the V_3 clusters, they are treated as objects if the number of solutes present in the cluster is higher than twice the number of vacancies (e.g. when there is more than 6 solutes in the clusters). This approximation is due to the fact that large V_3 - SLT_n complexes have been found to be very penalizing in terms of trapping effect.

The results of our simulations (presented in section 4.4.1) indicate that considering vacancy objects to be immobile leads to a too large vacancy cluster density. Hence, appropriate emission properties have to be associated with the vacancy objects. Since the emission frequencies of complex vacancy-solute clusters are unknown, two different hypotheses have been employed. The first one called *SLT_LIMIT* supposes that the emission frequencies are not affected by the presence of solutes atoms in the clusters and we use results from AKMC simulations using the “Pair2NN-PAW” in pure iron. The second hypothesis is called *SLT_AS_VAC*. In that scheme, one solute atom in the cluster is counted as one vacancy in the emission frequency calculation. Hence, a V_5 - SLT_5 is supposed to have the emission frequency of a V_{10} cluster. All the simulations presented below have been performed in a $60 \times 60 \times 120$ a_0 simulation boxes with absorbing surfaces along the z axis.

4.4.3 Vacancy object parameterization effects

This section presents the impact of the *SLT_LIMIT* and the *SLT_AS_VAC* hypothesis. The irradiation of aFe-0.05Cu-1.38Mn-0.69Ni-0.47Si (at.%) model alloy with a flux close to 10^{-5} dpa/s and the temperature set to 600 K has been simulated. The density and mean size of the nanofeatures formed during the simulation as a function of the dose are presented in Figure 4-49 and Figure 4-50. Figure 4-49 corresponds to the simulation using the *SLT_LIMIT* hypothesis while Figure 4-50 corresponds to the *SLT_AS_VAC* hypothesis.

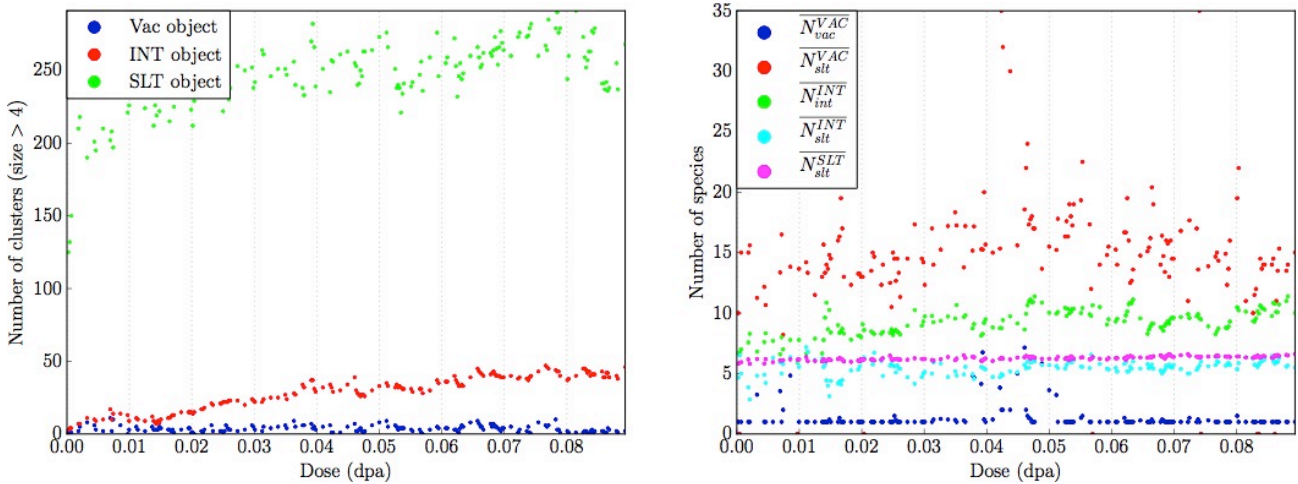


Figure 4-49: Evolution with the dose of the mean number of species in different types of clusters using the CDP parameterization and the *SLT_LIMIT* hypothesis. The cluster criterion was set to 5 species.

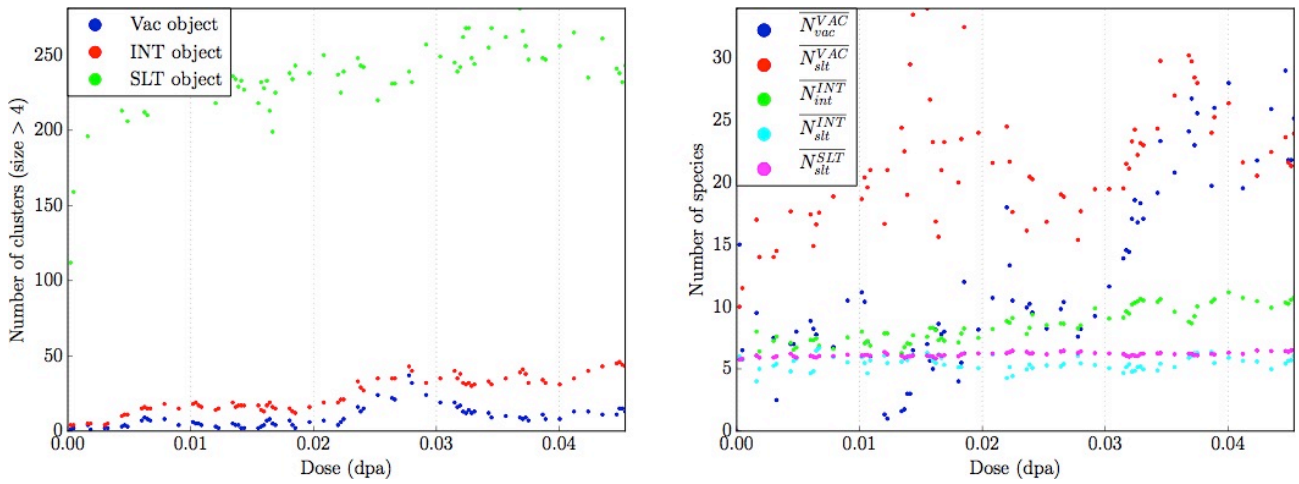


Figure 4-50: Evolution with the dose of the mean number of species in different types of using the CDP parameterization and the *SLT_AS_VAC* hypothesis. The cluster criterion was set to 5 species.

As the two previous figures suggest, treating the vacancy clusters as objects makes the doses that can be reached acceptable. These results also show that the different hypotheses do not have a major effect on the density and mean size of the SIA clusters and the solute clusters. However, from the vacancy population point of view, the two hypotheses lead to different results. While the vacancy population frequently reaches zero in the *SLT_LIMIT* case, this tendency is not observed in the *SLT_AS_VAC* case. This can be explained by the fact that vacancy emissions are less frequent in the *SLT_AS_VAC* case. Thus, the vacancy clusters take more time to dissociate and a new cascade is introduced before all vacancies annihilate/recombine. This effect can also be observed in the vacancy cluster mean sizes. In the *SLT_AS_VAC* case, large vacancy clusters are formed (as the large value of $\overline{N_{vac}^{VAC}}$ suggests) while only one vacancy remains in the simulation box before the introduction of a new cascade in the *SLT_LIMIT* case. These differences between the *SLT_LIMIT* and *SLT_AS_VAC* hypotheses have also been observed in the Fe-1.11Mn-0.68Ni, Fe-0.09Cu-1.11Mn-0.68Ni and Fe-0.18Cu-1.38Mn-0.69Ni-0.47Si (at.%) model alloys.

Concerning the mean composition of the objects formed, there is not much of a difference between the two hypotheses as can be seen in Figure 4-51 and Figure 4-52.

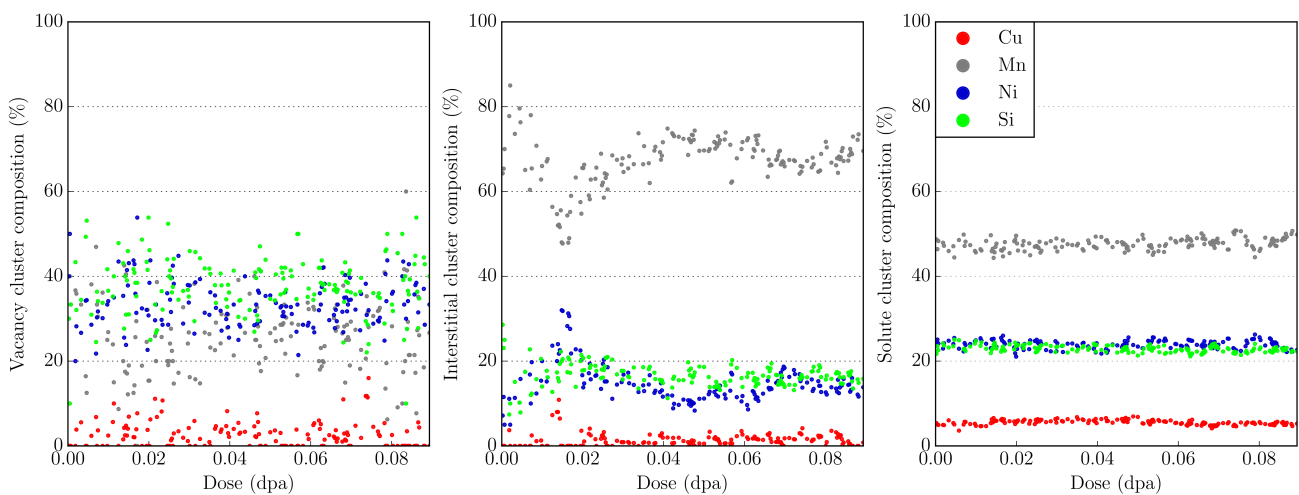


Figure 4-51: Evolution with the dose of the mean composition of the different types of clusters using the CDP model and the *SLT_LIMIT* hypothesis.

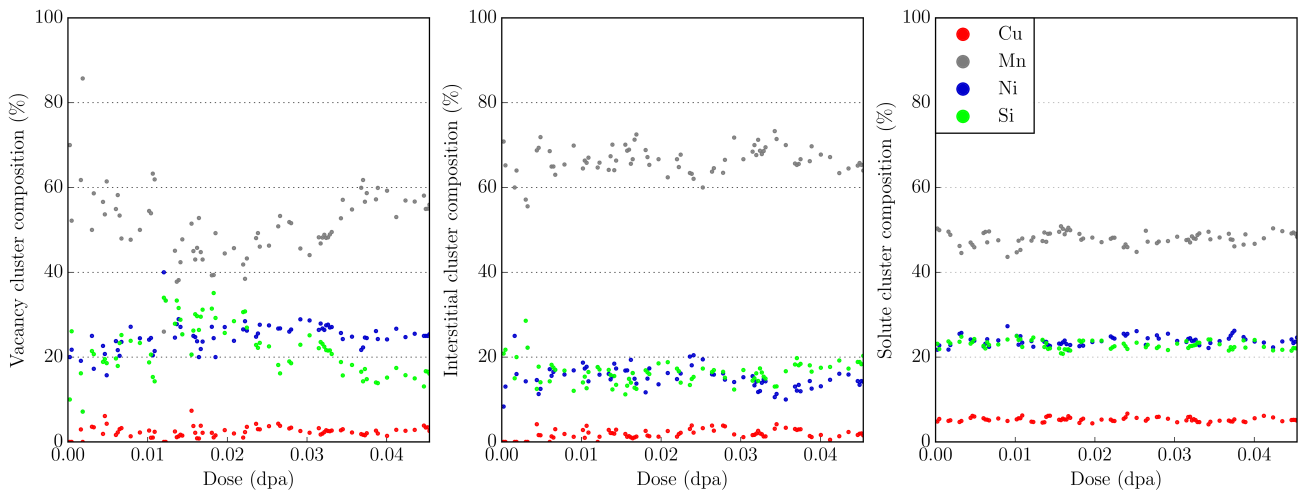


Figure 4-52: Evolution with the dose of the mean composition of the different types of clusters using the CDP model and the *SLT_AS_VAC* hypothesis.

The SIA and solute cluster mean compositions are also comparable using the *SLT_LIMIT* or *SLT_AS_VAC* hypothesis. In both cases, the mean composition of these objects does not change when the dose increases. Concerning the vacancy clusters, they tend to be more enriched in manganese using the *SLT_AS_VAC* hypothesis. This deviation can be explained by the fact that the two hypotheses do not lead to the same vacancy cluster population. In agreement with the binding energy models, in one case large vacancy clusters (*SLT_AS_VAC*) are formed whereas only V_1 are formed in the other case (*SLT_LIMIT*).

Concerning the improvements of the CDP model, one can observe that the solute clusters contain more Ni and Si than using the “Pair2NN-Vincent” parameterization (see Figure 3-38 in section 3.3.6). This was the purpose of the development of CDP model and our goal has thus been reached. However, the manganese is still the main element in the solute clusters while according to experimental results, it should be the nickel [17]. Looking at Figure 4-53, one can see that the CDP model predicts the formation of a few solute clusters larger than those observed using the “Pair2NN-Vincent” parameterization (see Figure 3-39 in section 3.3.6).

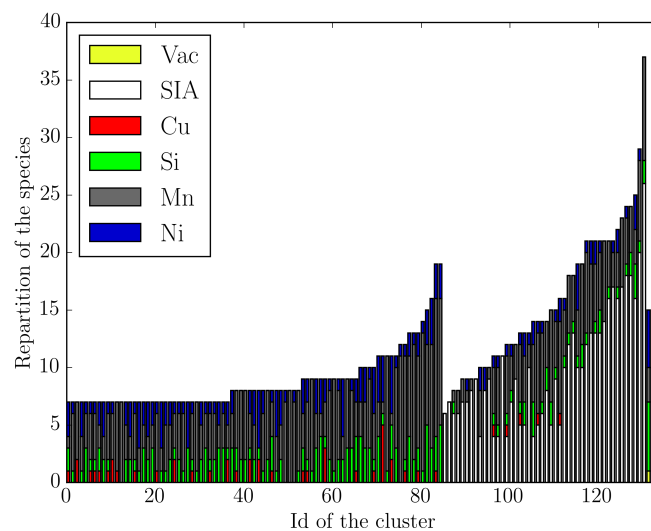


Figure 4-53: Microstructure obtained using the CDP model with the *SLT_LIMIT* hypothesis for the Fe–0.05Cu–1.38Mn–0.69Ni–0.47Si (at.%) irradiated at 90 mdpa at 600 K. The cluster size criterion was set to 7 species. For clarity, solute clusters with a size of 5 or 6 species were removed from the figure (there were 176 such clusters).

4.4.4 Flux and temperature effects

The effect of flux and temperature has also been investigated independently. For the simulations concerning the flux effect, they have all been performed using the *SLT_LIMIT* and *SLT_AS_VAC* hypothesis at 600 K. The fluxes employed were $\sim 10^{-5}$ and $\sim 10^{-7}$ dpa/s. Concerning the temperature effect, the flux has been set to $\sim 10^{-5}$ dpa/s using the *SLT_LIMIT* and *SLT_AS_VAC* hypothesis. Two temperatures have been tested: 600 and 700 K.

All these simulations have been performed on the Fe-1.11Mn-0.68Ni, Fe-0.09Cu-1.11Mn-0.68Ni, Fe-0.05Cu-1.38Mn-0.69Ni-0.47Si and Fe-0.18Cu-1.38Mn-0.69Ni-0.47Si (at.%) model alloys. Since the number of simulations is quite large, we will not present all the results obtained. However, the tendencies observed for a given alloy were found to hold for others.

Flux effects:

The first important result is that despite the use of the hybrid model, the calculations still take much time making high doses unreachable in low flux conditions.

The results also indicate that reducing the flux has no impact on the simulated microstructure when the *SLT_LIMIT* hypothesis is used. These results are consistent with the previous observation made in section 4.1.1. Due to frequent vacancy emission, the number of vacancies that remain in the simulation box before the introduction of a new cascade is very low. Hence, reducing the flux has no effect. On the contrary, using the *SLT_AS_VAC* hypothesis, it has been shown in section 4.1.1 that vacancy clusters are formed and tend to accumulate in the simulation box when employing the highest flux. In this case, reducing the flux gives more time for the vacancy clusters to dissociate. Thus, the number of vacancy clusters is frequently zero before the introduction of a new cascade and large vacancy clusters are rare. Figure 4-54 illustrates this observation in the case of the Fe-0.05Cu-1.38Mn-0.69Ni-0.47Si (at.%) model alloy.

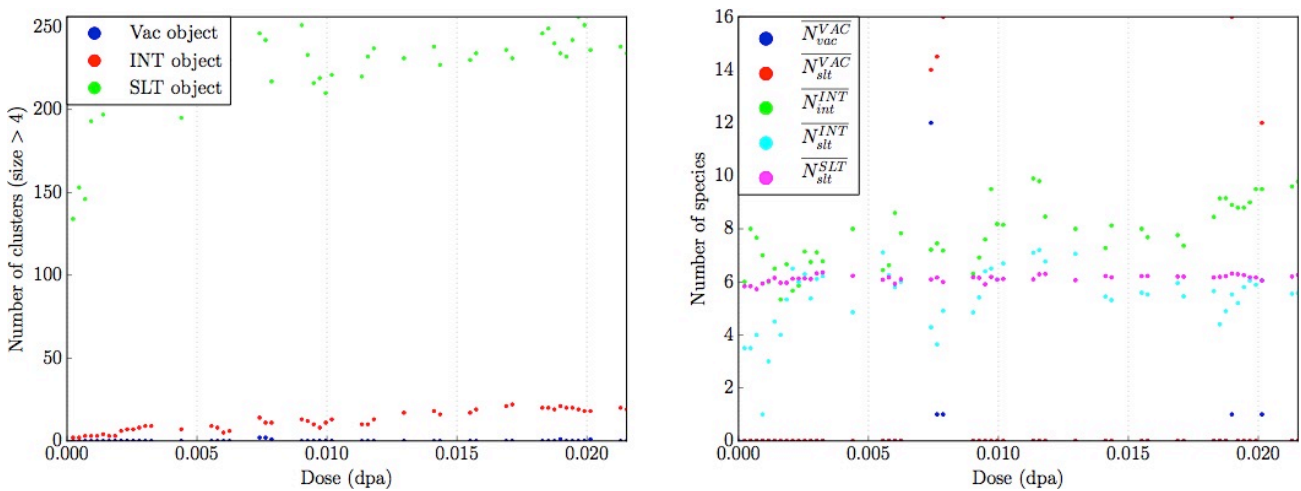


Figure 4-54: Evolution with the dose of the mean number of species in different types of clusters using the CDP parameterization and the *SLT_AS_VAC* hypothesis in the Fe-0.05Cu-1.38Mn-0.69Ni-0.47Si (at.%) model alloy for a flux of $\sim 10^{-7}$ dpa/s. The cluster criterion was set to 5 species.

Another interesting point is that the mean cluster composition is not affected by the reduction of the flux. In some simulations (especially in the FeCuMnNi case), reducing the flux leads to a decrease of the density and mean size of the SIA clusters. This can be explained by the fact that the recombination is favored when giving more time for the vacancy clusters to dissociate.

The final result that needs to be underlined is that the microstructures obtained using the *SLT_LIMIT* at high flux and the *SLT_AS_VAC* at low flux are similar. As the *SLT_LIMIT* hypothesis allows to reach higher doses than the *SLT_AS_VAC* case, we will use it to speed up the calculations in the study of the effect of Cu.

Temperature effects:

Our results indicate that increasing the temperature from 600 to 700 K makes the simulations much faster. While the mean time between two AKMC steps is certainly smaller in the highest temperature case, the reduction of the trapping effects induced by this increase of the temperature favored the recombination. Thus, the mean number of AKMC steps to perform between two cascades is smaller at 700 K than at 600 K. The second observation concerns the solute clusters. They are smaller and less numerous at 700 K than at 600 K. At 0.04 dpa, there are ~240 solute clusters at 600 K but only ~150 at 700 K. Figure 4-55 (which can be directly compared to Figure 4-53) illustrates this result.

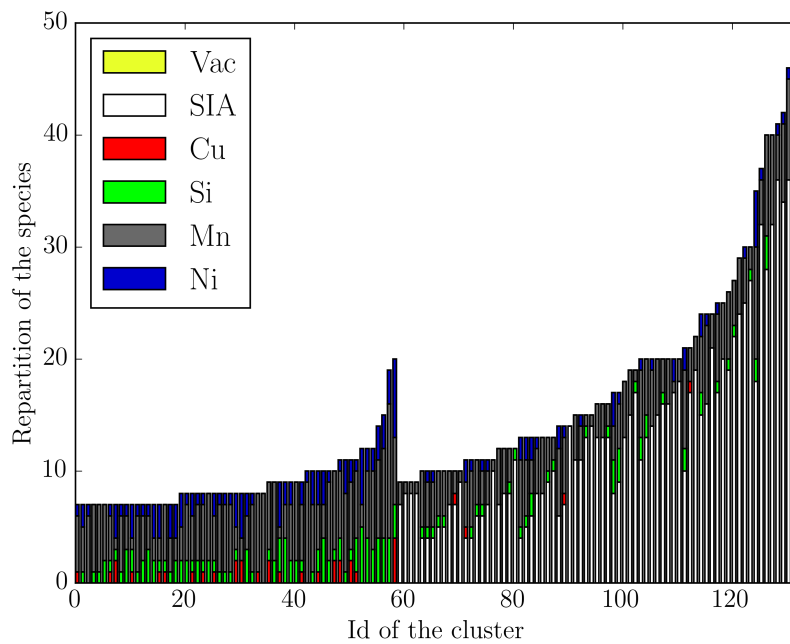


Figure 4-55: Microstructure obtained using the CDP model with the *SLT_LIMIT* hypothesis for the Fe-0.05Cu-1.38Mn-0.69Ni-0.47Si at.% irradiated at 300 mdpa at 700 K. For clarity, solute clusters with a size of 5 or 6 species were removed from the figure (there were 122 such clusters).

Furthermore, we also observed that the SIA clusters are not that much affected by the temperature increase. For the vacancies, the large vacancy clusters formed at 600 K using the *SLT_AS_VAC* hypothesis are no longer present as shown in Figure 4-56.

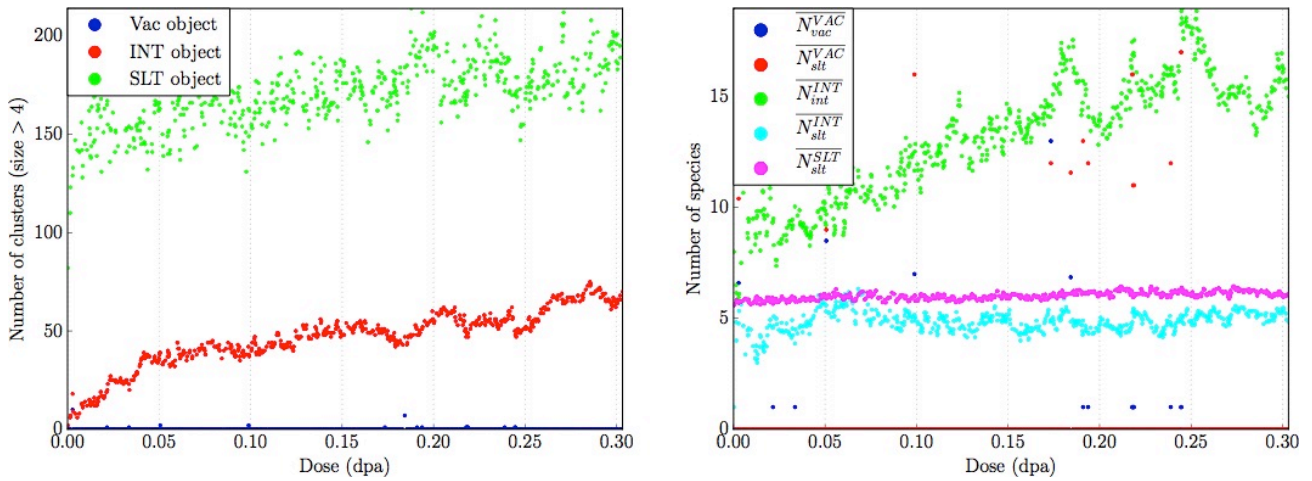


Figure 4-56: Evolution with the dose of the mean number of species in different types of clusters using the CDP parameterization and the *SLT_AS_VAC* hypothesis for the Fe-0.05Cu-1.38Mn-0.69Ni-0.47Si at.% irradiated at 700 K. The cluster criterion was set to 5 species.

Finally for all the alloys tested, the mean cluster compositions were not significantly affected by the increase of the temperature.

4.4.5 Copper effects

The effect of copper has been studied in the high flux regime ($\sim 10^5$ dpa/s). As shown in section 4.4.3, using the *SLT_LIMIT* or the *SLT_AS_VAC* hypothesis does not have an important effect on the mean composition of the SIA and solute clusters. However, in the high flux regime, the *SLT_AS_VAC* hypothesis leads to the formation of large vacancy clusters that are not observed experimentally. Thus, the *SLT_AS_VAC* hypothesis has not been used in these simulations. For this reason, all the results presented in this section have been obtained using the *SLT_LIMIT* hypothesis. The simulations were all performed in a $60 \times 60 \times 120 a_0$ simulation box with absorbing surfaces along the z axis. The temperature was set to 600 K.

First, the differences obtained between the Fe-1.11Mn-0.68Ni and the Fe-0.09Cu-1.11Mn-0.68Ni model alloys are compared. The density and mean size of the objects formed during the simulation as a function of the dose are presented in Figure 4-57 and Figure 4-58.

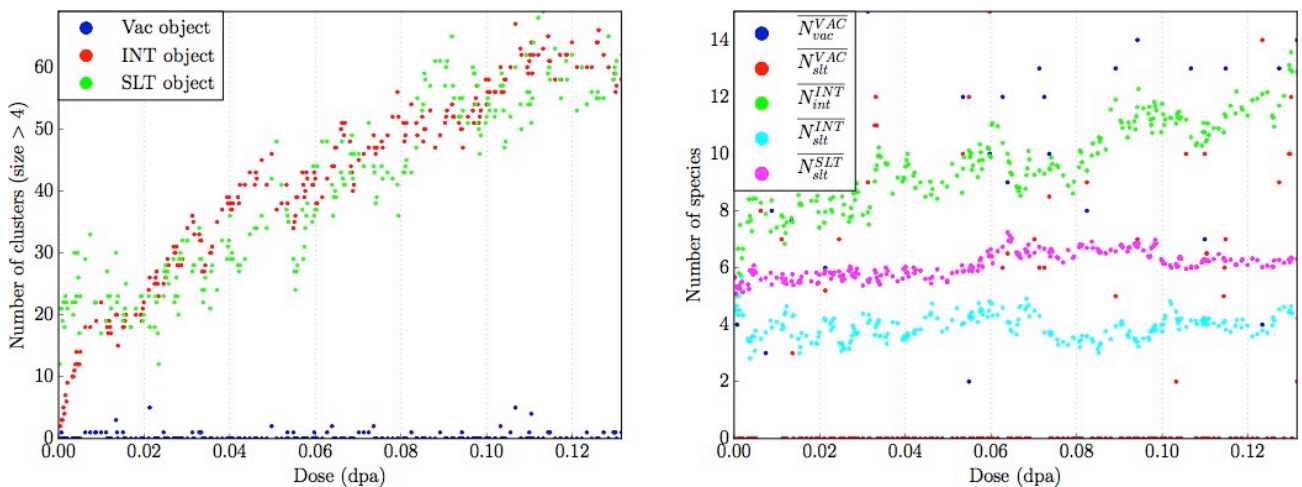


Figure 4-57: Evolution with the dose of the mean number of species in different types of clusters using the CDP parameterization and the *SLT_LIMIT* hypothesis in the Fe-1.11Mn-0.68Ni (at.%) model alloy. The cluster criterion was set to 5 species.

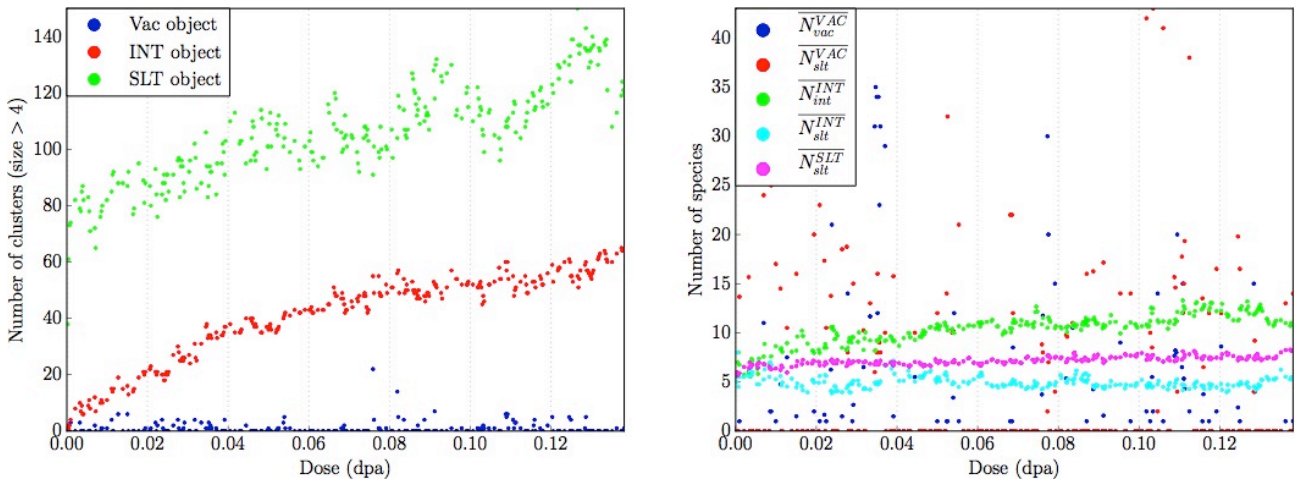


Figure 4-58: Evolution with the dose of the mean number of species in different types of clusters using the CDP parameterization and the *SLT_LIMIT* hypothesis in the Fe-0.09Cu-1.11Mn-0.68Ni (at.%) model alloy. The cluster criterion was set to 5 species.

Figures 4-54 and 4-55 exhibit only one major difference: the solute cluster density is indeed higher in the FeCuMnNi model alloy than in FeMnNi. This behavior is in agreement with experimental observations [16].

Concerning the mean composition of the clusters, Figure 4-59 shows that that SIA and solute clusters are mainly enriched in Mn in the FeMnNi model. When Cu is added, Figure 4-60 shows that the mean SIA cluster composition remains almost unchanged. These clusters do not contain much Cu. However, the observation is different for the solute clusters. The Cu content in these clusters is about 25% at 0.12 mdpa and the Mn content decreases from about 80% in the FeMnNi alloy to 50% in the FeCuMnNi alloy.

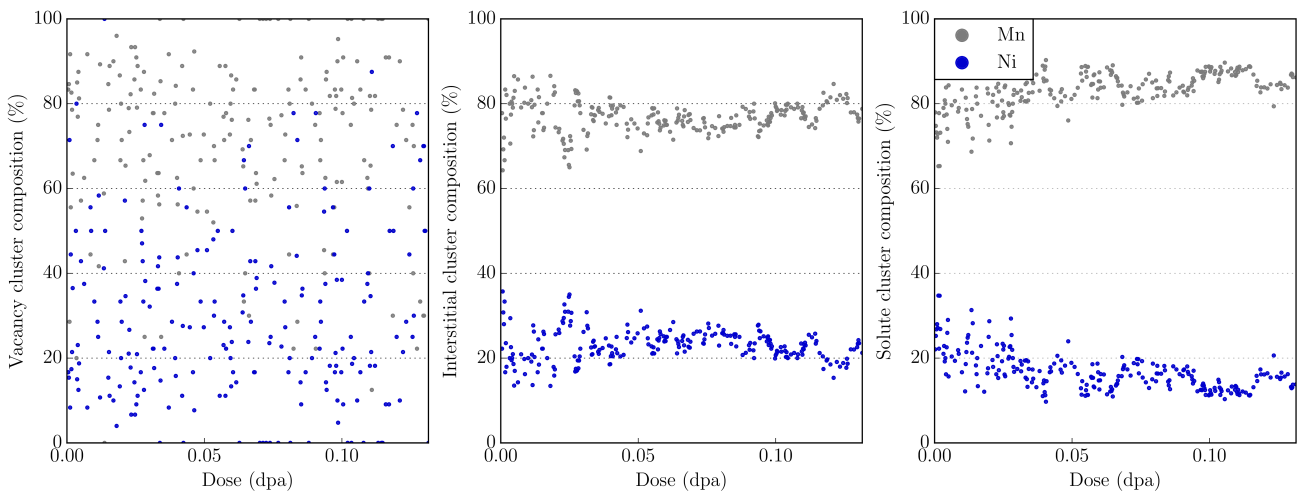


Figure 4-59: Evolution with the dose of the mean composition of the different types of clusters using the CDP model and the *SLT_LIMIT* hypothesis on a Fe-1.11Mn-0.68Ni (at.%) model alloy.

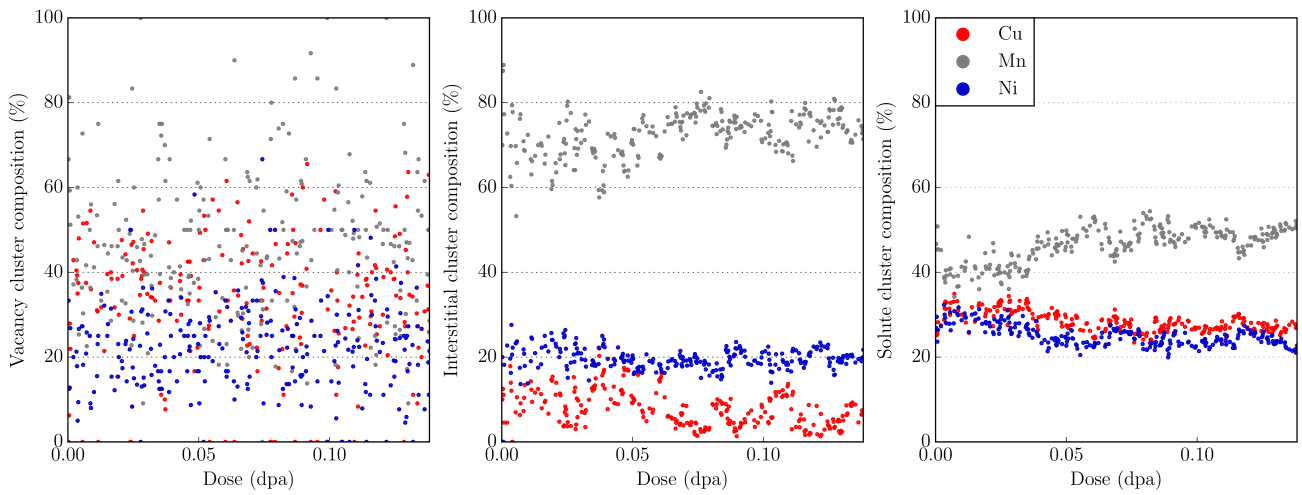


Figure 4-60: Evolution with the dose of the mean composition of the different types of clusters using the CDP model and the *SLT_LIMIT* hypothesis on a Fe-0.09Cu-1.11Mn-0.68Ni (at.%) model alloy.

The effect of copper has also been studied in two RPV model alloys. The compositions of these alloys are Fe-0.05Cu-1.38Mn-0.69Ni-0.47Si and Fe-0.18Cu-1.38Mn-0.69Ni-0.47Si (at.%). As shown in Figure 4-61 and Figure 4-62, the same increase of the solute cluster density observed when adding Cu to the FeMnNi alloy is found in these two RPV model alloys.

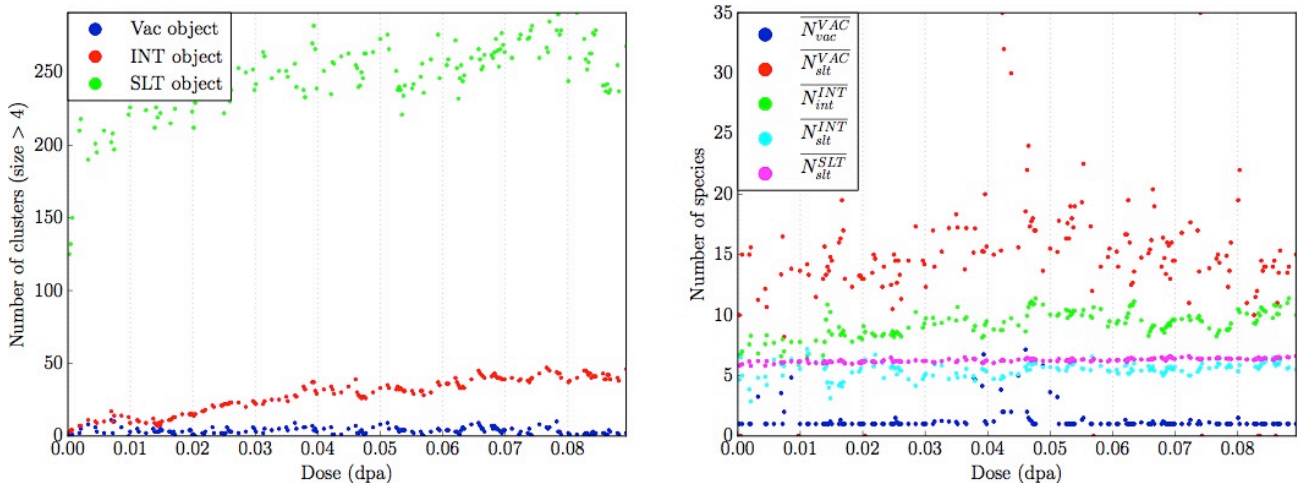


Figure 4-61: Evolution with the dose of the mean number of species in different types of clusters using the CDP parameterization and the *SLT_LIMIT* hypothesis in the Fe-0.05Cu-1.38Mn-0.69Ni-0.47Si (at.%) model alloy. The cluster criterion was set to 5 species.

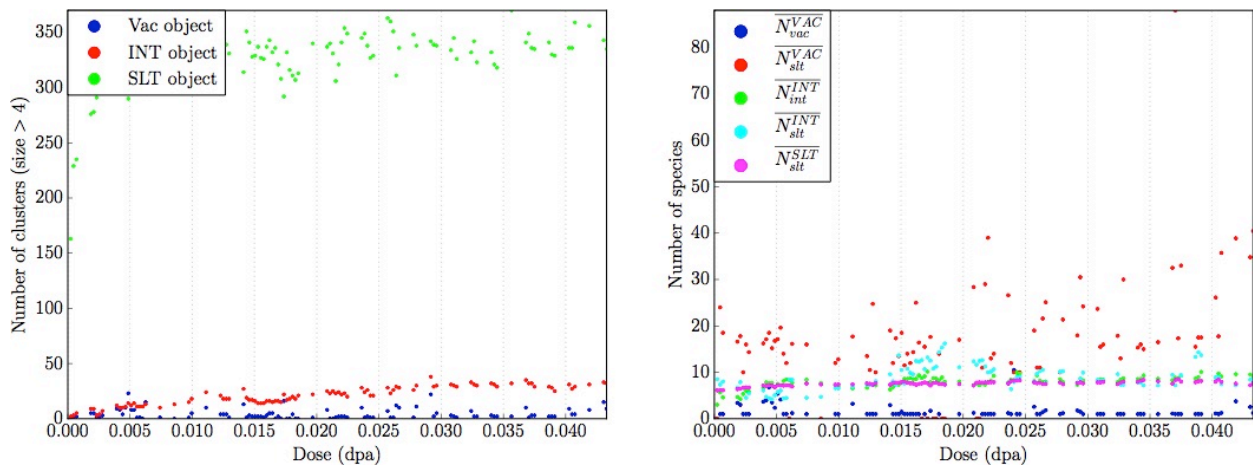


Figure 4-62: Evolution with the dose of the mean number of species in different types of clusters using the CDP parameterization and the *SLT_LIMIT* hypothesis in the Fe-0.18Cu-1.38Mn-0.69Ni-0.47Si (at.%) model alloy. The cluster criterion was set to 5 species.

Figure 4-63 and Figure 4-64 present the impact of copper on the mean composition of the clusters. The Mn, Ni and Si content of the SIA clusters appears to decrease and the Cu content increases. For the solute clusters, increasing the Cu content in the model alloy also leads to an increase of the Cu content in the solute cluster while the Mn and Si content decreases.

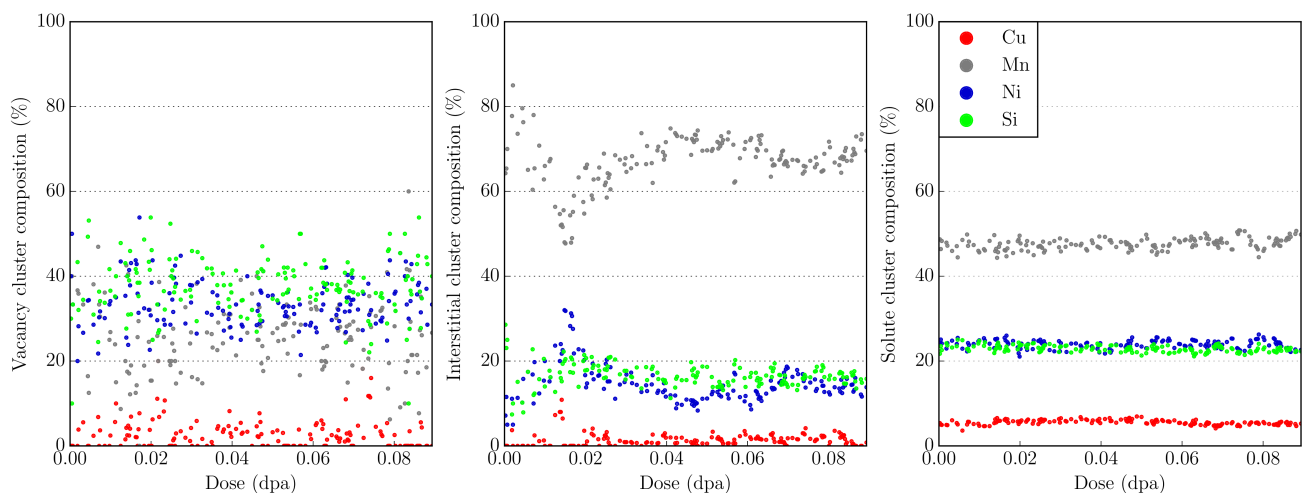


Figure 4-63: Evolution with the dose of the mean composition of the different types of clusters using the CDP model and the *SLT_LIMIT* hypothesis on a Fe-0.05Cu-1.38Mn-0.69Ni-0.47Si (at.%) model alloy.

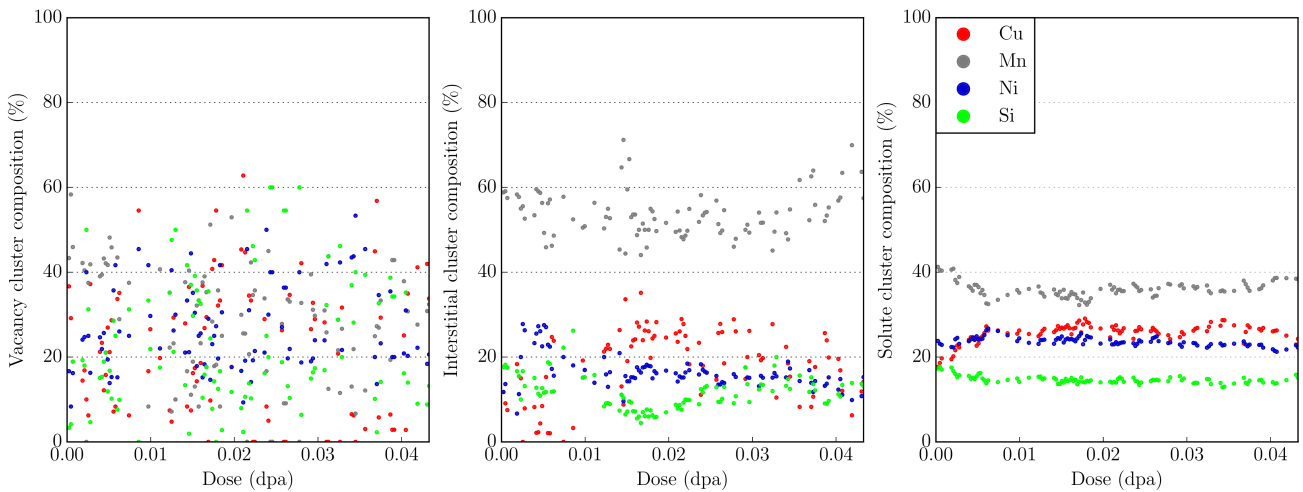


Figure 4-64: Evolution with the dose of the mean composition of the different types of clusters using the CDP model and the *SLT_LIMIT* hypothesis on a Fe-0.18Cu-1.38Mn-0.69Ni-0.47Si (at.%) model alloy.

The effects of adding copper in the matrix are summarized in Figure 4-65. Several observations can be made:

- Increasing the number of different solutes in the alloy leads to an increase of the solute cluster density.
- Adding Si atoms in the alloy seems to have an impact on the SIA cluster density. The Ni content of the SIA clusters also decreases;
- Adding Cu atoms to the alloy leads to a decrease of the Mn content in the solute clusters.

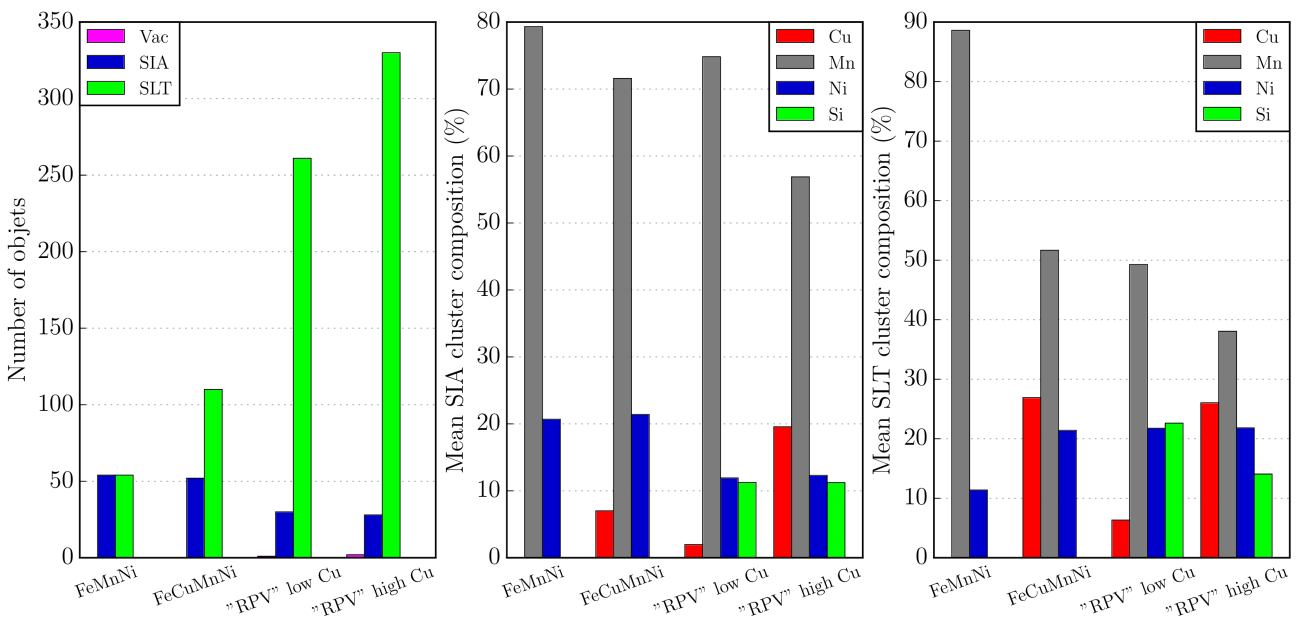


Figure 4-65: Comparison of the differences observed in the different alloys investigated. Results for the FeMnNi and FeCuMnNi model alloys were taken at 0.1 dpa. Results for the low and high Cu complex model alloys (denoted “RPV” in the figure) were taken at 0.04 dpa. These results have been obtained using the *SLT_LIMIT* hypothesis.

Figure 4-66 to Figure 4-69 assess the impact of the cluster size cutoff (presented in section 2.6.6 of the second chapter) on the results for the four model alloys simulated using the *SLT_LIMIT* hypothesis.

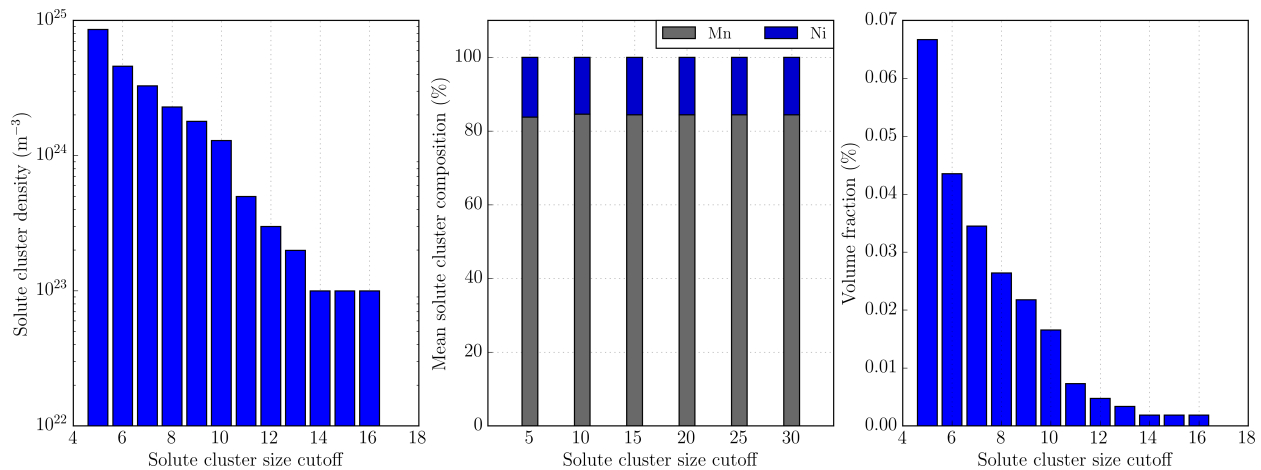


Figure 4-66: Evolution of the solute cluster density, mean composition, and volume fraction (respectively from left to right) as a function of the cluster size cutoff for the Fe-1.11Mn-0.68Ni (at.%) model alloy at 0.13 dpa.

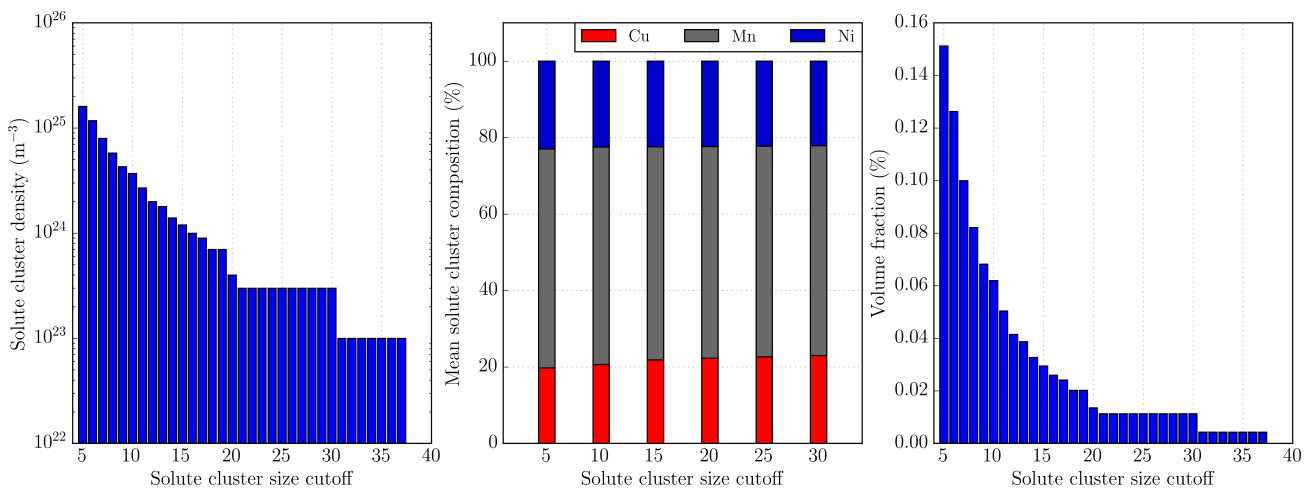


Figure 4-67: Evolution of the solute cluster density, mean composition, and volume fraction (respectively from left to right) as a function of the cluster size cutoff for the Fe-0.09Cu-1.11Mn-0.68Ni (at.%) model alloy at 0.13 dpa.

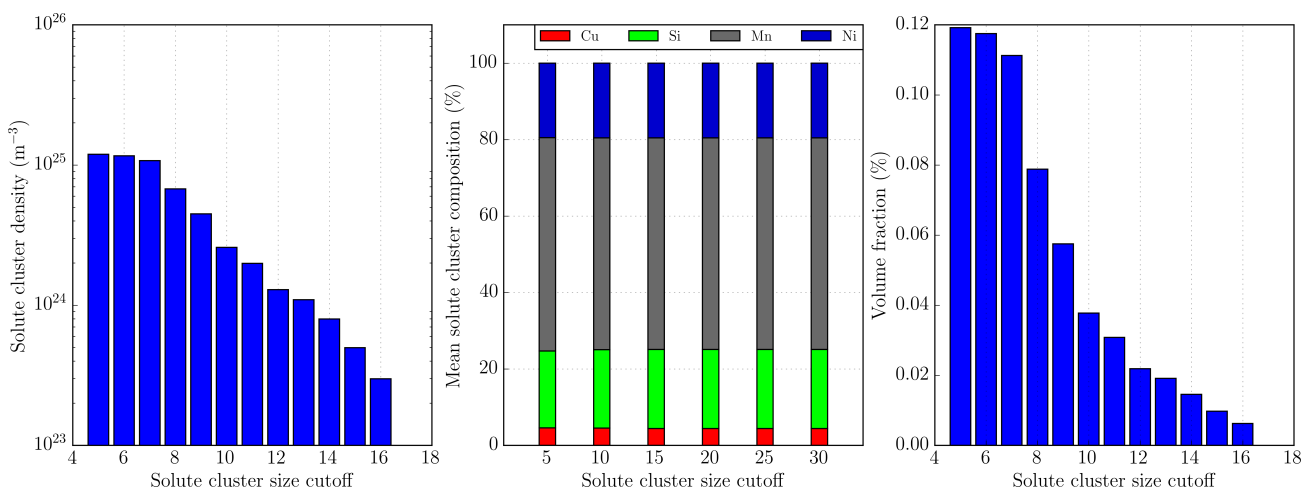


Figure 4-68: Evolution of the solute cluster density, mean composition, and volume fraction (respectively from left to right) as a function of the cluster size cutoff for the Fe-0.05Cu-1.18Mn-0.69Ni-0.47Si (at.%) model alloy (“RPV” low-Cu) at 0.09 dpa.

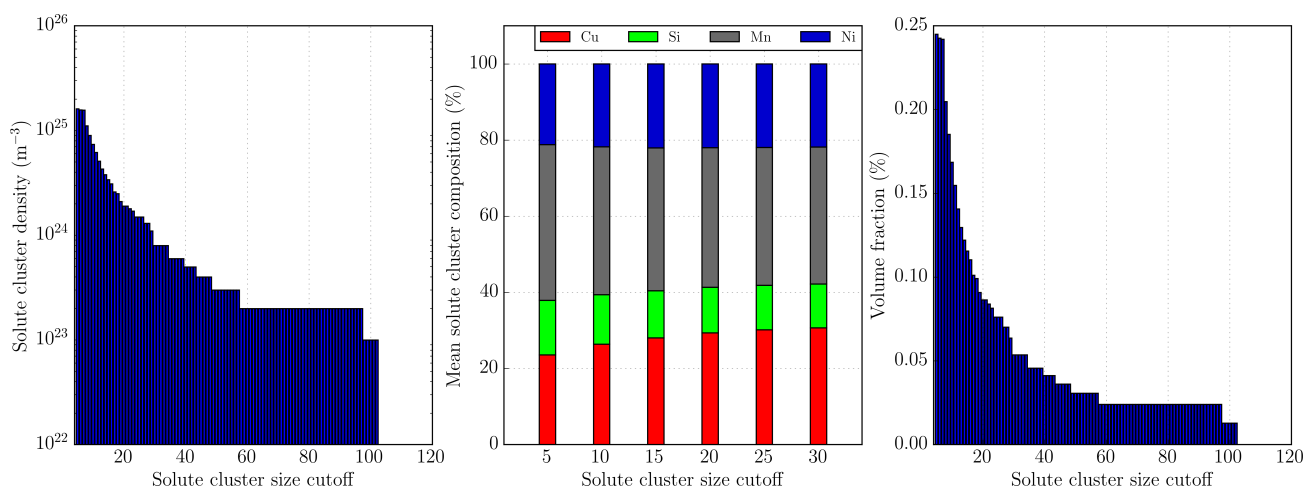


Figure 4-69: Evolution of the solute cluster density, mean composition, and volume fraction (respectively from left to right) as a function of the cluster size cutoff for the Fe-0.18Cu1.18Mn-0.69Ni-0.47Si (at.%) model alloy (“RPV” high-Cu) at 0.04 dpa.

The results indicate that the solute clusters that contribute the most to the solute cluster density are the smallest ones (size < 10). Large clusters (size > 30) are only observed in the model alloys containing a large quantity of Cu (e.g. Fe-0.09Cu-1.11Mn-0.68Ni and Fe-0.18Cu1.18Mn-0.69Ni-0.47Si (at.%)). The small clusters contribute the most to the total volume fraction. If we assume that the APT can detect solute clusters larger than size 12, our simulations overestimate the density of solute clusters for the two model alloys that contain the highest Cu content (since the cluster density should be lower than 10^{24} m^{-3}). Note however that solute clusters observed by APT are usually composed of a large fraction of Fe. Such dilute clusters are not observed in our simulations. Assuming that the cluster volume fraction should be in a range of about 0.3 – 0.4 % [16], with about 25 % of solutes and 75 % of Fe, we can estimate the partial solute cluster volume fraction to be close to 0.09 % which can be compared directly to our volume fractions (except in the FeMnNi case where the volume fraction is much lower than 0.1 %). The fact that the clusters formed in the experiments contain Fe has also an effect of their mean radius. A cluster with a radius of 1.5 nm (as observed in Huang’s RPV alloys [17]) contains close to 1200 atoms. If we remove the Fe atoms, we find that the cluster contains close to 240 solute atoms. For a 1 nm radius cluster (as observed in [16]), the correspondence is about 70 solute atoms. We do not observe such large clusters in our simulations. Hence, while the CDP model leads to larger solute clusters than the clusters obtained with our previous parameterization, they are still smaller than those observed experimentally.

We also find that mean compositions do not change with the cluster size cutoff for the FeMnNi and the low-Cu FeCuMnNiSi model alloys. However, there is an effect of the size of clusters on their mean compositions in the FeCuMnNi and the high-Cu FeCuMnNiSi model alloys: when the cluster size cutoff increases, more Cu tends to be found in the clusters.

4.4.6 Synthesis of the irradiation simulations with the hybrid CDP model

To reach the target dose, the CDP model has to be used with the hybrid AKMC/OKMC. Different emission models for the vacancy clusters have been employed. For a flux of $\sim 10^{-5}$ dpa/s, the model that provides the lowest emission frequencies (the *SLT_AS_VAC* model) allows the formation of large vacancy clusters. An effect of the flux has been observed in the case of a reduction of the flux from $\sim 10^{-5}$ dpa/s to $\sim 10^{-7}$ dpa/s in the case of the *SLT_AS_VAC* hypothesis. By giving more time to the vacancy clusters to emit, the formation of large vacancy clusters is hindered and they are thus not observed at the lowest flux. No flux effect has been observed concerning the solute clusters. Hence, the simulated microstructures using the *SLT_LIMIT* hypothesis at high flux are equivalent to those obtained using the *SLT_AS_VAC* at low flux. Another effect

that has been studied is temperature. Increasing the temperature from 600 K to 700 K reduces the trapping effects and the reachable doses are higher. However, the solute clusters are less numerous in the high temperature case while their mean composition remains unchanged.

The effect of Cu has been studied in the high flux regime and the results are in agreement with the experimental data: an increase of the Cu content leads to an increase of the solute cluster density. However, the solute cluster density is still overestimated while the volume fraction is underestimated.

Direct comparisons between simulated microstructures and experimental observations are still difficult to make. Solute clusters observed by APT are usually composed of a large fraction of Fe. And we do not observe such dilute clusters in our simulations.

4.5 Conclusion

A numerical method to explore the space of parameters has been developed to build a new cohesive model which explicitly takes into account the local concentration around a pair in the value of the pair interaction. By construction, this new cohesive model (CDP) is more flexible than the constant pair interaction model. When comparing the CDP model to other parameterizations present in the literature, we find that our model successfully describes a larger variety of objects (from small to large complex clusters). The new model also respects the specifications that motivated its creation: e.g. object stabilities more in agreement with the DFT predictions and an improvement of the transport through a vacancy mechanism.

The CDP model is numerically heavier than the previous pair interaction model and point defects get also trapped more easily (due to the larger value of the binding energies). Hence, a pure AKMC treatment of the vacancies makes the simulations too slow and the doses that can be reached to low. To accelerate the calculations the vacancy clusters have been treated as immobile objects (except for V_1 , V_2 and depending of the number of solutes V_3). Two models for the vacancy emission have been tested. Using this treatment, the target dose (0.1 – 0.2 dpa) has usually been reached. The reduction of the flux has an effect for the emission model providing the lowest emission frequencies. Concerning the improvement of the CDP model, the solute clusters formed are larger and more enriched in Ni and Si than in the previous cohesive model. This is a good point since it was the purpose of the development of this new model. However, the manganese remains the main element in the clusters while its concentration should be equivalent or lower to the nickel content.

4.6 Bibliography

- [1] C. L. Liu, G. R. Odette, B. D. Wirth, and G. E. Lucas, “A lattice Monte Carlo simulation of nanophase compositions and structures in irradiated pressure vessel Fe-Cu-Ni-Mn-Si steels”, *Materials Science and Engineering: A*, vol. 238, no. 1, pp. 202–209, 1997.
- [2] E. Vincent, PhD thesis, “Simulation numérique à l'échelle atomique de l'évolution microstructurale sous irradiation d'alliages ferritiques”, Lille University, 2006.
- [3] N. Maruyama, M. Sugiyama, T. Hara, and H. Tamehiro, “Precipitation and Phase Transformation of Copper Particles in Low Alloy Ferritic and Martensitic Steels”, *Materials Transactions, JIM*, vol. 40, no. 4, pp. 268–277, 1999.
- [4] K. Osamura, H. Okuda, and K. Asano, “SANS study of phase decomposition in Fe-Cu alloy added by Ni and Mn”, *ISIJ International*, vol. 34, no. 4, pp. 346–354, 1994.
- [5] M. K. Miller, K. F. Russell, P. Pareige, and M. J. Starink, “Low temperature copper solubilities in Fe–Cu–Ni”, *Materials Science and Engineering*, vol. 250, no. 1, pp. 49–54, 1998.
- [6] L. Messina, PhD thesis, “Multiscale modeling of atomic transport phenomena in ferritic steels”, KTH University, 2015.
- [7] P. D. Styman, J. M. Hyde, K. Wilford, A. Morley, and G. D. W. Smith, “Precipitation in long term thermally aged high copper, high nickel model RPV steel welds”, *Progress in Nuclear Energy*, vol. 57, pp. 86–92, May 2012.

- [8] L. Messina, M. Nastar, T. Garnier, C. Domain, and P. Olsson, “Exact ab initio transport coefficients in bcc Fe-X (X=Cr, Cu, Mn, Ni, P, Si) dilute alloys”, *Physical Review B*, vol. 90, no. 1, pp. 104203, Sep. 2014.
- [9] P. Olsson, T. P. C. Klaver, and C. Domain, “Ab initio study of solute transition-metal interactions with point defects in bcc Fe”, *Physical Review B*, vol. 81, no. 5, pp. 054102, Feb. 2010.
- [10] O. Senninger, PhD thesis, “Ségrégation et précipitation dans les alliages fer-chrome hors et sous irradiation”, Grenoble University, 2013.
- [11] E. Vincent, C. S. Becquart, and C. Domain, “Solute interaction with point defects in α Fe during thermal ageing: A combined ab initio and atomic kinetic Monte Carlo approach”, *Journal of Nuclear Materials*, vol. 351, no. 1, pp. 88–99, Jun. 2006.
- [12] H. Baker, *ASM Handbook Volume 3: Alloy phase diagrams, 1992*.
- [13] J. E. Zelenty, “Understanding thermally induced embrittlement in low copper RPV steels utilising atom probe tomography”, *Materials Science and Technology*, vol. 31, no. 8, pp. 981–988, Nov. 2014.
- [14] P. B. Wells, T. Yamamoto, B. Miller, T. Milot, J. Cole, Y. Wu, and G. R. Odette, “Evolution of manganese–nickel–silicon-dominated phases in highly irradiated reactor pressure vessel steels”, *Acta Materialia*, vol. 80, pp. 205–219, Nov. 2014.
- [15] R. E. Stoller, “The effect of free surfaces on cascade damage production in iron”, *Journal of Nuclear Materials*, vol. 307, pp. 935–940, Dec. 2002.
- [16] E. Meslin, M. Lambrecht, M. Hernández-Mayoral, F. Bergner, L. Malerba, P. Pareige, B. Radiguet, A. Barbu, D. Gómez-Briceño, A. Ulbricht, and A. Almazouzi, “Characterization of neutron-irradiated ferritic model alloys and a RPV steel from combined APT, SANS, TEM and PAS analyses”, *Journal of Nuclear Materials*, vol. 406, no. 1, pp. 73–83, Nov. 2010.
- [17] H. Huang, PhD thesis, “Influence de l’irradiation aux neutrons sur le vieillissement des aciers de cuves des réacteurs nucléaires à eau pressurisée”, Rouen University, 2012.

General conclusions and perspectives

The objective of this thesis was to improve an AKMC model that has been built to model and simulate the microstructural evolution experienced by the RPV steels under irradiation. In the simulations performed prior to this thesis, to observe a microstructure evolution, the flux simulated had to be very high (about 6 orders of magnitude greater than the in-service flux). In this condition, the dose reached was ~ 30 mdpa in 3 months of calculations. Hence, an acceleration of the simulation was required.

The first approach adopted to overcome the AKMC limitations has been to develop purely algorithmic optimizations in the LAKIMOCA code. It has been done by identifying the most time-consuming routines and by proposing some improvements. The advantage of the algorithmic optimizations is that they do not introduce any change or approximation in the simulation trajectory. The acceleration obtained on the runtime of the code is up to ~ 7 for the treatment of vacancy clusters. While this acceleration remains modest, it is very valuable when it comes to investigating the point defect cluster properties (such as diffusion and emission). The LAKIMOCA code has also been restructured importantly. These new foundations will make the future developments easier, faster and safer. Other optimizations have also been proposed in a model AKMC code. The sum of all of the optimizations employed makes the model code ~ 7 times faster on a typical irradiated RPV steel simulation.

Since algorithmic solutions were not sufficient enough to reach the target dose, the AKMC model had also to be modified. After collecting information from the literature about the KMC acceleration techniques, we realized that for each system, depending on its dimensionality, complexity and homogeneity, corresponds a specific acceleration method. Furthermore, the RPV model alloy under irradiation is penalized due to its 3D nature, the heterogeneous spatial distribution of walkers and the non purely random walks because of the presence of solute atoms. Therefore, the choice has been made to develop a hybrid AKMC/OKMC model. This was motivated by the fact that a large number of AKMC jumps were performed on quasi-immobile large point defect clusters. The first system studied by the hybrid method has been the pure iron system. Introducing an OKMC component in the model requires the knowledge of the macro rates involved in the simulations. Hence, a large panel of AKMC simulations have been performed on both vacancy and interstitial clusters with various sizes. These simulations were done to determine the migration and emission properties of the PD clusters. From this AKMC study, the vacancy clusters were found to be rather mobile and emission was observed. Concerning the interstitial clusters, their mobilities were found to be lower than the mobilities of vacancy clusters and no emission was observed. Moreover, the model predicted the SIA clusters above size 13 to be immobile.

Using the object properties obtained by means of AKMC, the hybrid method has been tested on isochronal annealing experiments still for pure Fe. We found that the hybrid method does not introduce any notable bias and the acceleration of the simulation was about 200. Turning to irradiation simulations, we managed to reach the target dose (0.1 – 0.2 dpa). However, the results highlighted some limitation in the AKMC model. First, due to the presence of absorbing surfaces aiming at simulating heterogeneities such as grain boundaries, no vacancy accumulation was observed in the simulations. This is not in agreement with the experimental observations. Consequently, no flux effect was observed, again in disagreement with experiments. To improve this aspect new features have been implemented in the code. On the one hand, a trap model has been introduced to reproduce the effect of impurities such as carbon in the material. On the other hand, a sink model has been developed to reduce the sink strength induced by the presence of absorbing surfaces. These new features make the accumulation of vacancies observable under irradiation.

For the solute treatment in the hybrid method, an attempt has been made to obtain the properties of the mixed solute-vacancy objects using AKMC. The focus was made on binary vacancy clusters. We found in FeCu simulated model alloy with high Cu concentration that the trajectories of the hybrid simulations were biased when compared to the standard AKMC. Building an OKMC model, for the FeCu system under irradiation, that competes with an AKMC model appeared thus to be very complex since the hybrid method is not

adapted to system where solute atoms precipitate. For the Vac-Mn/Ni clusters, the fact that they dissociate very easily makes the evaluation of their mobilities and emission frequencies difficult to obtain. Due to the complexity encountered to build an object treatment for vacancies even in binary alloys, the choice was made to let the vacancies evolve in an AKMC state. However, due to the immobile nature of large interstitial clusters (predicted by the model), an important quantity of computation has been saved and the target dose has been attained in RPV like steel. A sink model has also been employed for the simulation of the RPV under irradiation but reachable doses are much lower than in the absorbing surface case (typically 20 mdpa versus 150 mdpa). From the high dose RPV simulation using the hybrid method without the sink model, some conclusions have been made. Firstly, the model predicts too small and too many solute clusters. Secondly, the same artifact as in pure iron has been found when using absorbing surfaces. This will make the observation of a flux effect difficult. Thirdly, the mean solute composition of the clusters is different when compared to the APT observation. The manganese content in the clusters was indeed overestimated while the nickel and silicon ones were underestimated. This observation has led to the development of a new cohesive model aiming to reproduce recent results from DFT calculations.

After a comparison between different AKMC parameterizations present in the literature, the following conclusion has been made: pair interactions may not be sufficient to describe the energetic aspects of RPV complexity. Indeed, employing a “classic” 2NN pair interaction model appears not to be capable of describing the properties of complex nanofeatures as obtained by DFT. Moreover, the superiority of triplet interaction model over pair interaction model was not found to be so clear. Hence, a new cohesive model based on concentration dependent pair interactions (CDP) has been created. Due to the increase of the number of degrees of freedom, the CDP model is more flexible than pair interactions but it is also more difficult to parameterize. Thus, a numerical approach to explore the space of parameters was developed. The selection of the parameter set has been made on fundamental properties such as the binding energies, vacancy formation energies and mixing energies but also on the predicted stability of various objects studied using PAW DFT. The selected parameterization turns out to be predictive to describe the stability of small complex objects. On the down side, the increase in the new cohesive model complexity makes the simulations slower. From the numerical point of view, the number of AKMC steps per unit time is about 9 times lower than using the classic pair interaction model. From the physical point of view, the system experiences more trapping effects than before. This is due to the higher binding energies predicted by the model (in agreement with PAW DFT). However coupling the CDP model with the hybrid method makes the target dose reachable. Noticeable improvements concerning the composition of the solute clusters obtained during irradiation simulations using the new model have been observed. The nickel and silicon content in the clusters is higher than in the previous model. The solute clusters are also larger. This was the purpose of CDP model and the simulated microstructures are now more in agreement with the experimental observations.

Perspectives

Concerning the numerical aspect of LAKIMOCA, a new code structure based on function pointers has been proposed. The objective of this proposition is to avoid a large amount of unnecessary tests and also to make the introduction of new models very simple. From the performance point of view, implementing a back-jump algorithm that takes the locality of the jump into account will have great impact on the performance of the code. Currently, using a very simple back-jump algorithm already avoids an important number of jump frequency calculations. However, the number of calculations that can be avoided is higher. Avoiding those calculations may lead to an important speed-up making the large quantity of back-jumps less penalizing. The last issue concerning the AKMC code is memory usage. Currently, the entire crystal is stored in memory. This makes the simulation of large systems difficult. An original way to solve this issue may be to build an AKMC based on the OKMC logic. Indeed, in the OKMC only objects are stored in memory. From the AKMC perspective a solute atom could be considered as an object. This will make large systems accessible to the AKMC. However, to maintain the accurate AKMC treatment, the local environment around a point

defect will have to be actualized on the fly. Since the crystal is stored in memory in a “classic” AKMC, this process is fast (simply by going through an array). Using the OKMC logic implies a drop in performance due to the necessary distance calculations to perform the local environment update. It is a competition between memory usage and performance. However, simulating larger system might make parallelization algorithm more efficient because of smoothed spatial distribution of point defects when the sub-domain sizes increase.

From the atomistic point of view, several parts of the model could be improved. Now that a predictive cohesive model exists, the barrier model needs to be investigated in detail. A benchmark between the FISE model and results from DFT calculations (in realistic cases) is a necessity. Depending on the outcome of this benchmark, a new barrier model should (or not) be developed. If a new barrier model has to be developed, a simple approach may consist in giving a dependency on the local environment at the saddle-point for the calculations of jump frequencies. This way, the E_{a0} term in the FISE model will no more depend only on the atom that performs the jump but on the 6 nearest atoms at the saddle-point for instance. Moreover, a large database of DFT calculations already exists and may be used as input data for the development of a more precise barrier model. For the interstitial treatment, the model can also be improved. For the time being, the interstitial model implemented cannot simulate the complex motion of medium to large size interstitial clusters. Improving the on-lattice interstitial treatment from the atomistic point of view may be too complex. However, using a potential and a “kART like method” could be a way to obtain a parameterization for the SIA clusters in the object part of the hybrid method developed during this thesis.

Once the whole energetic model of the AKMC is validated, a construction of a large database of object properties depending on the solute composition might be achieved. Due to the combinatorial explosion, it will no be possible to treat all possible cases. However, using artificial neural network or sensitivity analysis models, expanding this database to unknown configuration might be possible.

With all these improvements, a precise prediction of the nano-structure evolution of RPV irradiated at high doses should be achievable.

Annex I LAKIMOCA profilings

a) Algorithmic acceleration

In order to accelerate the LAKIMOCA code, the first optimizations proposed in this PhD were purely algorithmic. The following figures present the profiling result associated with RPV steel (Fe-0.18Cu-0.69Ni-1.38Mn-0.47Si-0.01P (at.%) + 20 randomly distributed vacancies) simulations. The number of AKMC steps for the profiling was 5×10^7 . Figure 1 shows the profiling of the code before optimizations and Figure 2 after.

```
Each sample counts as 0.01 seconds.
```

% time	cumulative seconds	self seconds	calls	self s/call	total s/call	name
27.56	119.20	119.20	10659926082	0.00	0.00	calcul_dene_v1
15.95	188.21	69.01	4919965884	0.00	0.00	calcul_dene_v2
9.49	229.25	41.04	1021994314	0.00	0.00	eatom
8.27	265.01	35.76	409997157	0.00	0.00	calcul_de
8.12	300.15	35.14	50000000	0.00	0.00	one_deplacement
6.14	326.71	26.56	1300000000	0.00	0.00	do_dene_v1
3.37	341.29	14.58	50000000	0.00	0.00	do_jump
2.61	352.59	11.29	411509144	0.00	0.00	calcul_proba
2.60	363.82	11.23	202	0.06	0.06	ecrire2
2.26	373.59	9.78	600000000	0.00	0.00	do_dene_v2
1.38	379.55	5.96	50000000	0.00	0.00	choix_vacancy_jump
0.84	383.20	3.65	1844245735	0.00	0.00	inc_py
0.83	386.78	3.58	1844245735	0.00	0.00	inc_pz
0.81	390.30	3.53				find_amas
0.80	393.75	3.45	1844245735	0.00	0.00	inc_px
0.79	397.18	3.43	51438643	0.00	0.00	calc_proba_vac
0.56	399.61	2.43	51438643	0.00	0.00	nb_fia_in_vac
0.54	401.93	2.32	1029419914	0.00	0.00	inc_px1
0.47	403.97	2.04	1029419914	0.00	0.00	inc_pz1
0.45	405.93	1.96	1021994314	0.00	0.00	inc_pz2
0.45	407.87	1.95	972739434	0.00	0.00	inc_mx
0.42	409.69	1.82	1021994314	0.00	0.00	inc_px2
0.42	411.49	1.80	50	0.04	8.15	run

Figure 1: Profiling before optimizations (using the “Pair2NN-Vincent” parameterization).

```
Each sample counts as 0.01 seconds.
```

% time	cumulative seconds	self seconds	calls	self s/call	total s/call	name
22.79	33.43	33.43	50000000	0.00	0.00	one_deplacement
17.41	58.97	25.54	1300000000	0.00	0.00	do_dene_v1
13.61	78.94	19.97	51438643	0.00	0.00	calc_de_vac_FS
9.23	92.48	13.54	50000000	0.00	0.00	do_jump
7.87	104.03	11.55	202	0.06	0.06	ecrire2
6.63	113.76	9.73	600000000	0.00	0.00	do_dene_v2
5.60	121.97	8.21	202000000	0.00	0.00	eatom
3.51	127.12	5.15	50000000	0.00	0.00	choix_vacancy_jump
2.15	130.28	3.16	51438643	0.00	0.00	calc_proba_vac
1.74	132.84	2.56	51438643	0.00	0.00	nb_fia_in_vac
1.29	134.73	1.89	51	0.04	0.16	energy
1.24	136.55	1.82	50	0.04	2.50	run

Figure 2: Profiling after optimizations (using the “Pair2NN-Vincent” parameterization).

For the old version of LAKIMOCA, jump frequency calculations were consuming $\approx 55\%$ of the computation time ($calcul_dene_v1 + calcul_dene_v2 + calcul_de + calcul_proba$). With the new function, it costs $\approx 14\%$ ($calc_de_vac_FS$). The number of function calls is also quite lower with the new function than it is with original version.

b) Irradiation simulation

Figure 3 presents the profiling result associated to the Fe-0.18Cu-0.69Ni-1.38Mn-0.47Si-0.01P model alloy starting from a microstructure obtained at 10 mdpa at 600 K. This microstructure is called “advanced microstructure”. The number of AKMC steps for the profiling was 5×10^7 .

```
Each sample counts as 0.01 seconds.
```

%	cumulative	self	self	self	total	
time	seconds	seconds	calls	s/call	s/call	name
47.93	867.01	867.01	50000000	0.00	0.00	one_deplacement
35.16	1503.01	636.00	530369209	0.00	0.00	calc_proba_int
3.17	1560.39	57.38	50000000	0.00	0.00	choix_event
3.10	1616.54	56.15	50000001	0.00	0.00	sum_proba_all_int
2.11	1654.63	38.09	48649224	0.00	0.00	recomb_int_vac
0.92	1671.35	16.72	50000001	0.00	0.00	sum_proba_all_vac
0.80	1685.77	14.42	3706760884	0.00	0.00	inc_px
0.80	1700.18	14.41	3706760884	0.00	0.00	inc_py
0.69	1712.64	12.46	48649224	0.00	0.00	do_int_jump
0.67	1724.79	12.15	13207921	0.00	0.00	calc_de_vac_FS
0.63	1736.17	11.38	3706760884	0.00	0.00	inc_pz
0.46	1744.49	8.32	1350776	0.00	0.00	recomb_vac_int
0.39	1751.56	7.07	202	0.04	0.04	ecrire2
0.34	1757.74	6.18	8939759	0.00	0.00	change_local_energy_after_int_jump
0.30	1763.25	5.51	97298448	0.00	0.00	_prod_m_v_
0.28	1768.25	5.00	50	0.10	35.45	run
0.25	1772.84	4.59	8939759	0.00	0.00	compute_local_energy
0.24	1777.26	4.42	53	0.08	0.08	find_amas_all
0.23	1781.48	4.22	52	0.08	0.18	order_analysis
0.23	1785.67	4.20	44064240	0.00	0.00	eatom
0.14	1788.25	2.58	13207921	0.00	0.00	calc_proba_vac
0.11	1790.15	1.90	44064240	0.00	0.00	inc_mz2
0.10	1791.88	1.73	1350776	0.00	0.00	do_jumpacc_bcc
0.09	1793.44	1.56	51	0.03	0.18	energy
0.09	1795.00	1.56	50000001	0.00	0.00	proba_ext_event
0.07	1796.20	1.20	53	0.02	0.02	find_cu_alone
0.07	1797.39	1.19	48649216	0.00	0.00	absorb_border_int

Figure 3: Profiling from an advanced irradiation microstructure using the “Pair2NN-Vincent” parameterization.

It can be shown that about half of the computation time is spent in the *one_deplacement* routine. This routine is basically in charge of distance computation to see if the previous jump affects other jumps. A solution to this large amount of time spent on distance calculation is to use a linked-cell approach.

c) CDP simulation

Still from the advanced irradiated microstructure, a full AKMC simulation has been performed using the CDP model. Figure 4 presents the results of this profiling. The number of AKMC steps for the profiling was 5×10^7 .

```
Each sample counts as 0.01 seconds.
```

%	cumulative	self	self	self	total	
time	seconds	seconds	calls	s/call	s/call	name
62.35	3973.79	3973.79	409956826	0.00	0.00	eatom_uniq_CDP_opti2
12.34	4760.44	786.65	50000000	0.00	0.00	one_deplacement
6.27	5159.79	399.35	319969506	0.00	0.00	calc_proba_int
5.93	5538.03	378.23	889466824	0.00	0.00	eatom_uniq_CDP
2.17	5676.51	138.48	162079393	0.00	0.00	eatom_uniq_CDP_opti
1.37	5763.82	87.31	10202656055	0.00	0.00	inc_py
1.35	5849.83	86.01	13314029	0.00	0.00	recomb_vac_int
1.33	5934.88	85.05	10202656055	0.00	0.00	inc_pz
1.12	6006.49	71.60	10202656055	0.00	0.00	inc_px
0.91	6064.29	57.81	50000001	0.00	0.00	sum_proba_all_int
0.88	6120.17	55.88	188991770	0.00	0.00	count_around_atom_CDP
0.75	6168.14	47.97	50000000	0.00	0.00	choix_event
0.52	6201.36	33.22	900091928	0.00	0.00	calcul_proba
0.44	6229.36	28.00	36685971	0.00	0.00	recomb_int_vac
0.31	6249.11	19.75	19862257	0.00	0.00	update_local_DE_CDP_ac
0.30	6268.05	18.94	112511491	0.00	0.00	calc_proba_vac
0.26	6284.72	16.68	50000001	0.00	0.00	sum_proba_all_vac
0.22	6298.62	13.90	44064000	0.00	0.00	inc_mz2
0.20	6311.50	12.88	36685971	0.00	0.00	do_int_jump
0.11	6318.63	7.13	202	0.04	0.04	ecrire2
0.10	6325.27	6.64	572036219	0.00	0.00	calc_de_vac_CDP

Figure 4: Profiling from the advanced irradiation microstructure using the CDP model.

From this profiling, we note that the *one_deplacement* routine becomes negligible when compared to the heaviness of the CDP routines (all the routines containing the keyword CDP). While about half of the computation time is spent in *one_deplacement* using the Pair2NN-Vincent parameterization, only 12% is spent it using the CDP model. Despite all of the algorithmic optimizations made to make the CDP suitable for kinetic simulations (see Annex III), about 75% of the computation time is spent in the different CDP routines responsible for the jump frequency calculations or energy actualization.

Annex II

Proposal for future developments

The LAKIMOCA code has grown during the last decade to embed new cohesive models, new barrier models and new crystal geometries. These implementations have been made either by employing preprocessor conditional inclusions or by repeating several tests during the execution. While this method has not much impact on the overall performance of the code, it can make it more difficult to read, maintain and enhance. Another way to deal with all of the LAKIMOCA possibilities without increasing the sources complexity is to use function pointers. The idea is to declare a generic function to perform one specific task. For example it can be the function that computes the jump frequency of a point defect, the function computing the total energy of the system, the function that performs a jump etc. Function pointers will represent these generic functions. Hence, at the beginning of the simulation, these function pointers will point to the function of interest (depending on the user request). Figure illustrates this principle.

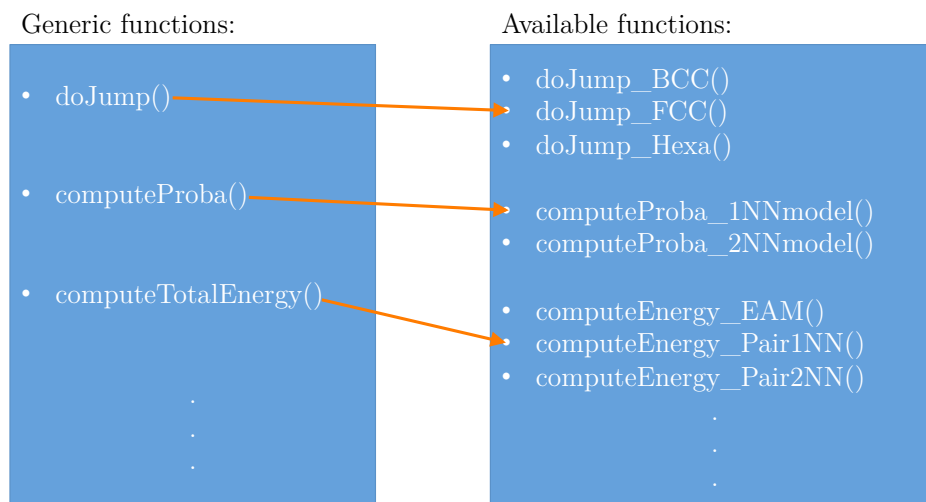


Figure 1: Illustration of the function pointers. Assuming the user requires a simulation on a FCC system using a 1NN cohesive model. At the beginning, the generic functions points to the appropriate functions. In the rest of the code, only the generic function is present.

The advantage of this method is that preprocessor conditional inclusions are no longer required. Moreover, tests are performed only one time (after reading the user input) so there is no need to repeat these tests in the loop over the AKMC steps. A comparison between the current way and the proposed number of tests using function pointers. The left code block represents the current way of doing tasks. The right code block used the function pointer.

```

#include <stdio.h>
#include <stdlib.h>
#include <performJumpA.h>
#include <performJumpB.h>

/**
 * Switches for the way to
 * perform a jump */
int performJump_methodA = 0;
int performJump_methodB = 0;

/**
 * nstep is the number of akmc
 * steps to performed.          */
double nstep = 0.;

int main(int argc, char *argv[])
{
    int i;
    /**
     * id of the PD that jumps */
    int id;
    /**
     * direction of the jump */
    int dir;

    /**
     * The user choose its simulation
     * method (for example the way to perform the
     * jumps, the number of akmc steps etc
     ...) */
    readUserInput();

    for(i=1; i<=nstep; i++){
        doSeveralThings();

        if(performJump_methodA==1){
            doJump_methodA(id, dir);
        } else if(performJump_methodB==1){
            doJump_methodB(id, dir);
        }
    }

    printf("ALL DONE\n");
    return 0;
}

```

```

#include <stdio.h>
#include <stdlib.h>
#include <performJumpA.h>
#include <performJumpB.h>

/**
 * Switches for the way to
 * perform a jump */
int performJump_methodA = 0;
int performJump_methodB = 0;

/**
 * nstep is the number of akmc
 * steps to performed.          */
double nstep = 0.;

/**
 * Pointer to a function that takes
 * two integers as argument and
 * returns nothing */
void (*doJump)(int,int)=NULL;

int main(int argc, char *argv[])
{
    int i;
    /**
     * id of the PD that jumps */
    int id;
    /**
     * direction of the jump */
    int dir;

    /**
     * The user choose it simulation
     * method (for example the way to perform the
     * jumps, the number of akmc steps etc
     ...) */
    readUserInput();

    if(performJump_methodA==1){
        doJump = &doJump_methodA;
    } else if(performJump_methodB==1){
        doJump = &doJump_methodB;
    }

    for(i=1; i<=nstep; i++){
        doSeveralThings();
        doJump(id, dir);
    }

    printf("ALL DONE\n");
    return 0;
}

```

Annex III

Performance aspects of the CDP model

In the new CDP cohesive model, the number of sites affected by a vacancy jump is much higher than in our previous pair interaction model (from 22 sites to 84). Figure 1 illustrates this increase in complexity.

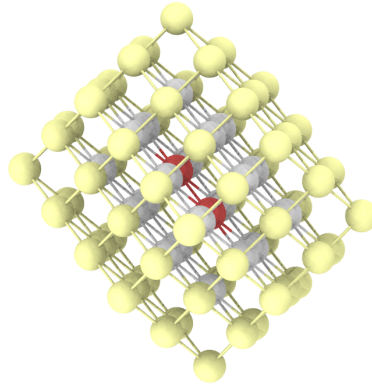


Figure 1: Illustration of the range of the CDP interactions around the jumping pair (red). The white sites are the 1NN and 2NN of the jumping pair (only these sites are affected in the previous 2NN pair interaction model). We call them “the first shell”. The yellow sites are the 1NN and 2NN of the first shell (called the second shell) have to be energetically actualized in the CDP model.

Increasing the complexity of a model often results in a decrease of the global performances. It was the case of the CDP model. In the FISE context, performing a jump requires to compute the energy variation after and before the permutation. A basic brute-force method to do so can be described as follows:

- Compute the total energy in a sufficient volume around the jump pair. As a first implementation, the volume corresponds to a square containing all the atoms presented in Figure 1.
- Perform a jump one of the eight different 1NN jump that the vacancy can perform.
- Recompute the total energy in the previous volume and calculate the energy difference with the initial state.
- Put back the PD to its original position.
- Return to the second step with another jump orientation.

Algorithmic solution:

This method was first implemented for the preliminary study of the CDP model. While it was useful for exploring the model, the slow down of the global execution of the code tends to become unmanageable for long-term kinetic simulations (especially when the number of defects is high). Figure 2 illustrates the issue in a schematic manner.

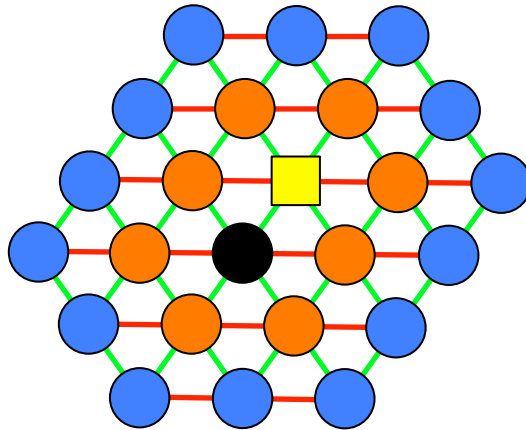


Figure 2: Visual support for the coordination variation after the jump of a vacancy involving an iron atom. The figure represents a slice of the volume shown in Figure 1. The orange atoms represent the first shell around the vacancy-iron pair. The blue atoms represent the second shell. 1NN distances are displayed in green while 2NN distances are in red.

Due to the current definition of the local concentration α , jumps involving a Fe atom can be distinguished from those involving a solute atom. Jumps involving solutes are the simplest to treat because there is no variation of the local concentration. In this case, only orange atoms and the permuting pair are affected by the on-site energy variation. In the case of a Fe migration, local concentrations of the atoms in the first-shell (as well as the atoms constituting the jumping pair) are affected. This implies on-site energy variation of the second-shell.

At the beginning of the simulation, all jump directions are tabulated. For each jump direction, the relative positions of the first/second-shell atoms to the vacancy are stored. The possible coordination changes are also stored in memory for each jump. This limits the number of large array calls to the minimum and it allows reasonable performances making irradiation simulations possible.

An attempt to parallelize the function in charge of the calculations of the jump frequencies has also been performed. Unlike the first attempt performed in chapter 3 section 3.2.2, the parallelized version does not have a negative impact on the runtime. However, it does not have a benefic impact too. Hence, the CDP model seems to be at the edge for making parallel calculations advantageous.

Annex IV

New commands in LAKIMOCA inputs

Introducing the OKMC/AKMC hybrid method, trap model and sink leads to new commands that can be used in the input file. The following list presents these new commands.

1) Hybrid related command (code compiled with `-DOBJ` option):

- `VAC_mobility filename`: Provide the path to the vacancy cluster properties file for the object treatment.
- `INT_mobility filename`: Provide the path to the interstitial cluster properties file for the object treatment.
- `Rebuild_Objns nsteps`: By default, the objects are rebuilt every `NRUN` AKMC steps (see LAKIMOCA documentation for more details). However, the user can get a more precise control on the object rebuild frequency by providing a value after the `Rebuild_Objns` tag.
- `vac_obj_size_cutoff size`: Under the `size` value, the vacancy clusters are purely treated in AKMC. Otherwise, there are treated in hybrid AKMC/OKMC.
- `int_obj_size_cutoff size`: Under the `size` value, the interstitial clusters are purely treated in AKMC. Otherwise, there are treated in hybrid AKMC/OKMC.
- `vac_nbr_slt_limit nlimit`: By providing a value to `nlimit`, the user can choose to consider vacancy objects as immobile when the number of solutes in the cluster is higher or equal to `nlimit`.
- `int_nbr_slt_limit nlimit`: By providing a value to `nlimit`, the user can choose to consider interstitial objects as immobile when the number of solutes in the cluster is higher or equal to `nlimit`.
- `int_1D_limit size`: Provide a 1D motion to the interstitial clusters when the size of the cluster is above the `size` value. However, the direction can change every time the object is rebuilt.

2) Trap commands (code compiled with `-DTRAP` option):

- `trap_C quantity`: Add randomly distributed traps in the simulation box according to the user `quantity` input in at.%.
- `Trap_Eb filename`: Provide the path to the trap parameterization file.

3) Sink command (no compilation option is required):

- `one_sink rvac rint xpos ypos zpos`: Add one sink at the $(xpos, ypos, zpos)$ location in the `T[][][]` array representing the crystal. The capture radius can be specified for both vacancies and interstitials (respectively `rvac` and `rint`). The distance is given in lattice unit squared

(giving a value of 4 corresponds to a 2NN distance).

4) CDP cohesive model command (no compilation option is required):

- `potential cdp_vij f filename`: Use the CDP model according to the *filename* parameterization file.

An example of an input file is given below:

```
Ncell 100 100 100
a 2.855
Te 563.
potential ppair2 d ./Vac_FeCuMnNiSiP_trap
paramint ./Int_FeCuMnNiSiP_I2CP_opti_Mn_P_trap
nu 6.0E12
NLOOP 500000
NRUN 10000000 10000000
kmc
NADDV 0
PBC 1
seed 79663962
one_sink 4 4 50 50 50
trap_C 0.026
Emig0 Fe 0.62
time_matrix 1
outxyz 1
analysis 1
analysis_cluster 2
analysis_tap 0
outsltdefxyz 1
vac_obj_size_cutoff 2
int_obj_size_cutoff 1
VAC_mobility vac.in
INT_mobility int.in
Rebuild_Objs 500000
int_1D_limit 6
Trap_Eb trap.in
drecomb_int 2.83
irradn 1E-1 nbs ../../rkn20_100
BJ_tag 0
```

This simulation performs irradiation in pure iron in a $100 \times 100 \times 100$ a_0 box with PBC in all direction at 563 K. A quantity of 0.026 (at.%) of traps is added as well as a sink with a 2NN capture radius at the center of the box. Vacancy and interstitial clusters are treated as object respectively from size 2 and 1. The objects are rebuilt every 500000 AKMC steps. Above size 6, SIA clusters perform 1D diffusion.

Annex V

New input file formats

1) Object properties in the hybrid method:

The input files are column text files with this format:

#size	nui(diff)	Emi(diff)	nui_eb(emiss)	Emi_eb(emiss)	eb2(emiss)
6	2.74e+13	1.07	1.75+15	0.62	0.86
7	3.97e+12	0.97	7.05+13	0.62	0.61
8	9.04e+12	1.07	1.07+15	0.62	0.86
9	3.15e+12	0.98	5.62+13	0.62	0.63
...					

- size: The size of the object in number of point defects
- nui(diff): Prefactor for migration jump frequency
- Emi(diff): Activation energy for migration jump frequency
- nui_eb(emission): Prefactor for emission frequency
- Emi_eb(emission)+eb2(emission): The sum of these two terms gives the activation energy of emission. Usually, Emi_eb is the migration energy of the vacancy in iron.

2) Object properties in the hybrid method:

The input files are column text files with this format:

#size	eb_vac	eb_int
1	0.	0.17
2	1.1	0.28
3	0.93	0.36
4	0.96	0.34
...		

- size: the size of the object in number of point defects
- eb_vac: binding energy (eV) between the vacancy cluster and the trap
- eb_int: binding energy (eV) between the interstitial cluster and the trap

3) CDP parameterization file format:

The input files are text files. The format is given below for the FeCu:

```

D
1 1 2 -0.52 1.
2 1 2 -0.518334 1.
1 2 2 -0.683033 1.
2 2 2 -0.478392 1.
C
1 1 2 -0.5 1.
2 1 2 -0.48 1.

```

```
1 2 2 -0.4 1.  
2 2 2 -0.63 1.  
@
```

When the parser reaches a *D* followed by a space or a newline, the code is aware that the next lines will refer to the dilute case. The first column corresponds to the interaction range (1NN or 2NN). The second and the third column refers to the atom type. In this example “1” corresponds to Fe and “2” to Cu (see the LAKIMOCA documentation for more details). The fourth column is the value of the interaction. The last column is the β parameter presented in chapter 4 section 4.3.1.

When the parser reaches a *C* followed by a space or a newline, the code is aware that the next lines will refer to the concentrate case. The syntax of this block is the same than the previous one. It is recommended to had an @ character at the end of a parameterization block to specify the end of the block. In between parameterization blocks, the user can write information about the properties of the parameterization.

Annex VI

The speed-check file

The file *speed-check.c* is a collection of routine to search for a suitable CDP parameterization. Before the introduction of these new functions, LAKIMOCA provided a library called *checkpoint*. This library was used to obtain an important number of properties provided by a given parameterization (such as E_b , E_{int} , E_{mix}). Due to the large number of properties, a call to the *checkpoint* functions leads to an important number of calls to the functions that generate and compute the total energy of the system. Hence, it is difficult to loop over the *checkpoint* functions when the number of parameterization to check becomes too large, and in the CDP parameterization we generated several millions of parameterizations. The *speed-check* library can be seen has a reduction of the *checkpoint* library. Since, the E_{coh} , E_b and E_{mix} are fixed in the parameterization research, the properties currently computed in *speed-check* are:

- The (100) and (110) interface energies
- The total binding energies related to a list of clusters provided by the user.

In order to check the total binding energies of clusters, the user has to provide a file called *list_poscar* in the simulation directory. The *list_poscar* file is given with this format:

```
N PATH_TO_POSCAR_FILE elem1 elem2 ... elemN DFT_value
```

Where N corresponds to the number of elements present in the POSCAR file containing the cluster, *PATH_TO_POSCAR_FILE* is simply the path to the POSCAR containing the cluster, *elemX* is the element as it appears in the POSCAR (e.g. Fe, Cu, Mn, Ni, Si, P) and *DFT_value* is the total binding energy predicted by DFT (provided for comparison with the parameterization).

An example of a *list_poscar* for a 108 Cu cluster and a 88 dilute B_2 Cu cluster is given below:

```
2 ../../cfg_vasp2/POSCAR108 Fe Cu 56.65
3 ../../cfg_vasp2/POSCAR88_44_44 Fe Fe Cu 5.7778
```

For these inputs, the speed-check library performed a loop over the free parameters of the CDP model with a given range and a given step for the pair interactions. At the end of the simulation, a large file is created. Each line of this file contains a tested parameterization with associated properties that have been computed. Then, using the script language of its choice, the user can select a parameterization that match the most the properties of interest.

Annex VII

X-Y-Z clusters properties using the CDP model

Figure 1 and Figure 2 present the prediction of the CDP model concerning the binding energy between a solute atom or a vacancy with the pair also composed of solute atoms or vacancies. As the results suggest, predictions of the CDP model are quite good for attractive objects. However, for low (or negative binding energies), the predicted binding energy is less in agreement with DFT calculations.

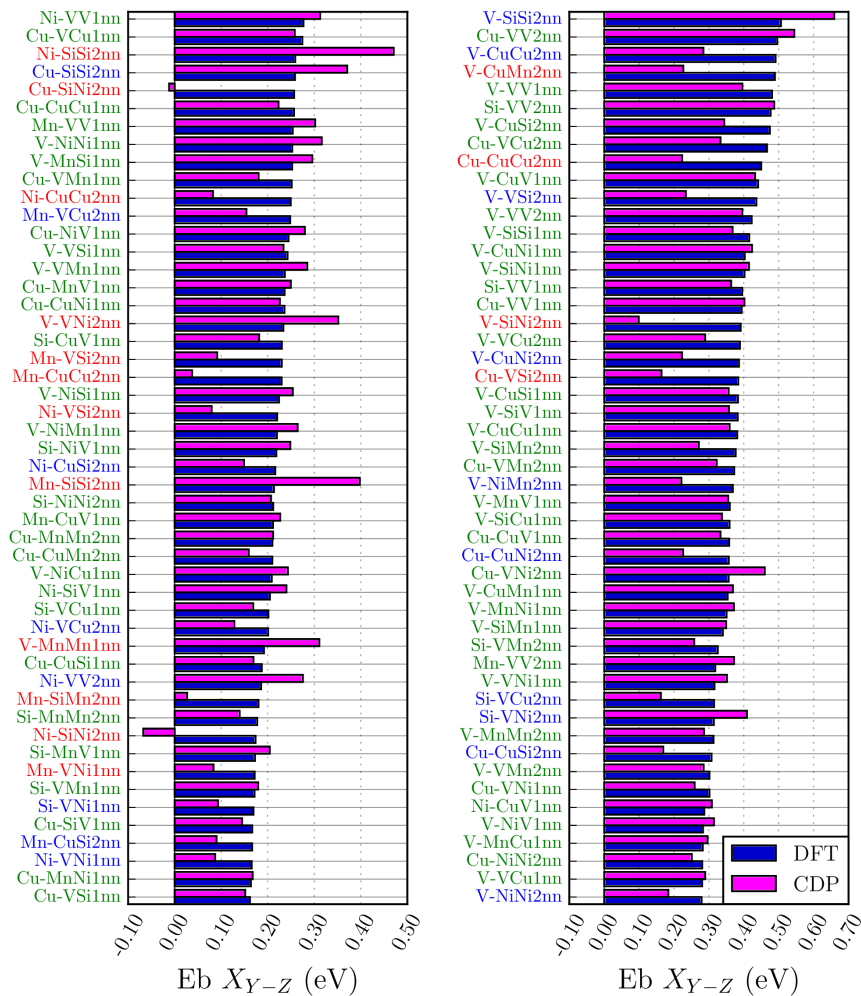


Figure 1: Binding energy between a specie X and a YZ pair for a given X-YZ triplet. 1nn and 2nn denote the nature of YZ pair. If the difference between the CDP prediction and the PAW DFT is less than 30%, the name of the cluster is written in green. If the difference between the CDP prediction and the PAW DFT is comprised between 30 and 50% the name of the cluster is written in blue. Otherwise, it is written in red.

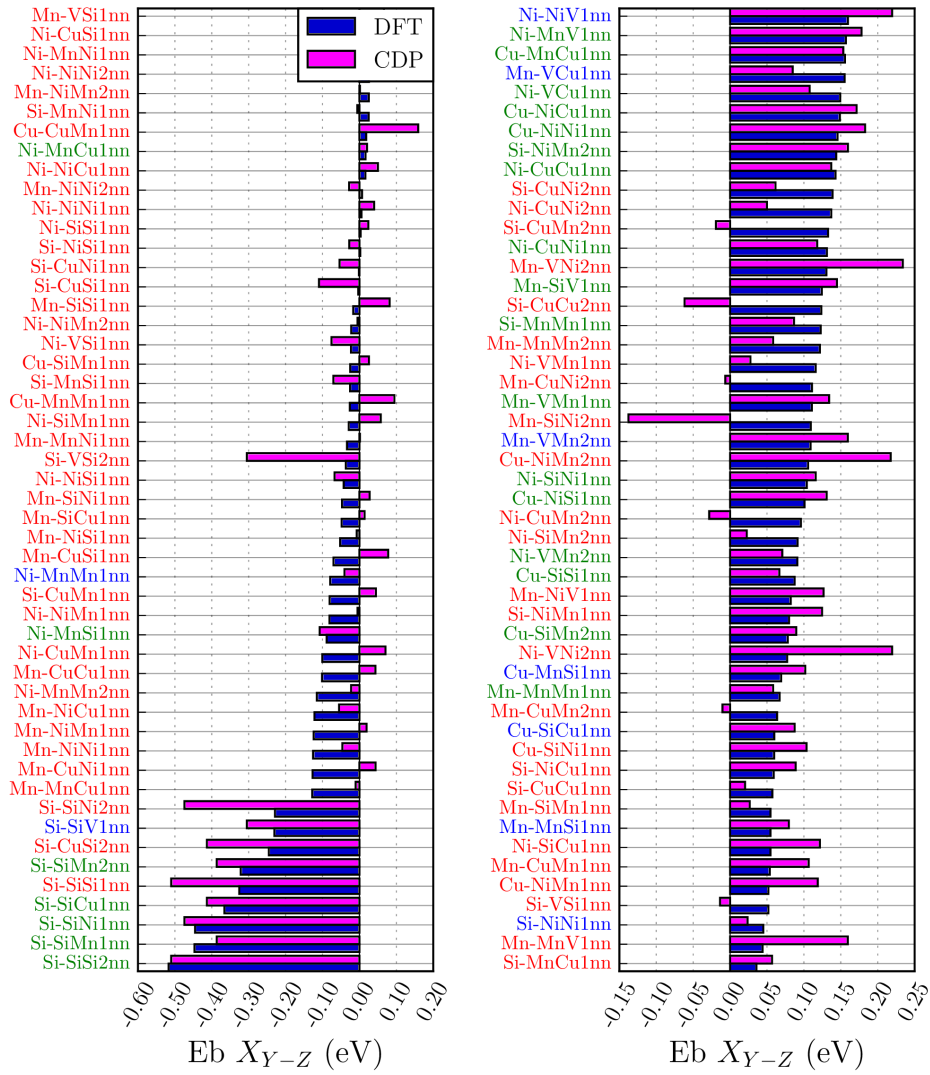


Figure 2: Binding energy between a specie X and a YZ pair for a given X-YZ triplet. 1nn and 2nn denote the nature of YZ pair. If the difference between the CDP prediction and the PAW DFT is less than 30%, the name of the cluster is written in green. If the difference between the CDP prediction and the PAW DFT is comprised between 30 and 50% the name of the cluster is written in blue. Otherwise, it is written in red.

Vers la prédiction de l'évolution de la microstructure sous irradiation d'alliages ferritiques modèles par une approche hybride AKMC-OKMC

Ce travail de thèse consistait en premier lieu à accélérer un modèle de Monte Carlo Cinétique Atomique visant à simuler l'évolution de la microstructure d'alliages modèles du type FeCuMnNiSiP représentatifs de l'acier de cuve sous irradiation neutronique. Cette accélération était nécessaire pour atteindre des doses ainsi que des flux comparables à l'expérience en des temps raisonnables. Pour cela, une accélération algorithmique du code de calcul LAKIMOCA a d'abord été réalisée. Les diverses optimisations apportées ont permis d'accélérer le code d'un facteur 7. Cette accélération ne s'avérant pas suffisante, l'approche retenue a été le développement d'une approche hybride entre une approche Monte Carlo atomique et Monte Carlo d'objets. La paramétrisation du modèle objet a permis de mieux comprendre les macro événements en jeux dans les simulations, mais s'est révélée être d'une grande difficulté lorsque la complexité chimique des objets devient trop importante. Néanmoins, l'approche hybride a apporté une accélération des temps de calcul d'environ deux ordres de grandeur permettant de simuler des doses correspondant à 40 ans d'irradiation en production. De ces résultats, différentes limitations du modèle ainsi que de sa paramétrisation ont été mises en évidence. La difficulté du modèle à reproduire des effets de flux a été comblée par l'ajout d'un absorbeur visant à réduire la force de puits des joints de grains ainsi que par l'ajout de pièges pour rendre compte de la présence d'impureté dans le fer pur. Les simulations à hautes doses dans les alliages du type FeCuMnNiSiP ont aussi mis en évidence des différences entre les microstructures simulées et celles observées expérimentalement. Ainsi, dans un second temps, un nouveau modèle de cohésion basée sur des interactions de paires dépendantes de la concentration locale a été développé et paramétré. Bien que le nouveau modèle de cohésion soit numériquement plus lourd, il a été possible d'atteindre la dose ciblée en le couplant à l'approche hybride. Les résultats obtenus sont en meilleur accord avec les calculs DFT récents ainsi qu'avec les microstructures expérimentales.

Mots clés : Monte Carlo cinétique, dommage d'irradiation, défauts ponctuels, alliages de Fe

Towards the prediction of microstructure evolution under irradiation of model ferritic alloys with an hybrid AKMC-OKMC approach

This PhD thesis work consisted, in the first place, in accelerating an atomic kinetic Monte Carlo model aiming at simulating the microstructure evolution of the FeCuMnNiP model alloys, representative of the reactor pressure vessel steels, under irradiation. This acceleration was required to reach, in a reasonable amount of time, doses and flux conditions comparable to the experimental ones. To do so, an algorithmic optimization has first been performed. The different optimizations introduced lead to an acceleration of the code of a 7 factor. Since this acceleration was not sufficient, the retained approach was to develop an hybrid between an AKMC and an OKMC. The parameterization of the object model provided a better understanding of the macro events involved in the simulations. It turns out that parameterize the model became too complex when increasing the chemical complexity of the objects. However, the hybrid approach brings an acceleration of two orders of magnitude allowing reaching doses corresponding to 40 years of irradiation in service condition. From these results, different limitations of the model as well as the parameterization were highlighted. The difficulty of the model to reproduce flux effect has been solved by adding an absorber that reduced the grain boundary sink strength. Traps have also been introduced to simulate the presence of impurities in pure iron. The high doses simulations in FeCuMnNiSiP model alloys also highlighted differences between the microstructures simulated and those observed experimentally. Thus, in a second time, a new cohesive model based on concentration dependent pair interactions has been developed and parameterized. While the new cohesive model is numerically heavier than the previous one, it has been possible to reach the target dose by coupling it with the hybrid model. The results obtained are in better agreement with recent DFT calculations and experimental microstructures.

Keywords: Kinetic Monte Carlo, irradiation damage, point defects, Fe alloys